Hyper-Velocity Impacts on Rubble Pile Asteroids

A thesis submitted for the degree of
Doctor of Philosophy

by

Jakob Deller

from
Bad Vilbel, Germany

School of Physical Sciences

University of Kent
Canterbury
U.K.

and

International Max Planck Research School for Solar System Science

Göttingen
Germany

July 2015

Summary

Most asteroids in the size range of approximately 100 m to 100 km are rubble piles, aggregates of rocky material held together mainly by gravitational forces, and only weak cohesion. They contain high macroporosities, indicating a large amount of void space in their interiors. How these voids are distributed is not yet known, as in-situ measurements are still outstanding.

In this work, a model to create rubble pile asteroid simulants for use in SPH impact simulations is presented. Rubble pile asteroids are modelled as gravitational re-aggregating remnant fragments of a catastrophically disrupted parent body, which are represented by spherical pebbles. It is shown that this approach allows to explicitly follow the internal restructuring of rubble pile asteroids during impact events, while preserving the expected properties of the bulk asteroid as known from observations and experiments. The bulk behaviour of asteroid simulants, as characterized by the stability against disruption and fragment size distribution, follows the expected behaviour and is not sensitive to the exact distribution of voids in the interior structure, but rather to the void fraction as the amount of consolidated void space in between the constituent fragment pebbles. No exact a priory knowledge of the fragment size distribution inside the body is therefore needed to use this model in impact simulations.

Modelling the behaviour of the large-scale rubble pile constituents during impact events is used as a tool to infer the internal structure of asteroids by linking surface features like hills or pits to the creation of sub-catastrophic craters. In this work, the small rubble pile asteroid (2867) Šteins is analysed. The flyby of the Rosetta spacecraft at Šteins has revealed several interesting features: the large crater *Diamond* close to the southern pole, a hill like feature almost opposite to the crater, and a catena of crater pits extending radially from the rim of the crater.

A possible link between these two structures and the cratering event is investigated in a series of impact simulations varying the interior of a plausible shape of Šteins prior to the event that formed crater Diamond. A connection between the cratering event and the hill is shown to be highly unlikely. Therefore, the hill is most likely a remnant of the formation of Šteins. Its size therefore helps to infer the initial size distribution of fragments forming the asteroid.

The formation of a fracture radially from the crater can be observed for rubble pile simulants with highly collimated voids. This fracture could plausibly form the catena of pits observed on Šteins. This can therefore serve as a link between observable surface features and Šteins internal structure. The interior of Šteins is most likely an aggregate of fragments that themselves are only lightly fractured, and large void spaces might be found inside the asteroid. As Šteins seems to be a good example of a YORPoid, an asteroid that has been evolved to a top-like shape by radiative forces due to the YORP effect, this gives first insights in the distribution of voids in the interior of this class of rubble pile asteroids.

Acknowledgements

There is a long list of people I want to thank for helping me during my PhD.

Firstly I wish to thank my full supervisory team, for their unfaltering support throughout the whole process. Thank you, Dr. Stephen Lowry, for all the help, guidance and discussions, for sending me to two memorable trips observing in Chile, and for always encouraging me to aim high. Dr. Colin Snodgrass, thank you for your frequent discussions, your effort to keeping close contact, and your constant encouragement. Dr. Mark Price, thank you for helping me through the misty waters of hydrocodes and the quick support whenever needed. Dr. Holger Sierks, thanks for your trust and for always clearing the way if needed.

I wish to thank the University of Kent for providing me the Postgraduate Research Scholarship of the School of Physical Sciences during the first part of my PhD time. I thank the International Max Planck Research School for Solar System Science at the University of Göttingen for providing me with a generous stipend during the rest of my time. I also thank the Centre for Astrophysics and Planetary Science (CAPS) and the Max Planck Institute for Solar System Research for providing workspace and all additional support needed.

There are many other persons I want to thank: Thanks to Agata, Tim, Paul, Chrysa, and all the other people in go'old Canterbury, not only in room 110 for fun and chats, also the sciency ones of course. Thanks to all my friends in Göttingen, especially Sebastian and Marc for all the help and fun. I'll never forget the time with you at all the conferences.

And of course thanks to my family and you, Johanna, just for everything.

Contents

List of Figures

List of Tables

Chapter 1

Introduction

Small asteroids in the size range of a hundred metres to a hundred kilometres are not monolithic bodies, but piles of rubble bound together mainly by gravitational forces and only weak cohesion. Little is known about the exact internal structure of these bodies. While to this day a handful of space mission acquired detailed images, shape models, and even a sample of micrometre size dust from the surface of rubble pile asteroids, no in-situ measurements of the interior have yet been accomplished.

Rubble pile asteroids are not primordial bodies from the origin of the solar system themselves, but rather second generation products of the disruption of larger, primordial bodies. In the ultimate goal to achieve an understanding of the formation and evolution of the solar system, small rubble pile asteroids are therefore a tool to understand the evolution dynamics of the Main Asteroid Belt.

In this work, a model to access the behaviour of large-scale rubble pile internal structure during impact events is presented. It is used to draw a link between the formation of surface features during impact events, and allows some conclusions on the unseen interior of the asteroid.

This chapter sets the stage of the new approach on modelling rubble pile asteroids in hypervelocity impact events. First, after a brief wrap-up of the origin of asteroids, the current understanding of their evolution and the rubble pile nature of small asteroids are discussed. Then follows an introduction to impact cratering and the numerical methods used in their investigation, and a discussion of the problem addressed in this work.
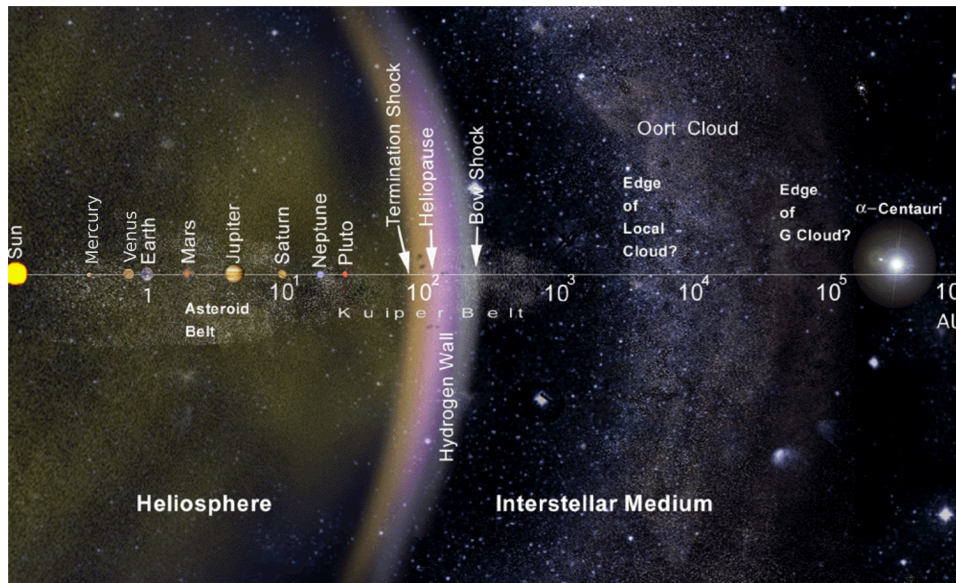
Figure 1.1: The solar system on logarithmic scale extending to α-Centauri. *After R. Mewaldt, P. Liewer Nasa/JPL, public domain*

1.1   Asteroids and Comets in the Solar System

Asteroids and Comets are remnants of the time when our solar system formed. Both are remainders of the population of planetesimals, the building blocks of protoplanets and eventually the planets themselves. The current solar system, extending over about 100 AU as seen in Figure 1.1, is dominated by the Sun which contains about 99.86 % of the system's known mass. The giant planets, dominated again by Jupiter and Saturn, contain 99 % of the remaining mass, while all the remaining objects, the four terrestrial planets, comets, asteroids and satellites together contain only the remainder, about 0.002 % of the solar system's mass.

Even if almost negligible in the mass balance, comets and asteroids record testimonies of the early solar system. Therefore, their study is essential to the understanding of the origin of the solar system. During time since the formation of the solar system 4.5 Ga ago, asteroids have surely been altered by numerous processes as collisions, internal heating, space weathering; only the understanding of these processes will allow us to disentangle original features from evolutionary ones.

1.1.1 The Solar System

In Figure 1.1, the solar system is displayed on a logarithmic scale, extending from the Sun almost in the centre of gravity until the main star on the next-closest system, α-Centauri, at a distance of 1.33 pc or 2.7×10^5 AU. The solar system is limited by the heliopause at ~ 100 AU, a border not yet reached, but approached by a human made object when the Voyager 1 spacecraft passed the termination shock at 94 AU in December 2004. The outer solar system beyond Neptune at 30 AU is still not well characterised, but in recent years the list of known Trans-Neptunian Objects (TNOs) has been expanded from the dwarf planet Pluto discovered in 1930, to 1241 objects with determined orbits accounted for in the[1] Minor Planet Center (MPC) in the year 2015.

The structure of the solar system is determined mostly by gravitational interaction of the planets. In the outer solar system, the four giant planets dominated by Jupiter and Saturn have depleted most of the smaller bodies except for those bound in resonant orbits the same distance, as for example the Trojans in Jupiter's orbit.

The inner solar system is characterised by the four terrestrial planets, with the Earth being the largest one. In between the orbits of Mars and Jupiter, the main asteroid belt is located. As seen in Figure 1.2 (and later in Figure 1.5), it is bound on the inside at the orbit of Mars, and at the outside by the gravitational influence of Jupiter. Gravitational resonances with Jupiter do empty certain orbits, opening well defined gaps known as the Kirkwood gaps which were first observed in 1866.

1.1.2 Asteroids in the Solar System

Asteroids are small, often irregularly shaped bodies, also called minor planets. There are usually distinguished from comets for the absence of ices, and no onset of activity even close to the Sun, although the discovery of Main Belt Comets (MBCs) and water on (1) Ceres has added some confusion in recent years. Currently, the Minor Planet Center lists 685 732 minor planets with determined orbits.
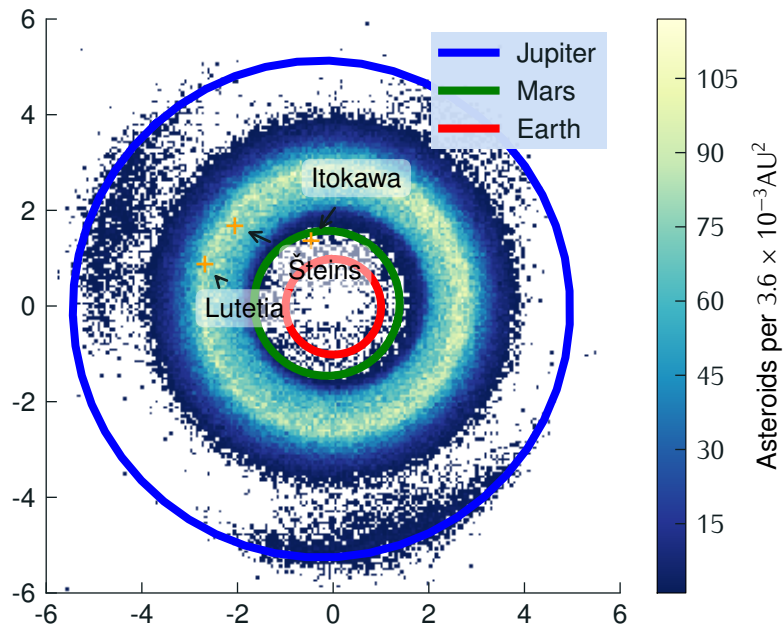
Figure 1.2:
Density plot of asteroids in the inner solar system. The highest density is in
the main belt, while the Trojans are clearly visible too. The position of three
asteroids of special interest in this work are marked. All positions refer to 1st
of January 2015. *Data retrieved from JPL/SSD* `http://ssd.jpl.nasa.gov/?sb_elem`
on Feb. 9th of 2015.

The Main Asteroid Belt

The vast majority of all known asteroids are found in the main asteroid belt. Main Belt Asteroids (MBAs) are defined as asteroids with semi major axis $2\,\text{AU} < a < 3.2\,\text{AU}$ and a perihelion distance $q > 1.666\,\text{AU}$. The largest body is the dwarf planet Ceres, with an equatorial radius[2] of $R_{\text{equator}} = 481.5\,\text{km}$, followed by (4) Vesta, (2) Pallas and (10) Hygiea. The mass of Ceres and Vesta together accounts for almost $40\,\%$ of the total mass of the main belt. Early on it was realised that the number of small bodies is much larger than the number of larger ones.

To derive a size distribution, the observed magnitude of asteroids has to be converted into a radius. As this requires knowledge of the surface parameters of each particular asteroid, this is a non-trivial problem. The apparent brightness of a reflecting body observed from Earth depends on the shape, surface reflectivity, distance and observation geometry. Usually, a geometric albedo A (often the symbol q is used) is assumed and the absolute visual magnitude H, that corresponds to the apparent magnitude of the object at $1\,\text{AU}$ distance to both Sun and Earth, is converted to a radius by the equation

$$D = \frac{1329}{\sqrt{A}} 10^{\frac{H}{5}}\,(\text{km}).$$

(1.1)

The geometric albedo is defined as the ratio of radiation emitted back into the direction of the light source (zero phase angle) to that of an flat, idealized diffusively Lambertian radiator with the same cross section. Reliable albedo determinations are rare, and Bottke et al. (2005b) argue that a constant albedo of $A = 0.092$ describes the population well, although this is clearly a simplification and differences between different compositional types are found as discussed later in Section 1.1.3

Dohnanyi (1969) showed that the power law behaviour is a result of collisional evolution. It represents the steady state where for each size bin the number of fragments produced by disruption of larger bodies equals the number of bodies in the size bin destroyed in collisional events. One of the first large surveys, the Palomar-Leiden survey (PLS, Houten et al. 1970) revealed in a sample of 2000 asteroids with visual magnitudes $H < 20$, that a single power law could not match the whole data, but a shift in power law exponent at $H = 17.5$ occurs.

---

[1] www.minorplanetcenter.org
[2] http://dawnblog.jpl.nasa.gov/2015/05/28/dawn-journal-may-28-2015/
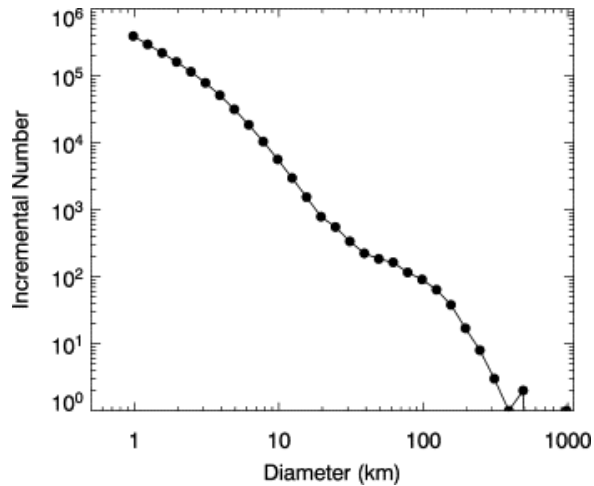
Figure 1.3: Incremental Size Frequency Distribution (SFD) of the asteroid belt population. The original data of the Sloan Digital Sky Survey (SDSS) in absolute magnitudes was converted into sizes assuming a geometric albedo of $A = 0.092$. *Reprinted from Bottke et al. 2005b*

O'Brien and Greenberg (2003) showed that the single exponent power law found by Dohnanyi (1969) indeed is a steady state for collisional evolved population, if the strength of bodies against disruption is not dependent on size. As will be discussed later, this is not the case: rather, the specific disruption threshold energy Q_D^* at which a body is disrupted is minimal for bodies with $R \approx 100\,\text{m}$ (see Section 1.3.6). The observed size distribution in more recent surveys, for example Sloan Digital Sky Survey (SDSS), Sub-Kilometer Asteroid Diameter Survey (SKADS, Gladman et al. 2009) and Subaru Main Belt Asteroid Survey (SMBAS, Yoshida and Nakamura 2007), show a more detailed picture. In the size distribution in Figure 1.3, several bumps in the distribution are seen, most notably at $D \approx 100\,\text{km}$, and less notable as the lower end of the size range, at $D \approx 3\,\text{km}$. Bottke et al. (2005b) were able to reproduce the frequency size distribution, and derived the radius dependency of Q_D^* that is later discussed in Section 1.3.6.

1.1.3 Colours and Classes of Asteroids

Colours and spectra inferred in large surveys allow us to classify asteroids into a number of classes. Chapman et al. (1975) found that asteroids could be clearly separated into two main classes. The *carbonaceous* asteroids, designated as class *C*, are asteroids with very low albedo and a neutral color. Their spectra could

6

be matched to carbonaceous chondrites, the darkest known meteorites, both in albedo as well as shape. Another class was found as having reddish colour and generally higher albedo, most showing absorption features of olivine or pyroxene. Their spectra could be related to ordinary chondrites meteorites (e.g. Chapman 1996), the most abundant meteorites found on Earth. They were designated as class *S* for *silicaceous*.

This classification was quickly amended by Bowell et al. (1978), mainly introducing the *M* class matching spectra of metallic, Nickel–Iron rich meteorites.

Today, two classification schemes are widely used, dividing the original classes further using principal component analysis and enhanced datasets: the Tholen classification and the SMASSII classification. Tholen (1989) classified asteroids into 14 types, with most of the asteroids falling into the *C* group, separated into the *B*, *F*, *G* and *C* classes mainly by albedo, the *S* class, and featureless *X* group containing *M*, *E* and *P* classes. The classification was based mainly on broadband spectra in the colours provided by the Eight-Color Asteroid Survey (ECAS, Zellner et al. 1985). Based on a large spectroscopic survey, the Small Main-Belt Asteroid Spectroscopic Survey Phase II (SMASSII, Bus 2002b), and the Small Main-Belt Asteroid Spectroscopic Survey in the near-infrared (SMASSIR, Burbine 2002) extending the spectra into the near infrared, (Bus 2002a) derived a new classification scheme purely based on spectral features. Mainly, as seen in Figure 1.4a the Tholen groups are conserved in the new scheme, and asteroids are classified in 26 classes based on the presence or absence of specific spectral features. This scheme was further updated by DeMeo et al. (2009).

Early on it was recognised that the distribution of classes in the main belt is not uniform. Figure 1.4a shows the fraction of *C* to *S* group asteroids throughout the main belt. Silicate-rich asteroids in group *S* are clearly dominant in the inner main belt, while rare in the outer part. Carbonaceous asteroids in group *C* are most abundant in the outer belt, while other types are slightly more abundant in the outer belt, but not showing as much variance. Additional peaks in their density distribution appear for the *C* group at 2.6 AU, and for the *S* at 2.85 AU. Models of the formation should not only explain the general predominance of *S* types in the inner belt, but also these secondary features.

There seems to be only a very weak dependency of the asteroid class to the observed size distribution. Gladman et al. (2009) found weak evidence for a shallower size distribution for bodies larger than equivalent to magnitude
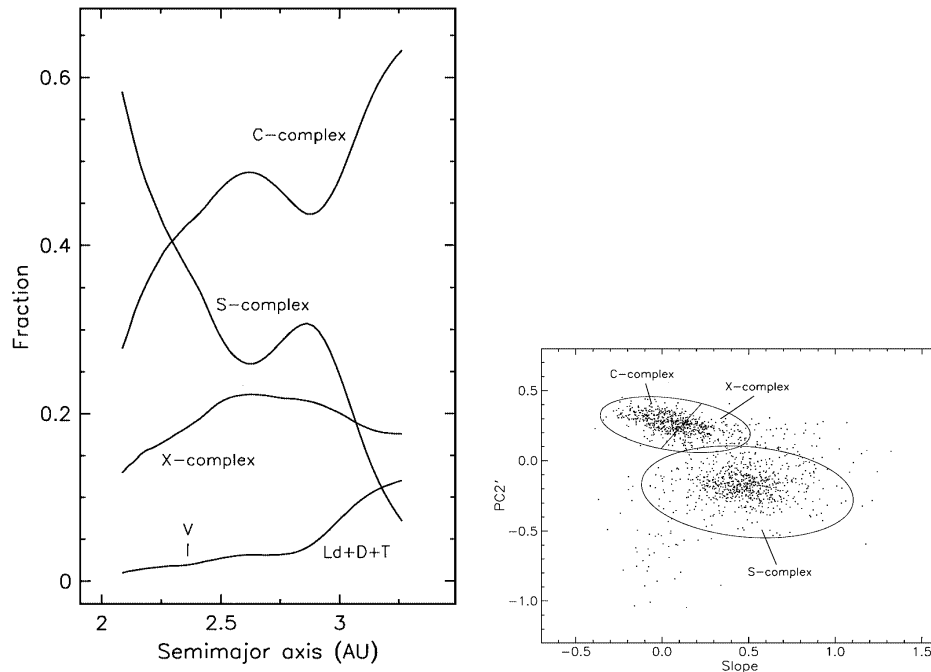
(a) Heliocentric distribution of asteroids larger $D > 20\,$km for each class complex, bias corrected.

(b) First two spectral components of the SMASSII depicting the *S*, *C* and the *X* complex. The PC2/component is mainly indicating the strength of the $1\,\mu$m absorption feature.

Figure 1.4: Asteroid classes and their distribution in the main belt from the SMASSII dataset *Reprinted from Bus 2002a*

$H < 19.5$ in the inner main belt, while August and Wiegert (2013) could not confirm any significant change in the power law slope. As position in the main belt is related to the type as seen in Figure 1.4a, this is an indication that the collisional evolution is similar for all asteroid classes.

1.1.4 Densities of Asteroids

The density of an asteroid is a fundamental property. Knowledge of volume and mass are needed to derive the bulk density, and knowledge of the mineralogy allows to determine the porosity. The link of meteorites to their parent body allows to measure the asteroids grain density on Earth, and together, they allow to infer the inner structure of objects.

Only half of the 24 classes in the SMASSII system have a conclusive link to a meteorite sample. In a large literature survey, Carry (2012) compiled a database
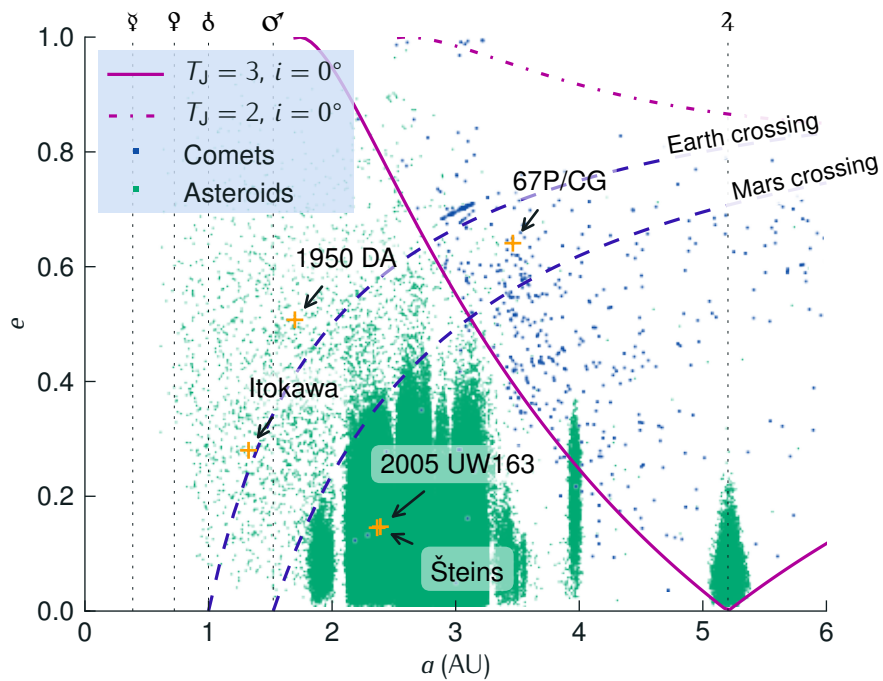
Figure 1.5: Distribution of asteroids and comets in the inner solar system. The Tisserand parameter, T_J, shows the dynamical bounding of the body to Jupiter: Most asteroids have $T_J > 3$, while most Jupiter family comets have $3 > T_J > 2$. Positions of some objects discussed in this study are marked. *Data retrieved from JPL/SSD* http://ssd.jpl.nasa.gov/?sb_elem *on Feb. 9th of 2015.*
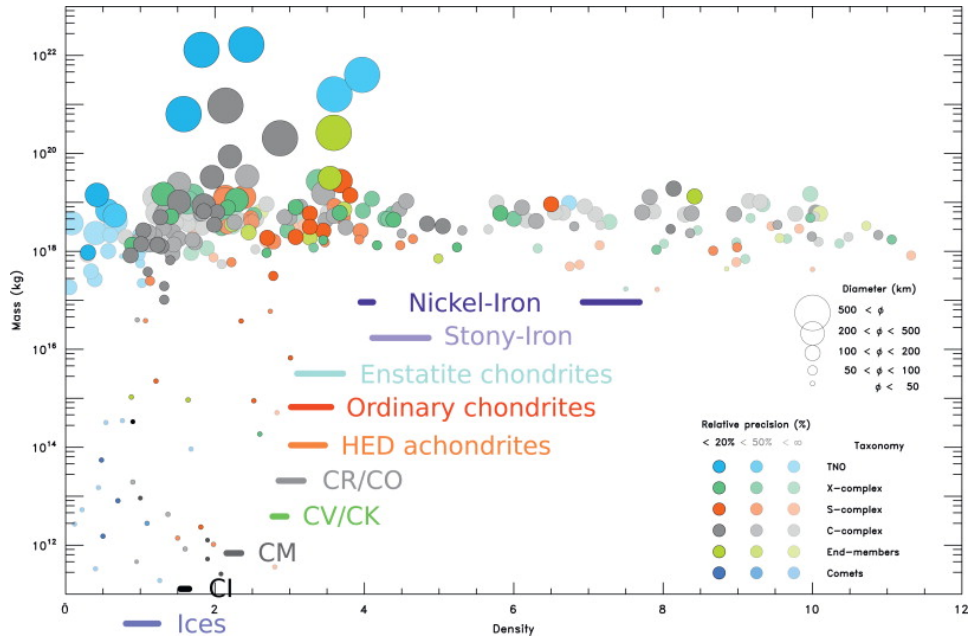
(a) Mass as a function of normalised density ($\rho/1000\,\mathrm{kg\,m^{-3}}$). Density ranges of meteorites linked to the asteroids and used to derive the grain densities are given, at arbitrary masses.
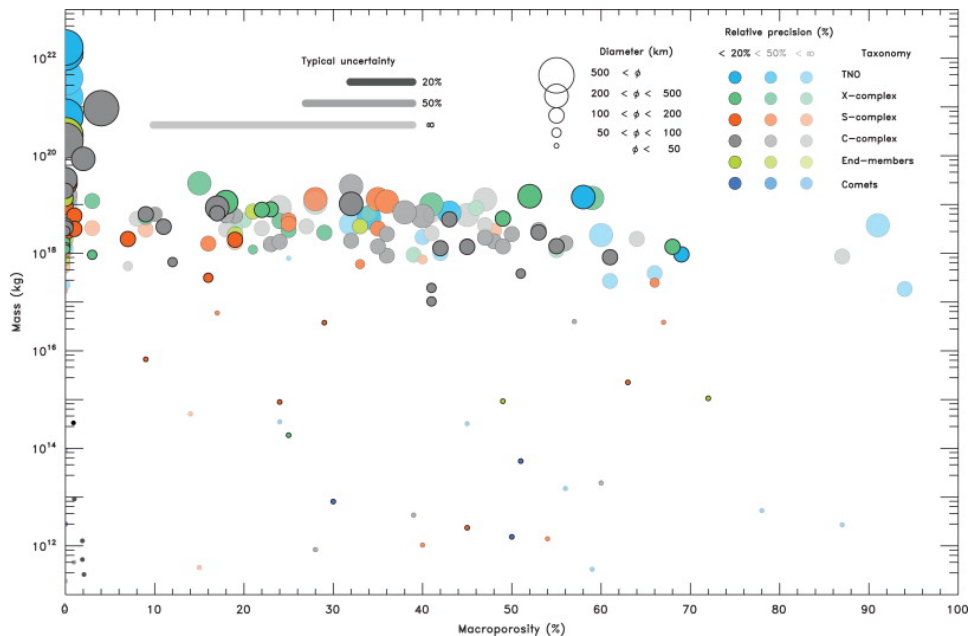
(b) Macroporosity of asteroids

Figure 1.6: Mass and macroporosity as a function of density for asteroids, comets and TNOs. The asteroid classification scheme refers to SMASSII (DeMeo et al. 2009). A total number of 287 objects are included, their relative number is not representative of the solar system. *Reprinted from Carry 2012*

of 287 small bodies with published mass and volume estimates. Most of the volume estimates rely on thermal modelling of mid-infrared radiometry with an estimated uncertainty of 10 %, while others are based on stellar occultations or spacecraft flyby with usually higher accuracy.

Figure 1.6 shows the sample of derived density estimates, most of them of C complex, 50 for both the S and X complex, and 15 as so called end-member classes, their relative numbers not being representative of the solar system.

The densities of C complex members range $\rho_{bulk} \approx 1300\,\mathrm{kg\,m^{-3}}$, up to $\rho_{bulk} \approx 2900\,\mathrm{kg\,m^{-3}}$. As can be seen in Figure 1.6a, there is a correlation of density and mass: more massive asteroids have a higher density. This seems only natural, as larger asteroids will have more lithostatic pressure, and pores and pebbles will be crushed.

The same trend is observed in asteroids of the S complex, where densities range about $\rho_{bulk} \approx 2000\,\mathrm{kg\,m^{-3}}$ to $3000\,\mathrm{kg\,m^{-3}}$. Ordinary chondrites have only a slightly higher density $\rho_{grain} \approx 2900\,\mathrm{kg\,m^{-3}}$ to $3600\,\mathrm{kg\,m^{-3}}$.

If the density of the assumed meteorite equivalent is assumed for the whole asteroid, the macroporosity is derived as the relative amount of void space or cracks larger than the micrometre scale inside the meteorites. In Figure 1.6b, it is shown that S complex members have lower macroporosities (less than 30 %) than C types (less than 60 %). This implies that S and C type asteroids have different formation history. The ordinary chondrites are igneous rocks, showing signs of being melted and having experienced higher temperatures, while carbonaceous chondrites are primitive, most likely not having experienced pre-formation melting. Carry (2012) argue that if the material in the melting and re-condensation process would acquire some cohesion, this would prevent the opening of large voids in impacts event below the disruption threshold.

1.1.5 Rotation Rate Distribution of Asteroids

The rotation rates of asteroids can be measured by lightcurve observations. The 2014 release of the LCDB contains 6979 measured periods, 4040 of high quality, as designated with a quality parameter $U > 2$ (for a definition of U, see Warner et al. [2009, Table 1]). The distribution of spin rates as a function of radius can be seen in Figure 1.7.

Based on a dataset of 688 asteroids, Harris (1996) was the first to realise the most striking feature of this distribution, a clear cut-off at a period. In his dataset, no asteroid was found with periods below $P \approx 2.2\,\mathrm{hours}$. On a larger
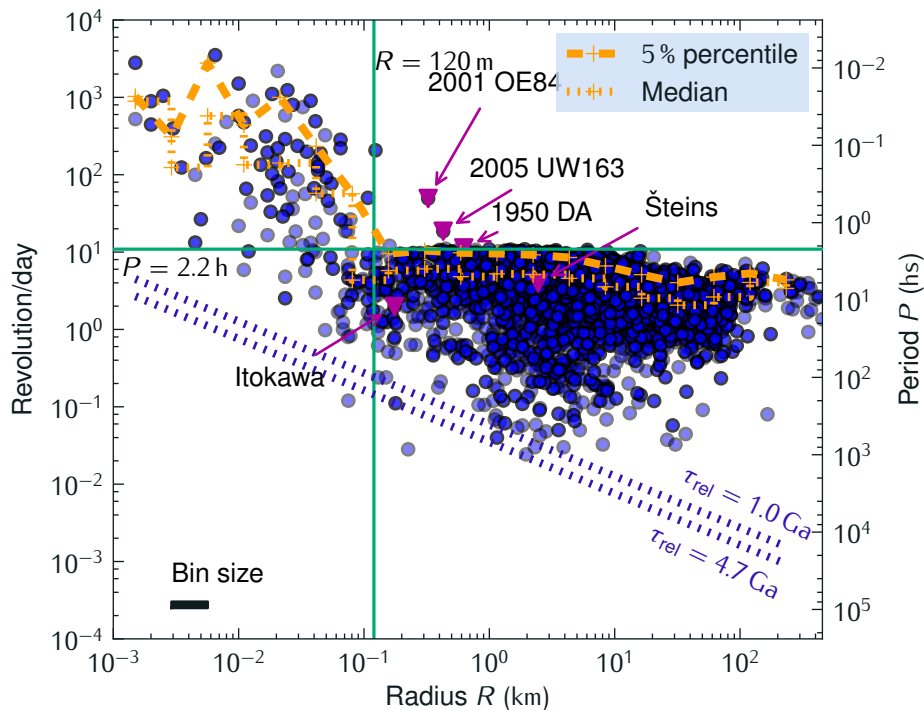
Figure 1.7: Rotation period in revolutions per day as a function of radius for
4040 asteroids in the Asteroid Lightcurve Database (LCDB) (Warner et al. 2014).
For asteroids larger than $R > 130\,\mathrm{m}$ a *spin barrier* is found at $P = 2.2$ hours.
The positions of both (2867) Šteins and (25143) Itokawa are marked, as well as
the superfast rotators 2005 UW163 (Chang et al. 2014), (2001) OE84 (Pravec
et al. 2002b) and (29075) 1950 DA (Rozitis et al. 2014).
Semi-transparent points have less well defined lightcurves than the solid ones
($U = 2$ and $U \geq 3$ for the LCDB quality parameter U, respectively). Lesser quality
data has been neglected in this plot ($U \leq 1$) The periods corresponding to
relaxation times of exited rotation due to internal energy dissipation of $\tau_{\mathrm{rel}} =$
$4.7\,\mathrm{Ga}$ and $\tau_{\mathrm{rel}} = 1.0\,\mathrm{Ga}$ are shown after Equation (1.2).

dataset, Pravec and Harris (2000) found a few fast-spinning asteroids, but all of them with sizes below $R_{\text{equiv.}} \approx 120\,\text{m}$. This cut-off is still clearly visible, as only a few asteroids so far have been found with periods shorter than 2.2 hours and radii larger than 130 m (Rozitis et al. 2014).

Almost all of the asteroids rotate in principal axis rotation. A few asteroids have been found in non-principal axis rotation (Pravec et al. 2005), all of them with long periods. In a non-rigid body, non-principal axis rotation causes stresses in the interior, which in return dampen the excited rotational state. Estimating typical parameters for the internal energy dissipation, Harris (1994) derived a size-dependent timescale for the relaxation τ_{rel} of excited rotational states. Assuming a timescale, the period-size dependency is:

$$P = 17(\text{hours}) \left(\frac{D}{(\text{km})} \right)^{\frac{2}{3}} \left(\frac{\tau_{\text{rel}}}{(\text{Ga})} \right)^{\frac{1}{3}}. \tag{1.2}$$

All object found in a tumbling state by Pravec et al. (2005) have periods longer than the line assuming a relaxation timescale of $\tau_{\text{rel}} = 4.7\,\text{Ga}$ as seen in Figure 1.7, but not all slow rotators are tumbling.

All the features of the asteroid belt are testimonial of the evolution of the solar system, and have to be explained by models of the solar system's history.

1.1.6 Formation of the Solar System

The observation of a large number of Proto-Planetary Disks (PPDs) around young stars in star-forming regions (see Figure 1.8 for an example of a direct detection, and for detection by infrared excess around young stars Haisch et al. [2001] and Wyatt [2008]) consolidated the view that stars and their planetary system form in the same astrophysical process out of the collapse of a cloud of interstellar medium of gas and dust.

The conservation of angular momentum in a contracting cloud naturally explains the formation of a thin, rotating disk around the protostar (Terebey et al. 1984; Armitage 2010). These disks have a lifetime of around 6 million years for solar like stars (Haisch et al. 2001), or even shorter for more massive stars (Carpenter et al. 2006), setting the timeline for planet formation.

In the PPD, thermal energy is added mainly by viscous processes during accretion, and by radiation from the host star. As the outer parts of the PPD receive significantly less stellar radiation, mid-plane temperatures decreases with stellar
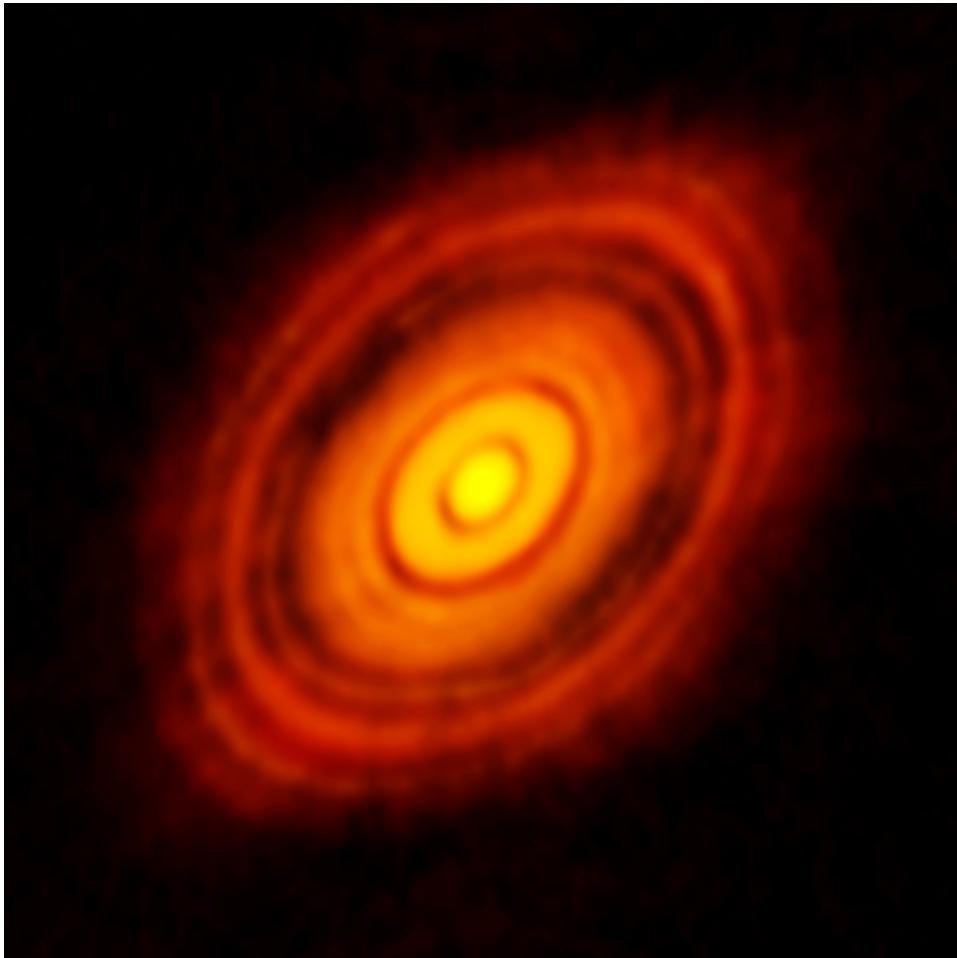
Figure 1.8: Protoplanetary disk surrounding the young star HL Tauri observed by ALMA. *Source: ALMA (ESO/NAOJ/NRAO),* *www.eso.org/public/images/eso1436a*

distance, dropping below the condensation temperatures for Calcium-Aluminium Rich Inclusions (CAI) and even water within 1 AU to 5 AU for a typical model of the early solar system (Boss 1998, Figure 1).

Forming first micro-metre sized dust, the condensed material quickly aggregates to millimetre or centimetre sized initially fluffy aggregates, that are compacted by frequent collisions (Zsom et al. 2010). At this stage, further growth by collisions is prevented by the so called bouncing barrier, as larger particles decouple from the gas in the PPD which leads to higher collision velocities. Therefore, centimetre sized bodies either bounce off or fragment in collisions (Güttler et al. 2010; Zsom et al. 2010).

To overcome the bouncing barrier, two very different scenarios have been proposed: In the mass transfer model, introduced by Windmark et al. (2012b), some 'lucky particles' at the lower end of the velocity distribution are enough to seed growth to planetesimals by mass-transferring collisions (Windmark et al. 2012a). In another model, local instabilities inside the PPD lead to overdense regions with low relative velocities, where merging collisions of larger bodies are possible and in the end a kilometre sized planetesimal is created.

These planetesimals code their position inside the PPD in their interior — because different materials have very different condensation temperatures, the composition of a planetesimal is indicative of the temperature at which the material was formed. The temperature, on the other hand, is directly linked to the position in the PPD, and again the condensation temperatures mark for each volatile species a *snow line*, the distance from the Sun at which the temperatures falls below the condensation. As water is by far the most abundant volatile species in comets, followed by a few percent of simple molecules like CO, CO_2 and CH_3OH (Bockelée-Morvan et al. 2004), cometesimals must have formed at least outside the water snow line, while most planetesimals form on the inside of the water snow line, although mixing processes in the later evolution could also explain asteroid formation outside of the snow line that would later migrate into the inner solar system. These bodies are a possible source for *C* type asteroids in the outer main belt (Walsh et al. 2012) when they loose the volatiles again, or might also source the population of MBCs recently discovered (Hsieh et al. 2004, 2010; Jewitt et al. 2010).

At this point, the formation of actual planets begins. Outside the ice frost line, where more condensed material is available, solid cores form big enough to overcome the critical core mass, when runaway gas accretion starts, and giant

planets form that open gaps in the PPD as seen in Figure 1.8. Inside the snow line, terrestrial planets form, not massive enough to capture the gas.

The whole formation process of the early solar system is quite complex. The recent advancements of techniques allowing the direct detection of extra-solar planetary systems, a multitude of protoplanetary disks imaged by modern telescopes, sophisticated computer models allowing to explore the processes involved in detail, and an ever increasing dataset of space missions and ground based surveys to understand the one in-situ model, the solar system, will hopefully lead to a deeper understanding of the processes involved. For this work, this interesting topic is merely touched to understand where asteroids fit into the picture. For further reading, the reader might want to see Armitage (2010), 'Astrophysics of Planet Formation', and the comprehensive Beuther et al. (2014), 'Protostars and Planets VI'.

Formation of Asteroids

The driving questions for the formation of the primordial asteroid belt is how to overcome the metre-sized bouncing barrier and form protoplanets or planetary embryos of a approximately 1000 km size. One important constraint for the initial Size Frequency Distribution (SFD) is the observed deviation in the size distribution of the current asteroid belt at $D = 100$ km seen in Figure 1.3.

In a attempt to model the growth phase of particles up to planetary embryos, Morbidelli et al. (2009) used a statistical coagulation/fragmentation code for collisional accretion. The only fit to the required SFD was achieved when using an initial size of 100 km for planetesimals. This led them to conclude that 'asteroids are born big', and that the first stage of planetesimal formation must somehow 'jump' from metre to hundred kilometre size. In a competing scenario, Weidenschilling (2011) was able to reproduce the primordial SFD from small planetesimals, even below 100 m using a particle-in-a-box simulation.

Several processes that could explain the creation of large planetesimals are discussed in the review by Johansen et al. (2014), 'The Multifaceted Planetesimal Formation Process'. Particle concentrations in the gas containing PPD can become unstable and lead to a runaway growth to planetesimal size. The streaming instability (Youdin and Goodman 2005; Johansen et al. 2012) where aerodynamic drag of solid particles moving relative to the gas exert a back-reaction force onto the gas. For larger particles that couple to the gas (a Stokes number of 1), overdense regions appear that reach almost 1000 times the gas density.

These overdense region can then gravitationally collapse to form planetesimals (e. g. Wahlberg Jansson and Johansen 2014).

1.1.7   Early Evolution of the Asteroid Belt

During their formation, the interaction with the gas leads to the migration of planets to the centre of the disk. Due to orbital resonances, the inward migration of an early Jupiter prevents the formation of a planet outside the orbit of Mars as well as shortening the reservoir of planetesimals for Mars, leading to the low mass of this planet. This inward migration process can be observed in many exoplanetary systems, and explains the existence and abundance of Hot Jupiters, giant gas planets that have orbits very close to their host star (Udry and Santos 2007). In the solar system, Jupiter's inwards migration was stopped only because there was another planet, Saturn. Orbital resonances with Jupiter caused a *grand tack* (Walsh et al. 2012), reversing their migration towards the outer solar system and catching the outer planets, Uranus and Neptune, forcing them to migrate outwards too. This scenario, called the Grand Tack and the Nice model in later stages, is mainly founded on the basis of numerical experiments, being able to reproduce most characteristics of todays configuration of the solar system starting at a likely, but arbitrarily chosen initial configuration (Tsiganis et al. 2005; Gomes et al. 2005; Morbidelli et al. 2005, 2012).

This scenario is challenged for example by the colour distribution found in TNOs (Hainaut et al. 2012). The colour characteristics of both Detached Disk Objects (DDOs) and hot Classical Disk Objects (CDOs) (for a definition see e g. Figure 3 in Lacerda et al. [2014]) can currently not be explained. While until now, the Nice model was always successfully adjusted to include new dynamical constrains, it predictive value is limited due to the large number of parameters involved.

In this process of reversing Jupiter's migration from inwards to outwards, most of the main asteroid belt was left, as a reservoir of planetesimals still gravitational influenced by Jupiter. Excitation of orbital parameters is especially strong in mean motion resonances: These are orbits, where the period of one of the bodies involved is an small integer multiple of the other body. The periodic occurrence of close approaches leads to a destabilization of the asteroid's orbit. These resonances with Jupiter deplete the asteroid belt, leading to the Kirkwood gaps observed in its present form. This constant stirring has also another consequence: small bodies in the solar system constantly suffer the

threat to be destroyed in a disruptive collision.

1.1.8 Collisional Evolution of the Asteroid Belt

In numerical experiments to infer the size distribution of the main belt after the formation of planetary embryos, prior to the runaway gas-accretion that formed Jupiter, Bottke et al. (2005b) were able to constrain the size-dependent collisional history of asteroids. While they found that asteroids larger than $D = 120\,\mathrm{km}$ are most likely primordial objects or left-over pre-planetesimals, most smaller asteroids are remnants of catastrophic disruptions. The exact size of this transition is model dependent, particularly on the assumed shape of the strength scaling parameterized by the disruption threshold Q_D^* (see Section 1.3.6). Binzel et al. (1989) found a transition in the statistical distribution of rotation periods at a size of $D = 125\,\mathrm{km}$, as they found that the distribution of rotation rates for bodies larger than this value followed a Maxwellian distribution, while smaller bodies show an excess of slow rotators. As a com-

Figure 1.9: Asteroid rotation rate as a function of radius. Same data as in Figure 1.7, but focused on the size range of $1\,\mathrm{km}$ to $150\,\mathrm{km}$. In the median, a clear V shape can be seen, with a minima at $R_{\mathrm{equiv.}} \approx 54\,\mathrm{km}$.

pletely collisional relaxed population should follow a Maxwellian distribution of rotation rates assuming Gaussian velocity distribution (Pravec et al. 2002a; Salo 1987), this leads to the conclusion that the large asteroids have preserved the characteristics of the primordial asteroid belt. This transition coincides with the minimum in the distribution of rotation rates shown in Figures 1.7 and 1.9 at $R_{\mathrm{equiv.}} \approx 54\,\mathrm{km}$, which could well be a confirmation of the primordial nature of these bodies. It is further supported by the age of the surface seen on the asteroid (21) Lutetia, with dimensions of $121\,\mathrm{km} \times 101\,\mathrm{km} \times 75\,\mathrm{km}$, showing in some re-

gions a SFD corresponding to a crater retention age of (3.60 ± 0.01) Ga (Sierks et al. 2011; Weiss et al. 2012). Lutetia is therefore most likely a primordial body.

While this does not signify that all asteroids smaller than this size range must be second-generation asteroids, fragments of disrupted large bodies should be abundant in the asteroid belt. The size distribution of asteroid families formed during collisional disruption of a large parent body was found to match only simulations that take gravitational re-accumulation into account (Durda et al. 2007; Benavidez et al. 2012). Also, simulations by Michel and Richardson (2013) have shown, that the rubble pile asteroid Itokawa can be formed by re-aggregation of a catastrophically disrupted parent body.

1.1.9   Radiative Forces as Driver of Asteroid Evolution

While gravitational forces can explain most of the dynamics in the solar system, in the last 20 years it became more and more clear that subtle radiative forces shape some aspects of the solar system significantly. In the case of asteroid families in the main belt, backwards integration of the orbits of family members resulted in a velocity field of the escaping ejecta that did not match the results found by the simulation of collision events. Another puzzling fact was the bimodal distribution of spin rates found on members of the Koronis family (Slivan 2002).

The constant crater production rate observed on lunar maria implies that the process delivering main belt objects into the Near-Earth Object (NEO) population is a continuous process, rather than supplied by sporadic but major events like collisions of very large objects, as these should result in a much larger number of asteroid families that is not observed (Nesvorný et al. 2002). Also, orbital distributions of the observed asteroid families do not fit in the image of a purely collisional evolved disruption event: the peak velocities in the size-velocity distribution are higher than expected, and the spin rates observed do not follow the expected Maxwellian frequency distribution (Vokrouhlicky et al. 2003; Michel et al. 2001). This all indicates that the classical model is not complete, and gravitation is not the only force shaping the evolution of asteroids.

In this situation, thermal effects that had been described almost 100 years ago in a pamphlet by I. O. Yarkovsky and picked up again by Opik (1951) got new attention. The radiation of the Sun, reflected or absorbed by the surface of a solar system object and then re-radiated into space can, under certain circumstances, alter the orbit and the rotation state of the asteroid.
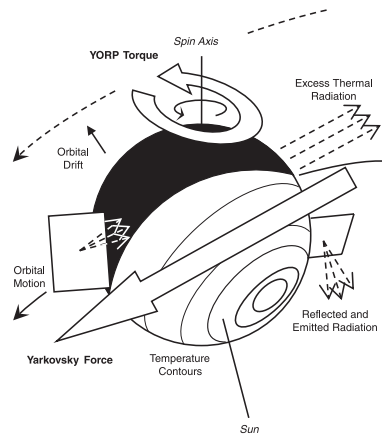
Figure 1.10:
Schematic of the Yarkovsky and
YORP effect on the orbit an spin
properties of small asteroids. *Reprinted from Rozitis and Green 2012*

For bodies roughly larger than the penetration depth of the annual or the
diurnal thermal wave, there are two effects which cause alteration of the body's
state of motion (see Figure 1.10 for a schematic): The Yarkovsky effect is caused
by the thermal inertia of the body. As the absorbed radiation is re-emitted after
a certain time delay, the body has rotated, resulting in a net force altering the
orbit. The Yarkovsky-O'Keefe-Radzievskii-Paddack (YORP) effect is a net force,
resulting from asymmetric features of the body, and altering its rotation rate
and obliquity. The two effects, Yarkovsky and YORP, are both results of solar
radiation, heating up the surface of the asteroid, transferring momentum to the
asteroids' surface, not only by the incoming radiation, but also and much more
important by the photons of the heat radiation emitted into space. A good review
of both effects can be found in Bottke et al. (2006), 'The Yarkovsky and YORP
effects: Implications for asteroid dynamics', a more recent one in Vokrouhlicky
et al. (2015), 'The Yarkovsky and YORP Effects'.

The Yarkovsky Effect

The Yarkovsky effect, first described around 1900, only received attention about
50 years later after a discussion paper by Opik (1951). A body heated by
absorption of solar radiation will re-emit the energy into space in the far infrared
according to the Stefan-Boltzmann blackbody radiation. Both the absorption
as well as the re-radiation transfer momentum to the body. In the case of an
ideal surface following Lambert's Law, and assuming instant re-radiation, the
net force acting on the body is directed radially. Therefore, the state of motion
is not changed. But real bodies have a non-negligible heat capacity, causing a

delay of the re-radiation. This delay is described by the empirical term *thermal inertia* γ, that subsumes the effect of surface thermal conductivity K, density ρ, material specific heat capacity c as $\gamma = \sqrt{K\rho c}$.

As the body rotates, causing the *diurnal* Yarkovsky effect and continues to move on its orbit causing the *seasonal* Yarkovsky effect, the hottest point on the surface does not any more point towards the Sun, resulting in a net force that decreases the semi major axis a of the orbit of the body.

Vokrouhlicky et al. (2015) describe the following characteristics of the Yarkovsky effect:

- The seasonal change in a is always negative, shrinking the orbit of the body, and most effective if the rotation axis of the body is in the orbital plane (obliquity $\Theta = \pm 90°$).

- The diurnal effect in contrast is able to shrink or expand the orbit, depending on the sign of $-\cos\Theta$. Retrograde rotators shrink, whereas prograde rotators expand their orbit.

- The Yarkovsky effect is strongest when the penetration depth of the thermal wave is of the order of the radius R.

- The diurnal effect is proportional to $\cos\Theta$, the seasonal to $\sin\Theta^2$. Therefore, the diurnal is maximal at $\Theta = 0°$ and $180°$, while the seasonal is maximal at $\Theta = 90°$.

Detection of the Yarkovsky effect has been possible directly on several asteroids, first by Chesley et al. (2003) on asteroid (6489) Golevka. While the acceleration due to the Yarkovsky effect is tiny, around $1\,\mathrm{pm/s^2}$ for Golevka, a NEO of $500\,\mathrm{m}$ radius, the change in orbit over a time of just about a decade resulted in an offset of $15\,\mathrm{km}$ compared to the position predicted based purely on gravitational forces, detectable in radar delay measurements to a high level of confidence.

The YORP Effect

When photons are radiated from a Lambertian radiator, a net reaction force normal to its surface will result from the momentum carried away by the photons. On a spherical body, the sum of all forces will be zero and no net force will be produced. This is, however, not true if the body has some wedge-like, asymmetric

feature as schematically seen in Figure 1.10: like a windmill, it can produce a torque, altering the rotation period and obliquity of a body. The acronym YORP (Yarkovsky-O'Keefe-Radzievskii-Paddack) was first used by Rubincam (2000) in a publication giving a thorough discussion of the effect. In a simplified model of a spherical asteroid with two wedges attached, a net torque is produced, because even if the radiation of both planes has the same magnitude, the different directions will cause a recoil that does not average out over one revolution.

The torque changes both the rotation as well as the obliquity of the asteroid, and its sign depends of the exact surface features and the thermal properties of the surface layer, thus for the calculation of YORP strength an accurate shape model of the asteroid is needed. The resulting force is given by the summation over all surface elements, the major unknown being the temperature of each element. The temperature has to be calculated from the incoming energy, determined by the solar radiation absorbed, depending on its shape and albedo, and how this energy is conducted into the body. In contrast to the Yarkovsky effect, YORP will be effective even when the thermal conductivity is zero, because the direction of the torque is mainly defined by the shape of the object.

To calculate the value of YORP torques exerted on the rotating asteroid, detailed thermophysical models have to be used. Rozitis and Green (2011), among others (e. g. Statler 2009; Breiter and Vokrouhlicky 2011), developed a thermophysical model of rough asteroid surfaces incorporating explicit treatment of partial shadowing, self-heating by thermal irradiation between surface elements, and thermal-infrared beaming. The effect of thermal-infrared beaming, or the strong non-lambertian re-radiation towards the Sun on rough surfaces, was further analysed (Rozitis and Green 2012), and global shadowing effect and self-heating was implemented (Rozitis and Green 2013). Applying the model to a set of asteroids with known shapes, Rozitis and Green (2013) found that while self-heating and shadowing had only small influence on the magnitude of the Yarkovsky effect, the YORP amplitude is indeed highly sensitive.

Both the dependency of rotation rate ω and the obliquity Θ can be described using Legendre polynomials (Vokrouhlicky et al. 2015). The amplitude of the YORP effect, C_{YORP}, is proportional to R^3, and inversely proportional to the principal moment of inertia I, which itself is proportional to $I \propto R^5$, resulting in a total dependency of $C_{\mathrm{YORP}} \propto R^{-2}$.

The roots of the second-degree Legendre polynomials lead to obliquity values of $\Theta \approx 55°$ and $\Theta \approx 125°$ where the amplitude C_{YORP} is zero, compellingly

explaining the vanishing of the rotation rate YORP effect at these values numeric-ally found before by Rubincam (2000). Also, observational evidence showed that the spin orientation in the collisional asteroid family Koronis (Slivan 2002) and Flora (Kryszczyńska 2013) are indeed not following a Maxwellian distribution, as collisional origin would produce, but rather distributed bi-modal, with 42° to 50° for prograde, and 154° to 169° for retrograde rotators in the Koronis family (Slivan et al. 2003). This gives indirect evidence for evolution due to YORP after the family creating event, and first hand evidence for the importance of the effect in the evolution of the asteroid belt.

The YORP effect was first detected directly by Lowry et al. (2007) and Taylor et al. (2007) on asteroid (54509) YORP. Using four years of high precision lightcurve data, a phase shift of $\mathrm{d}\omega/\mathrm{d}t = (35.0 \pm 3.5) \times 10^{-7}\,\mathrm{rad/d^2}$ was found (Lowry et al. 2007). This fitted well the YORP strength predicted by Taylor et al. (2007), based on a shape model derived from range-Doppler images.

Further detection have been made on five other asteroids so far, including Itokawa (Lowry et al. 2014). Itokawa not only showed a acceleration in rotation rate of $\mathrm{d}\omega/\mathrm{d}t = (3.54 \pm 0.38) \times 10^{-8}\,\mathrm{rad/d^2}$, but thermophysical modelling of the YORP strength using the detailed shape model from the Hayabusa mission revealed an offset of the centre of mass by approximately 21 m. This could be explained if Itokawa is not homogeneous, but instead composed of two separate bodies, a dense 'head' on a more porous 'body'.

Shape Evolution by YORP Spin-Up

The magnitude and sign of the YORP torque are both very sensitive to the exact shape of the asteroid. Recent studies seem to indicate a preference for spin-up (Vokrouhlicky et al. 2015). For essentially strengthless bodies, changes of the spin rate cause internal reconfiguration by relaxation of stresses compared to the hydrostatic equilibrium figure, although the idealised fluid equilibrium is never reached due to the non-negligible, though small surface friction between the rubble constituents.

Representing rubble pile asteroids using a soft-sphere approach, Walsh et al. (2008) and Sánchez and Scheeres (2012) showed that asteroids suspected to YORP spin-up indeed rearrange into a top-like shape (as example, see Figure 1.12), with a pronounced bulge at the equator, also denoted as a YORPoid shape (Lowry 2015). The final shape is depending on the properties of the granular material, as commonly described by the angle of repose, the critical
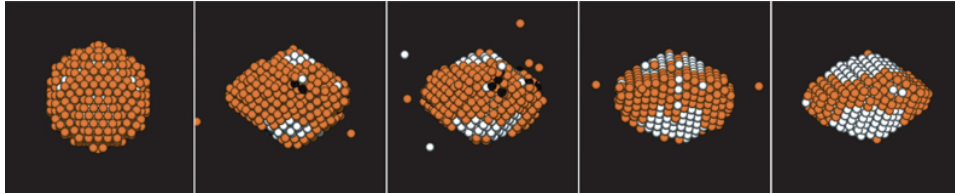
(a) Reorganisation of rubble pile asteroid model during spin-up, possibly produced by YORP. Spheres at the initial surface a coloured orange. Snapshots of approximately 1000 asteroid rotations are shown.
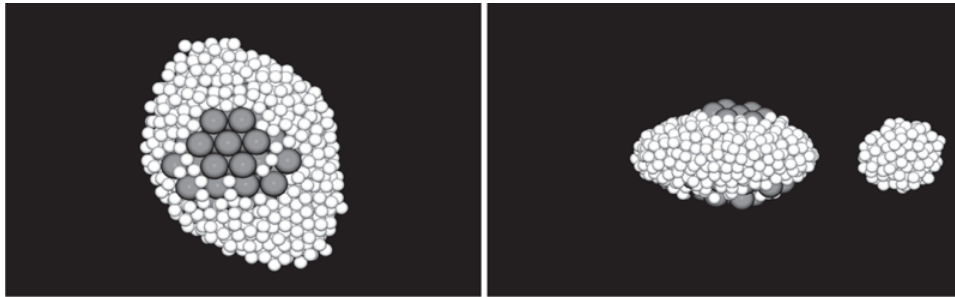
(b) Formation of a binary asteroid system in asteroids with a rigid core, looking down the primary spin axis (left panel) and looking along the equatorial plane (right panel).

Figure 1.11: The effect of YORP induced spin-up on rubble pile asteroids, as modelled using hard-sphere particles. *Reprinted from Walsh et al. 2008*
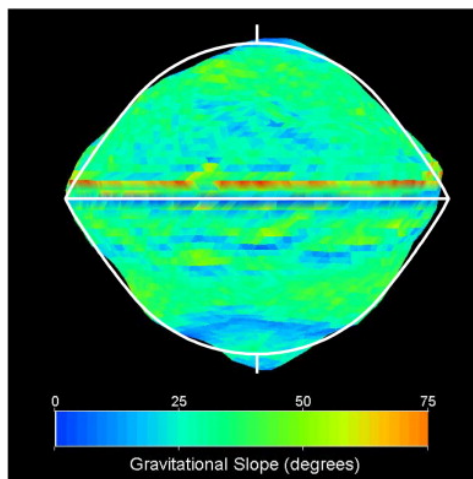
Figure 1.12: Constant-slope figure (white line) compared to the shape and gravitational slope of (66391) 1999 KW4 (Scheeres et al. 2006; Ostro et al. 2006). Critical slope angle was 37°. *Reprinted from Harris et al. 2009*

angle at which granular flow will start. As seen in Figure 1.11a, most of the material forming the equatorial bulge is reorganised surface material from the poles, rather than material from the interior of the body. This shape actually has been found in many asteroids, first of many in the primary asteroid of the binary asteroid pair 1999 KW4 (Ostro et al. 2006). Tanga et al. (2009) showed in a series of simulations, that indeed the observed distribution of axial ratios and therefore the bulk shapes of asteroid can be reproduced using a N-body approach of spherical 'pebbles' with surface friction. While this interpretation of top-shaped asteroids as being shaped by YORP induced spin-up seems conclusive, Statler (2015) cautions that the evidence is not yet without doubt. As YORP strength is strongly depending on asymmetric surface features, the amplitude of the rotational part will decrease when the bulk reshaping form exactly these top-like, symmetric shapes. This so called YORP self-limitation is seen in coupled N-body–YORP strength calculations (Cotto-Figueroa et al. 2015). In these simulations, for low internal angles of friction no evolution of top-shaped, axisymmetric bodies could be observed. Also, the timescale of changes in obliquity, at least for nearly axisymmetric bodies, is an order of magnitude shorter than for changes in rotation rate, therefore the observed bi-modal obliquity distribution does not necessarily attribute the top-like shape to YORP spin-up (Statler 2015).

During the spin-up of asteroids, not only an equatorial bulge is formed, but also material is shed from the equator, possibly under certain conditions forming a binary (see Figure 1.11b) (Walsh et al. 2008; Pravec et al. 2010; Sánchez and Scheeres 2012).

Under the condition, that the secondary asteroid is tidally locked and therefore the orbital and rotational periods are locked, Ćuk and Burns (2005) showed that the binary system itself is shaped by thermal emission forces on asymmetric bodies again. The Binary YORP (BYORP) effect acts in damping the binaries orbit, and synchronising the secondary's spin on timescales of 10^4 a to 10^5 a. Although there has not been any direct observation of the BYORP yet, a large campaign has been started to observe candidate systems. This process has been suggested as one of the possible origins of the bi-lobe structure of asteroid Itokawa (Lowry et al. 2014), that might have formed by the re-impact of a satellite formed earlier by mass-shedding.

1.2   The Interior of Asteroids

1.2.1   Models of the Internal Structure of Asteroids

Generally, a rocky body can be monolithic, fractured, or a rubble pile (Asphaug et al. 2002). A monolithic body contains practically no macroscopic voids and its strength is determined by the material itself. Therefore, it shows high tensile strength, and transmits stress wave efficiently. Surprisingly, this means that large monolith are easier destroyed by impact events than fractured or rubble pile bodies of the same size (e. g. Benz and Asphaug 1999)

   Because the size distribution of impactors follows approximately a power law, small impacts occur much more frequent than larger ones. Therefore, even if no disruptive impact event destroys such a monolith, frequent sub-disruptive impacts will shatter the interior. In this process, the body looses almost all tensile strength, but for impacts where the fragments are not dislocated the macroporosity is still very low and stress wave are transmitted almost as easily as in monolithic bodies (Michel et al. 2003). In impacts of higher energy, the fragments are dislocated and rearrange in a loose packing, significant void space is introduced and the result is a rubble pile asteroid. These bodies transmit stress waves very inefficient and have practically no tensile strength.

   If a large protoplanet of several hundred kilometre size is destroyed and dispersed in a collision event, gravity pulls together the resulting fragments to form a set of asteroids, sharing most attributes like composition and dynamics, but separating dynamically mostly due to size effects afterwards (Michel et al. 2015). The detection of several asteroid families give evidence of the frequent occurrence of these events. The smaller asteroids resulting from re-aggregation of fragments do not have enough mass and therefore hydrostatic pressure in their interior, to reprocess the material by melting the core and rearranging to a spherical shape. During this aggregation phase, where mainly low velocity impacts occur, asteroids are formed that are not compacted, but resemble more loosely bound piles of rubble, containing void space. This is matched in the derived void fractions for asteroids smaller than $R_{\mathrm{equiv.}} \approx 155\,\mathrm{km}$ of which both mass and radius have been measured, that show high macroporosities of up to 70 % (Carry 2012).

   While the image of monolithic, fractured or rubble pile interior is true for small asteroids, the existence of igneous meteorites is proof of melting and differentiation occurring in planetesimals (e. g. McCoy et al. 2006). For melting

of chondritic material, temperatures above $\sim 1223\,\mathrm{K}$ are needed. These temperatures can neither be reached by accretional heating nor decay of long-living radionuclids. Also, impacts events providing such temperatures throughout the body would most likely destroy the body in the process (McCoy et al. 2006). Currently the best candidate as a heat source is the decay of the short-lived radionuclid ^{26}Al. Decay products, mostly ^{26}Mg, are present in most classes of chondrites, and the ratio of ^{26}Al/^{27}Al found in CAI suggest that ^{26}Al was present and homogeneously mixed in the PPD (Huss et al. 2001). The halftime of ^{26}Al is $(0.705 \pm 0.024)\,\mathrm{Ma}$ (Norris et al. 1983). This is congruent with a fast formation of planetesimals within $4\,\mathrm{Ma}$ (Huss et al. 2001).

The Dawn spacecraft provided evidence for planetary tectonics on Vesta, consistent with a fully differentiated mantle/core structure (Buczkowski et al. 2012). The even larger Ceres has a low density, but nevertheless was described as a differentiated object due to its shape indicative of a gravitational relaxed object (Thomas et al. 2005). Even the much smaller asteroid Lutetia was found to be most likely partially differentiated (Weiss et al. 2012). Therefore, the interior of large asteroids probably differs widely from the structures found in small asteroid.

As the focus of this work is on small asteroids, in the following the interior of rubble pile asteroids is discussed.

1.2.2   Rubble Pile Asteroids

Most asteroids are not monolithic bodies, but consist of numerous smaller fragments, and are called rubble piles.

Richardson et al. (2002) summarised the arguments leading to this conclusion:

Spin barrier The observed spin barrier for asteroids larger than $R > 130\,\mathrm{m}$ (see Figure 1.7) that are found to not spin faster than $P = 2.2\,\mathrm{hours}$ (Pravec and Harris 2000). This is in good agreement with the assumption that asteroids larger than a few hundred meters are bound mainly by gravitation and negligible cohesion.

High macroporosity The high macroporosities found in asteroids. Not only have asteroids visited by spacecraft shown high values of macroporosity, like 40 % on Itokawa by the Hayabusa mission (Saito et al. 2006; Abe et al. 2006) and Šteins by Rosetta (Jorda et al. 2012), but also earthbound
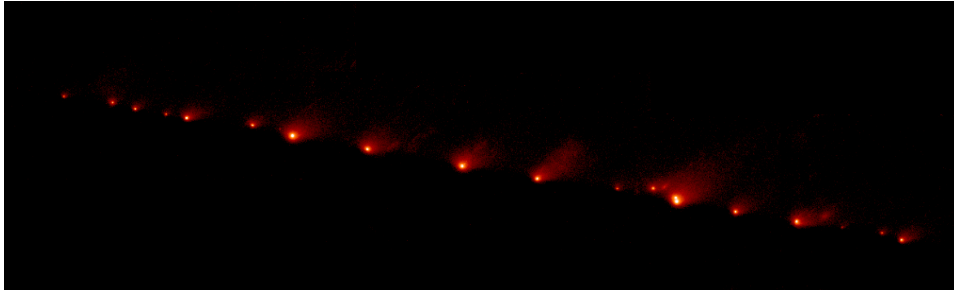
Figure 1.13: Comet D/Shoemaker-Levy 9 after it broke up into 21 almost equally large fragments lining up to 1.1×10^6 km in 1994. This indicated a very weak material strength, and could be simulated by using a cohesionless rubble pile model (Asphaug 1996). Composite of images taken by the Hubble Space Telescope in May 17, 1994. *Public domain, NASA, ESA, and H. Weaver and E. Smith (STScI)*

surveys of asteroids revealed macroporosities ranging up to 70 % for bodies with diameters smaller than 500 km (Carry 2012). These high values can be explained by void space between interlocking single constituent fragments.

Tidal breakup The observation of crater chains on Ganymede and Callisto or our Moon (Schenk et al. 1996) showed that tidal breakup as observed on comet D/Shoemaker-Levy 9 (SL9) was not a singular event. SL9 apparently had been disrupted by tidal forces during a close encounter within the Roche limit in July 1992, forming 21 fragments of 500 m to 1000 m size (see Figure 1.13). Modelling the breakup of SL9, used to provide an important benchmark for early (Asphaug and Benz 1994) as well as recent (Movshovitz et al. 2012) studies modelling granular materials. Schenk et al. (1996) estimate that such an event occurs every (275 ± 100) years in the Jovian system, which implies that most, if not all, comets have only weak strength.

Farinella et al. in 1982 concluded that almost all asteroids are outcomes of catastrophic collisional disruption events, and that asteroids smaller than 100 km have undergone multiple shattering and disruptions. Therefore, the constituents of a rubble pile asteroids are themselves fragments of a collision, and their size distribution and shape will be a result of the disruption event that destroyed the parent body. In the case of asteroids Eros and Itokawa, Michikami et al. (2010) endorsed this scenario by showing that the shapes of boulders

found on the surface match those of fragments of impact experiments.

1.2.3   The Spin – Size Barrier of Asteroids

Rubble pile asteroids larger than $\sim 100\,\text{m}$ are mainly bound by gravitation, and cohesive effects play a minor part in their long-term behaviour. This naturally also explains the apparent spin-size barrier found for asteroids with diameters larger than $150\,\text{m}$, that are found not to have periods shorter than $2.2\,\text{hours}$ (Pravec et al. 2002a; Kwiatkowski 2010).

   The critical rotation period $P_c = 2\pi/\omega$ for an object purely bound by gravitational forces is where gravitational acceleration at the surface equals the centrifugal acceleration at the equator.

$$\frac{GM}{R^2} = \omega_c^2 R, \tag{1.3}$$

where G is the gravitational constant, ω the angular frequency, R the radius of the object, and M the mass that can also be written in terms of the object's density ρ as $M = 4/3\pi R^3 \times \rho$. This leads to

$$P_c = \left(\frac{3\pi}{G}\frac{1}{\rho}\right)^{1/2} = 3.301 \left(\frac{[\text{g/cm}^3]}{\rho}\right)^{1/2} [\text{hours}]. \tag{1.4}$$

Again, assuming no cohesive forces, the observed spin barrier at $2.2\,\text{hours}$ corresponds to a density of $2250\,\text{kg\,m}^{-3}$. While this is mostly in agreement for densities of asteroids except iron-rich ones (class *Xc*, *Xk* and *K*, see Carry [2012], Table 3), some exceptionally fast spinning asteroids have been observed. The *S*-type asteroid OE84, with a mean diameter of $0.7\,\text{km}$ to $1\,\text{km}$ is rotating with a synodic period of just $(29.1909 \pm 1.0000)\,\text{min}$ (Pravec et al. 2002b). This is definitely faster than the spin barrier at $2.2\,\text{hours}$, implying that it indeed has significant cohesive strength.

   Rotating solid bodies are not limited by their tensile strength, but will fail on shear first (Holsapple 2007). The failure criterion is given by the Drucker-Prager relation: Failure occurs when the second invariant of the deviatoric stresses, given by the principal stresses σ_1, σ_2, σ_3 as

$$\sqrt{J_2} = \frac{1}{\sqrt{6}}\sqrt{(\sigma_x - \sigma_y)^2 + (\sigma_y - \sigma_z)^2 + (\sigma_z - \sigma_x)^2} \tag{1.5}$$
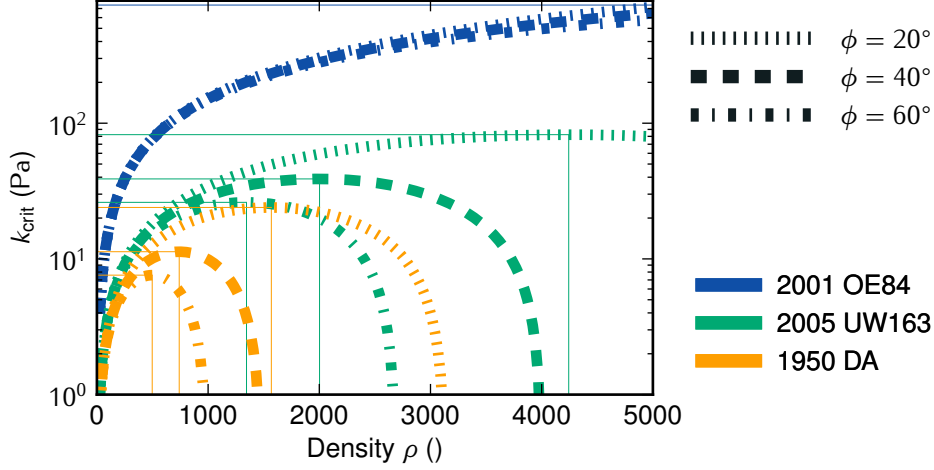
Figure 1.14: Minimal cohesion k_{crit} to prevent rotational disruption for the large superfast rotators found in Figure 1.7 as a function of density (x-axis) and angle of friction Φ of the surface regolith (see legend), as defined in Equation (1.10) and Equation (1.7).

is larger than the cohesion (shear strength at zero pressure), k, minus a pressure dependent factor:

$$\sqrt{J_2} \leq k - 3sp \qquad \text{Drucker-Prager criterion.} \qquad (1.6)$$

The pressure is given by the principal stresses as $p = \frac{1}{3}(\sigma_1 + \sigma_2 + \sigma_3)$. The slope given by the friction coefficient s can be related to the angle of friction Φ by

$$s = \frac{2\sin\Phi}{\sqrt{3}(3 - \sin\Phi)}. \qquad (1.7)$$

Following the discussion in Holsapple (2007), simplified to the case of a spherical asteroid of radius R, the volume-averaged normal stress components in a homogeneous rotating body rotating as $\vec{\omega} = [\omega_x, \omega_y, 0]$ are given by

$$\bar{\sigma}_x = (\rho\omega^2 - 2\pi\rho^2 GA_x)\frac{R^2}{5} \qquad \bar{\sigma}_y = (\rho\omega^2 - 2\pi\rho^2 GA_y)\frac{R^2}{5}$$
$$\bar{\sigma}_z = (-2\pi\rho^2 GA_z)\frac{R^2}{5}, \qquad (1.8)$$

where $A_{x,y,z}$ in the case of a spherical body are equal and have a value of $A = \frac{2}{3}$.

These volume averaged stresses can be used with the Drucker-Prager criterion

(Equation 1.6) to derive the critical value of cohesion, k, at which failure will occur

$$\frac{1}{6}[(\bar{\sigma}_x - \bar{\sigma}_y)^2 + (\bar{\sigma}_y - \bar{\sigma}_z)^2 + (\bar{\sigma}_z - \bar{\sigma}_x)^2] \leq [\bar{k} - s(\bar{\sigma}_x + \bar{\sigma}_y + \bar{\sigma}_z)]^2$$

(1.9)

$$\Longrightarrow$$

$$k \geq \rho\omega^2 \frac{R^2}{5}\left(\frac{1}{\sqrt{3}} + 2s\right) - 3s2\pi\rho^2 GA\frac{R^2}{5}.$$

(1.10)

In Figure 1.14, this critical value is plotted as a function of the asteroids density, ρ, and three angles of friction, Φ for the three superfast rotators found in Figure 1.7. For reasonable assumptions of a density between $2000\,\mathrm{kg\,m^{-3}}$ and $3000\,\mathrm{kg\,m^{-3}}$, only small values of at maximum a few hundreds of Pascal are needed to explain the stability of these bodies. This is comparable to values derived from lunar regolith, that has a cohesive strength of $100\,\mathrm{Pa}$ to $1000\,\mathrm{Pa}$ (Mitchell et al. 1974). For lunar regolith, the retrieved angle of friction is in the range of $35°$ to $50°$.

In a simplified case for spherical bodies these equations can be used to derive the critical cohesion for asteroids rotating at a certain rate. In Figure 1.14 these density dependent values for three superfast rotators are shown. In a detailed study on (29075) 1950 DA, Rozitis et al. (2014) derive a critical cohesion using the fully dynamically equivalent ellipsoid of equal volume at an angle of friction $\Phi = 40°$ of $64^{+12}_{-20}\,\mathrm{Pa}$. This is significantly higher than the value found by the analysis for spherical asteroid equivalents, where a comparable case leads to a value of just $12\,\mathrm{Pa}$. Therefore, the values presented in Figure 1.14 have to be seen as a lower limit. Nevertheless, it shows that bodies rotating faster than the spin barrier do not need to be monolithic bodies, but can still be seen as rubble pile asteroids with only weak cohesive strength.

Understanding impact processes is therefore a key to understanding the evolution of asteroid populations. Especially the stability of bodies against disruption is an important factor in shaping the size distribution. In general, bodies with higher void fraction are more stable than monolithic ones. While in monolithic bodies all energy is available to overcome the material strength, rubble pile asteroids absorb energy in compacting and destroying the voids first, therefore showing a higher resistance against disruption.

1.3   Impact Processes in the Solar System

Given the size and remoteness of asteroids, impact experiments cannot be performed on actual asteroids, nor on direct analogs similar in size. Impact laboratories are able to reproduce some of the conditions though: Impact experiments carried out at speeds of up to $7.5\,\mathrm{km\,s^{-1}}$ (e. g. Price et al. 2013, 2012) are routinely performed, directly comparable to the mean collision velocities in the main belt (Davis et al. 2002).

Direct observational evidence for impact events are the impact craters formed. Therefore, the study of crater formation is the first step in understanding physical processes during impacts of the scale of craters found on bodies throughout the Solar System.

1.3.1   Crater Formation in Impact Events

The process of crater formation is commonly divided into three main stages (Gault et al. 1974):

1. *Contact and compression*: Then the projectile make contact with the target, a shock wave is going at speeds faster than the local sound speed through both the target and the impactor. In this shock, pressures of up to Terapascal are reached. When this shock reaches the back side of the impactor, a rarefraction wave is reflected back, unloading the projectile and melting or vaporising it.

2. *Excavation*: A hemispherical transient crater cavity is formed by complex interactions of the reflected shock wave and the target surface. Material starts to flow in an initially radial outward pattern.

3. *Modification*: In this stage, when the kinetic energy of the excavation flow can no longer overcome gravitation or with cohesive strength of the target material, a reverse flow begins that raises a central uplift peak and, for large craters, the crater rim collapses, leading to complex crater shapes.

Often, there is an additional stage of hydrothermal activity in environments where water is available: Osinski et al. (2005) found evidence on the Haughton impact crater in Devon, Canada for moderate to low temperature hydrothermal processing of material, leading to mineralisation and significant changes in the crater appearance. Also, geological modification on long timescales has to be

considered when trying to determine original crater dimensions of eroded or otherwise weathered craters, as the apparent crater diameter observed after the rim eroded is significantly smaller than the crater diameter measured at the final rim after the impact, and accurate estimates of the latter are essential for applying crater scaling laws (Turtle et al. 2004).

1.3.2   Timescales During Impact Events

There is no clear separation of the three stages of impact event. Turtle et al. (2004) show that for craters on large bodies with significant gravity, the vertical excavation stops earlier than the horizontal growth in diameter (see Turtle et al. [2004], Figure 1C and 1D), blurring the boundary between excavation and modification stages.

Apart from the geological modifications, all cratering processes happen on a very short timescale. The shortest is the first *contact* stage, where the projectile penetrates the target. This penetration depth is usually only a few times the impactor diameter L deep, and the timescale τ_{cc} is governed by the impact velocity:

$$\tau_{cc} = \frac{L}{v_{imp}\,\sin\Theta}. \tag{1.11}$$

Therefore, for the Chixculub cratering event, that had an impactor radius between 7 km to 9 km, an impact velocity of $10\,\mathrm{km\,s^{-1}}$ to $20\,\mathrm{km\,s^{-1}}$ (Ivanov 2005), and most probably an obliquity of $\Theta = 45°$, this stage therefore lasted about 1.0 s to 1.6 s. For a head-on impact of a 4 m sized impactor at $5.5\,\mathrm{km\,s^{-1}}$, a typical velocity for asteroid–asteroid collisions in the main belt, this stage would last for only a few milliseconds.

When the shock wave has traveled from the impact zone to the back of the impactor, the pressure is unloaded, as the material is uplifted. At this stage, the projectile is unloaded, melted and/or vaporized, and does not further influence the crater forming process. The passage of the shockwave accelerates material which starts to form the excavation flow and the transient crater cavity. Material in the upper zone is ejected ballistically, and forms the ejecta curtain, that falls back to form the ejecta blanket when it is not lost due to insufficient gravity. About 1/3rd of the transient cavity is formed by excavated material, while the larger part is displaced material. The rim of the crater is lifted during this process, and spallation occurs at the surface around the opening cavity. The depth to
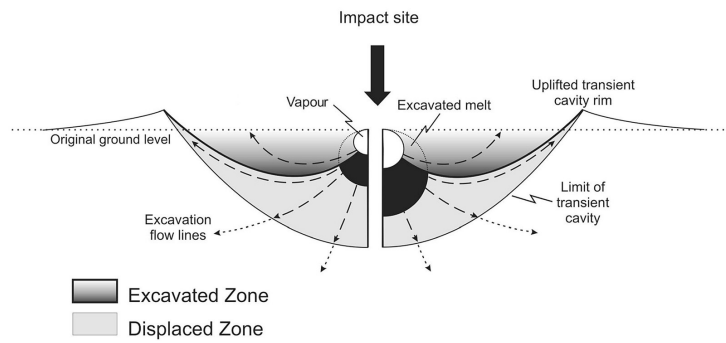
(a) Theoretical cross-section through a transient cavity showing the excavation flow direction and the target lithology. *Reprinted from Osinski and Pierazzo 2012 (Figure 4.2)*
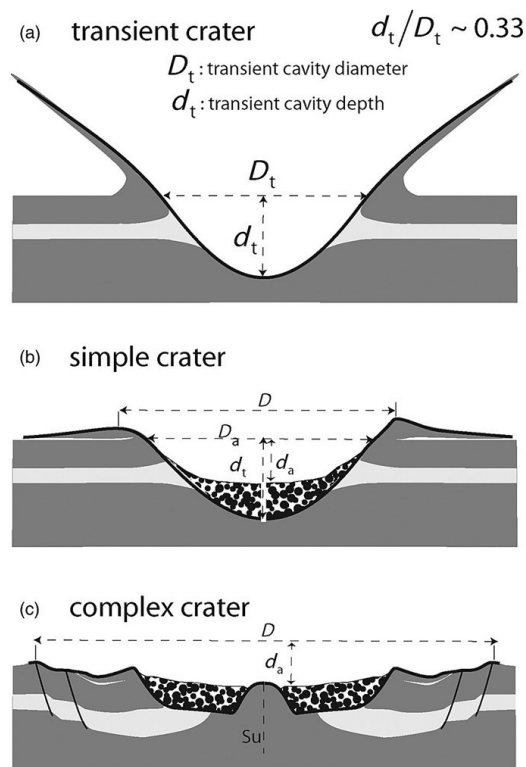
(b) Schematic cross-section through a transient crater (Panel a), a final simple crater (b) and a complex crater (c). *Reprinted from Osinski and Pierazzo 2012 (Figure 5.1)*

Figure 1.15: Schematics showing stages of the cratering process and different crater morphologies

diameter ratio for the transient cavity is generally taken as $d_{tc}/R \approx 1/3$ (Melosh 1989). The length of this phase is dependent on the details of the excavation flow. Neglecting strength effects, and on gravity dominated flows on planetary impacts with surface gravity g it can be estimated as approximately the free-fall time for the depth d_{tc} of the transient cavity (Melosh 1989),

$$\tau_{exc} = \sqrt{\frac{2d_{tc}}{g}}. \tag{1.12}$$

This is usually a few hundred times longer than the contact and compression timescale τ_{cc}. Generally, the excavation stage ends when the diminishing shock wave energy can no longer overcome the gravitational potential for gravity dominated cratering events, or cohesion for smaller, strength dominated, events. As this does not happen simultaneously all along the surface of the transient cavity (Turtle et al. 2004), again the excavation stage cannot be clearly separated from the modification stage.

1.3.3   Crater Morphology

For simple craters as for example crater Linné in Figure 1.16a, forming in strength-dominated impacts, the final crater shape is similar to the transient cavity. Material that has been uplifted is now falling back, filling part of the cavity, and the steep walls collapse, increasing the cavity diameter by 10 % to 20 % (Kenkmann et al. 2012). Therefore, the final depth-to-diameter ratio is around $d_{crater}/R \approx 1/5$.

In cases where gravity is dominant and the target strength is overcome during the subsequent collapse, complex crater shapes are formed. They show an uplifted crater floor with most of the transient cavity collapsed, as seen on crater Tycho in Figure 1.16b. They are much shallower than simple craters, and the crater is enlarged by a factor of 1.5 to 2.0 compared to the transient cavity.

The transition between both morphologies — the simple and the complex crater — is a function of surface gravity and target strength (Kenkmann et al. 2012). On Earth, the largest simple crater has a diameter of about approximately 3.8 km (Garvin and Grieve 1982; Earth Impact Database 2011), whereas the largest simple craters found on the Moon have diameter of about 16 km (Wood and Anderson 1978). Overall, Melosh and Ivanov (1999) find that the transition from simple to complex craters is inversely proportional to the surface gravity.
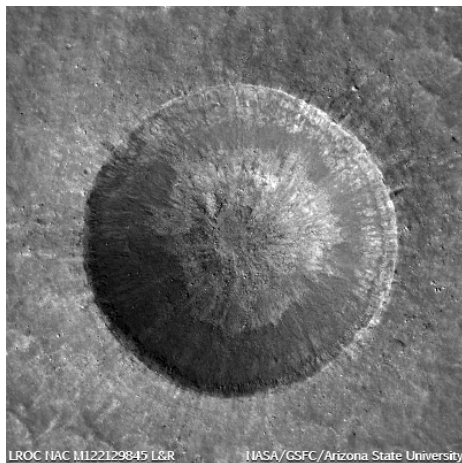
(a) Crater Linné on the Moon as example of a simple crater, where the cratering process is dominated by material strength. The crater has a diameter of 2.4 km and a depth of 600 m *Source: Lunar Reconnaissance Orbiter Camera, NASA/GSFC/Arizona State University*
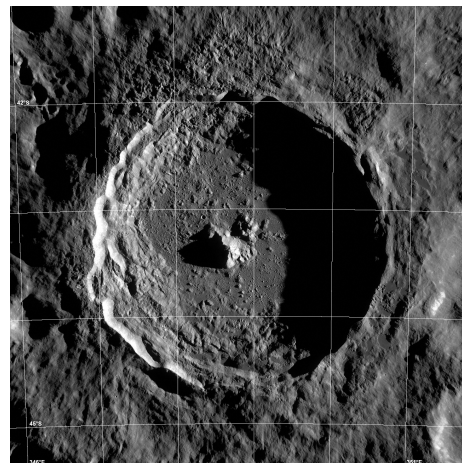
(b) Mosaic image of crater Tycho on the Moon as example of a complex crater structure where gravitational forces lead to complex structures as the central uplift and the terassed rim. The crater has a diameter of ∼ 82 km and a depth of 4700 m *Source: Lunar Reconnaissance Orbiter Camera, NASA/GSFC/Arizona State University*

Figure 1.16: Two lunar craters as example of simple, strength-dominated (a) and complex, gravity-dominated (b) structures.

Therefore, on small bodies of a few kilometre size, any crater large compared to the bodies' diameter is expected to show morphology of a simple crater, as shown in Figure 1.15b, Panel (b).

1.3.4   Peak Pressure during Cratering Events

In impact events the highest pressures are observed in the first stage during contact and compression. The shock wave traveling through both the impactor and the target leads to very high pressures and temperatures. The shock wave is usually described as a discontinuity: from conservation of energy, mass, and momentum, the Hugoniot conditions can be derived:

$$\rho_2(v_s - v_p) = \rho_1 v_s \qquad \qquad \text{Conservation of mass}$$

$$(1.13a)$$

$$p_2 - p_1 = \rho_1 v_p v_s \qquad \qquad \text{Conservation of momentum}$$

$$(1.13b)$$

$$E_2 - E_1 = \frac{1}{2}(p_1 + p_2)\left(\frac{1}{\rho_1} - \frac{1}{\rho_2}\right) \qquad \text{Conservation of energy.}$$

$$(1.13c)$$

Here, the subscript 1 and 2 refer to the material just before and after the shock front, respectively. v_s and v_p denote the shock and the particle velocities, p the pressure, ρ is the density, while the inverse $1/\rho$ corresponds to the specific volume per unit mass.

   This system has to be closed using a fourth relation. An equation of state (EOS) which relates thermodynamic quantities in the form $p = p(\rho, E)$, but for many materials the EOS is not well determined, especially under extreme conditions as experienced during hypervelocity impacts. Fortunately, experimental data show that for many materials the particle velocity, v_p, can be approximated by a linear dependency on the shock velocity, v_s, and thus using this relation the system can be closed:

$$v_s = C_1 + S_1 v_p. \qquad \qquad (1.14)$$

As Equation (1.14) does not specify thermodynamic quantities, it does not allow us to infer temperatures of the shocked material, but only the pressure. Values for the constants C_1 and S_1 have been tabulated for many materials (e.g. Marsh

1980; McQueen et al. 1967; Nakazawa et al. 1997). Peak pressures for typical hypervelocity impacts (a few km s^{-1}) range from a few Gigapascal to thousands of Gigapascal (Melosh 1989).

1.3.5 Oblique Impacts

Gilbert (1893, Figures 10–12), assuming an isotropic source of impactors, derived a differential probability dX of an impact to happen in the interval of obliquity from Θ to $\Theta + \mathrm{d}\Theta$ on a spherical body neclecting gravitational effects:

$$\mathrm{d}X = 2\sin\Theta\cos\Theta\,\mathrm{d}\Theta. \tag{1.15}$$

Pierazzo and Melosh (2000b) showed, that the same expression holds true for large bodies where gravitational forces cannot be neglected. This directly leads to the observation that the majority of impacts should happen at an obliquity of $\Theta = 45°$, and almost none directly vertically. Only 23.4 % of impacts happen outside the interval of $\Theta = 20°$ to 70°, and only 3 % head on (Θ between 80° and 90°).

Surprisingly, the final shape of craters is circular in all cases for impacts of obliquity $\Theta > 30°$. For non-cohesive materials like sand, even for $\Theta > 15°$ (see Figure 1 and 2 Gault and Wedekind 1978) impacts result in circular craters. Below these limits, circularity of the crater becomes a function of impact velocity and material properties. In a series of micron-scale impacting experiments, Wozniakiewicz et al. (2014) found four silica targets ellipticity rising above length/width > 1.1 for impacts below $\Theta > 45°$. Nevertheless, impact events do leave traces of the obliquity of the projectile and simulations have shown that the fate of the impactor is highly dependent on the impact angle (Pierazzo and Melosh 2000a). The material ejected in impacts with a low impact angle ($\Theta < 30°$) is almost completely ejected from the crater, while for steep impacts ($\Theta > 60°$) all the material is smeared over the crater walls. The authors also find a decrease of vaporisation with impact angle, and an inhomogeneous distribution of melt material towards the direction of impact.

1.3.6 Threshold for Collisional Disruption of Asteroids

A major parameter for collisional models is the stability of a body against disruption. As this is a function of many parameters, such as material strength, size,

impact geometry, and impact energy, analytical models need to be derived from experimental data.

The transition from cratering regime into disruption of the body is characterised by the catastrophic disruption threshold Q^*, which is defined as the normalised energy at which the mass of the largest remnant fragment has exactly 50 % of the target's mass M_{tar}:

$$Q^* = \left. \frac{E_{kin,\text{imp}}}{M_{\text{tar}}} \right|_{M_{\text{lr}}=50\,\%\,M_{\text{tar.}}} \tag{1.16}$$

It is important to note if the mass of the largest remnant fragment was determined *before* any gravitational re-aggregation of fragments took place, or *after*. In the first case, only monolithic blocks after shattering are considered, and they are usually denoted as Q_S^*. In the latter case, the largest fragment consist of several accumulated blocks of monoliths, and is itself a rubble pile. This value is usually denoted as Q_D^*, and in many cases is simplified to the point where exactly 50 % of the mass is ejected with velocities exceeding the escape velocity (Holsapple 2009). For impacts involving bodies of comparable mass, the mass of the impactor has to be taken into account. To formulate a generalised disruption criterion as a function of mass ratio, impact angle and impact velocity, Leinhardt and Stewart (2011) formulate the disruption criterion in terms of an equivalent equal mass impact energy, $Q_{RD\,1:1}^*$, called the principal disruption curve. The authors observe a linear relation between $Q_{RD\,1:1}^*$ and an effective radius defined by $R_{C1}{}^3 = (M_{\text{tar}} + M_{\text{imp}})/(\frac{4}{3}\pi\rho_0)$ where $\rho_0 = 1000\,\text{kg/m}^3$ is the reference density.

Holsapple et al. (2002) compiled the first list of scaling relations found in the literature (see Figure 1.17). It can be seen, that while the models differ by orders of magnitude, two regimes can be distinguished. For targets smaller than $R_{\text{tar}} = 200\,\text{m}$, the strength against disruption decreases with radius. This is explained by the increasing probability for initial cracks for bodies with growing size. Most theories assume that the strength is determined by tensile failure (e.g. Housen and Holsapple 1990), unlike in the case of rotational disruption, where shear strength limits the body's stability (Rozitis et al. 2014). Weibull (1939) first formulated a statistical description of the number of cracks in a material, and related the strength of a certain volume to the size of the largest flaw that can stochastically be found in it. The tensile strength of a volume V scales in
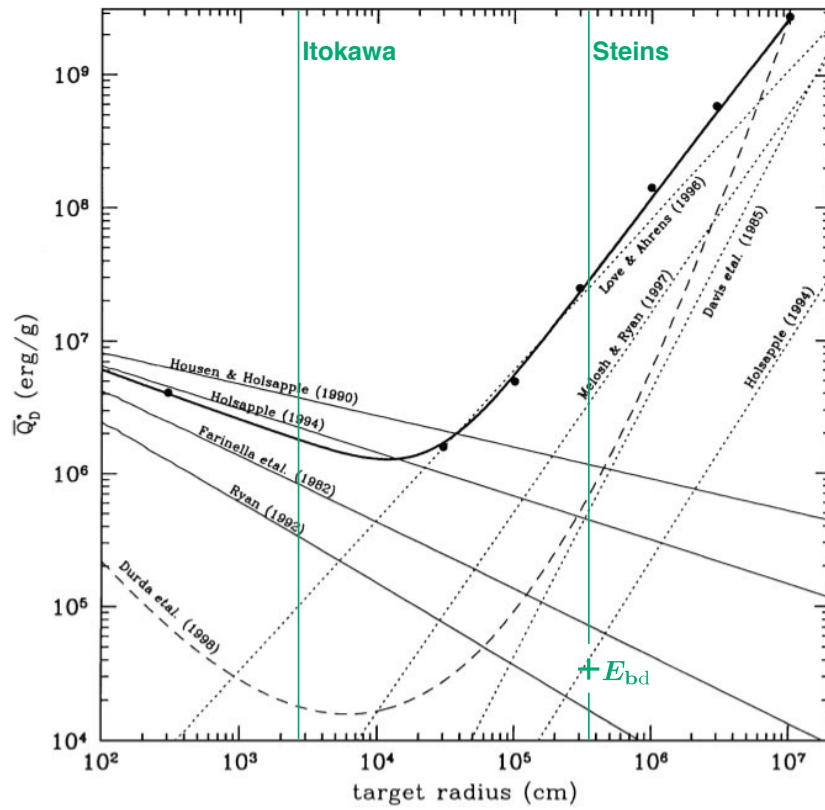
Figure 1.17: Comparison between the mean catastrophic disruption threshold Q^* determined by Benz and Asphaug (1999) for basalt targets at $v_{\mathrm{imp}} = 3\,\mathrm{km\,s^{-1}}$ (bold line) and semi-analytical models found in the literature. Radii of the volume-equivalent spheres for asteroids Itokawa and Šteins are added, as well as the gravitational binding energy E_{bd} of Šteins (see Section 4.4.2 and Equation [4.2]). *Reprinted from Benz and Asphaug 1999*

this approach as

$$\sigma \approx (k_W V)^{1/m_W}, \tag{1.17}$$

and is controlled by the Weibull parameters k_W and m_W. As the probability for cracks occurring increases with volume, it results in weakening asteroids with increasing radius. Housen and Holsapple (1999, see Figure 3) found a value for the Weibull exponent in Georgia Keystone granite of $m_W = 12.0 \pm 0.5$. This is significantly higher than the value found in the same study for dynamical impact experiments, leading to values between $m_W = 8.91 \pm 0.42$ and $m_W = 9.26 \pm 0.58$. This indicates that the static model is an oversimplification, and the assumption that only the size of the largest flaw has to be accounted for is not valid.

Additionally, the dynamic strength of material decreases with loading time. Because collisions with larger bodies have longer loading time, this leads, again, to a weakening with larger body radius. By dimensional analysis, Housen and Holsapple (1999) found the relation

$$Q_S^* \propto \left(\frac{2R}{(km)} \right)^{\left(\frac{-9\mu}{2m_W - 3} \right)} \left(\frac{v_{imp}}{(km\,s^{-1})} \right)^{(2 - 3\mu)}. \tag{1.18}$$

The parameter μ is the velocity dependency of the *coupling efficiency parameter C* that was introduced by Holsapple and Schmidt (1982) and explored by Holsapple and Schmidt (1987). Looking for a way to describe impacts where the impactor is small (defined as being negligible in size compared to the target), the authors found that in this point-source solution the energy of the impactor is released into the target in a way that the product

$$R_{imp}(v_{imp})^{\mu}(\rho)^{\nu} = C \tag{1.19}$$

is constant. The parameter C is therefore a unique measure of the impact magnitude.

Both parameters μ and ν have to be determined in experiments. For both the limiting cases in the pure strength and the pure gravitational regime, ν is found to be $1/3$. The velocity exponent μ is constrained into the range of $\mu = 1/3$ and $\mu = 2/3$. It determines the dimensionality of the coupling: for $\mu = 1/3$, the coupling is proportional to the impactor momentum, and for $\mu = 2/3$ it is

proportional to the impactors kinetic energy. For porous material, momentum scaling is expected, and indeed values of $\mu = 0.41$ are found for both sand and dry soil (see Table 1 in Holsapple 1993). Taylor (1950) used a point-source solution to relate the radius of the first nuclear explosion to the energy released by the explosion. He found that the extension of the shock front into an ideal gas scales with the *energy* released. This corresponds to $\mu = 2/3$ and denotes the energy scaling limit. Neither of the two limits are found purely in nature, but values of $\mu = 0.55$ are found for different rock types as well as water.

For larger bodies, gravitational forces become more important. The escape velocity scales with the inverse square root of the radius: $v_{\mathrm{esc}} = (2GM/R)^{\frac{1}{2}}$. The energy needed to escape the gravitational field is proportional to the mass and the square of the velocity. The mass M is proportional to R^3. Therefore the energy needed to escape from the collision increases with R^2. This is an upper limit, as already shown by Housen and Holsapple (1990). By dimensional analysis, they found a dependency on the parameter μ of the disruption threshold in the gravity regime:

$$Q_D^* \propto \left(\frac{R}{(\mathrm{km})} \right)^{3\mu} \left(\frac{v_{\mathrm{imp}}}{(\mathrm{km\,s}^{-1})} \right)^{(2-3\mu)}. \tag{1.20}$$

The efficiency of generating high-velocity fragments and therefore coupling the kinetic energy of the impactor to the kinetic energy of the fragments is rather low. Leinhardt and Stewart (2011) find that only a small amount of mass is actually accelerated above escape velocity, confirming results found earlier by Ryan and Melosh (1998). An effect accounting for *gravitational strengthening* is the additional lithostatic stress that has to be overcome before fracturing. It is given by

$$p_l(R) = 2/3\pi G \rho^2 (R^2_{\mathrm{ast}} - R^2), \tag{1.21}$$

and effectively increases the local maximum stress (Benz and Asphaug 1999).

The transition between the *strength* and the *gravity* regime can be seen in Figure 1.17 at a radius of a few hundred meters. The minimum of the scaling law derived by Benz and Asphaug (1999) is at $R \approx 100\,\mathrm{m}$ to $200\,\mathrm{m}$, Melosh and Ryan (1997) find a transition radius of $R \approx 400\,\mathrm{m}$ and Love and Ahrens (1996), although omitting strength effects in their simulations, find a value of $R \approx (250 \pm 150)\,\mathrm{m}$

Asteroid Itokawa with an equivalent radius of $R = 164\,$m is therefore just at the boundary between the two regimes, and therefore expected to be a relatively weak body, while Šteins is already in the gravitational regime.

In the scaling laws shown in Equations (1.18) and (1.20), material parameters are incorporated using the parameters m_{W}, ν, and μ. These also parameterize the dependency of the disruption threshold on the target porosity. As Love et al. (1993) found, porosity is actually an important parameter in the target's resistance against disruption: In a series of hyper-velocity impact experiments on sintered soda lime glass beads of $50\,\mu$m and $2500\,$kg m^{-3} with porosities ϕ_b ranging from 5 % to 60 %, the authors found that their four data points for disruption threshold could be well described using an exponential dependency on the compressive strength $Y_{\mathrm{i\,lim}}$:

$$Q_D^* = (7.57 \times 10^6\,\mathrm{erg\,g^{-1}}) \left(\frac{Y_{\mathrm{i\,lim}}}{(100\,\mathrm{MPa})} \right)^{0.45} (1 - \phi_b)^{-3.6}. \qquad (1.22)$$

(Although SI-units are used throughout the work, in the case of normalised impact energies cgs-units are used to facilitate comparison with older work.) This shows that the dependency on the porosity is actually much stronger than on the compressive strength of the material, and that the resistance against disruption strongly increases with porosity.

This observation is also supported by results of Jutzi et al. (2010b), who run a series of numerical impact experiments at six sizes ranging from 3 cm to 100 km varying the material description for porous and non-porous targets to investigate a 'nomimal' strength case as well a 'weak non-porous' and a 'strong porous' case by adapting the shear- and tensile strength accordingly. In the strength regime, they find a strong dependency of the disruption threshold on the material strength. The authors find that depending on both the shear- and tensile strength, but mostly the shear strength, the disruption threshold can differ by orders of magnitude. Also, the authors find that in the strength regime, porous targets are much more resistant to disruption than non-porous ones, but that this cannot be said in the gravity regime. There, the authors find a strong dependency of Q_D^* only for non-porous targets. This leads to cases where non-porous targets can be harder to disrupt than the same-size porous targets, depending on the strength of the material.

1.3.7   Modelling of Hyper-Velocity Impacts

In an attempt to verify scaling laws used to link lab-sized experiments to impacts on planetesimals or even collisions of planet-sized bodies, numerical methods are used to simulate these events.

In the early era of numerical modelling only the very first stage of crater formation could be modelled and all strength of the material was neglected due to limitations in available computing power (Bjork 1961), therefore only solving the hydrodynamic equations was possible and such codes were branded as hydrocodes. Today, such 'hydrocodes' are far more advanced, and detailed material models can be taken into account. Also still referred to as hydrocodes, 'shock physics' codes would be a much more accurate naming, as the purely hydrodynamic treatment is no longer a valid approach.

However, even today computational power is the limiting factor when modelling impact events. Because these events span over a large number of magnitudes both spatially, from cohesive forces on an atomic level to kilometre sized bodies, as well as temporally, where supersonic waves and the long-term fate of ejected material have to be considered, numerical codes have always to be a compromise between accuracy and usability. Therefore, in many impact simulations the interior of rubble pile asteroids are treated as homogeneous, monolithic material, and the existence of internal voids and porosity is incorporated using an adapted material model (e. g. Collins et al. 2011). While this approach is able to reproduce the bulk properties of asteroids, it does not tell us how the rubble pile interior might be rearranged during an impact event.

1.3.8   Evolution of Shock-Physics Codes

During the initial stage of an impact, the material's tensile strength only plays a minor part, as the extreme pressures quickly fluidise the material, so that all tensile strength is lost, and a purely hydrodynamic analysis can give insights into the physical processes (Bjork 1961; Ahrens and O'Keefe 1977). The same applies for the first stage in explosion cratering, mainly undertaken to understand the formation of large-scale explosion craters caused by nuclear fusion bombs (Orphal 1977a,b). The assumptions of essentially a strength-free material holds true only for the contact and compression stage of the event, usually the very first tens of milliseconds (Bjork 1961, 60 ms). However, 40 years later from the pioneering work of Bjork and co-workers, computational capabilities have

advanced such that complicated material models can be included in hydrocodes.

A large number of publications have been published on the Chixculub cratering event, during which a very large asteroid, or comet, impacted into the Earth and is suspected to have caused the extinction of the dinosaurs and a major transformation of the Earth's atmosphere (Schulte et al. 2010), for example by Pope et al. (1994), Pierazzo and Melosh (2000a), Collins (2002), Ivanov (2005) and Saito et al. (2008). The Chixculub crater, a circular structure of around 200 km diameter, discovered by geologists mapping the Mexican gravity anomalies on the search for oil, was first connected to an impact crater by Hildebrand et al. (1991).

In an effort to model this event, Collins (2002) extended the SALE (Melosh et al. 1992) code to include material weakening by 'acoustic fluidization', the reduction of strength by extreme pressure fluctuations in strong vibrations produced by the expanding shock wave to explain the end-stage collapse of the crater rim. Ivanov (2005) extended the EOS he used to explain the large quantities of sulphur dioxide produced and mixed into the atmosphere, leading to the subsequent mass extinction event by the thermal decomposition of calcite and anhydrite bound in limestone forming the uppermost layer of the impacted region.

An important step in the evolution of shock physics codes was the extension from two dimensional models, that had to assume either cylindrical symmetry or infinite plates in one axis, to fully three dimensional models. Assumptions on symmetry in impacts are hard to justify, mainly because by far the most impact happen at oblique angles: As discussed in Section 1.3.5, virtually no impacts happens vertically, but rather 50 % of all impact have an angle of obliquity between 30° to 60°. Although requiring considerably more computational resources, 3D simulations are therefore necessary even for homogeneous target structure to simulate realistic cratering events.

1.4 Simulating Impacts on Rubble Pile Asteroids

While it is clear that rubble pile asteroids have high macroporosities and therefore must contain void spaces in the interior, little is known of the exact distribution of these voids. Possible distributions range from very small voids in a homogeneous, highly porous material, to large void spaces in between interlocking, solid fragments.

Herrmann ([1969]) introduced a way to model the behavior of porous media using the distension parameter, α, the ratio of the material's density with and without void space. α is related to the porosity, ϕ, via $\alpha = (1 - \phi)^{-1}$. In the so called P-α model, the equation of state that defines the pressure, p, for a certain state of density, ρ and internal energy, e, for porous materials is derived from the equation-of-state of the solid matrix material $p = f_s(\rho, e)$. Carroll ([1972]) use a simple relation of $p = f_s(\rho, e) \cdot \alpha^{-1}$. Wünnemann et al. ([2006]) extended this idea to a strain-based porosity model, where the equation of state depends on the accumulated volumetric strain calculated from the original volume, V_0, and the change in volume at a certain step V':

$$\varepsilon_V = \int_{V_0}^{V'} \frac{1}{V} \, \mathrm{d}V = \ln \frac{V'}{V_0} = \ln \frac{\alpha}{\alpha_0}. \qquad (1.23)$$

An overview of the currently used strength models in recent shock codes can be found in Holsapple ([2009]). None of these models include inhomogeneities in the target asteroids, that these rubble-pile bodies must possess, but instead rely on an average porosity.

Jutzi et al. ([2010b]) studied numerically the influence of sub-resolution porosity on the disruption threshold Q_S^* at the transition from strength- to gravity regime. They found that while in the strength regime, the disruption threshold does strongly increase with increasing porosity, in the gravitational regime the dependency on porosity is much smaller, and depending on the exact strength assumed the effect can be an increase as well as a decrease in resistance against disruption.

There have been only a few approaches so far to explicitly model the internal structure of rubble pile asteroids. Michel et al. ([2003]) introduced a model of pre-fractured rubble piles to link the Karin asteroid family to a disrupted, initially non-monolithic parent body. Arguing that a monolithic body will be fractured by multiple, uncorrelated small impacts, Michel et al. ([2004b]) create randomly shaped fragments in a asteroid using a seed-and-grow algorithm. Material at the boundary of two fragments is marked as *damaged*, and void space is introduced by randomly removing some of the fractured material.

This model was used to study the creation of asteroid families, as well as a study on asteroid Šteins by Jutzi et al. ([2010a]), that revealed a preference for an monolithic interior of Šteins before the impact that formed the largest crater
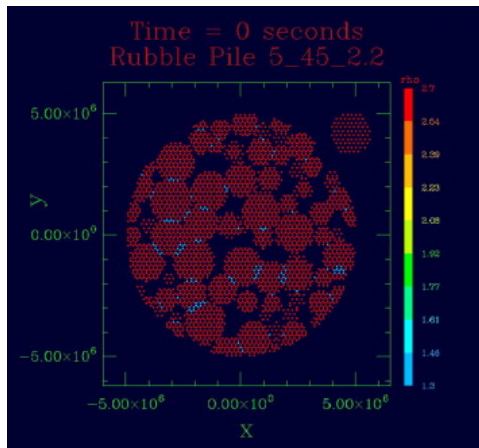
Figure 1.18: Image of a rubble pile target as used by Benavidez et al. (2012). The colour bar denotes the density. *Reprinted from Benavidez et al. 2012*

Diamond transformed it into a rubble pile body that is seen today.

Geretshauser et al. (2011) modelled collision events of centimetre sized pre-planetesimals, in an attempt to reproduce results of laboratory experiments on growth beyond the bouncing barrier (Güttler et al. 2010). These dust agglomerates, formed by collisional coagulation, are highly porous, fluffy dust aggregates. Inhomogeneities in the pre-planetesimals are simulated by varying the local filling factor using a superposition of Gaussian functions. Interestingly, the authors found that pre-planetesimals having more inhomogeneities are weaker than homogeneous bodies, which is contrary to the behaviour found for larger rubble pile asteroids, where a higher porosity actually increases the strength against disruption.

Benavidez et al. (2012) introduced a rubble pile model for a series of Smoothed Particle Hydrodynamics (SPH) simulations comparing rubble pile and monolithic asteroids in family-forming events. The asteroid is represented by a spherical shell filled with an uneven distribution of basalt spheres, with radii ranging from 8 % to 20 % of the radius of the parent body. SPH particles at the contact zone of two spherical fragments are reduced to a lower density to simulate damaged material.

1.4.1 Motivation of this Work

While there has been some work modelling the heterogeneous interior of rubble pile asteroids in impact simulations, as by Michel et al. (2003), and Geretshauser et al. (2011), and Benavidez et al. (2012), no systematic study of the behaviour of large-scale fragment structure in rubble pile asteroid in impact events has been published so far. While the high macroporosities found in rubble pile asteroids

(a) Image of the asteroid Itokawa taken by the Hayabusa spacecraft. *Source: JAXA,* `http://global.jaxa.jp/article/` `special/hayabusa_sp3/index_e.html`

(b) Asteroid Šteins imaged by the OSIRIS camera system on board of Rosetta *Source: ESA ©2008 MPS for OSIRIS Team MPS/UP-D/LAM/IAA/RSSD/INTA/UPM/DASP/IDA*

Figure 1.19: Itokawa and Šteins, two rubble pile asteroids visited by spacecraft

mean that these bodies must contain void space, the exact nature of these voids is not yet understood. As most of the smaller asteroids are remnants of disrupted, large parent asteroids, one possibility is to view them as aggregates of fragments bound together by gravity during re-aggregation after the disruption event. The size distribution of the constituent fragments in rubble pile asteroids is not yet known, and there is yet no direct measurement of an asteroids interior by in-situ spacecraft experiments. If the surface of asteroid Itokawa is indicative for the interior, the interior of Hayabusa's main mission target consists of numerous fragments of the shape and size of the boulders seen in Figure 1.19a. The fragments follow a cumulative power law with slope −3.1 (Michikami et al. 2008). Apart from the boulders seen on surface of Itokawa, is there any other possibility to infer the interior of rubble pile asteroids from surface features? In images taken during the flyby of Rosetta at the small asteroid (2867) Šteins as the one shown in Figure 1.19b, some surface structures might tell a story of its interior. A large crater close to the southern pole is testimonial of a large-scale impact event, that might have globally rearranged the whole body. This work tries to determine if other surface features as a hill structure almost opposite to the crater, or a series of aligned pits are related to the large-scale pebble structure in the interior of the asteroid. A link between surface features and the rubble pile interior is one of the few ways to learn about the internal structure, as long as no in-situ measurements of rubble pile interiors are performed and imaging data of asteroid surfaces is the only thing available.

How these pebbles are arranged in the interior is therefore still an open

questions, and much of it is probably defined during the formation of the asteroid. In this work, a model is proposed that starts at the formation phase of rubble pile asteroids as aggregates of large pebbles. In impact simulations, performed using the Smoothed Particle Hydrodynamics (SPH) approach, the influence of the large scale pebble structure on the outcome of impact events is analysed. Asteroid Šteins is taken as a test case to establish a possible link between rubble pile structure and surface features.

This work focusses on small asteroids at the boundary between the strength regime for catastrophic disruption and the gravitational regime, where re-aggregation significantly alters the mass of the largest surviving fragment and therefore the stability of the asteroid against disruption. This corresponds to the size of a few hundred metres to a few kilometres. Asteroid Itokawa and the slightly larger asteroid Šteins are two examples of this region, and thanks to the Hayabusa and the Rosetta missions, accurate shape models of both bodies are available and can be used for impact simulations.

1.4.2   Thesis Layout

First, the technical details of the modelling tools are discussed in Chapter 2. In Chapter 3 the strategy to build rubble pile asteroid simulants for numerical impact experiments is presented. A series of test simulations on a target equivalent in volume to Itokawa are performed to infer the sensitivity of the resulting rubble pile simulants to the parameters chosen in the model creation process.

Asteroid Šteins as an rubble pile asteroid showing a large, near-critical crater is used in Chapter 4 to test a link between surface features and the re-arrangement of the large scale pebble structure in the crater forming impact event. A possible pre-impact shape is derived and a series of test simulations performed is described.

In Chapter 5 the applicable range of the modelling approach is discussed. For asteroid Šteins, plausible evolution scenarios are discussed, and the influence of the impact event that formed the large crater on the southern pole on YORP induced shape evolution is tested.

Chapter 2

Methods

2.1 Numerical Simulations of Impact Events

Numerical simulations of material behaviour under load are based on the principles of continuum mechanics. Material is treated in a statistical sense as a continuum, and therefore the molecular structure can be ignored. The material fills all space in the spatial domain of interest, and can be describe by continuous functions. Furthermore, usually homogeneity and isotropy is assumed, that means there are no preferred directions, and in one medium all points have the same properties. A detailed introduction is given for example in Malvern (1969), 'Introduction to the mechanics of a continuous medium'.

The governing equations are given by the conservation of mass, momentum, and internal energy. In the Lagrangian description, following the mass, these can be written as

$$\frac{\mathrm{d}\rho}{\mathrm{d}t} = -\rho \frac{\partial v_i}{\partial x_i} \qquad \text{Conservation of mass} \qquad (2.1a)$$

$$\frac{\mathrm{d}v_i}{\mathrm{d}t} = \frac{1}{\rho} \frac{\partial \sigma_{ij}}{\partial x_j} + \frac{F}{\rho} \qquad \text{Conservation of momentum} \qquad (2.1b)$$

$$\frac{\mathrm{d}e}{\mathrm{d}t} = \frac{1}{\rho} \frac{\partial v_i}{\partial x_i} + \frac{1}{\rho} s_{ij} \dot{\varepsilon}_{ij} \qquad \text{Conservation of energy,} \qquad (2.1c)$$

where

$$\rho \text{ is density}$$

x is position

v is velocity

σ is stress

F is external force per unit mass

e is internal specific energy

s is the deviatoric part of the stress tensor

$\dot{\varepsilon}$ is the deviatoric strain rate.

If not otherwise noted, all units are in SI, and summation over pairwise indices is assumed. The deviatoric part of the stress tensor is defined by splitting the stress tensor in two parts

$$\sigma_{ij} = s_{ij} + \delta_{ij} p \tag{2.2}$$

using the isotropic stress p that is equivalent to the pressure $p = \frac{1}{3}(\sigma_{11} + \sigma_{22} + \sigma_{33})$. The deviatoric stress model describes the deformation of material. It is a function of stress, strain, pressure, and internal energy and is called the constitutive model or strength model:

$$s_{ij} = s(\varepsilon_{ij}, \dot{\varepsilon}_{ij}, p, e). \tag{2.3}$$

The exact formulation of this relationship is usually semi-empirically chosen to model laboratory measurements of material behavior. A good overview is given in Malvern (1969, Chapter 6), and a discussion of models used in recent impact simulations in Holsapple (2009) and Collins et al. (2012).

Additionally, the system of equations has to be closed by an equation of state (EOS). This is a thermophysical relation between state variables, usually given in the form

$$p = p(\rho, e). \tag{2.4}$$

The EOS describes the set of allowed states in the material. The phase diagram for many materials under the extreme pressures occurring during the contact and compression stage are not well known, therefore simple empirical relations as given by the Mie-Grüneisen (Grüneisen 1912) and Tillotson (Tillotson 1962) EOS. Neither of these EOSs allow for the of temperature directly and therefore melting and vaporization cannot be treated. More recently, Analytic Equations
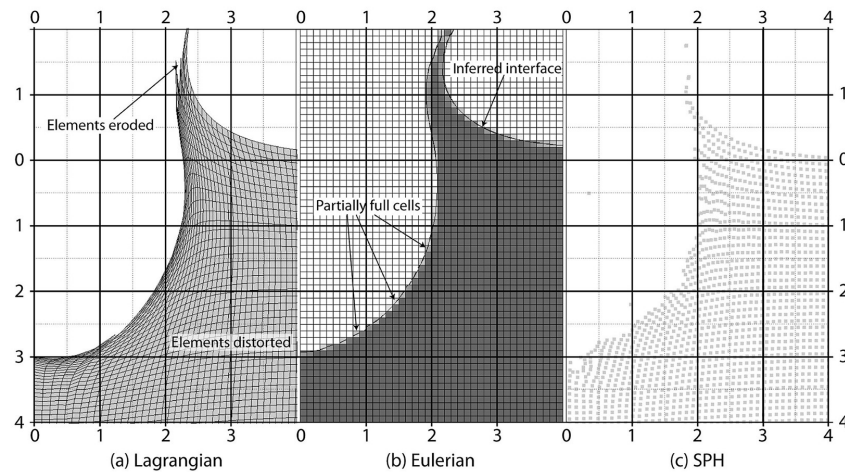
Figure 2.1: Discretization schemes used in shock impact codes. Timeframes for impact simulations using Lagrangian (Panel a), Eulerian (Panel b), and SPH (Panel c). The Lagrangian and SPH simulations where produced using `Autodyn` by M. Price, the Eulerian using `iSALE`. *Reprinted from Collins et al. 2012*

of State for Shock Physics Codes (ANEOS) (Thompson 1990) used analytical, thermodynamic consistent formulation to calculate the state using a computer code, including the vapor phase and melting. This approach has been extended to include multiple solid phase transitions by Melosh (2007), and is still under development (Collins and Melosh 2014).

2.1.1   Discretization of the Continuum Model

To solve the equations describing the continuum mechanics of materials numerically, a discrete representation has to be found. This is still an approximation of the problem: therefore, finding the approximation with introduces the smallest error while being numerically efficient is the crux of impact modelling.

Most formalisms divide the spatial domain into a set of nodes on a grid. Physical properties are known at the grid nodes, and can be interpolated in between. Because it naturally conserves the mass, Lagrangian schemes are often used, where the grid nodes follow the flow of material (see Figure 2.1[a]). This leads to deformation of the cell and can result in extreme cell dimension ratios. As the timestep has to be lower than the signal traveling time of the shortest cell dimension, this results in extremely short timesteps needed. Therefore, often extremely deformed cells are either removed (eroded) from the simulation, or

split into multiple cells and the material redistributed.

Eulerian grid have nodes fixed in space, and the flow of material has to be modelled leading to cells only partially filled (see Figure 2.1[b]), and the surface not being defined directly causing artificial numeric diffusion. Also, the history of the material, the strains and fractures it has experienced, is lost, and mixing of multiple materials in one cells might require interpolation between two different EOSs. Also, the full spatial domain has to be resolved in the grid, resulting in much larger numbers of grid points needed than for Lagrangian formalisms. Still, as the deformation of cells in hypervelocity impact simulations is usually extreme, Eulerian approaches are used in many codes, for example CTH (McGlaun et al. 1990). Many improvements can be used to increase efficiency and accuracy, such as adaptive mesh refinement and surface reconstruction (e. g. Hageman and Walsh 1971).

The Arbitrarily Lagrangian Euler (ALE) formalism is an attempt to integrate the surface-conserving features of the Lagrangian formulation with the stability against cell distortion of Eulerian grids. While the exact approach varies for each implementation, in general calculations are preformed in the Lagrangian formulation, but at a limiting distortion of a cell, the content of the cell is remapped in an additional 'advection' step onto an underlying Eulerian grid.

A widely used shock physics code of this kind is iSALE. Originating from the SALE code, Melosh et al. (1992) introduce a Grady-Kipp type damage model, added support for multiple EOSs, and tested the code against an extensive suite of laboratory experiments. Next, Ivanov et al. (1997) modified the code to handle multi-material problems and strength effects, and implemented the use of pre-tabulated ANEOS equation of state relations for rocky materials (Ivanov 2003).

The code was extended to iSALE by Collins et al. (2004) and Wünnemann et al. (2006), including a model to treat sub-resolution porosity based on the strain. This so called ε-α model was improved for highly porous materials by Collins et al. (2011). Creation of porosity due to dilatancy was included by Collins (2014).

Although iSALE is a widely used and well tested shock physics code, gravitational forces have been implemented only recently. It is implemented as a self-consistent central gravity field for the simulation of giant impacts onto spherical planetary bodies. In the context of this work, focussed on asteroids at the transition size from purely strength dominated to gravity dominated behaviour

the influence of gravity in highly non-spherical bodies was to be tested. There-
fore, a gravitational N-body code had to be used. Because the SPH formalism
uses particles to describe the continuous medium, the ease of integration led
to the decision to use the SPH solver in `Autodyn`, a shock physics code package
developed originally by Century Dynamics, Inc. and ANSYS (Century Dynamics
Ltd 2000).

2.1.2 Smoothed Particle Hydrodynamics

The Smoothed Particle Hydrodynamics (SPH) formalism provides a gridless lag-
rangian method, where all characteristics are evaluated at the position of pseudo
particles. Developed by Lucy (1977) as a Monte-Carlo approach to test fission
of optically thin protostars and improved to an interpolation scheme by Gingold
and Monaghan (1977) and Monaghan (1988), it became widely used in fluid
dynamic problems due to its simple formulation for three dimensional problems
(Stellingwerf and Wingate 1994). Each particle represents mathematically an
interpolation node at which all material properties are known. At every point in
space material quantities are interpolated by evaluating the surrounding particles
using a kernel function. The kernel function W is required to be continuous
and differentiable. Gradients in physical quantities are obtained by analytic
differentiation by the interpolated functions. The choice of kernel function is
arbitrary: there are infinitely many possible kernels (Monaghan 1988). For
practical purposes, kernel functions that are equal to zero after a certain distance
are used. This means that only nearest neighbouring nodes have to be evaluated,
greatly improving efficiency.

In the implementation of the SPH solver in `Autodyn`, the value of a physical
quantity at point x is approximated by (Hayhurst and Clegg 1997)

$$f(x) \approx \int f(x')W(x - x', h)\mathrm{d}x' \tag{2.5}$$

and derivatives by

$$\nabla \cdot f(x) \approx \int \nabla \cdot f(x')W(x - x', h)\mathrm{d}x'. \tag{2.6}$$

The discrete form of the derivative for function $f(x_i)$ at the position x_i is

given by

$$\nabla \cdot f(x_i) \approx -\rho_i \sum_{j=1}^{N} M_j \left(\frac{f(x_i)}{\rho_i^2} + \frac{f(x_j)}{\rho_j^2} \right) \cdot \nabla W(x_i - x_j, h). \tag{2.7}$$

Here ∇W is the gradient with respect to x_j, M mass and ρ density.

While the choice of kernel function is arbitrary, a widely used one is formulated in Swegle et al. (1994) that uses a cubic B-spline:

$$W(R_{ij}) = \begin{cases} \frac{C}{h^D} \left(1 - \frac{3}{2}R_{ij}^2 + \frac{3}{4}R_{ij}^3 \right) & R_{ij} < 1 \\[2mm] \frac{C}{4h^D} \left(2 - R_{ij} \right)^3 & 1 \leq R_{ij} < 2 \\[2mm] 0 & R_{ij} \geq 2. \end{cases} \tag{2.8}$$

Here, R_{ij} is the distance between nodes i and j normalised by the smoothing length h, $R_{ij} = |x_i - x_j|/h$. D is the dimensionality of the problem, and the constant C is given by

$$C = \begin{cases} \frac{2}{3} & D = 1 \\[2mm] \frac{10}{7\pi} & D = 2 \\[2mm] \frac{1}{\pi} & D = 3. \end{cases} \tag{2.9}$$

The derivative of W at x_j is then given by

$$\frac{\partial W}{\partial R_{ij}} = \begin{cases} \frac{3C}{h^{D+1}} \left(-R_{ij} + \frac{3}{4}R_{ij}^2 \right) & R_{ij} < 1 \\[2mm] \frac{-3C}{4h^{D+1}} \left(2 - R_{ij} \right)^2 & 1 \leq R_{ij} < 2 \\[2mm] 0 & R_{ij} \geq 2 \quad . \end{cases} \tag{2.10}$$

Using these relations, the governing equations are discretized. The resulting forms and their derivation using the kernel W in Equation (2.8) can be found in Swegle et al. (1994). Approximations of the strain and the strain rate tensor were formulated by Libersky and Petschek (1991) and allowed the implementation of strength models. Therefore, not only fluid dynamic problems could now be analysed with the SPH formalism, but strength effects in shock physics could be addressed. The strain rate tensor at position x_i is approximated by (Libersky

and Petschek 1991):

$$\dot{\varepsilon}_i^{\alpha\beta} \approx \frac{1}{2} \sum_{j=1}^{N} \frac{M_j}{\rho_j} \left(x_j^\alpha - x_i^\alpha \right) \frac{\partial W}{\partial x_i^\beta} + \frac{1}{2} \sum_{j=1}^{N} \frac{M_j}{\rho_j} \left(x_j^\beta - x_i^\beta \right) \frac{\partial W}{\partial x_i^\alpha} \qquad (2.11)$$

$$\alpha, \beta \in \{1, 2, 3\}.$$

Here, i and j are node indices, α and β dimension indices. Benz and Asphaug (1995) extended the strength model to simulate brittle solids, and since then SPH methods are widely used in impact shock physics.

An inherent limitation of the SPH formalism is the lack of a well defined surface of the described solid body. Because of the interpolation scheme used, all fundamental properties are smeared out over a range of two times the smoothing length h weighted by the kernel function W used (Equation [2.8]). Therefore, interfaces between distinct solid bodies have to be implemented explicitly by constructing a virtual interface plane when two bodies overlap within a smoothing length (e. g. Century Dynamics Ltd [2000]). Otherwise, the material at the interface is treated as a continuum, effectively welding those two bodies into a single solid body.

In the simulations presented in this work, for both SPH solvers used there was no special treatment of SPH solid body interfaces implemented, leading to exactly the described welding effects described above. The implication of this approach will be discussed in Section 5.2.3

2.1.3 The SPH Solver in `Autodyn`

The impact simulations presented in Chapter 3 of this work were run using `Autodyn`, a 3D shock physics code. The SPH solver used here has been described by Hayhurst and Clegg (1997).

It was validated for hypervelocity impacts by on spacecraft shield by Birnbaum et al. (1996), compared to a Lagrangian finite element code and experimental X-ray data on debris cloud expansion by Faraud et al. (1999) and has been used for modelling impacts of interstellar material with velocities of up to $300 \, \text{km s}^{-1}$ collected by the aluminium foil targets on the Stardust mission (Price et al. 2012). It was successfully used to simulate the disruption of rotating targets in light-gas gun experiments (Morris et al. 2013b). It has been compared to other shock physic codes using a Tillotson equation of state in a study by Pierazzo et al. (2008).

`Autodyn` provides an interface of `Fortran` routines to implement user-defined material models (Ansys Inc 2012). The EOS, the constitutive model, as well as erosion and failure handling routines can be accessed, and internal data structures can be manipulated. Therefore, in principal arbitrary accelerations can be applied to all nodes.

To avoid numeric instabilities, `Autodyn` sets a lower velocity limit for nodes, usually at 1×10^{-8} in simulation units. The limit results in a cut-off of smaller values, which are set to zero. As gravitational forces on small bodies are on order of magnitudes smaller than impact-induced loads, this cut-off value has to be lowered significantly. Unfortunately a cut-off limit below 1×10^{-11} resulted in numerically unstable results. Therefore, the implementation of gravitational forces is not currently possible within `Autodyn`.

Parallel treatment is included using domain decomposition at the beginning of the simulation: the nodes are spatially decomposed into groups, and each group is assigned to a thread. Therefore, in simulations with large deformations where these groups might spatially mix, efficiency is non-optimal but by using four processing cores in parallel, a reduction in computing time of 40 % could be achieved.

2.1.4   The SPH Solver in `LS-DYNA`

Because this work includes simulations of impacts on bodies larger than a few hundred metres which are in the gravitational scaling regime of strength (see Section 1.3.6), the explicit treatment of gravitational forces is of high interest. After a short series of tests the shock physics code `LS-DYNA` proved to allow a robust implementation of full self-gravitation into the SPH solver. Therefore, simulations on larger bodies were done using `LS-DYNA` extended with user-generated subroutines.

The SPH solver in the shock physics code `LS-DYNA` is very similar to the implementation in `Autodyn` and was incorporated into the code by Lacome (2000). The same kernel function W described in Equation (2.8) is used. Details of the implementation are found in the manual (Livermore Software Technology Corporation 2006).

A preliminary comparison against other solvers available in `LS-DYNA` for penetration simulations into concrete material was performed by Schwer (2004). Akarca et al. (2008) published a study on large-strain deformation behavior of aluminium comparing the Eulerian and SPH solvers in `LS-DYNA` and found good

Parameter	Symbol	Value	Unit
Reference density	ρ_0	3214	kg m^{-3}
Gruneisen coefficient	Γ	1	none
Parameter C1	C_1	6.22	m ms^{-1}
Parameter S1	S_1	0.83	none
Intact strength at zero pressure	Y_{i0}	90	MPa
Coeff. internal friction	μ_i	0.8	none
Limiting intact strength, Y_M	$Y_{i\,\text{lim}}$	1500	MPa
Damaged strength	Y_{d0}	1.0	MPa
Coefficient of internal friction	μ_i	0.6	none
Limiting damaged strength	$Y_{i\,\text{dam}}$	2500	MPa
Plastic strain at failure, limit	ε_{fc}	1.0×10^{-4}	MPa
Linear coefficient	B	1.0×10^{-5}	none
Limiting pressure	p_c	300	MPa
Erosion at geometric strain	ε_{ero}	0.9	none

Table 2.2: Material parameters for olivine material used in this work. See Section 2.1.5 for the exact formulation of the model. (Marsh 1980; Collins et al. 2004)

agreement of the simulated stress-strain behavior and experimental data for both. A recent comparison of the SPH implementation to grid-based methods has been done by Goyal et al. (2014) for impacts on aircraft fan blades.

LS-DYNA offers large scale parallelization both on shared memory systems as well as on distributed memory systems. As the gravitational code interfaced with LS-DYNA was optimized for shared memory systems only using OpenMP, the shared memory version of LS-DYNA was used in the simulations described in Chapter 4.

2.1.5 Material Parameters

In order to solve the equations constituting the material model, a large number of input parameters have to be defined. In this Section, the equations and parameters used in the SPH impact modelling are summarized. This approach has already been used in many studies (e.g. Collins et al. 2004). The asteroid material is described using a simple approach based on a Mie-Grüneisen equation of state, extended by a strength and a failure model adapted from Collins et al. (2004). All parameters are displayed in Table 2.2.

In all simulations in this work, olivine was used as a material that is commonly found in asteroids. Olivine originates from the mantle of differentiated asteroids

(Burbine et al. 1996), and is therefore expected to be found in asteroids that have been created of re-aggregated material from a catastrophic disruption event.

There are not much data available about the behaviour of olivine under high stress states. To avoid additional complexity, a simple linear equation of state derived from the Rankine-Hugoniot equations for jump conditions connecting physical parameters at a discontinuity (such as a shock front) is used. As discussed in Section 1.3.1 most solids follow a linear relationship between the velocity of the impact v_{imp}, and the velocity of the shock front v_{s} (see Equation [1.14], $v_{\text{s}} = C_1 \cdot v_{\text{imp}} + S_1$, [e.g. McQueen et al. 1967]). This is used together with a Mie-Grüneisen form of the equation of state (Mie 1903; Grüneisen 1912) based on the principal Hugoniot that connects every possible state described by density, shock velocity, and specific internal energy ρ, v_{s}, and e reachable after a shock from the initial set of ρ_0, v_{imp}, and e_0:

$$p = p_H + \Gamma \varrho (e - e_H) \tag{2.12}$$

where

$$p_H = \frac{\rho_0 C_1^2 \mu (1 + \mu)}{(1 - (S_1 - 1)\mu)^2} \tag{2.13}$$

and

$$e_H = \frac{1}{2} \frac{\varrho_H}{\varrho_0} \left(\frac{\mu}{1 + \mu} \right). \tag{2.14}$$

Here $\mu = \frac{\varrho}{\varrho_0} - 1$ denotes the compression, and Γ the Grüneisen coefficient that describes the dependency of the pressure from the internal energy at constant volume: $\Gamma = V \left(\frac{\partial p}{\partial E} \right)_V$ and is usually set to 1.

Marsh (1980) measured shock velocities as a function of impact velocities $v_{\text{s}}(v_{\text{imp}})$ for olivine. This data was fitted, and the resulting parameters C_1 and S_1 are listed in Table 2.2.

A more detailed strength model to describe the behaviour of material damaged by accumulated high yield stress was included. Strength in this model is separated into the behaviour of the intact material, where the yield strength, Y_{i}, is described by a Lundborg model, and damaged material, where the yield strength, Y_{d}, is given by a Coulomb dry-friction law. The strength model is adapted from the model described in detail by Collins et al. (2004), and the yield strengths are give by

$$Y_i = Y_{i0} + \frac{\mu_i p}{1 + \frac{\mu_i p}{Y_M - Y_{i0}}} \tag{2.15}$$

$$Y_d = Y_{d0} + \mu_i p. \tag{2.16}$$

Damage is described by the parameter $D \in [0,1]$ introduced by Ivanov et al. (1997). D_{dam} measures the plastic strain that is accumulated since the start of the simulation in each cell. Following the approach of Collins et al. (2004), the damage is defined as the ratio of accumulated plastic strain ε_p by the plastic strain at failure ε_f,

$$D_{\text{dam}} = \min\left(1, \frac{\varepsilon_p}{\varepsilon_f}\right). \tag{2.17}$$

As a measure for the plastic strain ε_p, the second invariant of the strain tensor is taken. The plastic strain at failure is modelled to be linear with pressure, bound by a limiting pressure p_c below which the limiting strain is set to ε_{fc}:

$$\varepsilon_f = \max\left(\varepsilon_{\text{fc}}, B(p - p_c)\right). \tag{2.18}$$

The effective yield strength is then simply calculated using

$$Y = (1 - D_{\text{dam}})Y_i + D_{\text{dam}}Y_d. \tag{2.19}$$

Following the implementation in Collins et al. (2004), for all pressures large enough that $Y_d > Y_i$, the yield strength is taken to be Y_i. Additionally, particles with a geometric strain larger than ε_{ero} are 'eroded' and removed from the simulation.

For olivine there are no data available for the parameters in this strength model. Therefore parameters for terrestrial granite were used, that have been studied by Collins et al. (2004). Given other assumptions, and since the main aims of this study are not to validate strength models of olivine, this is a reasonable starting point.

The material model used in this work is simplified in many ways. There is no dependency of strength on strain rate or sample size. Both the failure law Equation (2.17) as well as the EOS are simplified relations, to not complicate the simulations by using a parameter space larger than necessary.

Already Grady and Kipp (1980) found in a series of impact experiments and subsequent modelling of fragmentation of oil shale a strong dependency on the strain rate. The authors explained the increase in strength with increasing strain rates as a consequence of finite activation and growth time of cracks during dynamic tensile loading, because cracks grow at a fixed speed related to the sound speed of the material. The rate dependency is therefore most important for tensile failure, and less for shear failure, which is also noted by Holsapple (2009). Tensile failure occurs during unloading of the rarefaction wave, mostly at the near-surface region and beneath the crater floor (Collins et al. 2004). Therefore, for cratering events, mostly the last stage, the modification stage (see Section 1.3.1), is affected by the tensile strength description.

The implemented model also does not take into account strength scaling with size. As pointed out in Section 1.3.6, Weibull (1939) related the increased likelihood to find cracks in a larger volume to a reduction of strength with sample size, controlled by the Weibull parameters k_W and m_W (see Equation [1.17]). Neglecting the size and strain rate dependency in the material description will therefore lead to a size-independent resistance against disruption in the strength regime, so that Q_S^* is constant as opposed to the decrease of Q_S^* with size formulated by Housen and Holsapple (1999) in Equation (1.18) and seen in Figure 1.17. The consequence of the simplification in the material model is most likely an overestimation of the asteroids resistance against disruption, as the decrease of strength with size is not captured which is the dominant size depend effect in the strength regime.

2.2 Gravitational Forces in High-Resolution Impact Simulations

For a body consisting of N elements, the gravitational force on the j-th is calculated by summing up all gravitational forces to all other mass elements i:

$$F_j = G \sum_{\substack{i=1 \\ i \neq j}}^{N} \frac{M_i M_j}{\left| x_i - x_j \right|^2} \vec{x}_{ij} = M_j \ddot{x}_j.$$ (2.20)

Here, $\vec{x}_{ij} = \vec{x}_i - \vec{x}_j$ is the distance between two elements.

Analytical solutions of the corresponding equations of motion, a system of N coupled differential equations of order 2 that can be transformed into a system

of $2N$ coupled differential equations of first order, exist in the general case only for $N = 2$. For the three body problem, some restricted cases can be solved, but for the general case, numerically integrating the equations of motions is needed.

The only exact solution requires for the calculating the forces to loop over every other x_i for every x_j, and therefore the computational complexity is

$$t_{\text{direct}} = \mathcal{O}(N^2). \tag{2.21}$$

Here, accuracy depends only on the integration scheme used. In most schemes, the accelerations will be assumed to be constant during the timestep dt. Simple schemes additionally assume a constant velocity during the timestep, while higher order schemes evaluate the forces multiple times per timestep. The error is directly controlled by the timestep, which has to be small enough to ensure the desired precision. Because of this, solving the gravitational forces directly becomes an immensely time-consuming task for large N even considering the fast development of computational resources.

The first numerical integration of the N-body problem was produced by Hoerner (1960) to test Chandrasekhar's theoretical predictions for the relaxation times of stellar clusters. It became possible, after Hoerner got access to a new, transistor based electronic computer at the University of Tübingen, because the existent computer models G1 and G2 at the Max Planck Institute for Physics, based on vacuum tubes, took almost half a second for the calculation of a single square root (Hoerner 2001). The new machine allowed to integrate systems of up to 16 objects for 3 relaxation timescales. So the advances of computers determined the systems possible to approach computationally, a fact that holds still true in the era of clustered GPU computing and direct summation of $N = 8 \times 10^6$ objects by Capuzzo-Dolcetta et al. (2013).

Therefore, several approaches have been tried to reduce the computational time needed to calculate approximated gravitational forces without introducing uncontrollable errors.

Direct methods In fact, solving the full equation of motion is done for systems where high precision is needed (Capuzzo-Dolcetta et al. 2013) or for moderate N. This approach is often used when a central body dominates the gravitational potential, as in the case of a system with a central star. Using symplectic integrator schemes, where the hamiltonian of the system is integrated exactly and therefore energy is implicitly conserved, Chambers

(1999) developed the `Mercury` code widely used in the field of solar system dynamics, a code partly used also in the development of the Nice model (Tsiganis et al. 2005). A version modified by J. E.Chambers and the author of this thesis has also been used in the study of the stability of planets in a circumbinary system (Deller 2012; Beuermann et al. 2012).

A second symplectic N-body code is `SWIFT` and its derivate `SyMBA` (Duncan et al. 1998). In general, by using higher order integration schemes the numerical error can be significantly reduced, allowing for less integration points and larger timestep, at the trade-off of increasing the computational cost of each integrated timestep.

Particle mesh methods These methods exploit the fact that the Poisson equation of the gravitational potential,

$$\nabla^2 E_{\text{pot}} = 4\pi G\rho, \tag{2.22}$$

can be easily solved in the fourrier-transformed form. The fourrier transformation can be efficiently calculated if the density distribution is mapped on a mesh — therefore its accuracy depends on the mesh resolution used. This approach is of advantage if computational speed is of greater importance than accuracy. A widely used code of this type is `PMFAST` (Merz et al. 2005).

Tree-code methods In this approach, mass elements are grouped hierarchically, and forces to distant groups of particles are approximated using the gravitational potential of the whole group. Barnes and Hut (1986) proposed a first algorithm using a three-dimensional *oct-tree* sorting scheme, where elements in the three-dimensional space are hierarchically sorted into the corresponding octant until each cell contains just a single element. As the decomposition of this tree coincides with the structure of the distributed mass elements, the authors claim that a more rigorous error treatment is possible compared to the usage of different tree sorting algorithms. In the search for algorithms efficient on large computer clusters, parallelization became a key target. Many codes have been developed with this target, namely the still widely used Parallel k-D Tree Gravity code (`PKDGRAV`), (Dikaiakos and Stadel 1997). This code uses a k-D tree balanced sorting algorithm, that will be discussed in Section 2.2.1.

All methods have in common, that based on some criteria (e.g. the *opening angle θ*) gravitational interaction between nearby particles is calculated directly, while otherwise the gravitational potential of pseudo particles containing groups of mass elements will be evaluated.

For all tree-sorting algorithm, it is assumed that the number of gravity force evaluations does not scale any more with N^2, but instead the computational complexity is:

$$t_{\text{tree}} = \mathcal{O}(N \log N).$$

(2.23)

This behavior was indeed found to be true for a practically useful parameter set by Hernquist (1987).

As always, the each code has some trade-offs, and the best suited will probably be different for each problem. In the problem involved here, the number of particles is large ($N \approx 7 \times 10^5$ to 1×10^6 particles), and the smallest timestep needed is mostly determined by the shock physic calculations. Also, a large number of the mass elements are bound in the target body, and in many simulated non-catastrophic impact events will not change their neighbour relations. Therefore, a tree code method seems to be a logical choice.

Regularisation

Newtons's law of gravitation diverges in the case of two mass elements coming very close together, as the force is going with the cubed inverse of the distance, $F_{i,j} \propto x_{i,j}^{-3}$. When integrating the discrete form of the equation, this becomes problematic, as rounding errors become significant when $x_{i,j}^{-3}$ is in the order of the relative precision of the implementation used, and infinite values will result when the calculated distance is equal to zero.

To circumvent this, the problem is regularized using the *softening parameter* $\zeta \ll 1$. The modified gravitational force is given by

$$F_j = G \sum_{\substack{i=1 \\ i \neq j}}^{N} \frac{M_i M_j}{\left| x_i - x_j \right|^2 + \zeta} \vec{x}_{ij}.$$

(2.24)

2.2.1 An Efficient k-D tree Gravitation Solver

The shock physics code used in this study, LS-DYNA, did not include any gravitational forces except for the possibility to define a global gravity vector. It exposed, however, an interface to define for each node arbitrary forces before the total resulting strains in the current cycle are calculated (CADFEM, priv. communication and Livermore Software Technology Corporation 2006). Therefore, an additional routine had to be developed integrated into LS-DYNA to efficiently calculate forces induced by self gravity.

In the following the layout of the implemented algorithm is described. The aim is to find an efficient and flexible way, that can be tailored by the choice of a set of parameters to perform well in a range of different use cases: It should be usable both as additional subroutine in LS-DYNA, when the number of particles used as well as the timestep is controlled by the hydrodynamic part, but also as a stand-alone program using smaller numbers of particles to follow the long-term gravitational evolution after the actual impact happened. The approach is to:

- construct a balanced binary k-D tree, where all leaves contain at most N_{emax} particles

- create for each leaf a list containing all tree nodes that

  - have to be evaluated using direct summation

  - will be evaluated by using the gravitation multipole moment of the contained mass distribution

- evaluate the forces for each mass element in each leaf.

The code is targeted to run at a cluster of 12 AMD Opteron machines, with 64 cores running at 2.4 GHz using QDR InfiniBand technology. In principal, it is therefore possible to apply efficient distributed memory parallelization techniques (Massively Parallel Processing [MPP]) that could be implemented using Message passing interface (MPI). As the main purpose is to extend the shock physics code LS-DYNA, which was available only supporting shared memory, and the ease of implementation, currently only shared memory is supported making use of OpenMP.

Tree Creation

To avoid duplicating data provided by the interface to `LS-DYNA`, the tree works on the index containing node numbers rather than on the mass nodes themselves. The algorithm is described in the listing Algorithm 2 (see Appendix B), and outlined as follows:

Create root node   All mass elements are added to the first root node.

If the number of mass elements is greater than N_{emax}: Recursivley distribute elements   A new tree node is initialised, elements are distributed to daughter nodes, and gravitational moments are calculated:

- According to the current tree level l, the longest dimension d is identified by

$$d = l \mod D, \tag{2.25}$$

  where $D = 3$ as the simulations are run fully three-dimensionally.

- All elements are sorted along axis d. The sorting is done using a stable merge sort algorithm. An unstable sorting algorithm would lead to overlapping cells, as at each level only one dimension is sorted.

- All elements are bisected along dimension d into two daughter nodes

- Stop recursion when the cell contains at most N_{emax} particles.

Calculate node properties   The following properties are calculated for each node:

- Centre of mass x_{cms}

- Centre of cell x_{cell}

- Total mass M_{tot}

- Opening radius R_θ which is defined by

$$R_\theta = \frac{2}{\sqrt{3}} \max\left(|x_i - x_{\text{cms}}|\right) + \max\left(|x_i - x_{\text{cell}}|\right)$$
$$\text{for all mass elements } i \tag{2.26}$$

- Quadrupole moment of mass distribution in cell

Determine interaction lists   For each leaf cell, two lists have to be created:

1. The Particle–Particle (PP) list contains mass elements to which the gravitational forces have to be calculated by direct summation

2. The Particle–Cell (PC) list contains cells to which gravitational forces are approximated using the cell's gravitational moments.

The algorithm is displayed in Algorithm 2, Algorithm 2. Starting from the root cell, for each subcell it is checked (see Line 11) if the subcell's gravitational moment is a good approximation, or it has to be opened an each individual daughter cells have to be checked again. Additionally, at this point is is assured that the cell ratio is not larger than the maximum cell ratio allow, $C_{\max}$. In the first case the subcell is added to the PC list. If the cell is a leaf itself, the particles contain are added to the PP list.

Calculate accelerations   At this point it is possible to efficiently calculate accelerations due to gravity for all mass particles. The algorithm is displayed in Algorithm 3, Algorithm 2. First, all accelerations between particles in the leaf cell are calculated, then by direct summation accelerations to nearby particles listed in PP list, and then the gravitational moments of cells in the PC list are evaluated.

In Figure 2.2 the PP and PC lists that are evaluated for calculating the forces to one example cell is shown.

Timestep

The most computationally expensive parts of the process are normally the creation of the k-D tree and determination of the interaction lists. The cost for calculating the accelerations varies depending on the parameters used. When N_{emax} is equal to the number of particles N, only one cell is created and the algorithm is equivalent to direct summation. When the opening angle θ is so large that the opening radius of any cell will be larger than the particle domain, the algorithm actually performs worse than direct summation.

During calculation of the shock state of materials the timestep might become very small. As particles might not move far enough during a single timestep to change the neighbour relations, an algorithm was included to check if particles leave the boundaries of their cell. The tree is only build every N_{steps} time steps.
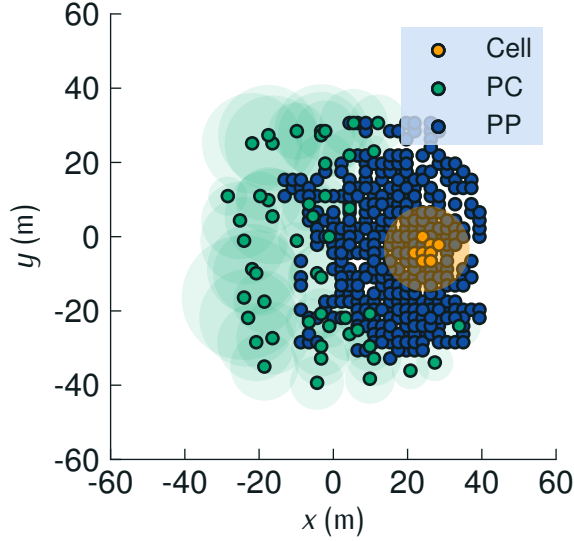
Figure 2.2: Gravitational interaction lists for a single cell in the central slice through a spherical asteroid representation. For cell particles as well as particles in the Particle–Particle (PP) list, forces are calculate by direct summation, while particles inside cells in the Particle–Cell (PC) list are approximated evaluating the gravitational moments of the cell. In this example, the *opening angle* was set to $\theta = 0.7$, the maximum number of particles per cell $N_{emax} = 8$.

The algorithm checks if the distance of the current particle position to the centre of the cell is smaller than $R_{save} \times R_{cell}$. If this is true for all cells, the gravitational forces are calculated using the old tree relations. In this process, no accuracy is lost. As the calculation of the forces is only of complexity $\mathcal{O}(N)$, this algorithm can save a considerable amount of computational time especially at the beginning of the simulation where most particles are at rest.

Ramptime

Because the gravitational forces are treated as additional nodal forces in the impact code, care has to be taken to avoid numerical instabilities at the beginning of the simulation. Therefore, gravitational forces in our program are scaled by a *ramptime parameter* t_{ramp}:

$$F_{eff} = \min\left(1, \frac{t}{t_{ramp}}\right). \tag{2.27}$$

Test have shown that this parameter should be chosen to be a few times the initial time step used.
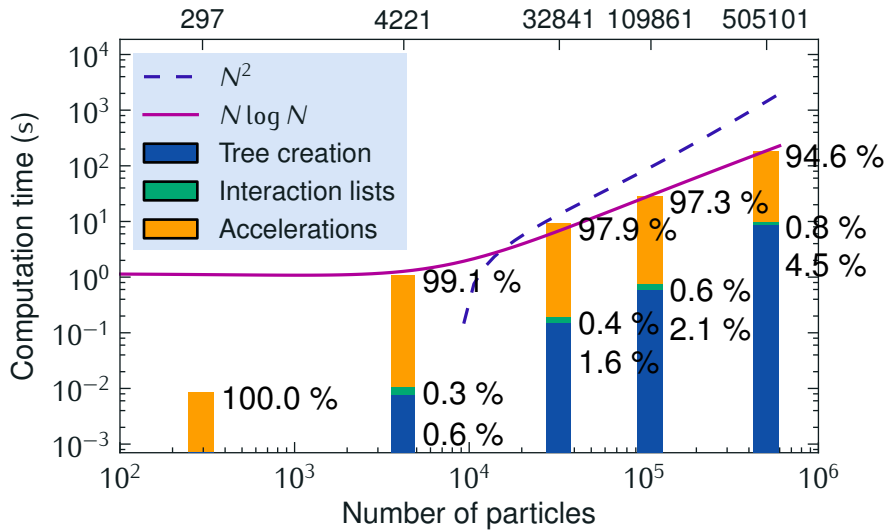
Figure 2.3: Computational time as a function of the number of particles for a typical set of parameters (Opening angle $\theta = 0.6$, particles per cell $N_{\text{emax}} = 200$). The relative contributions of the task to build the tree, prepare the interaction lists, and the calculation of the gravitational accelerations is also noted. The behavior is well fitted using the function $f(n) = a + bN + N \log N$, but not using a quadratic function of N. For this test, a single core on a 2.4 GHz Intel Core 2 Duo was used.

Performance

In Figure 2.3 it can be seen that the implementation does actually scale with $N \log N$. Because of the large N_{emax} of 200 particles per cell used, most of the time is actually taken by calculation of the gravitational accelerations, but the ratio decreases with larger N.

To choose an optimal N_{emax} the comparison seen in Figure 2.4 was performed. While the time spent for tree creation decreases with larger N_{emax}, the calculation of accelerations becomes much more time consuming. The optimal value is clearly between 4 and 16. For all further applications, a value of $N_{\text{emax}} = 8$ was chosen.
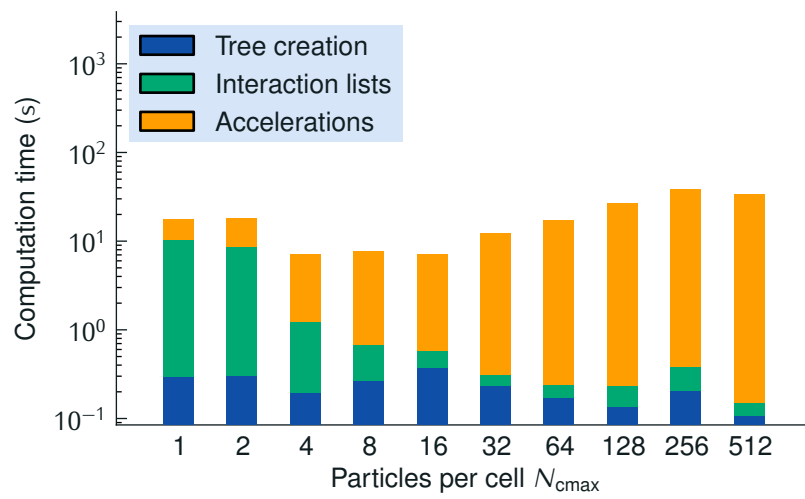
Figure 2.4: Computation time as a function of the number of particles per cell, N_{emax}. All tests used the same configuration with a total of $N = 32\,841$ particles.

Chapter 3

A New Approach to Modelling Impacts on Rubble Pile Asteroid Simulants

3.1 Rubble Pile Asteroid Simulants

The model presented in this work has two main applications: to better understand the stability of rubble pile asteroids against disruption, and to learn how the large-scale interior structure is imprinted to changes on the surface during non-disruptive cratering events away from the impact site. In this chapter the approach to modelling rubble pile simulants in impact simulations is described, and the sensitivity to the choice of initial parameters is tested.

Previous approaches to explicitly model rubble pile asteroid interiors so far have been discussed in Section 1.4, but are summarised again here: Michel et al. (2002) and Jutzi et al. (2010a) introduced a model for pre-fractured rubble piles, in which randomly sized fragments are connected by 'damaged' material. Geretshauser et al. (2011) investigate the collisions of inhomogeneous pre-planetesimals. These planetesimals, formed by collisional coagulation, are highly porous, fluffy dust aggregates, and inhomogeneities in a spherical asteroid are described by a random algorithm based on Gaussian distributions of the

local filling factor. Benavidez et al. (2012) introduced a rubble pile model where the asteroid is represented as a spherical shell filled with an uneven distribution of basalt spheres, with radii ranging from 8 % to 20 % of the radius of the parent body.

The new approach presented here schematically includes the formation stage of rubble pile asteroids. While there are competing scenarios for the formation mechanism for rubble pile asteroids, the conclusion of Farinella et al. (1982) that almost all smaller asteroids are fragments of large asteroids that have been disrupted, is used to provide the formation process.

Alternatively, rubble pile asteroids could form by shattering initially monolithic asteroids in multiple non-catastrophic impact events. Michel et al. (2004b) argue that a parent body, once monolithic, would not yield internal fragments following a well defined power law when shattered by many uncorrelated small impacts, but rather a conglomerate of randomly shaped fragment and structures.

The asteroids formed by the model represent simulants of rubble pile asteroids that formed by gravitational accretion of fragments. In order to understand the evolution of the large scale internal structure of these bodies, and resulting surface features, a method to explicitly model the response of rubble pile constituent parts to hyper-velocity impacts was developed. Including the accretion phase, models of the interior of rubble pile asteroids are created in a three step process, as schematically shown for a shape model of Šteins in Figure 3.1: The formation of the asteroid is modelled as a gravitational aggregation of spherical *pebbles*, that form the building blocks of the target. This aggregate is converted into a high-resolution SPH model, which also accounts for macroporosity on the surface of, and inside, the pebbles.

3.2   Hydrocode Impact Simulations

To simulate high-velocity impacts on these models, the Smoothed Particle Hydrodynamics (SPH) solver in the shock physics code `Autodyn` was used (Birnbaum et al. 1996). While shock codes using different discretization strategies, like the widely used `iSALE` code (Collins et al. 2004; Elbeshausen et al. 2009), have advantages of more accurate treatment of material interfaces, the introduction of gravitational forces to study the long term behaviour of the ejecta profits from the more straightforward calculation of gravitational forces in the gridless SPH method. Therefore, initially the SPH solver in `Autodyn` described in Sec-

tion 2.1.3 was used. When it became clear that the interface of `Autodyn` would
not support the dynamic range occurring by the combination of gravitational
and short-ranged forces induced by the shock, the SPH solver in `LS-DYNA` was
used for simulating impact on the larger asteroid Šteins. As all simulations in
this chapter are on a small asteroid below the transition size to the gravitational
regime, all are done using `Autodyn` and neglecting gravitational forces.

While this approach is unable to resolve pebbles smaller than a few times
the SPH resolution as characterised by the *smoothing length*, h, it is a useful tool
to understand the movement of the larger pebbles inside a rubble pile asteroid.
Although it has been found before that rubble pile asteroids absorb impact energy
more efficiently and are therefore more stable against disruption (see Holsapple
2009), this approach allows the fate of the constituent pebbles *during* impact
events to be followed. Changes in the large scale internal structure of the rubble
pile during the collision can be followed, and therefore major surface features
like hills or depressions might be connected to the collisional history of the body.

In this chapter, first the asteroid simulant model is discussed in Section 3.3,
then the influence of the internal structure and size distribution of the pebbles
on the outcome of impact simulations is tested. A suitable parameter space
is chosen for a series of test simulations using a typical collision of two small
asteroids in the main belt, as described in Section 3.4. The results are discussed
in Sections 3.5 and 3.6.

The new method reproduces the expected overall response of rubble pile
asteroids to hyper-velocity impact events, while providing the possibility to trace
surface changes resulting from internal reconfiguration of the major building
blocks.

3.3   Creating Rubble Pile Asteroid Simulants

The approach to modelling impacts on rubble pile asteroids consists of three
stages, as shown in Figure 3.1: first, the rubble pile is formed as a gravitational
aggregate of hard sphere pebbles which follow a defined size distribution. This
aggregate is then transformed into a model suitable for SPH simulations by
excising the actual asteroidal shape of interest from the gravitational pebble
aggregate and exporting it into the `Autodyn` shock physics code. In this step, an
inner structure of the pebble itself is assumed, so porosity inside the pebbles
is accounted for. Finally, the actual impact simulation using the SPH solver in
`Autodyn` is performed.

**Random positioning
of pebbles**

**Gravitational collapse
using N-body code**

**Cutting out the asteroid
shape**

Filling with SPH particles
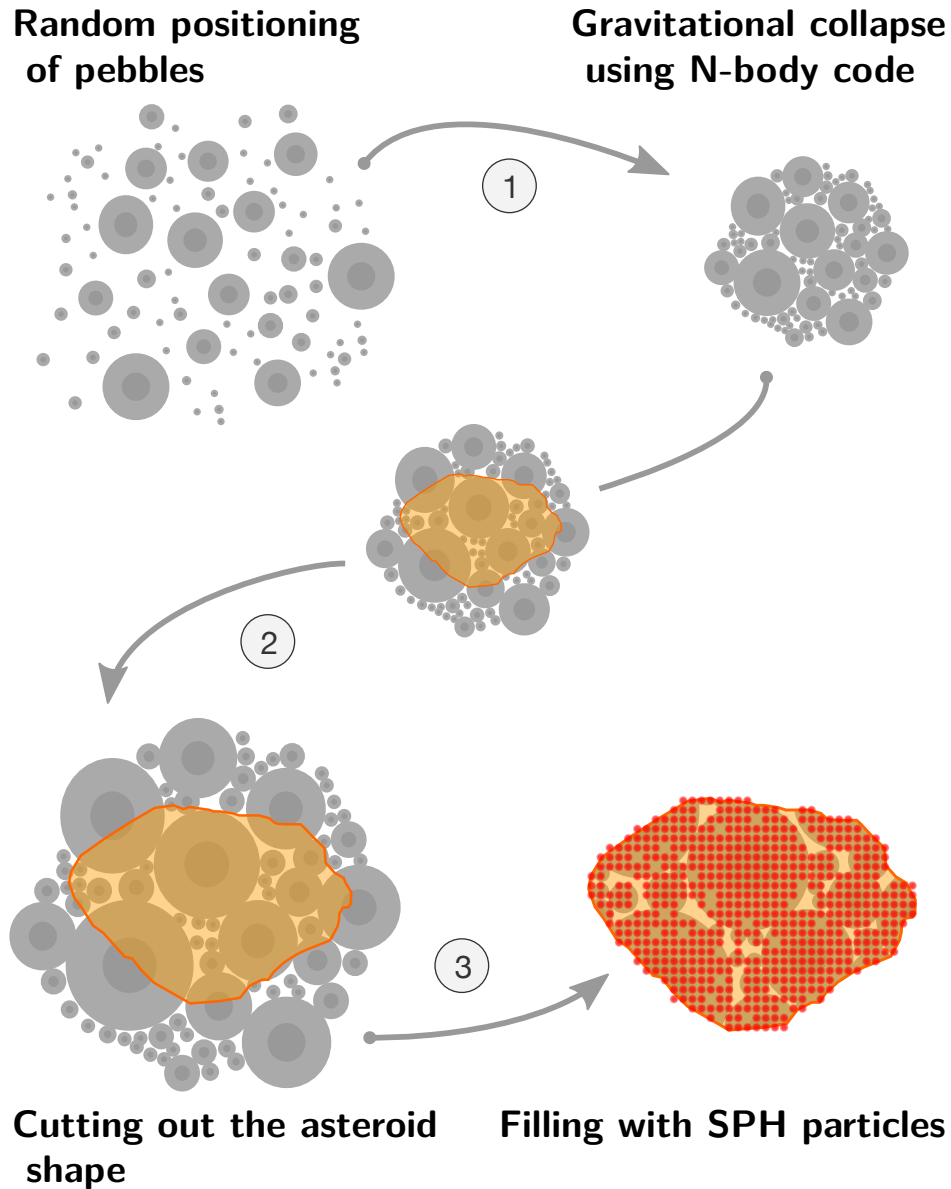
Figure 3.1: Schematic of the new approach to model rubble pile asteroids as explained in Section 3.3. The pebbles are represented by hard-sphere particles, following a certain size distribution, e.g. the size distribution in Equation (3.1). These pebbles are randomly distributed in space, and gravitationally collapse into an aggregate (Step 1). A asteroid shape is excised (Step 2), and the pebbles are filled with SPH particles following a local porosity function, e.g. Equation (3.3) (Step 3). In this Figure the shape model of asteroid (2867) Šteins is used, but in general arbitrary shapes can be used. Note that the size of the SPH particles are not to scale, and that the structure of the single pebbles is just for illustration purposes. An example of a resulting SPH impact model can be found in Figure 3.4.

3.3.1 Interior of Rubble Pile Asteroids Forming as Gravitational Aggregate

The starting point is a set of spherical pebbles randomly distributed in space. These constituent pebbles follow a defined size distribution, that emulates the characteristics of real asteroids. In a scenario where the asteroid formed after a much larger asteroid broke up due to a major impact event, the size distribution can be inferred from impact simulations of these large-scale events. Fragment size distributions are often fitted using cumulative power laws such that $N_R(>R_s) \propto R^{-\alpha}$, where $N_R(>R_s)$ is the sum of all pebbles with radii larger than R_s, R is their radius and α is a constant describing the slope of the size distribution. Tanga et al. (1999) formulate a semi-empirical model with a power law slope of $\alpha = 4.49 \pm 1.00$ for non-disruptive impact events resulting in asteroid family creation, and a slope of $\alpha = 4.89 \pm 0.15$ for highly disruptive events.

In a different scenario, where rubble pile asteroids form by low-speed collisions of pre-existing asteroids, the size distribution of the pebbles will follow the observed size distribution of small asteroids. Using data of the Palomar-Leiden survey (PLS, Houten et al. 1970), a cumulative power law slope of $\alpha = 1.95$ for bodies with diameters between 2 km to 5 km were found (Kresak 1976; Davis et al. 2002). Newer surveys like the Sub-Kilometer Asteroid Diameter Survey (SKADS, Gladman et al. 2009) showed a power law slope of $\alpha = 2.5$ for asteroids with sizes between 1 km to 8 km. Values of impact crater sizes on asteroid Šteins also fit in this regime, as there are found to follow cumulative power law distribution with slope α between 1.3 and 3 (Besse et al. 2012). Also, the size distribution of boulder on asteroid Itokawa follows a cumulative power law with slope 3.1 ± 0.1 (Michikami et al. 2008).

While in both scenarios the source material of the pebbles are likely to follow power law distributions, it should be noted that the assumption of a power law for the pebble size distribution is just a starting point, and it is necessary to make further assumptions to be able to use them in the code presented here. The choice of the limiting radii (i.e. the smallest and the largest pebble) is purely based on the setup and resolution of the model: allowing pebbles larger than the radius of the target will most likely result in a monolithic target. Equally, pebbles with a size below the size of a single SPH particle will be smoothed out and behave like a monolithic target too. $R_{\min}$ should therefore be a least four times the resolution, as given by the smoothing length parameter h, and $R_{\max}$

smaller than half the target's radius. Determining the influence of these three parameters — power law slope α, minimum radius R_{min} and maximum radius R_{max} on the outcome of an impact simulation — is one of the main aims of this chapter.

Creating Gravitational Aggregates

The aggregates are created by placing hard spherical pebbles randomly in space following the specified size distribution, and then calculating the gravitational interactions until collapse is completed. The code used is Rebound (Rein and Liu 2012), a versatile and modular code for calculating gravitational interactions of particles. As at this point no integration of the gravity solver and the shock physics code was implemented, the k-D tree code developed and described in Section 2.2 was not used.

To create the set of pebbles following the desired size distribution, the radius R_i of the ith pebble from a uniformly distributed variable $u \in \mathcal{U}[0,1]$ is determined by

$$R_i = \left(\left(R_{\mathrm{max}}{}^{-\alpha+1} - R_{\mathrm{min}}{}^{-\alpha+1} \right) \cdot u_i + R_{\mathrm{min}}{}^{-\alpha+1} \right)^{\frac{1}{-\alpha+1}}, \quad u_i \in U = \mathcal{U}[0,1].$$

(3.1)

The gravitational collapse is calculated in Rebound using a very simplistic particle–particle interaction model. A coefficient of restitution of 0.4 is assumed, which allows for a quick aggregation process. An example of such a gravitational aggregate can be seen in Figure 3.2. The corresponding size distribution is shown in Figure 3.3. While the size distribution of the total set of pebbles follows exactly the power law function, the size distribution of pebbles inside the excised asteroid shape is affected in two ways: first, the large pebbles seem to be overrepresented in the centre of the agglomerate. Second, some pebbles intersect the surface of the excised asteroid shape and only part of their volume count towards the asteroids volume. The equivalent radii of these volumes are at the left of R_{min} in Figure 3.3 and show that the overall size distribution is not significantly affected.

Converting Into Impact Model of SPH Particles

The gravitational aggregate of pebbles formed in the first step is then transformed into a SPH model by using the location of the solid pebbles to modulate a local
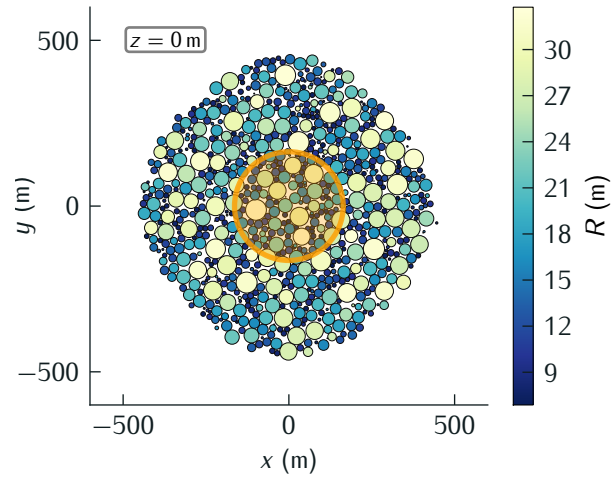
Figure 3.2: Central slice through a gravitational aggregate of pebbles forming a spherical asteroid of roughly 500 m radius. The power law slope of the radius distribution is $\alpha = 2.5$, the limiting radii are: $R_{min} = 6.7$ m and $R_{max} = 32$ m. The size distribution of all pebbles inside the orange sphere is shown in Figure 3.3. The orange sphere is the shell of an asteroid with $r = 164$ m that is excised and converted into the SPH model seen in Figure 3.5 (a). The colour denotes the actual radius of the pebble, which might be larger than the radius of the circle in the intersection shown here.
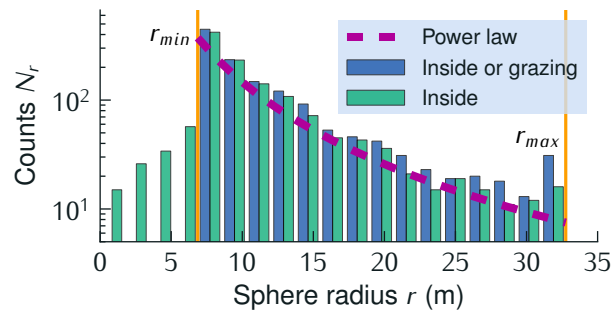
Figure 3.3: Distribution of radii in the gravitational aggregate shown in Figure 3.2 that are inside or grazing the surface of the excised asteroid shape. The dotted line represents the power law function $N_r \propto r^{-2.5}$. The *inside or grazing* set refers to all pebbles that touch the surface of the asteroid shape or lie inside, while for the *inside* the radii of spheres of volume equivalent to intersecting volume of pebbles at the asteroids surface and the asteroid are included and lead to the pebbles with radii smaller than R_{min}. The limiting radii are plotted too.

porosity function $\phi(x)$. SPH particles are placed on a grid filling the desired target shape at a position, $\vec{x}$, if a randomly chosen variable $p \in \mathcal{U}[0,1]$ is lower than the local porosity value $\phi(x)$ which is given by:

$$\phi(x) = \begin{cases} \phi(R_{x,i}) & x \text{ is inside pebble } i \\ 0 & \text{elsewhere}, \end{cases} \tag{3.2}$$

where $R_{x,i} = |\vec{x} - \vec{R}_i|/R_i$ is the distance of $\vec{x}$ to the centre of the nearest pebble i at $\vec{R}_i$ of the gravitational aggregate normalised by the pebble's radius R_i. The radial porosity function $\phi(R_{x,i})$ describes the density profile within each pebble. Again, this is poorly constrained. It can be argued that monolithic fragments of a major disruption event will have been further fractured in the re-aggregation phase, mostly on their upper layers, which would lead to pebbles that are solid in the inside and fractured (i.e. porous) on the outside. Such a profile with a bulk porosity of ϕ_b, could be modelled using the following smooth function

$$\phi_{\text{in}}(R_{x,i}) = \frac{2R_{x,i}^2}{2R_{x,i}^2 - 2R_{x,i} + 1} \cdot \phi_b. \tag{3.3}$$

Integrated over the full normalised radius $R_{x,i} \in [0,1]$, it returns the value for the bulk porosity, ϕ_b, and the distribution function is strictly less than 2. Therefore, as long as $\phi_b < \frac{1}{2}$, the overall porosity can be easily controlled by the parameter ϕ_b.

For centimetre-sized, highly porous aggregates, Beitz et al. (2012), Weidling et al. (2012), and Kothe et al. (2013) showed that in further collisional evolution, material is compacted at the surface layers. A test simulation using such a profile with higher porosity in the centre of the pebbles showed a small, but significant difference in the mass excavated during a cratering event: the same impact configuration excavated 6.7 % of the target's mass, compared to only 2.4 % using the pebble porosity profile in Equation (3.3). As the pebbles in the new model are not centimetre, but metres in scale, the profile that is fragmented more at the outside seems to be more realistic. All the following simulations therefore use the profile defined by Equation (3.3).

There are now two levels of macroporosity in the models: the voids between the spheres, and inside the material itself. Therefore it is possible to control the bulk porosity of the rubble pile models regardless of the void space fraction in

the gravitational aggregates. A cut through the central slice of a highly porous SPH model is shown in Figure 3.4. As laid out in Section 2.1.5, there is no sub-resolution porosity added to the material description, and all porosity is explicitly resolved.

3.3.2 SPH Simulations and Material Parameters

The actual impact simulations are run using `Autodyn` as described in Section 2.1.3. The material parameters can be found in Table 2.2. An overview of the experiments conducted is compiled in Table 3.2.

Because of the difficulties in obtaining good numerical proxies for the expected asteroid material, some experiments were conducted varying the most salient parameters, Y_{i0} and μ_i. As a result, a strong influence of the shear strength was observed. A value reduced by a factor of ten to $Y_{i0} = 9\,\text{MPa}$ lead to a 14% smaller mass of the largest remnant fragment (M_{lr}). The coefficient of internal friction, on the other hand, seemed not to influence the result, as a value of $\mu_i = 0$ lead to a reduction of only 3% in M_{lr}.

3.4 Assessing the Influence of Rubble Pile Structures on Impact Simulations

To validate the approach on explicitly modelling rubble pile internal structure, it is necessary to understand the influence of all parameters controlling the model. Mainly, the model presented here is defined by the size distribution of the pebbles used to form the gravitational aggregate. As a starting point, the power law in Equation (3.3) was chosen, with three free parameters α, R_{min}, and R_{max}, to create the pebbles used for the gravitational aggregate. These three parameters are not directly constrained by observational evidence, and knowing how sensitive impact simulations are to these initial conditions is crucial to assessing the validity of such simulations in inferring anything about asteroidal collisional evolution.

The model was tested in a series of impact simulations representing a typical impact in the main asteroid belt into an asteroid of size equivalent to Itokawa. In this section, first the chosen characteristics of the test cases are described, and then the set of rubble pile simulant configurations are explained.
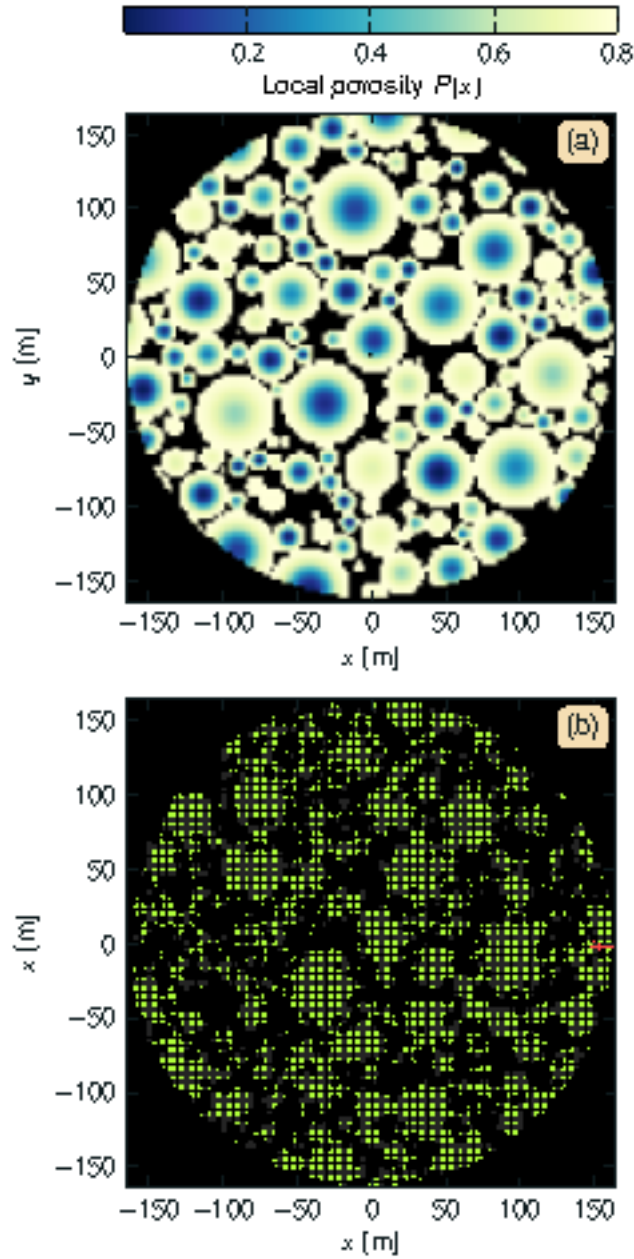
Figure 3.4: Map of the local porosity function $P(r_{x,i})$ described by Equation (3.3) (top, panel a). The model was created using the gravitational aggregate in Figure 3.2 in the central slice at $z = 0\,$m. On the bottom in panel (b), the resulting grid of SPH points is shown. To highlight the effect, a high total void fraction in this model of $\phi_b = 0.58$ has been chosen.

3.4.1   Impact Event and Target Properties

The impact event was chosen to represent a typical impact on a small asteroid
in the main belt. At as this point, gravitational forces are not taken into account,
and a spherical asteroid simulant, volume equivalent to asteroid Itokawa was
chosen. Itokawa is just at the transition from the strength- into the gravity
regime, and the detailed shape model available as a result of the Hayabusa
mission provided an interesting case the test simulations presented here could
be compared with in future work. The radius of the volume-equivalent sphere is
$R_{tar} = 164\,\mathrm{m}$.

Simple, head-on impact events on a single, non-rotating target have been
calculated. The impact velocity was fixed to $5.5\,\mathrm{km\,s^{-1}}$ as an intermediate
value for relative impact velocities of two main belt asteroids that range from
$4.22\,\mathrm{km\,s^{-1}}$ to $(5.81 \pm 1.88)\,\mathrm{km\,s^{-1}}$ (Davis et al. 2002).

From scaling laws described by Holsapple (2009), the impact energy expec-
ted to match the disruption threshold for the given target radius was derived.
Considering the fixed velocity, this directly translates into a radius of $R_{imp} = 4\,\mathrm{m}$
for a monolithic impactor, assuming the same bulk density and material as the
asteroid.

The models contain approximately 700 000 SPH particles with a smoothing
length, h, of 2.54 m. The value of the bulk macroporosity for all simulations
except one monolithic case is 30 %.

3.4.2   Parameter Space of Rubble Pile Simulants

As described in Section 3.3.1, the power law used in this study (Equation [3.1])
contains three free parameters: slope α, and limiting radii R_{min} and R_{max}. Three
values for the cumulative power law slope have been used: the observed slope
in the main belt, $\alpha = 2.5$, (e. g. Gladman et al. 2009) that is similar to the slope
for a collisionally relaxed population (Dohnanyi 1971), and the slope resulting
from impact events without re-accumulation, $\alpha = 4$ (Tanga et al. 1999). For
comparison with older data, simulations with $\alpha = 1.95$ (e. g. Kresak 1976; Davis
et al. 2002) have been conducted.

Practical considerations have to be used to define the limiting sphere radii.
The lower boundary is not only given by the resolution defined by the smoothing
length h — each pebble should be represented by at least 32 SPH particles —
but also by the fact that an aggregate too tightly packed will be indistinguishable

Slope α	1.95	2.5	4
Minimal radius of pebbles, R_{min} (m)	6.86	13.72	20.58
Maximal radius of pebbles, R_{max} (m)		32.8	82

Table 3.1: Matrix of parameters to construct the pebble size distribution used in the creation of the gravitational aggregate explored in this study.

from a monolithic material. The influence of the lower limit has therefore to be tested, and accordingly simulations for $R_{min} = 6.86$ m, 13.72 m and 20.58 m have been executed, which corresponds to multiples of 2.5, 5.5 and 8 times the smoothing length h. The upper limit should be chosen so that a single sphere is considerably smaller than the asteroid itself. Values of $R_{max} = 1/5 \cdot R_{tar}$ and $R_{max} = 1/2 \cdot R_{tar}$ have been tested. All parameter values tested are listed in Table 3.1.

3.5   Comparing Outcomes of Simulations

To assess the influence of the three parameters discussed, numerical simulations for each point in the parameter matrix in Table 3.1 have been conducted. Additionally, more detailed experiments on a subset of these parameters, described as Sets (a) and (b), have been run and compared to two non-rubble pile test cases (Sets [c] and [d]). All experimental configurations are described in Table 3.2. As a representative example, two impact simulation outcomes for equal parameters of the slope α and R_{min}, but differing in maximum radius R_{max} are shown in Figure 3.5. To compare the outcomes of a large number of simulations, various metrics are defined. In the following, these metrics and the results of the simulated test cases are discussed.

3.5.1   Influence on the Fragment Size Distribution and Mass of the Largest Remnant

One natural metric is the fragment size distribution, and the relative mass of the largest remnant fragment to the body's initial mass. Although it is reasonable to use this to compare different simulations in this study, it is more difficult to compare the results in this work to other researchers' simulations, or observational data on asteroid families, as the gravitational aggregation that will follow after the disruptive impact event is not calculated. The determination of the fragment

	Pebble size distribution			Impactor	Metric	Result in Figure
	α	$R_{\min}$ (m)	$R_{\max}$ (m)	R_{imp} (m)		

Experiment 1: Influence of the gravitational aggregate parameters.

	All permutations of α, $R_{\min}$ and $R_{\max}$ in Table 3.1			4	M_{lr}	3.10, 3.9

Experiment 2: Testing influence of the exact impact location

	α	$R_{\min}$	$R_{\max}$	R_{imp}		
Set (a)	1.95	6.86	32.8	4	M_{lr}	3.7
Set (b)	4	6.86	32.8	4	M_{lr}	3.7

Experiment 3: Testing rubble pile model against monolithic targets

	α	$R_{\min}$	$R_{\max}$	R_{imp}		
Set (a)	1.95	6.86	32.8	2 to 8	Q_D^*	3.8 (3.5, 3.6)
Set (b)	4	6.86	32.8	2 to 8	Q_D^*	3.8 (3.5, 3.6)
Set (c)	Monolith, random macroporosity			2 to 8	Q_D^*	3.6, 3.8
Set (d)	Monolith, no macroporosity			2 to 8	Q_D^*	3.6, 3.8

Table 3.2: Compilation of simulated impact configurations. Sets (a) to (d) are specific configurations referred to in the text. The three parameters of the pebble size distribution define the characteristics of the gravitational aggregate (see Section 3.3.1). The impactor radius defines the impact energy, as all impactors had a velocity of $5.5\,\mathrm{km\,s^{-1}}$. The metric denotes the quantity used to compare a set of simulations. The mass of the largest remnant fragment, M_{lr}, can be derived for every simulation, while the disruption threshold Q_D^* is the energy at which M_{lr} is exactly 50 % of the target's mass. For more details, please refer to Section 3.5.

The largest set of simulations is experiment 1, the complete matrix of power law parameters to test the influence of the configuration of the gravitational aggregate. The results are discussed in Section 3.5. In experiment 2, the error margin caused by the arbitrarily chosen impact location on the inhomogeneous target was determined. The result is discussed in Section 3.5.1. Experiment 3 is testing the response of rubble pile model simulants in impact simulations compared to simple monolithic targets. This is discussed in Section 3.6.
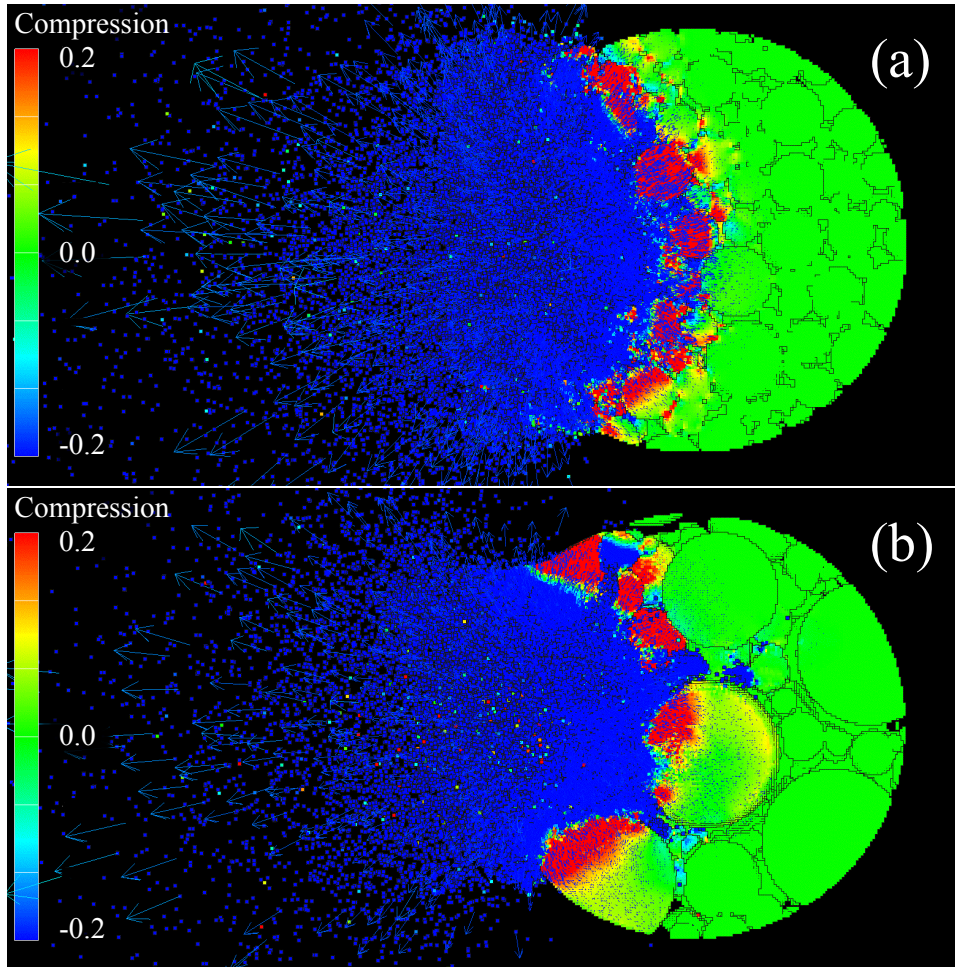
Figure 3.5: Distribution of material compression as given by $\rho/\rho_0 - 1$, where ρ_0 is the initial density at the start of the simulation, in impact simulations for two different internal structures after 2.8 seconds. Model **(a), top** was created using the gravitational aggregate shown in Figure 3.2 ($\alpha = 2.5$, $R_{min} = 6.86$ m and $R_{max} = 32$ m). Model **(b), bottom** was created using an aggregate differing in the maximum radius of the pebbles used ($\alpha = 2.5$, $R_{min} = 6.86$ m and $R_{max} = 82$ m). There is no regolith layer included.

size distribution is done using `Autodyn`. In `Autodyn`, a fragment is defined as a
conglomerate of SPH particles that are all connected within a smoothing length,
h, within which failure did not occur (Ansys Inc 2012). The mass of the largest
remnant fragment, M_{lr}, is defined as the largest intact fragment as determined
by this algorithm. All simulations where stopped after 30 s, as by this time no
further significant alteration could be observed.

The fragment size distribution is only helpful if it does not directly reflect the
size distribution of the pebbles that formed the gravitational aggregate used to
construct the model. This is checked by examining the outcome of the set of test
calculations: if there is a direct dependency, this should be reflected by a strong
correlation of the model parameters and the largest remnant fragment. The
change in slope of the cumulative fragment size distribution for four simulation
setups described as Sets (a) to (d) in Table 3.2 has been tested, two of which
(Sets a and b) have been created using the rubble pile model discussed here
(See Figure 3.6). While they obviously differ in the mass of the largest remnant
fragment, they also differ in the characteristic of the slope. For both models
that do not include the internal rubble pile structure described in this work, but
rather small, unconnected voids leading to the same macroporosity of 30 % (Set
c) or no voids at all (Set d), the slope is less steep than in the cases of rubble pile
model (Sets a and b). The slope of model (c), containing random porosity, is
similar to the models (a) and (b), while the model with no porosity (d) is clearly
distinct. The slope for Set (a) and Set (b) are very similar, while the power law
slope used to create the gravitational aggregates had been −1.95 and −4.00,
respectively. This indicates that the initial slope of the pebble size distribution
and the resulting fragment size distribution are not identical.

A series of impact simulations on identical target configuration has been
analysed to quantify the influence of the impact location on the mass of the
largest remnant fragment. At a randomly picked impact site, there are two
extreme cases: either the impactor hits a large pebble, or the impactor will hit
a void between pebbles. In Figure 3.7, it is shown that the mass of the largest
remnant fragment differs by not more than 4 %, with a standard deviation of
roughly 1 %. Therefore, the typical error for each value of the mass of the
largest remnant fragment in the following discussion can conservatively be
regarded as ±2 %. Interestingly, this does not seem to depend on the exact
pebble configuration at the impact zone.
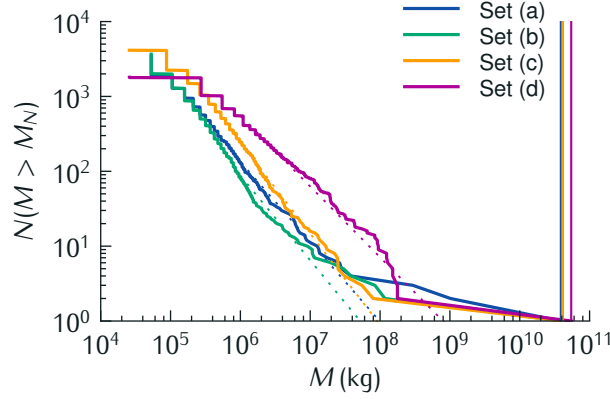
Figure 3.6: Cumulative distribution of fragment mass for four different simulation setups: Set (a) $\alpha = 1.95$, $R_{\min} = 6.86\,\mathrm{m}$, $R_{\max} = 32.8\,\mathrm{m}$; Set (b) $\alpha = 4$, $R_{\min} = 6.86\,\mathrm{m}$, $R_{\max} = 32.8\,\mathrm{m}$; Set (c) Random porosity; Set (d) No porosity. All impacts have been calculated using an impactor of $R_{\mathrm{imp}} = 4\,\mathrm{m}$ at $5.5\,\mathrm{km\,s^{-1}}$. The vertical lines on the right denote the mass of the largest remnant fragment M_{lr}, and the dotted lines are fitted power law distributions.

3.5.2 Influence on the Specific Disruption Energy Threshold Q_D^*

While material strength usually means a measure of what kind of stress or strain states a certain material is able to withstand, it can also define a strength of a whole body to withstand disruption at a certain impact energy. This empirical value is usually given by the parameter, Q_D^*, defined in Equation (1.16). It represents the normalised impact energy $E_{\mathrm{kinimp}}/M_{\mathrm{tar}}$, at which the mass of the largest remnant, M_{lr}, is exactly half the mass of the target, M_{tar}. This denotes the transition from the cratering regime to disruption regime of the target body.

An additional complexity is the re-accumulation of ejected material. For bodies larger than a few hundred meters, the gravitational forces are able to prevent shattered fragments from dispersing (Holsapple 2009). As discussed in Section 1.3.6, in this so-called gravitational regime, the specific energy required to disrupt the asteroid increases with asteroid radius, and is given by Q_D^* as the specific energy at which the largest remnant after the re-accumulation has exactly 50 % of the target's mass. In the series of simulation presented here, re-accumulation is not taken into account. As the target has a radius of just $R_{\mathrm{tar}} = 164\,\mathrm{m}$, it is just at the transition between strength and gravity regimes, and therefore Q_S^* and Q_D^* will not differ significantly.

In Figure 3.8, the largest remnant fraction as a function of the specific impact
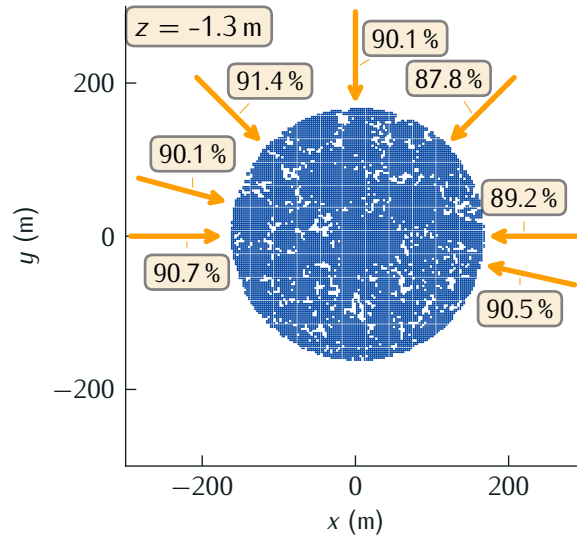
(a) This model was created using the parameters $\alpha = 4$, $R_{\text{min}} = 13.72\,\text{m}$ and $R_{\text{max}} = 82\,\text{m}$. See description below for further details.
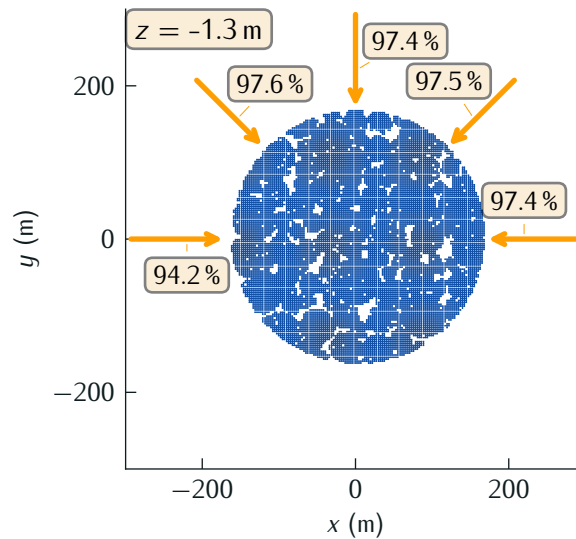
(b) This model was created using the parameters $\alpha = 1.95$, $R_{\text{min}} = 6.8\,\text{m}$ and $R_{\text{max}} = 32.2\,\text{m}$. See description below for further details.

Figure 3.7: Mass of the largest remnant fragment in percent of the target mass for different impact locations on two different asteroid models. Each box corresponds to the outcome of a single simulation run on the same model, the arrow indicating the impactor velocity vector. The impactor was a monolithic asteroid with $R_{\text{imp}} = 4\,\text{m}$ at a velocity of $v_{\text{imp}} = 5.5\,\text{km}\,\text{s}^{-1}$. This gives an estimate of the error assigned to resulting largest remnant masses for individual simulations.

energy for four different target configurations is shown. For Set (d), the one that includes no voids at all, there is a sharp transition from the cratering regime to the disruption regime at $Q_D^* = 1.29 \times 10^6 \, \text{erg g}^{-1}$. This sharp transition is known from laboratory scale experiments for the disruption of non-porous targets and has been reproduced by other simulations (Benz and Asphaug 1999). For all three cases that include void space, i.e. the models created using the rubble pile model (Sets a and b), as well as the model using randomly distributed void space (Set c), this sharp transition is smoothed, and shifted toward higher specific energies. Therefore, void space actually strengthens the asteroids, a behaviour observed in numerical experiments before (Holsapple 2009).

A study by Jutzi et al. (2010b) focussed on the transition from the strength to the gravity regime for solid bodies as well as bodies containing sub-resolution voids. Scaling laws derived from numerical simulations at six sizes ranging from 3 cm to 100 km using an impact incidence angle of 45° and $v_{\text{imp}} = 5 \, \text{km s}^{-1}$ give an expected disruption threshold for the target size discussed here of $Q_D^* = 3.05 \times 10^6 \, \text{erg g}^{-1}$ and $Q_D^* = 1.89 \times 10^6 \, \text{erg g}^{-1}$ for porous and solid material, respectively. This is in good agreement with the values found in this work, as seen in Figure 3.8: $Q_D^* = 5.5 \times 10^6 \, \text{erg g}^{-1}$ and $Q_D^* = 1.29 \times 10^6 \, \text{erg g}^{-1}$ for porous and solid material, respectively. The rubble pile model presented here seems to be slightly more resistant against disruption, but it is not clear how much of this difference is attributed to different material model formulations and parameters.

Because of the simplified material model description, that does not include size or rate dependency (see Section 2.1.5), it is expected to overestimate the resistance against disruption of the asteroid simulants. This is not found to hold true for the simulants with solid material, that are in fact found to be weaker than the models simulated by Jutzi et al. (2010b). This can in part be explained by the higher yield strength of 3.5 GPa used by the Jutzi et al. (2010b) compared to a yield strength of 1.5 GPa used in this work, but still highlights the need to implement a more advanced material model in further studies.

3.6 Results — Sensitivity to Model Parameters

One of the main objectives of this study is to assess the influence of the three free parameters used to create gravitational aggregates in the model — the power law slope α, the limiting radii R_{min} and R_{max} — on the outcome of impact events.
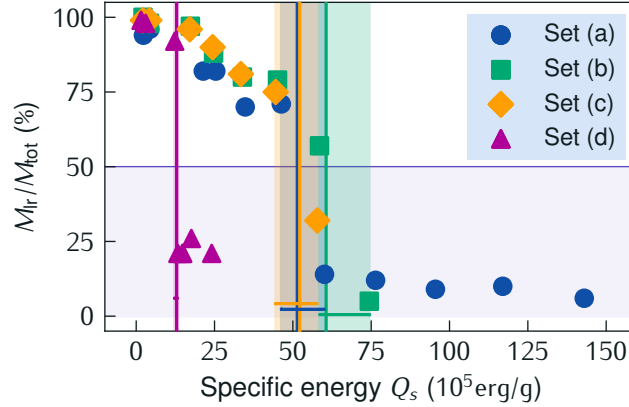
Figure 3.8: Specific impact energy plotted against the relative mass of the largest
remnant for four different settings 30 s after impact.
Set (a) $\alpha = 1.95$, $R_{min} = 6.86$ m, $R_{max} = 32.8$ m; Set (b) $\alpha = 4$, $R_{min} = 6.86$ m,
$R_{max} = 32.8$ m; Set (c) Random porosity; Set (d) No porosity.
The vertical lines denote the linear interpolated position at which the largest
remnant has 50 % of the target's mass, or Q_D^*, the shaded regions show the
enclosing interval.
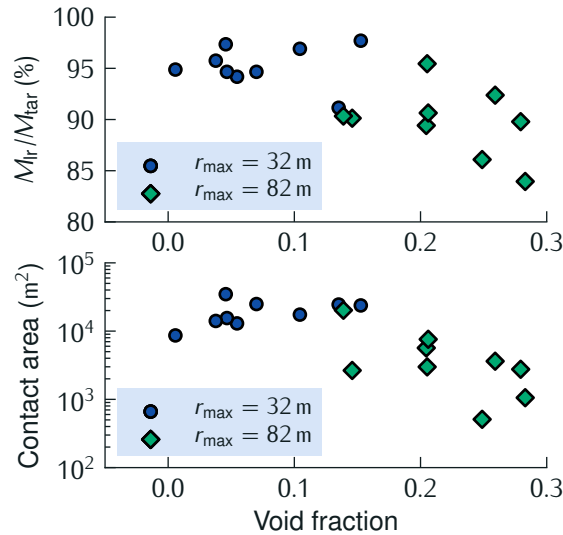
Figure 3.9: Relative mass of the largest remnant (upper panel) and pebble
contact area (lower panel) as a function of the void fraction in the gravitational
aggregate for all simulation configurations described in Table 3.2, experiment
1. The pebble contact area is defined as the sum of all contact areas between
pebbles inside the rubble pile simulant.

Numerical experiments for all combinations of these three parameters found in
Table 3.1 have been conducted. As the inner structure of the rubble pile asteroid
models is controlled only by the power law parameters used, no direct control
of the void fraction defined as the space in between the pebbles and the ratio of
overall asteroid volume is given. Instead the overall bulk porosity ϕ_b is equal to
30 % in all models. Therefore, Figure 3.9 shows that models with larger pebbles
($R_{max} = 82$ m) keep more void space open, while smaller pebbles ($R_{max} = 32$ m)
fill the voids. This geometric effect causes a higher void fraction if there are
more large pebbles, while the pebbles will have less internal porous space. The
figure also shows that a higher void fraction increases the mass excavated by
the same impact energy. This effect is discussed later.

In Figures 3.10 and 3.10, the resulting mass of the largest remnant fragment
for each internal configuration after a calculated impact event with an impactor
speed of $4 \, \text{km} \, \text{s}^{-1}$ is shown. The following observations can be made:

**The larger the void fraction, the smaller the mass of the largest remnant
fragment M_{lr} (see Figure 3.9)** As the bulk porosity is constant, a larger
void fraction means more *connected* voids rather than smaller, distributed
voids. The larger pebbles themselves contain less porosity, and therefore
behave more like a solid material that has a lower resistance against
collisional disruption, or in other words a lower disruption energy Q_D^* (see
Figure 3.8). Through the solid larger pebbles, energy is transmitted into
the centre of the asteroids more readily, additionally weakening the body.

**For small $R_{min} = 6.9$ m, there is less dependency on the decrease in strength
for larger R_{max} (Figure 3.10f)** This might be because this case resembles
more of a solid body with randomly distributed voids, as the small pebbles
fill the space between the large pebbles evenly.

**The slope α seems to have no clear effect on the strength (Figures 3.10a
and 3.10c):** only a slight increase of strength when α is changed from
$\alpha = 1.95$ to $\alpha = 4.00$ is observed. This increase is in most cases barely
significant, as the error for a single simulation is around 2 % (see Sec-
tion 3.6), and the increase is for most cases between 2 % to 5 %. Still,
the increase is observed for all sets of r_{min} and r_{max}, and can therefore not
easily be dismissed as a numerical artefact.
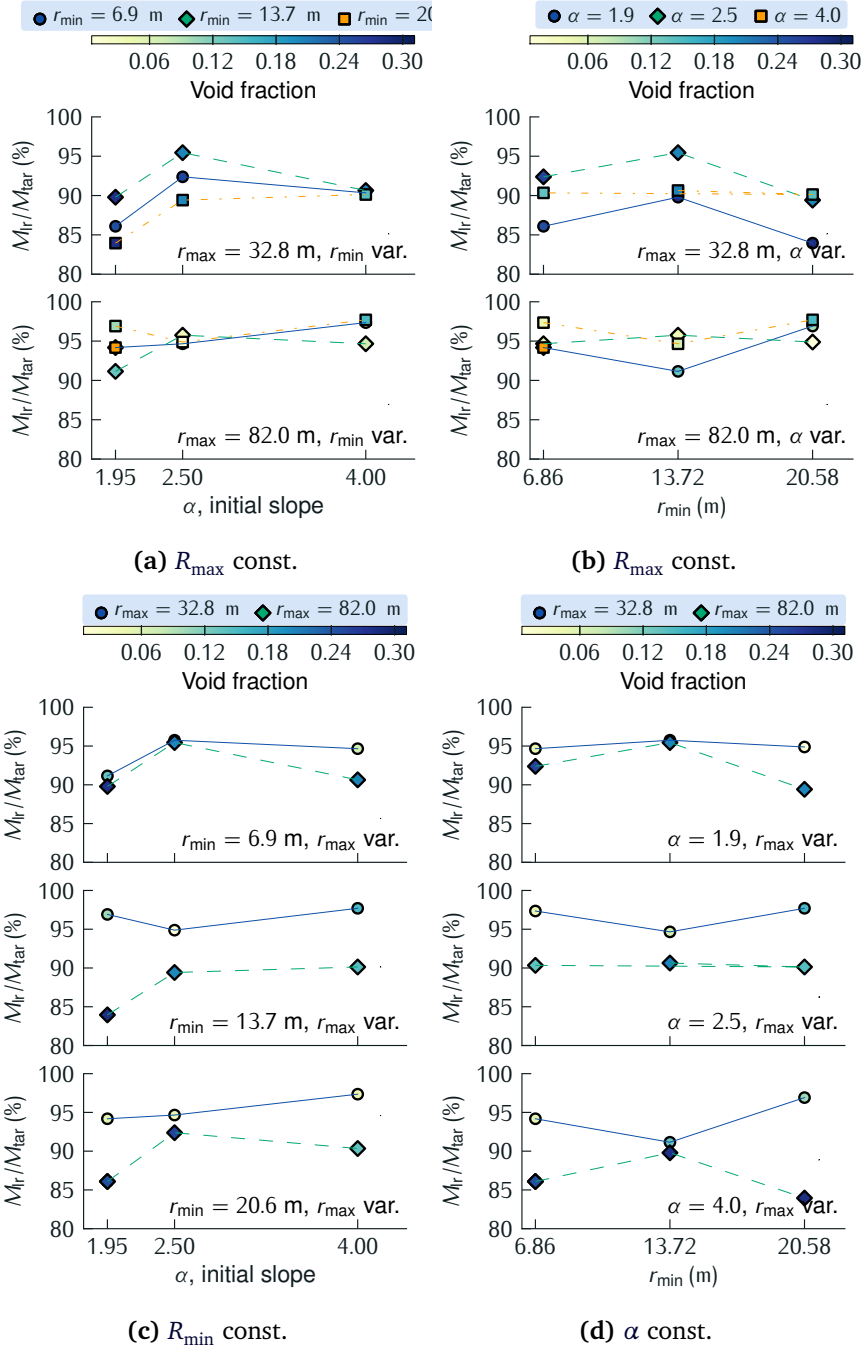
Figure 3.10: Mass of the largest remnant fraction after an impact of a $R_{imp} = 4\,\mathrm{m}$ asteroid at $v_{imp} = 5.5\,\mathrm{km\,s}^{-1}$ for different internal structures of the target. The targets have been formed as an $R_{tar} = 164\,\mathrm{m}$ asteroid, the internal structure derived from a gravitational aggregate formed using a set of three parameter α, R_{min}, and R_{max} of the value matrix in Table 3.1. The individual error bar in relative mass is $\pm 2\%$ (see Figure 3.7 and Section 3.5.1). Each sub-figure shows the same set of data. (Figure continued on page 92)
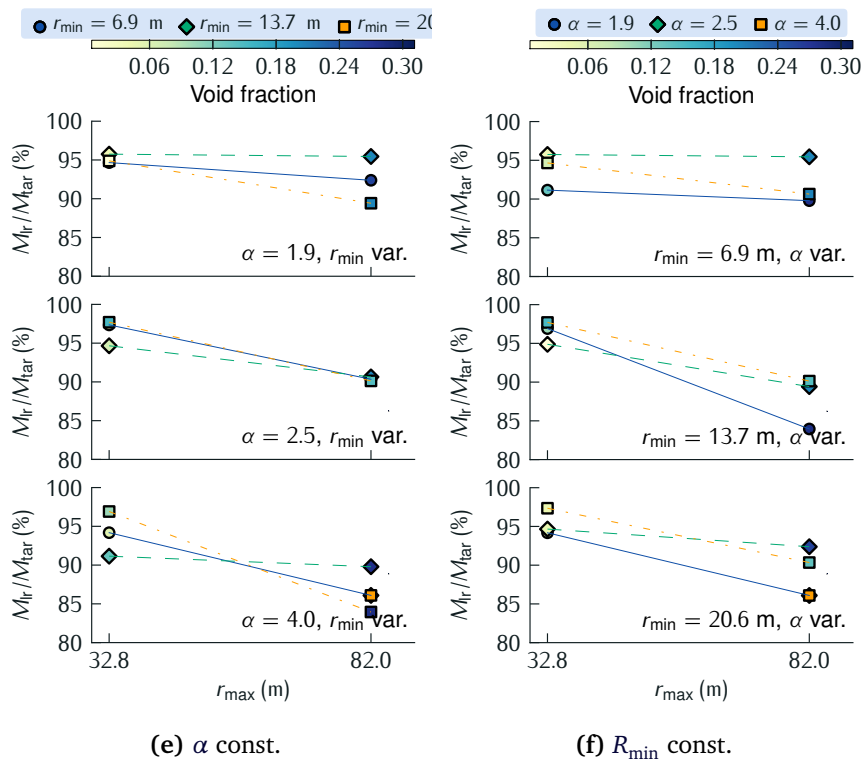
Figure 3.10 (continued): Mass of the largest remnant fraction after an impact of a $R_{imp} = 4\,\mathrm{m}$ asteroid at $v_{imp} = 5.5\,\mathrm{km\,s^{-1}}$ for different internal structures of the target. The targets have been formed as an $R_{tar} = 164\,\mathrm{m}$ asteroid, the internal structure derived from a gravitational aggregate formed using a set of three parameter α, R_{min}, and R_{max} of the value matrix in Table 3.1. The individual error bar in relative mass is $\pm 2\%$ (see Figure 3.7 and Section 3.5.1). Each sub-figure shows the same set of data.

The lower cut-off radius R_{min} seems to have no clear effect on M_{lr} (Figures 3.10b and 3.10d) While for $R_{\mathrm{max}} = 82\,\mathrm{m}$ the strength increases with R_{min}, and for $R_{\mathrm{max}} = 32\,\mathrm{m}$ it decreases, this effect is small and not significant.

A larger upper cut-off radius R_{max} results in less resistance to disruption (Figures 3.10e and 3.10f) This is not an effect of the increasing size of the pebbles, but rather by the correlation of void space and R_{max} (See Figure 3.9).

A lower cut-off radius of $R_{\mathrm{min}} = 6.9\,\mathrm{m}$ results in an insensitivity to the upper cut-off radius R_{max} (Figure 3.10e, up most panel) The unconnected void space with many small pebbles of only $1/24$ of the asteroid's radius behaves like a solid material with random porosity, indicating that a lower cut-off radius of $R_{\mathrm{min}} = 6.9\,\mathrm{m}$ is too small to represent an asteroid model of loosely bound rubble. This is just a factor 2.7 larger than the smoothing length $h = 2.54\,\mathrm{m}$ that limits the resolution of the simulations presented here. A possible solution could be not to assume void space between the pebbles, but to fill it with a highly porous material described using a continuum material model or porous media.

In summary, the only clear correlation is between the resistance against disruption and void fraction. Therefore, the exact choice of the arbitrary parameters α, R_{min}, and R_{max} does not significantly influence the outcomes of impact simulations in a direct way, and no physical explicit derivation of these parameters is needed.

For a lower cut-off pebble radius of $R_{\mathrm{min}} = 6.9\,\mathrm{m}$, the model becomes insensitive to the upper cutoff radius R_{max}. This is most likely an effect of chosen resolution, governed by the smoothing length $h = 2.54\,\mathrm{m}$. In conlusion, for a rubble pile representation R_{min} has to be chosen as $R_{\mathrm{min}} > 3 \times h$.

The main mechanism is the amount of the large-scale bulk porosity given by connected voids between pebbles rather than small scale porosity given by single void cells inside the pebbles. Because the total bulk porosity ϕ_b is kept constant in all simulations, if most of the porosity is given by connected void space, the pebbles themselves are more solid. Like a solid asteroid, in the strength regime the disruption energy threshold Q_D^* for solid pebbles is lower than for a porous one, as studies by Love et al. (1993) and Jutzi et al. (2010b) have

shown (see Section 1.3.6). This leads to easier shattering of the pebbles that form the asteroid and causes a larger fraction of the mass to be excavated, and, consequently, to a lower mass of the largest remnant fragment M_{lr}.

Although there is a clear dependency of the internal structure as represented by the void space and the mass of the largest remnant fragment, the disruption threshold itself seems to be less sensitive to this. The three models with a bulk porosity of 30 % (Sets [a], [b] and [c]) have a very similar disruption threshold of $Q_D^* = (5.1,\ 6.1\ \text{and}\ 5.2)\,\mathrm{erg\,g^{-1}}$, respectively. The void fraction for the models used in Set (a) and Set (b) are 0.055 and 0.045, respectively. Therefore, even as at first sight the disruption threshold Q_D^* seems to decrease with increasing void fraction, the validity of this trend is called into question by the disruption threshold of model Set (c) that contains no large-scale voids at all and therefore a void fraction of 0. It is important to recall that the trend to smaller M_{lr} with increasing void fraction is found in the cratering regime. Even if in Section 3.5.1 it was shown that the exact local configuration at the point of impact changes the mass of the largest remnant fragment by at most 2 %, the excavation efficiency measured by M_{lr} in the cratering regime might be a more local characteristic especially if large pebbles are involved, while the disruption threshold Q_D^* measures a more global quantity.

Another contributing factor is the 'welding' of distinct pebbles at the contact zones into a continuous material resulting from the spatial smoothing of physical parameters in the SPH formalism (see Section 2.1.2). The area affected by this welding can be calculated from the contact area of pebbles inside the asteroid simulant model. In Figure 3.9 it can be seen that the mass of the largest remnant fragment M_{lr} and the pebble contact area are highly correlated. In cases with high void fraction, that correspond to models with $R_{\max} = 82\,\mathrm{m}$, the contact area is small, because the pebble size distribution contains large pebbles and fewer small pebbles. The small contact area leads to a smaller welding area and consequently to a lower bulk shear strength of the model is expected. This is, however, counteracted by the increased strength of the larger boulders as opposed to conglomerates of many small boulders. Therefore, the net effect of the contact surface area on the resistance against disruption of the rubble pile asteroid simulant is not clear, and the observed correlation between this area and the mass of the largest remnant fragment does not support a finding of causality.

3.7   Summary

The explicit modelling of the inner structure in rubble pile asteroids when simulating impact events is not only important to support abstract material models for brittle materials, but might also help to understand the interior of asteroids from observing surface features such as depressions, impact craters or hill-like structures. The exact distribution of the void space that asteroids with high bulk porosities must contain — up to 60 % — is not known. Are there cavities inside rubble pile asteroids, created by interlocking large pebbles constituents, as the series of aligned crater-like pit features on Šteins (Keller et al. 2010) might suggest? This will be discussed in Chapter 4.

This work proposes a new way to create simulants for rubble pile asteroids, starting at the formation phase. In the model, the interior of a rubble pile asteroid is an agglomerate of spherical pebbles following a size distribution governed by a power law. This is only a first approach and an arbitrary choice, but supported by the size distributions observed in collisionally evolved populations (Dohnanyi 1971) and observations of asteroid families (e. g. Gladman et al. 2009). The pebble size distribution used to form the gravitational aggregate includes three free parameters: the power law slope α, and the cut-off radii $R_{\min}$ and $R_{\max}$. All these parameters are hard to constrain by observational evidence. Therefore, in this Chapter the sensitivity of the impact outcomes on the choice of these parameters was determined by running a series of test simulations.

The choice of the parameters used to form the gravitational aggregate does not appear to directly influence the outcome of collisions, but rather the only direct correlation observable is to the void fraction, the void space in between the pebbles. If there is a higher void fraction, and therefore a higher fraction of connected voids inside the asteroid as opposed to unconnected void single cells, the 'strength' of the asteroid decreases as shown by the decreasing mass of the largest remnant fragment in Figure 3.9. The void fraction is only indirectly controlled by the parameters of the model, and entangled in all three of them. For this reason, direct conclusions on the influence of the three model parameters are not straightforward. However, this does mean that a priori knowledge of the size distribution of the component parts of a rubble pile is not necessary to construct rubble pile asteroids simulants for impact experiments. This means a generic rubble pile model can be used to study the outcomes of different collisions, without concern that the experiment is influenced by assumptions

about the precise internal structure.

The lower cut-off limit is seen to be dependent on the chosen simulation resolution, given by the SPH smoothing length h. For values of $R_{\min} < 3 \times h$, the exact distribution of pebbles does not influence the result any more, and is undistinguishable from randomly distributed voids.

The main effect of the model is an overall strengthening of the asteroids' resistance against collisional disruption compared to a non-porous asteroid, as seen in the higher disruption energy threshold Q_D^* for these models (Figure 3.8). This effect is explained by the energy needed to compress the voids and has been observed before (Holsapple 2009).

Chapter 4

Impacts on Rubble Pile Asteroid Šteins

In this chapter, the new approach to modelling rubble pile asteroids during impact events is applied to a real asteroid. The model as described in Chapter 3 is focussed on the large scale rubble pile structure. Asteroid Šteins is a good example of a small asteroid with rather high macroporosity. During the flyby of the Rosetta spacecraft, about 60 % of the surface were imaged by the OSIRIS camera system. This allowed, together with ground based observations, to gain a full, detailed shape model of the asteroid. As Šteins exhibits a large, probably just sub-critical crater and several other features that might be related to the impact event creating this crater, Šteins is the perfect test object for the rubble pile asteroid simulant model presented here. Applying the model and using it in a series of impact simulations, the plausibility of a link between the cratering event and several surface features observed on Šteins is tested and implications for the internal structure of the asteroids are discussed.

4.1 Asteroid Šteins

The MBA Šteins was discovered in 1969 by the Soviet-Ukrainian astronomer Nikolay Stepanovich Chernykh. It was named after Kārlis Šteins, a Soviet-Latvian astronomer working on evolution of comet orbits. The asteroid is part of the inner main belt, with a slightly eccentric orbit ($\epsilon = 0.145$) at a semi-major axis $a = 2.3\,\text{AU}$ (see Figure 1.5 and Table 4.1). Determination of physical parameters only started in 2004, when Šteins was selected as a flyby target when Rosetta
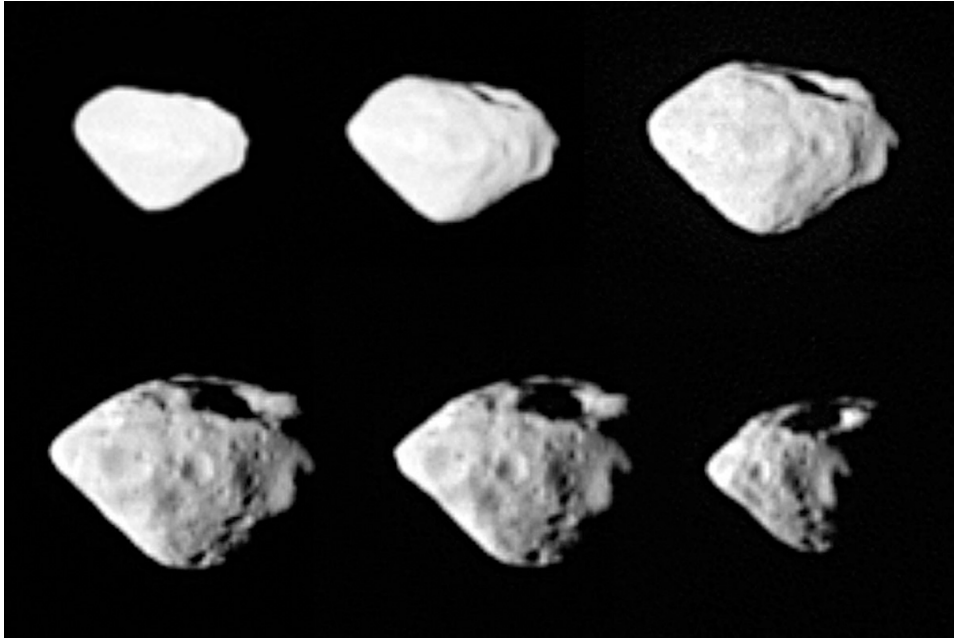
Figure 4.1: Asteroid (2867) Šteins, a *diamond in space,* imaged by the OSIRIS camera system during a flyby in 2008 from a distance of 800 km. In concurrence with IAU rules, for the retrograde rotating asteroid Šteins the southern pole is pointing to the top of the figure. *Source: ESA ©2008 MPS for OSIRIS Team MPS/UPD/LAM/IAA/RSSD/INTA/UPM/DASP/IDA*

		Šteins	Ref.
Period	hours	6.049	*
Dimensions	km	$6.830 \times 5.700 \times 4.42(10)$	*
$R_{\text{equiv.}}$	km	2.63(13)	*
	Orbital parameters		
ϵ	none	0.145 199 06(5)	†
a	AU	2.364 467 23(2)	†
q	AU	2.021 148 8(1)	†
i	°	9.932 86(5)	†
Ω	°	55.392 01(3)	†
ω	°	250.977 19(4)	†
M_a	°	216.859 40(2)	†

* Jorda et al. 2012   † JPL/MPC

Table 4.1: Orbital parameters of Asteroid Šteins.
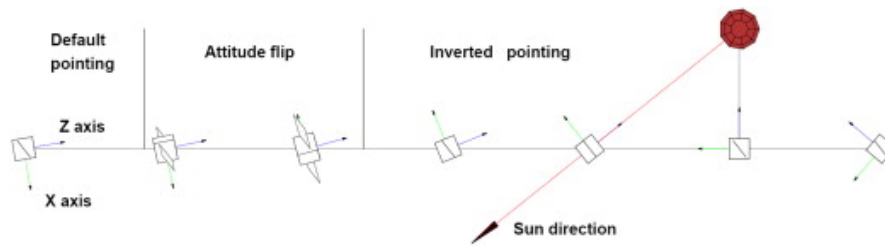
Figure 4.2: The roll maneuver performed by the Rosetta spacecraft during the flyby at asteroid Šteins showing the imaging geometry and the solar position. *Reprinted from Accomazzo et al. 2010*

was on already on route to comet 67P/Churyumov-Gerasimenko (67P/CG). The first determination of the period was done by Hicks et al. (2004), who found a value of $P = (6.06 \pm 0.05)$ hours, and Weissman et al. (2005, 2007, 2008) who determined the period to (6.0490 ± 0.0095) hours. Additionally, assuming colours derived based on a hypothetical phase function slope parameter of $G = 0.15$, a taxonomic class of type S was proposed. First spectroscopic observations where published by Barucci et al. (2005). They revealed similarities to the spectra of the EL Atlanta meteorite, placing Šteins in the class of E-type asteroids.

E-type asteroids exhibit relatively high albedos. Therefore, the albedo found by Fornasier et al. (2006) of 0.45 ± 0.10 was additional confirmation of the taxonomic class. Polarimetric parameters determined by these authors supported this conclusion even more. Using the albedo value, a first guess of the diameter could be calculated as $D = 4.6$ km. The taxonomic class was further confirmed by far-infrared observations using the Infrared Spectrograph (IRS) (Barucci et al. 2008).

Previous to the flyby maneuver of Rosetta, planned for the 5th of September 2008, the on-board camera system OSIRIS was used the Narrow Angle Camera (NAC) to obtain a full lightcurve of Šteins on multiple occasions. A full lightcurve taken on 11th of March 2006 together with ground-based observation have been used to derive a surface shape model (Lamy et al. 2008). Using a lightcurve inversion technique developed by Kaasalainen (2001a,b) revealed a body of almost spherical shape with axial ratios of $a/b = 1.17$ and $a/c = 1.25$.

4.1.1   Rosetta's Flyby at Asteroid Šteins

On the way to its main target, 67P/CG, Rosetta was steered to fly close by two
asteroids: Šteins and Lutetia. The encounter with Šteins happened on the 4th
of September 2008, passing Šteins at a relative velocity of $8.6\,\mathrm{km\,s^{-1}}$, and at
a distance of just 800 km at closest approach. To maintain constant pointing
on the object, during the flyby a roll maneuver by almost 180° was performed.
The maneuver is described in detail in a paper by Accomazzo et al. (2010), and
displayed in Figure 4.2.

During the flyby, the OSIRIS camera system (Keller et al. 2007) was scheduled
to take images using both the NAC as well as the Wide Angle Camera (WAC).
10 min before closest approach, the NAC camera encountered an internal error
and went into safe mode. Therefore, images with the highest resolution of
80 m/pixel were taken by the WAC (Keller et al. 2010). Approximately 60 % of
the surface was imaged during the flyby. Both cameras took around 840 images
during approach and flyby, around 253 in which the asteroid is spatially resolved,
although due to the rapidly changing geometry only a small part of the surface
is visible in multiple images: Besse et al. (2012) found only four images usable
for crater detection, covering 44 % of the surface in total with an overlap of only
14 %. A series of images with the highest resolution is shown in Figure 4.1. It
already shows many striking features:

- The large crater close to the southern pole, later named Diamond, at
  latitude 50°

- The brilliant-cut diamond like shape with a pronounced bulge on the
  equator resembling a YORPoid shape with a deformation due to the large
  crater

- A series of crater like pits spanning from north to south at longitudes of
  $-20°$ to $-25°$

- A variety of crater structures ranging over a wide size range and some
  deep and some shallow

- A depression bounded by a hill like feature spanning from the northern
  pole to the equatorial ridge at a longitude of $\sim 100°$.

Analysing the data collected by the flyby maneuver, a series of studies have
been published, as summarised in the following and discussed in more detail

below: Keller et al. (2010) released a first series of images as well as preliminary estimates for age and shape and surface spectral properties. Leyrat et al. (2010) concluded that the imaged surface does not exhibit surface inhomogeneities larger than 4 %, while Schröder et al. (2010) found that the interior of crater Diamond at the southern pole is bluer than the rest of the body. Marchi et al. (2010) derived by determining the cratering statistics the age of Šteins surface to be in the range of 154 Ma to 1.6 Ga, and a collisional lifetime of 2.2 Ga.

Jutzi et al. (2010a) simulated the impact that might have formed the crater Diamond, and conclude that the asteroid might have been a monolithic body, but surely was fractured into a rubble during the impact. The size of the crater raised some questions because at first it seemed large compared to the diameter of Šteins. Burchell and Leliwa-Kopystynski (2010) deduced that the ratio of crater to asteroid size is not larger than found on other bodies suspected to be fractured or loosely bound rubble piles.

Later, Jorda et al. (2012) published a detailed shape model of Šteins together with a thorough analysis of the asteroid's physical properties and defined the local coordinate system using the centre of crater Spinel as the origin at lon/lat 0°/0°. Besse et al. (2012) determined crater sizes and ellipticities by detailed modelling to identify and study all craters imaged on the surface. In this paper, the official list of named surface features as accepted by the International Astronomical Union (IAU) was included. Notably, the largest crater Diamond, that has been named crater Ruby in some publications, was now uniquely identified.

4.2   Šteins as a Rubble Pile Asteroid

As there is no direct measurement of the internal structure of Šteins, and neither the mass nor the macroporosity can be directly determined, the fact that Šteins is a rubble pile asteroid cannot be directly verified. Nevertheless, there is a lot of evidence supporting this hypothesis:

- Šteins is classified as an E-type asteroid. These are related to enstatite achondrite meteorites (Gaffey et al. 1989) (Aubrites). Aubrites are meteorites that have been exposed to high temperatures above 1000 K, and can therefore not be primordial (McCoy et al. 1999). Such high temperatures cannot be explained in formation theories for such a small body. This means that Šteins is an agglomerate of fragments originating from a much larger, differentiated body that has been catastrophically disrupted.

- As Burchell and Leliwa-Kopystynski ([2010]) point out, only a moderate level of porosity is needed to explain Šteins survival of the impact that formed crater Diamond. The observed crater diameter to asteroid size ratio, $D/R_{\text{equiv.}} = 0.79$ is in the same range as the Martian moon Phobos and the asteroids (243) Ida and (433) Eros, which have a macroporosity of about 20 % to 35 %, and are fractured. (253) Mathilde or Deimos have a higher $D/R_{\text{equiv.}}$ ratio of 1.2 to 1.6 and seem to be indeed loosely consolidated rubble piles (Burchell and Leliwa-Kopystynski [2010], see Figure 3). Therefore, it seems reasonable to assume that Šteins has at least a macroporosity of about 20 %, but a larger value is still in agreement with observations if Diamond is not a critical size crater.

- The overall shape does look very similar to other bodies that have undergone reshaping due to rotational spin-up caused by the YORP effect. Most effective for small to intermediate-sized asteroids, the YORP effect as described in Section 1.1.9 causes changes in obliquity and spin based on asymmetric shape features (Rubincam [2000]). If the spin of an asteroid increases, the local gravitational slope changes and leads — in the case of loosely bound rubble pile asteroids — to the transport of material from the poles to the equator of the body, depending on the critical angle of repose of the surface material. This process has been modelled using N-body codes by Walsh et al. ([2008]). Harris et al. ([2009]) simulated shapes assuming a constant critical angle of repose of surface material as seen in Figure 4.3a.

  These constant-slope figures (see Figure 4.3a) show the pronounced equatorial ridge, that has been found in the shapes of many small asteroids denoted as YORPoids. A famous example is asteroid 1999 KW4, where Ostro et al. ([2006]) and Scheeres et al. ([2006]) first suggested a rubble pile interior based on mass and bulk density as well as a radio-echo based shape model. Many small asteroids seem to have shapes with a pronounced equatorial ridge. While 1999 KW4 is the primary body of a binary asteroid system, the reshaping process by YORP might be influenced by the presence of a close satellite. Still, as seen in Figure 4.3 Šteins looks remarkably similar to this body that is only slightly smaller $(R_{\text{equiv.}} = [1.32 \pm 0.04]\,\text{km})$, providing further evidence of a rubble pile structure.

- The impact that formed the crater Diamond at the southern pole will have
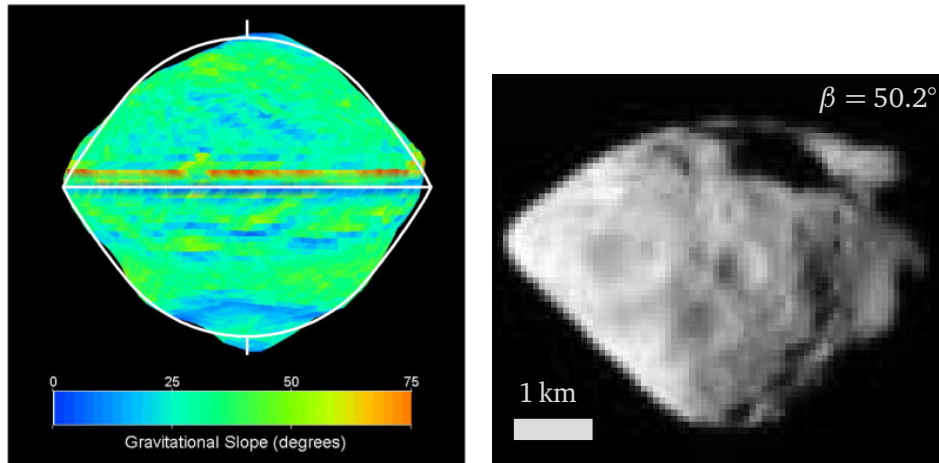
(a) Constant-slope figure (white line) compared to the shape and gravitational slope of 1999 KW4 (Ostro et al. 2006; Scheeres et al. 2006). Critical slope angle was 37°. *Reprinted from Harris et al. 2009*

(b) WAC image taken at closest approach with a resolution of $\sim 80\,\mathrm{m\,pixel^{-1}}$.

Figure 4.3: Comparison of the apparent shape of Šteins and 1999 KW4, both examples of the typical top-like YORPoid asteroid shaped by spin-up due to the YORP effect.

shattered the body even if it was monolithic before (Jutzi et al. 2010a). The authors aimed to recreated the shape of Diamond using a either monolithic, non-porous, a monolithic, porous, or a rubble pile structure formed as a 'fractured body' (Michel et al. 2004b). They found a preference for the formation of the expected shape for monolithic, non-rubble pile models. However, the shape of Šteins strongly suggest shaping due to YORP spin-up, which requires a only weakly cohesively bound rubble pile interior to work. Furthermore, Marchi et al. (2010) find a dichotomy in cratering age, that lead to the conclusion that some event erased all craters below a certain size limit. These two distinguishable ages of small and large surface craters can best be explained if the cratering event that formed Diamond was not as destructive to Šteins as the simulations by Jutzi et al. (2010a) suggest.

4.2.1 Mass Estimates

Because of the small size of (2867) Šteins, and the flyby geometry, a direct measurement of the asteroid's mass by the Radio Science Investigation (RSI),

using Doppler shift of Rosetta's radio link signal, was not possible (Schulz et al. 2009; Accomazzo et al. 2010). Instead, indirect methods have to be used to estimate the bulk density and derive the mass using the defined shape.

The volume of Šteins is relatively well constrained by the shape model derived from OSIRIS images combined with ground-based observations: $V = (76 \pm 11) \, \text{km}^3$ (Jorda et al. 2012). The large error bar is caused by the relatively low number of images, the rather coarse image resolution and the fact that only 60 % of the surface have been imaged. The other hemisphere was reconstructed using the inversion of ground based lightcurve data under multiple observing geometries (Kaasalainen 2001b, 2011). This technique is not able to reproduce the convex hull of the asteroids shape (Kaasalainen 2001b), and cannot compete to the resolution of the spacecraft images. The spatial resolution on this hemisphere is about 200 m, whereas in the area imaged by OSIRIS the resolution is approximately 20 m (Jorda et al. 2012).

The *E*-type asteroids like Šteins are linked by asteroid (1862) Apollo to enstatite achondrite meteorites or aubrite (Gaffey et al. 1992). Macke et al. (2011) determined properties of 9 out of 22 known non-Antarctic aubrite meteorites. Mean value for the grain density is $\rho_{\text{grain}} = 3200 \, \text{kg m}^{-3}$, with porosity ranging from $\phi_{\text{micro}} = 2 \, \%$ to 21.5 % (average 9 %). The grain density is very close to that of pure enstatite which has $3100 \, \text{kg m}^{-3}$.

Burchell and Leliwa-Kopystynski (2010) conclude by the ratio of the largest crater radius to the diameter of Šteins, that a macroporosity of at least $\phi_{\text{macro}} = 20 \, \%$ can be assumed. Generally, rubble pile asteroids can have macroporosities of up to 60 % (Britt et al. 2002). The total bulk porosity is then given by the sum of macro- and microporosity: $\phi_b = \phi_{\text{macro}} + \phi_{\text{micro}}$

Finally, the mass can be estimated by

$$M_{\text{ast}} = V \times \rho_{\text{grain}}(1 - \phi_b). \tag{4.1}$$

Using this, Šteins mass is estimated as $M_{\text{Šteins}} = 1.45 \times 10^{14} \, \text{kg}$ assuming a total porosity of 40 %, and $M_{\text{Šteins}} = 1.95 \times 10^{14} \, \text{kg}$ assuming a total porosity of 20 %. In the following, if not noted otherwise, a total porosity of $\phi_b = 40 \, \%$ will be used to investigate the upper range of possible values.

4.2.2   Characterization of Šteins

Cratering

Šteins' surface exhibits many crater-like structures. After Rosetta's flyby at Šteins, Besse et al. (2012) used images in four different geometries, one of them a NAC image and three of them WAC images near closest approach, to determine the crater statistics on Šteins. With a spatial resolution between $81\,\mathrm{m\,pixel^{-1}}$ and $106\,\mathrm{m\,pixel^{-1}}$, completeness could only be achieved for larger craters. Also, limited phase angle coverage made it hard to detect shallow craters. In total, 44 % of the surface was analysed, and 42 crater-like features have been detected (see Figure 4.4).

Detected crater diameters range from 150 m to 2100 m for crater Diamond. Only 4 craters are larger than 1000 m. Both Marchi et al. (2010) and Besse et al. (2012) find, using the standardized R-Plot approach (Crater Analysis Techniques Working Group et al. 1979) where the crater diameter is plotted relative to the total number of craters, the surface accounted for, and the limiting sizes, that the crater count for radii of less than 1000 m is not saturated.

Interestingly, a strong dichotomy on Šteins surface has been found. Besse et al. (2012) report a crater density that is a factor of 3.6 higher for latitudes of $-40°$ to $40°$ as for longitudes of $40°$ to $150°$. In the following, the first region will be referred to as *densely cratered*, while the latter one will be called *sparsely cratered*. The authors argue that the difference is too large to be explained by observational bias only, although the illumination conditions are different for each region. Both regions exhibit a very different crater size distribution: while the densely cratered region has a power law exponent of -1.5 ± 0.2, the exponent in the sparsely cratered region is -3.3 ± 0.2. This might be related to the cratering event that formed crater Diamond, which is placed almost at the opposite side of Šteins, at a latitude of $-51.6°$, although the mechanism leading to the observed dichotomy is not clear. Another possibility is the existence of a second large crater in the unimaged part of Šteins: the ejecta blanked created by the fall-back of material ejected in such an event could have covered small craters in the sparsely cratered region.

In the depth-to-diameter ratio, no significant differences between the two regions are found except for a surplus of deep craters $d/D > 0.15$ in the densely populated area. The distribution is quite broad, ranging — excluding some outliers — from 0.055 to 0.2.

The catena of crater extending from the rim of crater Diamond to the north is discarded as impact structures, mainly because the chances to find such an alignment are slim.

Age of Šteins by Crater Statistics

If the orbit of an object and the flux of possible impactors for this orbit is known, the observed crater density can be used to determine the age since the last surface-erasing event. Marchi et al. (2010) have combined the crater statistics on Šteins with the impactor flux size distribution by dynamical models (Bottke et al. 2005a), to estimate the age of Šteins surface after the last resurfacing event. Applying two different crater scaling functions, the authors propose an age of Šteins surface as (154 ± 35) Ma (model by Nolan et al. [1996], NSL) or 0.49 Ga to 1.6 Ga (model by Holsapple and Housen [2007], HSL).

Interestingly, Marchi et al. (2010) also found a dichotomy in the crater scaling, notably for crater diameters smaller than $D < 0.5$ km to 0.6 km. Fitting only craters with diameters $D < 350$ m, ages of (32 ± 4) Ma (NSL) and 72 Ma to 237 Ma (HSL) were derived. The authors suggests, that craters smaller than 500 m have been erased in the event creating crater Diamond, which would then be dated by the latter fit. As a lower limit to the crater forming event, the time required to accumulate the observed small crater numbers is given by only 2 Ma to 10 Ma.

The main process erasing craters is *seismic shaking*, that is induced by either both large and small scale impacts, as well as secondary low-speed impacts of ejecta falling back to the surface (Hofmann 2014). Also, during the internal reconfiguration leading to the YORPoid shape by spin-up, seismic shaking causes the erosion of craters and is more efficient at eroding small craters. This effect has been observed on asteroid Itokawa by Miyamoto et al. (2007).

As a mean collisional time for asteroid Šteins, Marchi et al. (2010) applied the collision rates of the best-fitting model in Bottke et al. (2005b) to derive an mean collisional age of ~ 2.2 Ga. This is longer than the age of the surface, implying that the surface of Šteins has been altered after the formation of the asteroid.
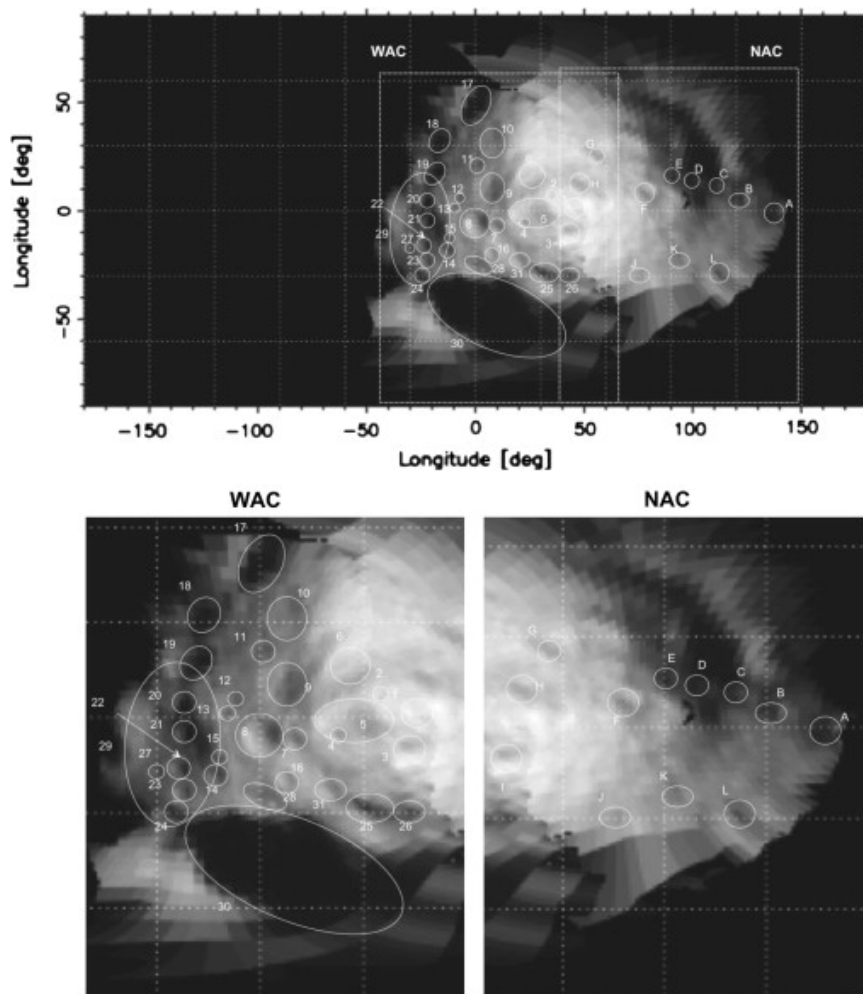
Figure 4.4: Craters on asteroid Šteins. Numbers refer to craters determined using WAC images, letters to those found using NAC images. *Reprinted from Besse et al. 2012*
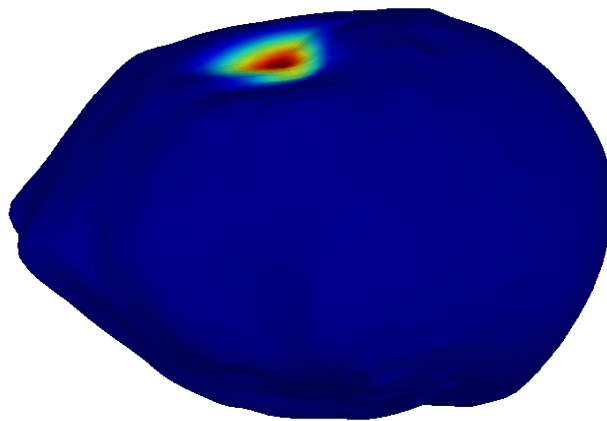
Figure 4.5: Crater Diamond identified on the shape model of Šteins (Jorda et al. 2012). Colour refers to radial distance to the original shape model. In compatible viewers, an interactive 3-D model is displayed.

4.2.3   The Crater Diamond on Šteins

Close to the southern pole, at 13.4°,−54.6° lon/lat, Šteins exhibits a very large, circular crater with a diameter of $D = 2100\,\text{m}$ (Besse et al. 2012), estimating the achieved precision to about 140 m.

As the crater is at the southern pole, and the obliquity of Šteins is approximately $\Theta = 172°$ (Jorda et al. 2012), the floor of the crater is not visible in the images (see Figure 4.6), and therefore the depth is only poorly constrained. Besse et al. (2012) determined a best fit value of $d = 294\,\text{m}$, but estimating the accuracy to only about 50 %. This results in a ratio of $d/D = 0.14 \pm 0.07$.

The ratio between the crater diameter and the asteroid's equivalent radius is $D/R_{\text{equiv.}} = 0.79 \pm 0.05$. This value is comparable to the largest craters found on asteroids Ida, Phobos and Eros, while other asteroids like Deimos have values between 1.2 to 1.6 (Burchell and Leliwa-Kopystynski 2010) for the largest crater. Burchell and Leliwa-Kopystynski (2010) therefore conclude that the crater size is not abnormally large on a small body like Šteins.

Morris et al. (2013a) proposed the hypothesis that Diamond is not an classical impact crater created by an non-dispersive late-stage impact at all. They conducted a small-scale impact experiment of an $R_{\text{imp}} = 2.5\,\text{mm}$ steel sphere onto a $R_{\text{tar}} = (37.5 \pm 0.5)\,\text{mm}$ cement sphere, rotating at an angular speed of $\omega = 21.6\,\text{rad}\,\text{s}^{-1}$, corresponding to an asteroid of Šteins' size with an period of $P = 5.66\,\text{hours}$, similar to the period of Šteins. The impact velocity was $v_{\text{imp}} = 4.54\,\text{km}\,\text{s}^{-1}$, corresponding to a specific energy of $Q = 1066\,\text{J}\,\text{kg}^{-1}$ In the fragments resulting from this impact, Morris et al. (2013a) found one particular fragment that in overall shape closely resembled the shape of Šteins, including the crater features corresponding to Diamond. This provides an additional explanation of the features seen on Šteins as the direct outcome of an disruption event of a larger parent body, but the apparent erasing of smaller craters only as seen by Marchi et al. (2010) cannot be explained if not by a major impact event.

4.2.4   The Hill Feature on Šteins

In the NAC images, prior to closest approach (see Figures 4.6a and 4.7a), there is a bright, elongated feature visible near the rim of Šteins. It is described as the *northern hill* in Jorda et al. (2012), extending over $\sim 2\,\text{km}$ with an elevation of 120 m to 15 m. Although only observed in a single geometry, and therefore constrained only by photoclinometry rather than stereographic shape
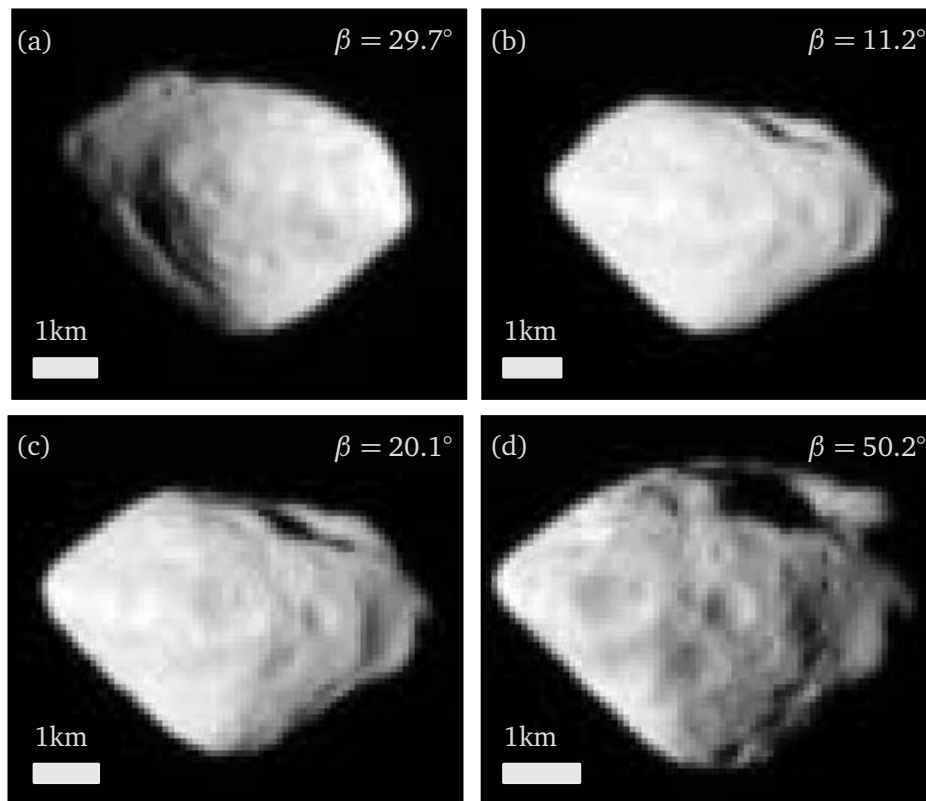
Figure 4.6: Šteins at different phase angles β from the OSIRIS flyby. Panel 4.6a was taken by the NAC camera, while the others are taken by WAC. By convention, as Šteins rotation is retrograde, the south pole points up. The images have been scaled by a factor of three using nearest neighbour interpolation. Note the changing illumination conditions on crater Diamond near the southern pole.
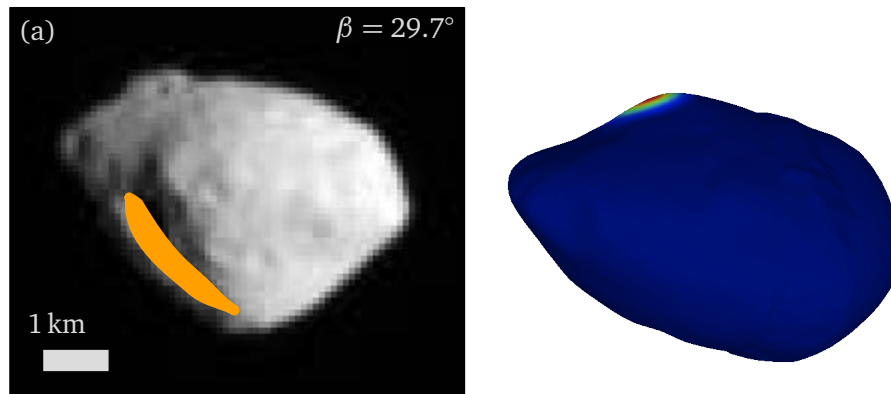
(a) Highlighting the hill-like structure 125° away of crater Diamond. The feature is seen mainly as a bright, elongated structure, but only constrained in NAC images under very similar observing geometries.

(b) A circular, hill like feature at a similar angular distance to crater Diamond as a model for the hill feature.

Figure 4.7: A hill like feature on Šteins at approximately 125° angular distance to crater Diamond.

reconstruction, an interpretation as a crater rim is discarded for the lack of an apparent crater and the linear slope of the feature. The authors write:

> It is therefore conceivable that the above feature corresponds to a very large monolithic fragment that emerged from the surrounding pile of smaller pieces either by direct pressure exerted by the impactor of the crater Ruby [Note: in the paper, crater Diamond is referred to as Ruby] (the hill is approximately diametrically opposite to that crater) or the spreading of the surrounding smaller fragments as the reshaping proceeded (Jorda et al. 2012).

In the following, the general idea of a hill forming during an impact event on the opposite side of the asteroid is discussed. Due to the current assumption on spherical pebbles in the model for the interior of Šteins applied here, the possibility of a hill forming by the rise of a spherical, coherent fragment initially just below the surface is discussed. This is used as an initial test case for the formation of structures as the feature observed by Jorda et al. (2012).

Therefore an elevated, but more circular feature at a similar angular distance to Diamond was chosen. In reproducing this feature (see Figure 4.7b) the general feasibility of such an assumption is tested.

Designation	Diameter m	Depth m	Ratio	Description
17 Agatea	500	125	0.25	Elongated
18 Amethysta	450	81	0.18	Elongated, possible dual crater
19 Citrinea	610	79	0.13	Circular
20 Opala	400	50	0.125	Circular, marginally elongated
21 Garneta	390	51	0.13	Circular, marginally elongated
22 Jadea	260	62	0.24	Circular, disturb the rim of 30
23 Peridota	270	24	0.09	Uncertain, depression?
24 Lapis	440	44	0.1	Very uncertain

Table 4.2: Dimensions of the depression pits in the catena as measured by Besse et al. (2012). Designations can be found in Figure 4.4. *Reprinted from Besse et al. 2012*

4.2.5   The Catena of Aligned Pits on Šteins

Extending from the northern pole to almost the rim of crater Diamond, a series of pits is seen on the surface of Šteins. These correspond to the 'crater-like features' measured in Besse et al. (2012). While the alignment of the pits clearly indicates a common origin, the very similar size seems to contradict an impact origin. Keller et al. (2010) and Marchi et al. (2010) argue that a partial drainage of regolith into an underlying fracture formed by the impact event that created Diamond, or even pre-existing internal inhomogeneities, are a more likely explanation of this feature.

Chains of craters are observed on other bodies too. Schenk et al. (1996) studied crater chains on Callisto and Ganymede, as well as the Earth's Moon and Mercury, and found several chains of typically 6 to 20 craters. Some of these extend radially from large impact crater basins, and are therefore classified as secondary impact events. These are particularly frequent on larger bodies like the Moon and Mercury, but less frequent on smaller bodies. The observed ratio of the diameter of the primary crater basin to secondary crater diameters is ~ 25, far larger than the ratio observed on Šteins with craters around $D = 400\,\text{m}$, approximately 1/5 of the diameter of Diamond.

Other crater chains are linked to impacts of objects that have been dispersed
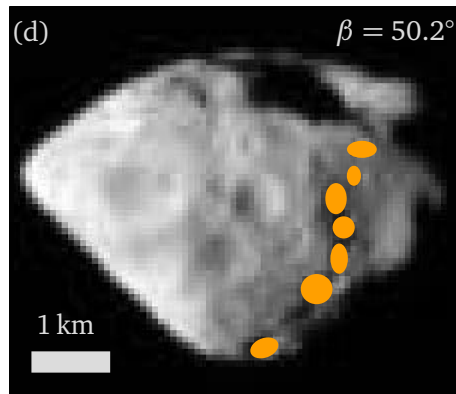
Figure 4.8: Highlighting the catena of pit-like features on Šteins. WAC image taken at closest approach, resolution $\sim 80.8\,\mathrm{m\,pixel^{-1}}$.

by gravitational tidal forces like SL9 when passing Jupiter. While this in principle is a viable explanation for crater chains on larger bodies (Schenk et al. 1996), in the case of Šteins it is regarded as very unlikely. The small orbital separation reflected in the short distances of the craters would only be realistic very shortly after the tidal disruption event, and therefore only in a moment of the orbital evolution where both bodies quasi simultaneously undergo a close encounter with a large body.

4.3 Simulating Crater-Forming Impacts on Asteroid Šteins

Asteroid Šteins as a rubble pile asteroid with a spacecraft-data derived shape model is a test-case for the model presented in Chapter 3. The model focusses on the large-scale structure of the interior of rubble pile asteroids, and possibly provides a tool to determine a link between surface features and the configuration of constituent fragments in the interior.

In a series of impact experiments recreating the crater Diamond near the southern pole of Šteins, a possible link between the internal configuration and two specific surface features is investigated: the hill-like structure at a longitude of $\sim 100°$ and the aligned pit chain at longitudes of $\sim-20°$ to $-25°$.

In the following the parameters for the SPH shock physics code are discussed. As Šteins is at the transition size of the strength- to the gravity regime, gravitational forces had to be included into the numerical treatment. For this reason, a different shock physics code was used than in the simulations presented in Chapter 3. The influence of the gravitational forces on the outcome of impact

113

simulations is estimated. Then, the surface features to be reproduced are discussed, and a plausible pre-impact shape for asteroid Šteins is derived. Finally, a series of impact simulations to recreate crater Diamond is presented and links to the surface features are investigated.

4.3.1 Model Parameters

On the resolution provided by OSIRIS images, the surface of Šteins looks smooth, showing no boulder like features at a size of $\sim$ 80 m to 200 m. Instead, the whole surface is covered in a thick regolith layer. Therefore, the size of pebbles in the inside of the asteroid cannot be inferred by the images, as it was at least partly possible on Itokawa (Michikami et al. 2010). For asteroid Lutetia OSIRIS images showed a number of boulders on the surface in the range of approximately 60 m to 300 m (Küppers et al. 2012). By their spatial distribution, most of Lutetia's boulders can be attributed to cratering events, therefore most likely not being representative of the constituent fragments in the interior of the asteroid. The thick regolith layer covering the surface of Lutetia prohibits a direct measurement of any constituent fragments, and most likely the same holds true for asteroid Šteins.

Instead, for the following simulations a size distribution following the power law in Equation (3.1) with a slope $\alpha = 1.95$ was chosen. Limiting the number of particles at approximately 800 000, the corresponding smoothing length h is 34.2 m. The minimum cut-off radius is $R_{min} = 65$ m. The maximum radius is chosen between $R_{max} = 300$ m and $R_{max} = 500$ m. As shown in Chapter 3, the sensitivity of the impact outcome to the exact choice of this parameters is small. Although Šteins material has been characterised as enstatite, material parameters for enstatite are hard to find, and therefore olivine was chosen with the same parameters as used in Chapter 3 as a material proxy (see Table 2.2).

For the following simulations, the SPH solver in LS-DYNA was used, because it was not possible to implement self-gravitational forces into the Autodyn solver used for the simulations in Chapter 3.

4.4 The Influence of Gravitational Forces on Simulated Impacts on Šteins

4.4.1 Šteins as Asteroid in the Gravitational Strength Regime

Šteins, with an volume-equivalent radius of $R_{\text{equiv.}} = 2.63\,\text{km}$ (Jorda et al. 2012), is just at the beginning of the so-called *gravitational regime*, described in Section 1.3.6 and Figure 1.17. The final stage of an impact event is governed by gravitational re-aggregation of fragments, but the material strength cannot be neglected.

4.4.2 Šteins's Gravitational Binding Energy

To estimate the role of gravitation on the material strength, the gravitational binding energy is a first reference point. The gravitational binding energy or total gravitational potential energy for a spherical body of constant density is given by (e.g. Carroll and Ostlie 2007, p. 297)

$$E_{\text{bd}} = \frac{3}{5} G \frac{M^2}{R}. \tag{4.2}$$

Using the parameters of Šteins as discussed above, a binding energy of Šteins of $3.24 \times 10^{21}\,\text{erg}$ is derived. This means that the specific binding energy of Šteins, $E_{\text{bd}}/M_{\text{Šteins}} = 2.2 \times 10^4\,\text{erg}\,\text{g}^{-1}$ is considerably lower than the expected disruption threshold Q_D^*. This threshold denotes the energy at which impacts transition from cratering to disruption and is discussed in Section 1.3.6. As evident in Figure 1.17 (found on Page 40) different models differ widely. Using the rock-like parameters from Benz and Asphaug (1999) gives a value for Šteins of $Q_D^* = 1.38 \times 10^7\,\text{erg}\,\text{g}^{-1}$. While this is still several magnitudes larger than the gravitational binding energy, a clear transition at the size of Šteins can be seen in the size dependency of Q_D^*. Therefore, full and explicit treatment of gravitational forces was included a into the SPH code LS-DYNA. For a description of the method see Section 2.2.

While for the first stage of crater formation, during contact and compression, gravity mainly acts as an overburden pressure decreasing material strength, the later stages that act on longer timescales are affected more.

4.4.3 Following the Ejecta

After shock relaxation, which acts on a very short timescale τ_{cc} as described in Section 1.3.2, the last stage of crater formation is dominated by gravitational interaction and acts on a timescale several magnitudes longer. As the timestep of the shock code used cannot be increased without losing physical meaning beyond the signal travel time on the resolution length scale, several million time steps have to be calculated to model such relatively slow events. Therefore, different strategies have to be employed to infer the end stage of an impact event in the gravitational regime.

A common approach is to split the simulation into two regimes, and use dedicated codes for each. Michel et al. (2001) used first SPH to calculate the disruption of a large asteroid, and stopped the simulation when fractures ceased to propagate. The considered impact conditions led to full disruption of the parent body. Therefore, each SPH pseudo particle could easily be mapped onto a single hard-sphere particle, and the re-aggregation could be calculated using a purely gravitational N-body code.

While using this approach efficient calculation of the gravitational stage is possible, care has to be taken during the hand-over from the impact to the gravitational code if fragments consist of more than one SPH pseudo particle. Benavidez et al. (2012) described the problems in a similar hand-over attempt in only partially disruptive impact events. Because the hard-sphere particles used in the gravitational code cannot be overlapping, the radius-equivalent smoothing length, h, of the SPH code is not transferable to the gravitational part. Thus, the radius and density of the particles has to be adapted, conserving the mass.

In a simplified approach to estimate the ejecta eventually lost to the body, the escape velocity can be taken into consideration. The concept is to compare the kinetic energy of the fragment to the gravitational potential at the point of the particle. If the first exceeds the latter, the particle is considered lost to the final remaining body. The speed at which both are equal is called the escape velocity v_{esc}, and for a single particle in the gravitational potential of a point symmetric mass M at distance R given by

$$v_{esc} = \sqrt{2\frac{GM}{R}}. \tag{4.3}$$

Because the end-stage of impact simulations differs considerably from the as-

sumption of point symmetry, the local escape velocity for each particle has to be evaluated by summation of the gravitational potential distribution of all other particles. For this purpose, the same gravitational k-D tree code as described in Section 2.2 was used. The main shortcoming of this estimation is the assumption of a static gravitational field, but the only solution avoiding this assumption would be a full integration of the motion of all particles by an N-body simulation until all ejecta either settled or escaped.

The velocity of the ejected material as a function of mass is sometimes approximated by a power law (e. g. Davis et al. [2002]), but Jutzi et al. (2010b) found that the wide spread of velocity values for a given mass prevent the description as a simple power law. Here, the ejection probability of not fragments, but single SPH pseudo particles is discussed to give a first approximation of the mass lost during the impact event. In Figure 4.9 and Figure 4.10, a non-disruptive impact simulation on a low resolution Šteins simulant is compared including (Figure 4.9) and excluding (Figure 4.10) gravitational forces. While visually the outcome of both simulations look very similar (Figures 4.9a and 4.10a), the ejecta velocity distribution is slightly different. Figures 4.9b and 4.10b show the velocity distribution for both simulations, separated in particles gravitationally bound ($|v| < v_{esc}$, right panel) and gravitationally lost ($|v| \geq v_{esc}$). For this comparison, the ejection speed is compared to the local escape velocity, not taking into account the direction of the velocity vector and therefore ignoring subsequent particle collision that would eventually lead to a further loss in momentum, so the mass of ejected material is likely to be overestimated.

It can be observed that the ejecta velocities are slightly higher in the case where gravitational forces are included. In the case including gravitational forces, a total of 8.1 % of the mass are eventually lost, compared to a total of 7.8 % without gravitational forces. While this is below the error margin that was associated to the uncertainty of the mass of the largest remnant fragment of about ± 2 % discussed in Section 3.5.1, in this case of identical impact configurations this effect is only attributed to the gravitational forces. This is not the expected result: Indeed, the gravitational forces should increase the lithospheric pressure, preventing fractures to form, as they have to overcome this additional pressure.

To interpret this surprising result, several possible causes are discussed. The additional lithospheric pressure might lead to damage in the material in the material model implemented, the additional kinetic energy might increase the kinetic energy deposited into the ejecta, or the numerical treatment of the

gravitational forces in the SPH solver of LS-DYNA used in the set of simulations presented here is leading to spurious results.

The additional lithospheric pressure applied as an isotropic lithostatically equilibrated stress given by Equation (1.21) at the centre of asteroid Šteins is about 5.1 kPa, several magnitudes below the yield strength of the material. Lithospheric pressure should prevent fractures to form, and therefore strengthen the material. In the simplified material model here, where no sub-resolution fracturing is implemented (see Section 2.1.5), this effect is neglected because only sub-resolution fractures would form at these small pressures and therefore the expected increase in bulk strength is lost, but no explanation for the observed decrease in strength is provided by this mechanism either.

The potential energy converted into kinetic energy of the impactor is rather small. The distance of the impactor centre to the target surface for the largest projectile with $R_{\mathrm{imp}} = 80\,\mathrm{m}$ is 130 m, as the projectile was started at a height of 50 m. The converted potential energy is given by

$$\Delta E_{\mathrm{pot}} = E_{\mathrm{pot}}(R_{\mathrm{tar}} + 130\,\mathrm{m}) - E_{\mathrm{pot}}(R_{\mathrm{tar}}) \tag{4.4}$$

$$= GM_{\mathrm{tar}}M_{\mathrm{imp}} \int\limits_{\infty}^{R_{\mathrm{tar}}+130\,\mathrm{m}} \frac{1}{R^2}\mathrm{d}R - \int\limits_{\infty}^{R_{\mathrm{tar}}} \frac{1}{R^2}\mathrm{d}R$$

$$\approx 6.1 \times 10^8\,\mathrm{J},$$

which is negligible when compared to the kinetic energy of the impactor of $E_{\mathrm{kin}} = \frac{1}{2}M_{\mathrm{imp}}v_{\mathrm{imp}}^2 = 4.1 \times 10^{16}\,\mathrm{J}$. This can therefore be ruled out as the cause of a weakening.

To ensure that the higher impact velocities when gravitational forces are included is not a numerical artefact by the implementation of the gravity solver and its integration into the impact code LS-DYNA, the dynamic relaxation of a low resolution Šteins simulant was analysed (see Figure 4.11). Dynamic relaxation time is given by the ramp-up time during which the forces due to gravity are linearly increased from zero to their respective value (see Section 2.2.1) and an additional time until the movement of particles due to the increase of stresses has ceased. Whenever the ramp-up time was choosen to be long enough to include at least a hundred time steps, the hydrostatic pressure profile shown in Figure 4.11 developed and dynamic relaxation was found after a few additional

timesteps. In particular, no damaged material was found. Therefore, the source of the unexpected high ejecta velocities could not be found. This might indicate that the strength model used is not ideally suited for the gravitational regime. For further studies, a more advanced material model including rate effectes and sub-resolution fractures should be used.

The overall outcome might not be affected, though, as Benz and Asphaug (1999) point out, the enhanced role of gravity is dominated by the difficulty of fragments escaping the gravity well. Because the re-aggregation has not yet taken place, the mass of the largest remnant fragment in the gravity-included case will increase with time, therefore the final largest remnant may well be larger in the gravitational case than in the one excluding gravity.

4.5 Reproducing Surface Features Observed on Šteins

The rubble pile asteroid Šteins shows several surface features that can possibly be linked to restructuring processes of the internal structure during impact events. When the impact that created crater Diamond erased craters smaller then $D = 500\,\text{m}$ (Marchi et al. 2010), the internal structure of Šteins was rearranged too.

The question to be addressed using the rubble pile simulant representation described in Chapter 3 is: *Are there surface features on Šteins that are caused by the reconfiguration of the internal structure during the impact event that created crater Diamond?* Such a feature would help to understand the large-scale pebble structure of Šteins, and might be used to constrain formation scenarios and the past evolution of this YORPoid shaped rubble pile asteroid.

4.5.1 Possible Pre-Impact Shape of Šteins

To test the feasibility of a hill-forming event during the impact that created crater Diamond, first a possible pre-impact shape of Šteins has to be constrained.

Two processes are applied — filling the crater Diamond, and levelling the region where the hill feature is expected to form.

The crater is identified by visual determination of the crater centre, and assumed to be circular, and selecting all shape model vertices inside a sphere of radius R_{crat} around the centre. Next, a plane is fitted to the crater vertices, allowing to determine the surface normal of the crater. This plane is extruded
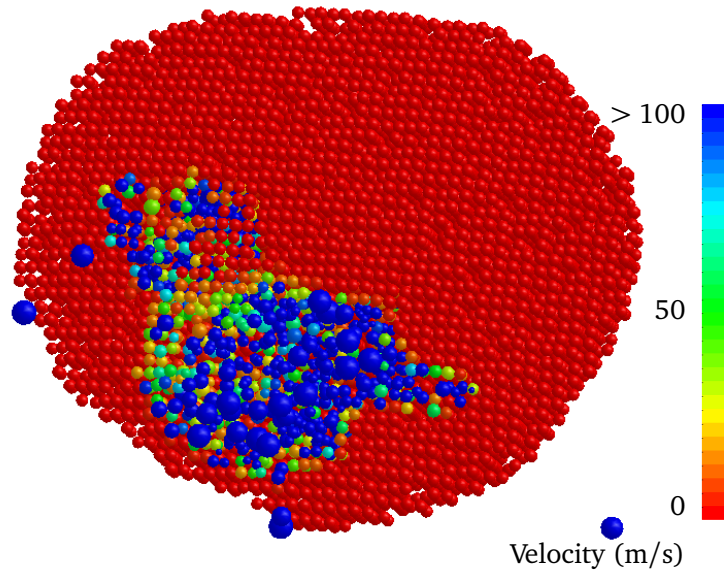
(a) Absolute velocity of SPH particles. Sphere radii represent half the smoothing length, $R_i = 0.5h$.

(b) Velocity distribution of SPH pseudo particles. Horizontal axis is the particle distance d_{imp} to the impact site. Particles on the left panel are eventually lost, unbound to the final body: the velocity is larger than the local escape velocity v_{esci}, while the right panel shows bound particles ($v_i > v_{esci}$) Note that in this logarithmic plot, particles with velocities $v = 0\,\mathrm{m\,s^{-1}}$ are not accounted for in the number density, but are included in the total mass calculation.

Figure 4.9: Velocity distribution and displacement of particles for a simulated impact on Šteins. The impactor had a velocity of $v_{imp} = 5.5\,\mathrm{km\,s^{-1}}$ and a radius of $R_{imp} = 80\,\mathrm{m}$. In this simulation, gravitational forces *have* been included.
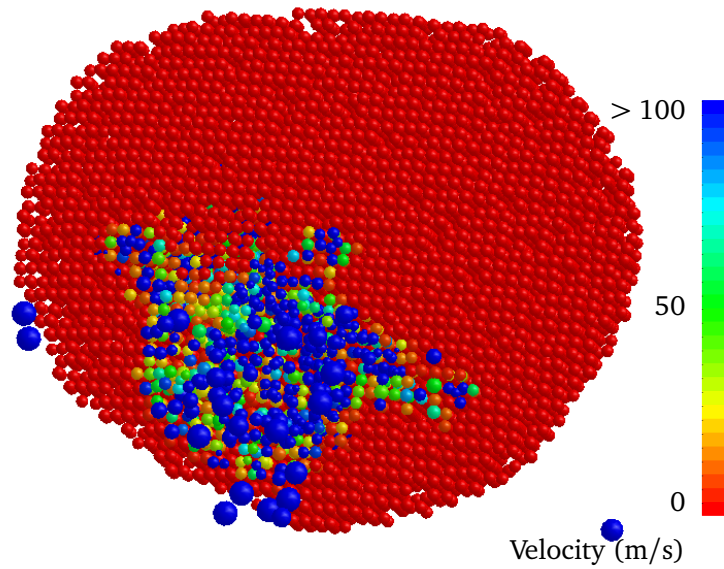
(a) Absolute velocity of SPH particles Sphere radii represent half the smoothing length, $R_i = 0.5h$.

(b) Velocity distribution of SPH pseudo particles. Horizontal axis is the particle distance d_{imp} to the impact site. Particles on the left panel are eventually lost, unbound to the final body: the velocity is larger than the local escape velocity $v_{\mathrm{esc}i}$, while the right panel shows bound particles ($v_i > v_{\mathrm{esc}i}$) Note that in this logarithmic plot, particles with velocities $v = 0\,\mathrm{m\,s^{-1}}$ are not accounted for in the number density, but are included in the total mass calculation.

Figure 4.10: Velocity distribution and displacement of particles for a simulated impact on Šteins. The impactor had a velocity of $v_{\mathrm{imp}} = 5.5\,\mathrm{km\,s^{-1}}$ and a radius of $R_{\mathrm{imp}} = 80\,\mathrm{m}$. In this simulation, gravitational forces *have not* been included.
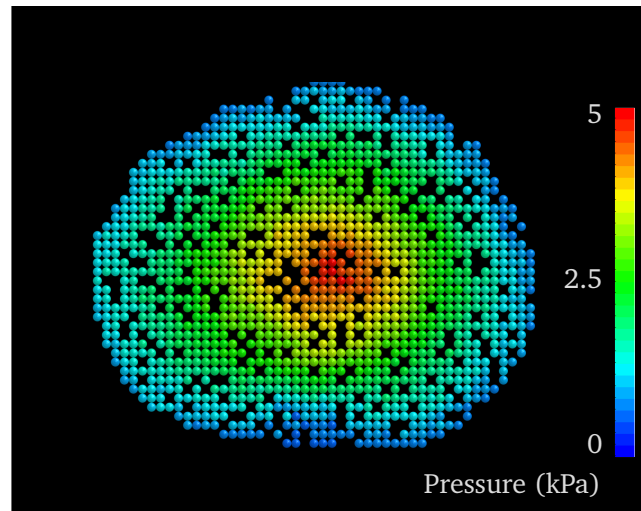
Figure 4.11: Slice through a low-resolution Šteins simulant showing the equilibrium pressure after dynamic relaxation without impactor present. The radius of the SPH pseudo particles corresponds to $1/2h$ or half a smoothing length. No sign of predamage could be found.

by a visually chosen height along the surface normal, and all crater vertices are projected onto the plane, again in the direction of the surface normal.

This plane is now merged into the original shape model by interpolating between both, ensuring the new shape smoothly interlinks with the old without introducing artefacts at the crater boundary.

To detect the uprise of a hill, a levelled plane was introduced to the shape model by a process very similar to the above, except that the plane is fitted only to the faces lying at the border of the selected region, and no extrusion is applied. The result is a level plane, fitting without artefacts into the original shape model, following the contours of the surrounding surface.

The resulting shape can be seen in Figure 4.12a. In volume, the new shape is $3.9 \times 10^7 \, \text{m}^3$ smaller than the original shape, but this is only 0.5 ‰ of the total volume and significantly smaller than the uncertainty in the original volume.

4.5.2   Setup of Impact Simulations

All impact simulations where again carried out using typical parameters found in the main asteroid belt. The velocity was chosen to be $v_{\text{imp}} = 5.5 \, \text{km s}^{-1}$, considered a typical value for asteroid–asteroid collisions (Davis et al. 2002).
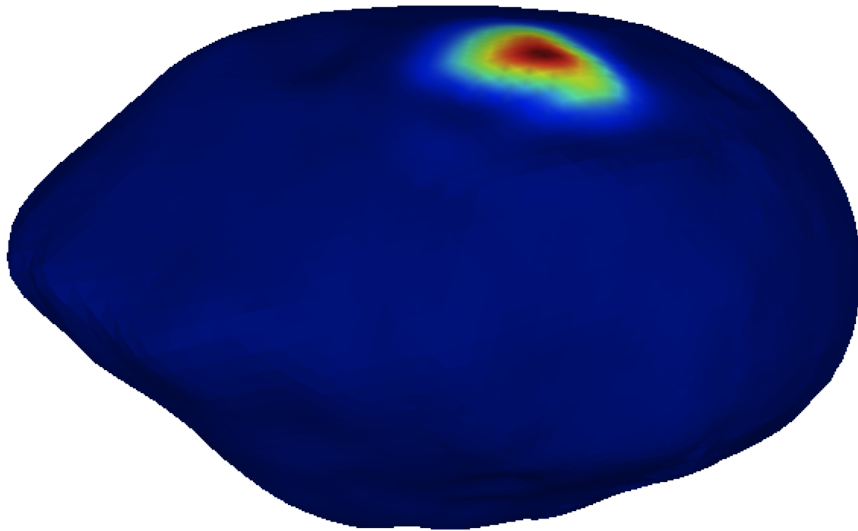
(a) Crater Diamond identified on the shape model of Šteins (Jorda et al. 2012) and replaced by spherical interpolation of the region inside the crater rim. Colour refers to depth relative to a plane fitting the rim of the crater. In compatible viewers, an interactive 3-D model is displayed.
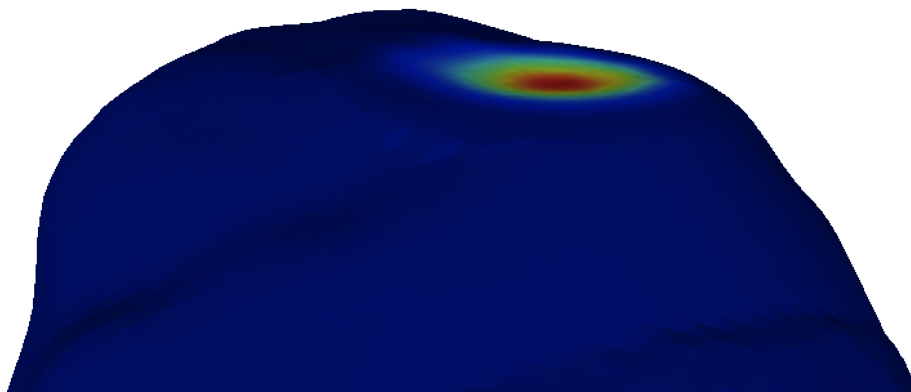
(b) The levelled surface to test for possible hill feature created in impact events on rubble pile asteroids.

Figure 4.12: A possible pre-impact shape for asteroid Šteins.

From the scaling laws discussed in Section 1.3.6 and Figure 1.17, a specific disruption energy threshold of $Q_D^* = 5 \times 10^6\,\mathrm{erg\,g^{-1}}$ to $1 \times 10^7\,\mathrm{erg\,g^{-1}}$ was estimated, assuming an olivine impactor with 30 % porosity and therefore a bulk density of $\rho_{\mathrm{bulk}} = 2240\,\mathrm{kg\,m^{-3}}$. This corresponds to an impactor radius of $R_{\mathrm{imp}} = 80\,\mathrm{m}$ to 100 m. To investigate different impact regimes, the impactor radius was varied between 30 m and 80 m.

The material parameters used for olivine are displayed in Table 2.2. The bulk porosity was set to $\phi_b = 40\,\%$ in all simulations.

Three main models were tested in a series of impact experiments:

model (Sa)   A pebble of 300 m radius was placed under the levelled area of the pre-impact shape. The pre-impact shape and the placed pebble is shown in Figure 4.13. The model parameters to create the gravitational aggregate power law size distribution were: $\alpha = 1.95$, $R_{\mathrm{min}} = 65\,\mathrm{m}$ and $R_{\mathrm{max}} = 500\,\mathrm{m}$. The void fraction as the amount of void space between the pebbles of the gravitational aggregate in the body is 42.1 %. See Figure 4.13 for a representation.

model (Sb)   A pebble of 500 m radius was placed under the levelled area of the pre-impact shape. The parameters to create the gravitational aggregate were the same as in model (Sa). The void fraction in this model is 13.4 %. See Figure 4.14 for a representation.

model (Sc)   A pebble of 600 m radius was placed under the levelled area of another pre-impact shape where the levelled mountain has been placed at a different location as seen in Figure 4.15. The void fraction in this model is 16.4 %. See Figure 4.15 for a representation.
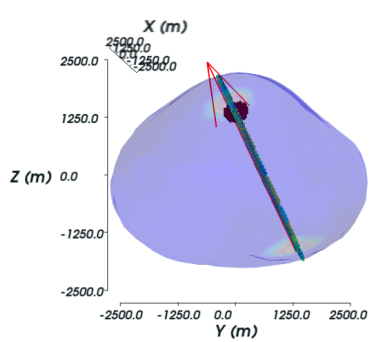
(a) View of the $z - y$ plane.
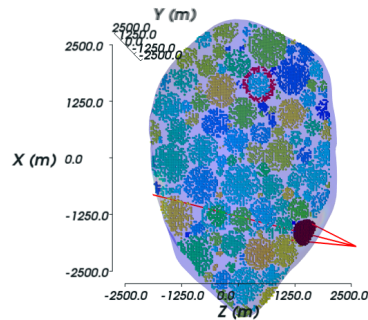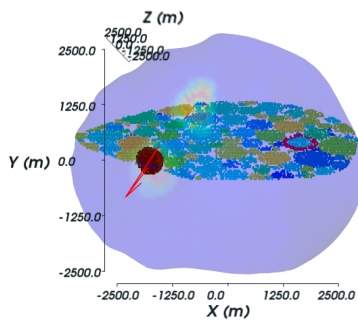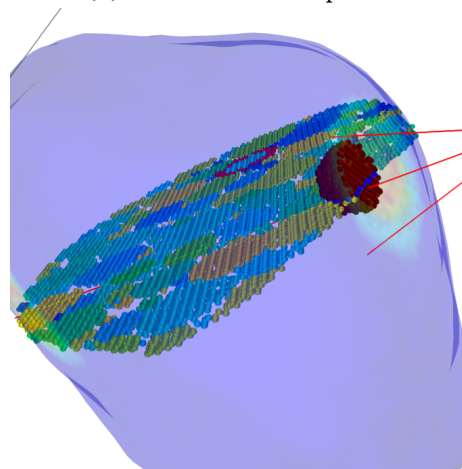
(b) View of the $x - z$ plane.

(c) View of the $x - y$ plane.

(d) View showing the impactor plane and the pebble where a hill might form during the impact event.

Figure 4.13: Šteins simulant model (Sa) for impact simulations showing the impact velocity vector, going from the position where the crater Diamond has been levelled out toward the pebble that has been placed where a hill could form. SPH pseudo particles in a plane parallel to the x axis that contains the impact velocity vector are shown to highlight the internal structure. This plane corresponds to the plane shown in Figures 4.16 to 4.18.
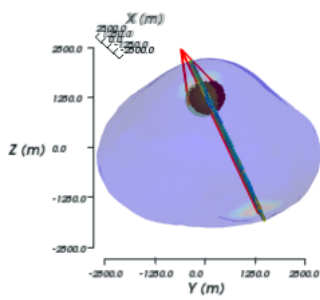
(a) View of the $z - y$ plane.
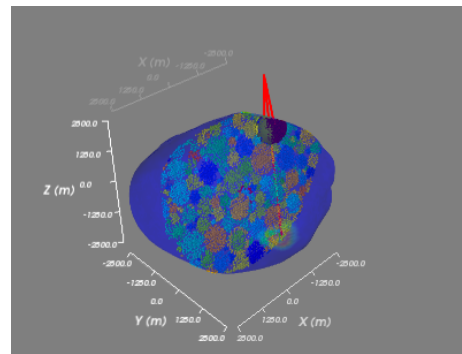
(b) View showing the impactor plane and the pebble where a hill might form during the impact event.

Figure 4.14: Šteins simulant model `(Sb)`. It is almost equivalent to model `(Sa)`, but the radius of the pebble is 500 m.
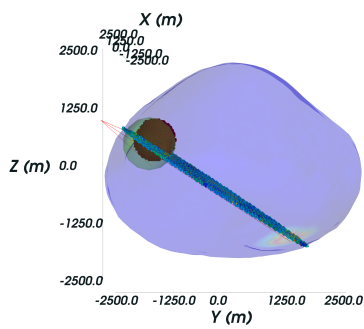
(a) View of the $z - y$ plane.
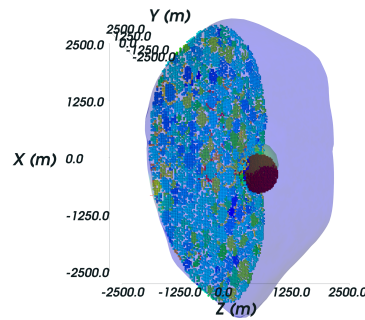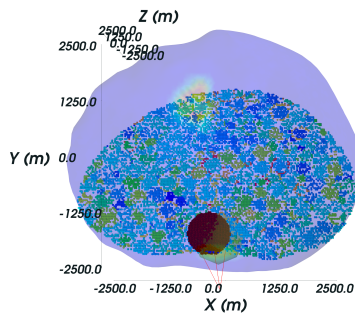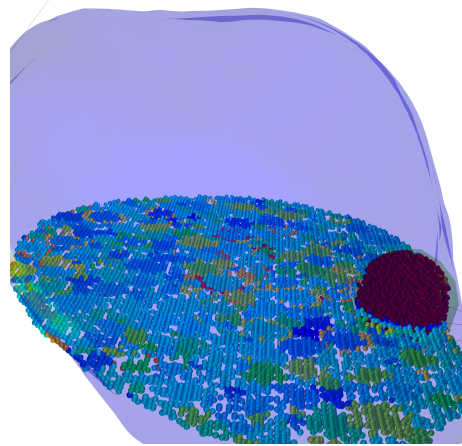
(b) View of the $x - z$ plane.

(c) View of the $x - y$ plane.

(d) View showing the impactor plane and the pebble where a hill might form during the impact event.

Figure 4.15: Šteins simulant model (`Sc`) for impact simulations showing the impact velocity vector, going from the position where the crater Diamond has been levelled out toward the pebble that has been placed where a hill could form. SPH pseudo particles in the impact vector plane are shown to highlight the internal structure. This plane corresponds to the plane shown in Figures 4.21 to 4.24.
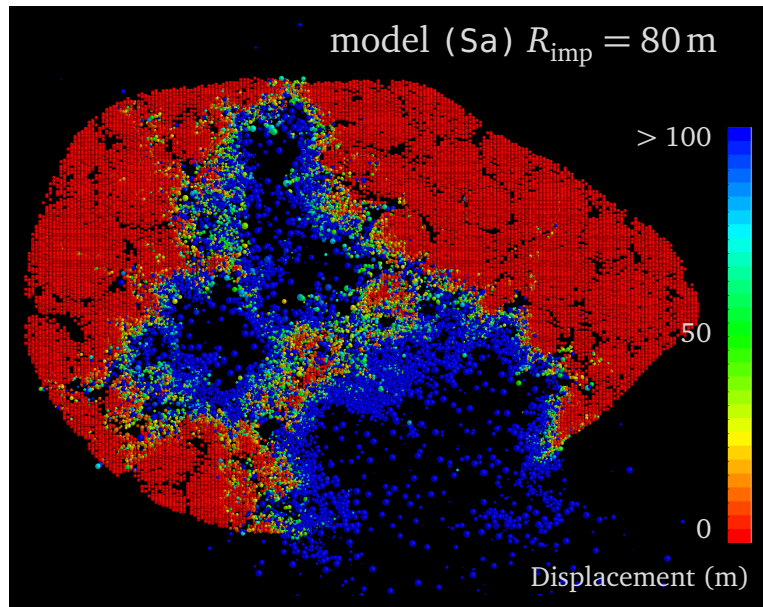
Figure 4.16: Slice through Šteins simulant model (`Sa`) impacted at $v_{imp} = 5.5\,\mathrm{km\,s^{-1}}$. The impactor radius was $R_{imp} = 80\,\mathrm{m}$.

4.5.3 Impact Simulation Results

The results of impact simulations for the asteroid simulant models (`Sa`), (`Sb`) and (`Sc`) with impactor radii $R_{imp} = (30, 50$ and $80)\,\mathrm{m}$ are displayed in Figures 4.16 to 4.24.

It can be seen that in all cases the impact with an impactor radius of $R_{imp} = 80\,\mathrm{m}$, corresponding to a specific impact energy of $Q = 5 \times 10^6\,\mathrm{erg\,g^{-1}}$, the body is disrupted.

The void fraction seems to affect the outcome. While for models (`Sb`) and (`Sc`) with similar void fraction the front of the excavated material is mostly well defined, in the case of (`Sa`) with a significantly higher void fraction the front where material has been moved is broader and extends far into the asteroid's interior.

4.5.4 Formation of a Hill Opposite to the Impact Zone

In none of the simulations is the pebble placed to form a hill displaced, and no hill formation was observed. Under the range of impact conditions tested here no link between the cratering event forming crater Diamond and the formation of the hill seen in Figure 4.7a could be established. More energetic impact events
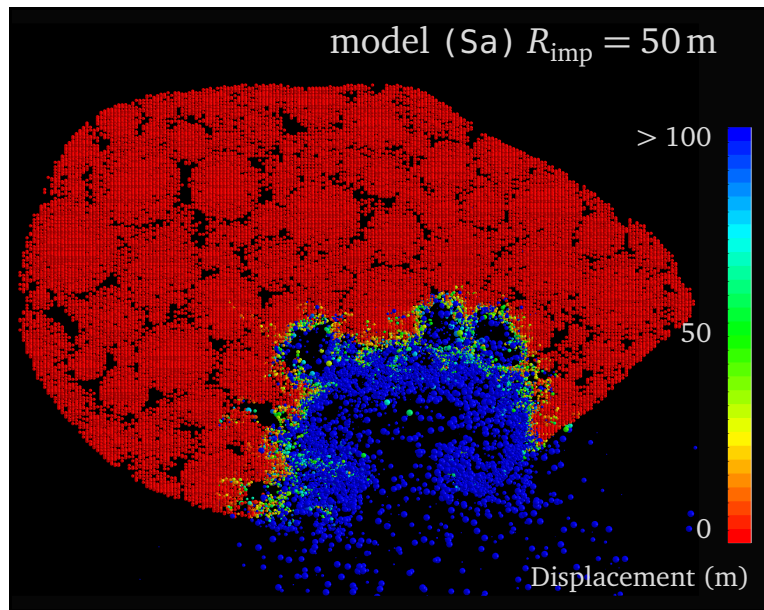
Figure 4.17: Slice through Šteins simulant model (Sa) impacted at $v_{imp} = 5.5\,km\,s^{-1}$. The impactor radius was $R_{imp} = 50\,m$.
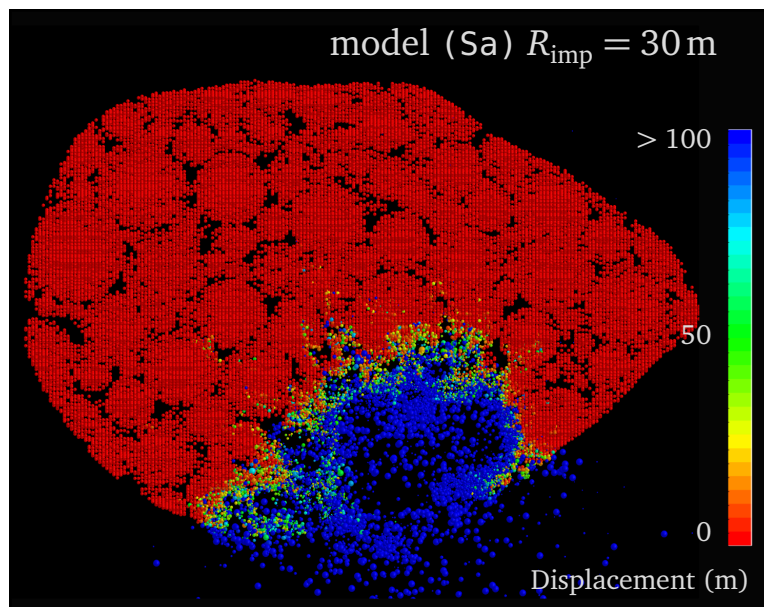
Figure 4.18: Slice through Šteins simulant model (Sa) impacted at $v_{imp} = 5.5\,km\,s^{-1}$. The impactor radius was $R_{imp} = 30\,m$.
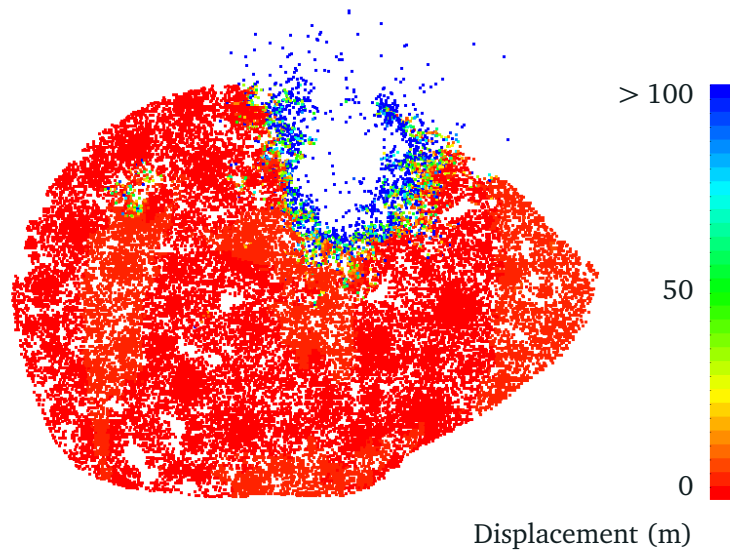
Figure 4.19: Slice through Šteins simulant model (Sb) impacted at $v_{\text{imp}} = 4.5\,\text{km}\,\text{s}^{-1}$. The impactor radius was $R_{\text{imp}} = 50\,\text{m}$.
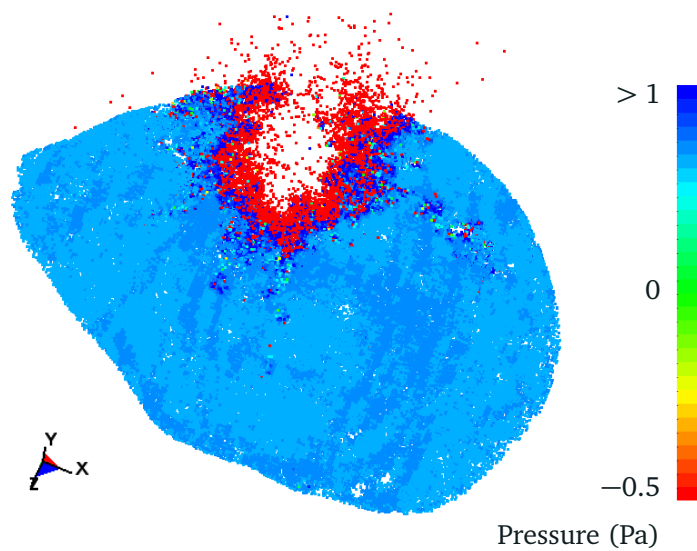
Figure 4.20: View of Šteins simulant model (Sb) impacted at $v_{\text{imp}} = 4.5\,\text{km}\,\text{s}^{-1}$. The impactor radius was $R_{\text{imp}} = 50\,\text{m}$.
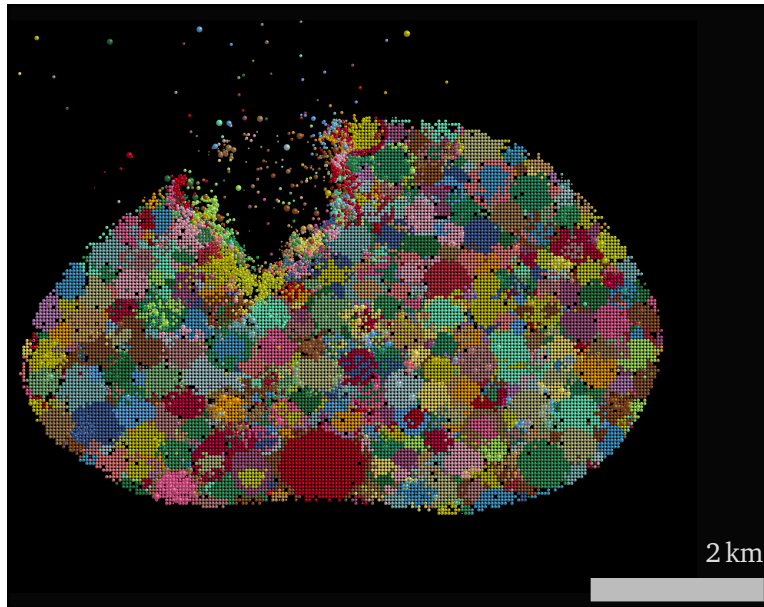
Figure 4.21: Internal structure of Šteins simulant model (Sc), as shown in Figure 4.23.
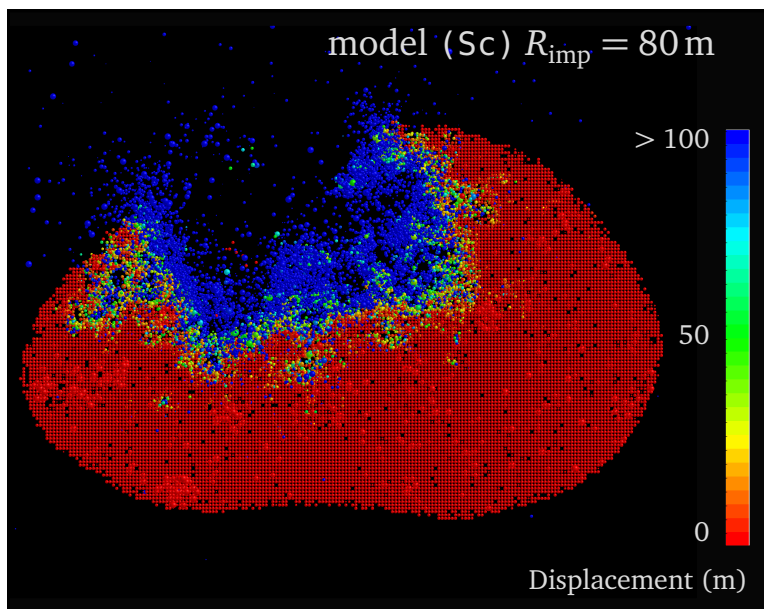
Figure 4.22: Slice through Šteins simulant model (Sc) impacted at $v_{\mathrm{imp}} = 5.5\,\mathrm{km\,s^{-1}}$. The impactor radius was $R_{\mathrm{imp}} = 80\,\mathrm{m}$.
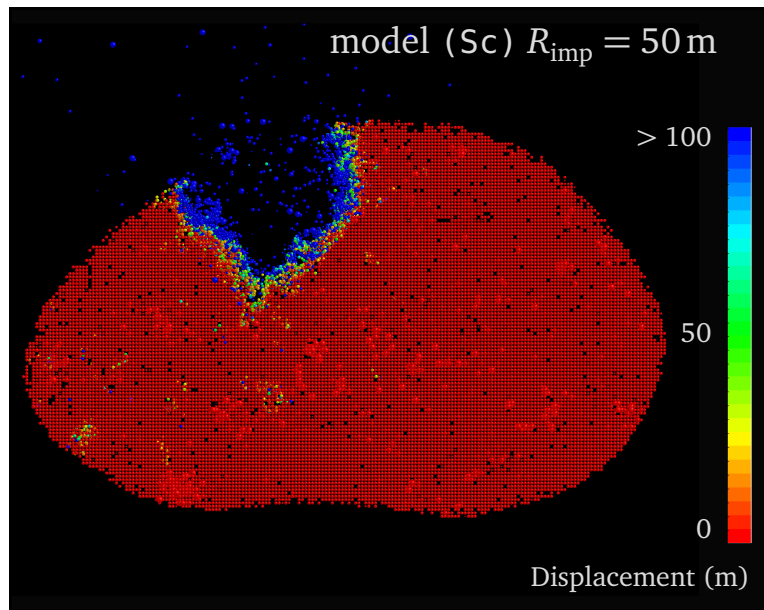
Figure 4.23: Slice through Šteins simulant model (Sc) impacted at $v_{\text{imp}} = 5.5\,\text{km}\,\text{s}^{-1}$. The impactor radius was $R_{\text{imp}} = 50\,\text{m}$.
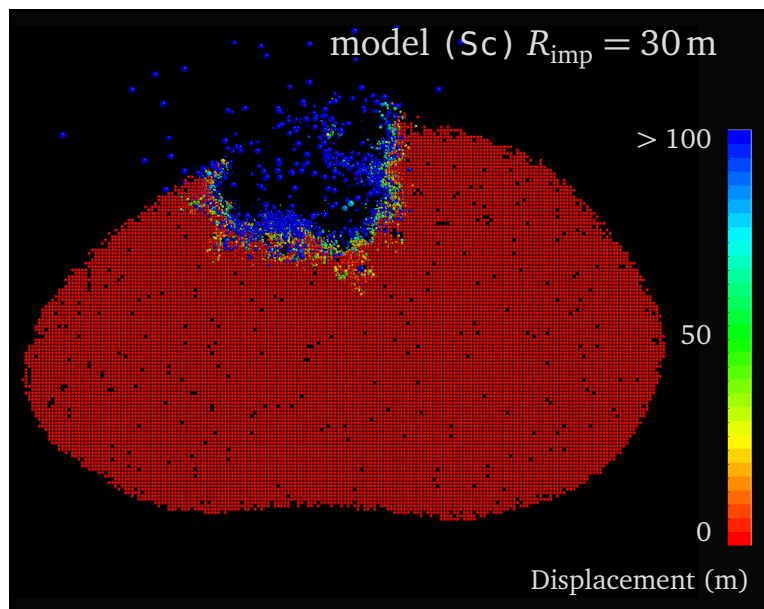
Figure 4.24: Slice through Šteins simulant model (Sc) impacted at $v_{\text{imp}} = 5.5\,\text{km}\,\text{s}^{-1}$. The impactor radius was $R_{\text{imp}} = 30\,\text{m}$.

that might cause more internal reconfiguration will destroy the asteroid, as seen in the simulation with an impactor of radius 80 m. Therefore, it is considered to be unlikely that the hill is a result of a cratering event. Alternatively, the hill feature is a remnant of the formation history of Šteins. As discussed in Section 1.1.9, the observed top-like shape of Šteins can be explained by the reshaping process outlined in Walsh et al. (2008), where increasing the spin rate, for example due to YORP forces, leads to transport of material from the poles to the equator as well as to seismic shaking during the reshaping. This seismic shaking may lead to either size segregation and vertical sorting due to the so-called 'Brazil nut effect' (e.g. Tancredi et al. 2012), or the redistribution of surrounding smaller fragments, leaving the large fragment forming the hill feature.

Assuming the hill is indeed a coherent fragment, its dimension could allow to infer the size distribution of the pebble constituents in Šteins. Extending over 2 km, and elevated 120 m to 150 m, assuming a cylindrical profile leads to an estimated volume of 2.8×10^8 m^3, equivalent to a sphere of radius $R_{equiv.} =$ 493 m. As distribution of pebbles by gravitational aggregation tends to show an overabundance of large pebbles in the centre, this might indicate the existence of large fragments in the size range of the hill in the interior of Šteins.

Inspection of the output from the simulations by looking for a coherent movement of single pebbles rising above the surrounding surface did not reveal possible hill candidates. Therefore, it is unlikely that impacts with different impact angles would lead to the eventual formation of a hill.

4.5.5 Formation of Cracks

Material displaced by the passing shock wave is guided by inhomogeneities of the internal structure. In impact simulations on model (Sa), which has the highest void fraction of 42.1 %, the propagation of the material displacement can be seen to follow the link in between pebbles, leading to the subsequent formation of a fracture reaching the surface perpendicular to the crater rim. Figures 4.25 and 4.27 shows the final state and development of a network of fractures during an impact simulation. In Panel Figure 4.25a and Figure 4.27 it can be seen that some of the fragments extend through the asteroid's interior to the surface. The radial extent is about 2 km; three of the fractures have been annotated in Figure 4.27. Interestingly, the fractures do not extend to the surface over their whole length, but rather emerge from a few hundred meters depth
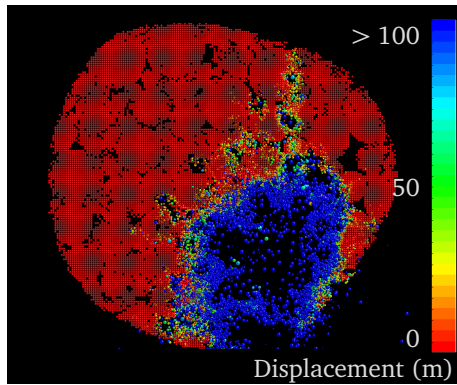
(a) Displacement of SPH pseudo particles in the x–y plane at $z = -1000$ m.
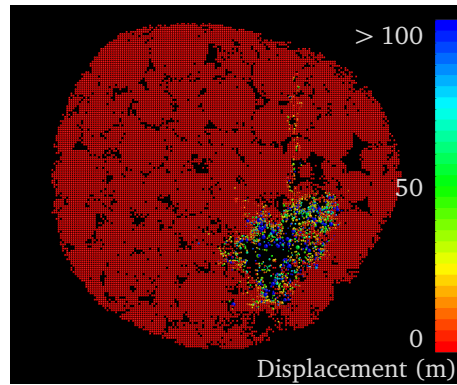
(b) Same as Panel (a) shortly after impact.
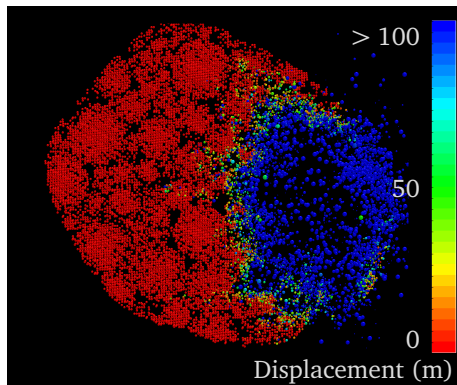
(c) Displacement of SPH pseudo particles in a plane perpendicular to the impactor 300 m below the impact point.
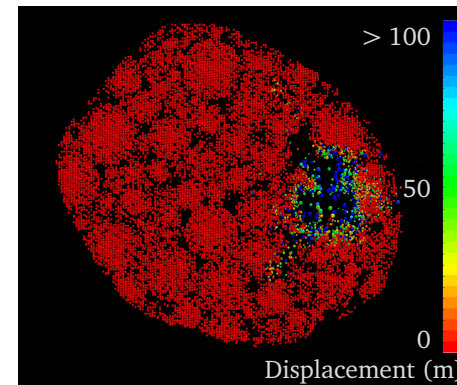
(d) Same as Panel (c) shortly after impact.

Figure 4.25: Fractures forming in a simulated impact event on model (Sa) with an impactor of $R_{\mathrm{imp}} = 50$ m.
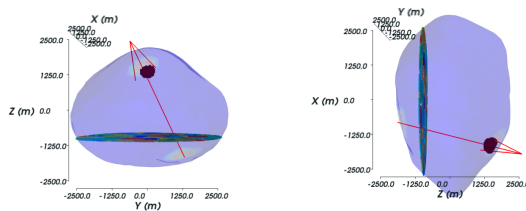
(a) View of the z – y plane.   **(b)** View of the x – z plane.

Figure 4.26: The same model (Sa) as shown in Figure 4.25, with the plane at $z = -1500$ m shown in Figures 4.16 to 4.18 and 4.25.
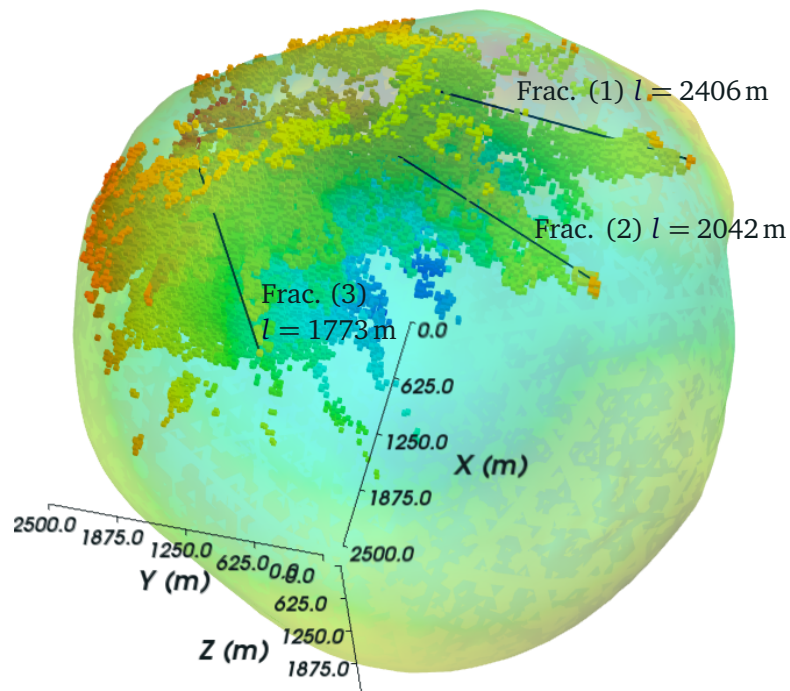
Figure 4.27: The network of fractures that developed inside the asteroid at the end of the simulation run on shape model (Sa) with an impactor of $R_{\mathrm{imp}} = 50\,\mathrm{m}$ as seen in Figure 4.25. Displayed are all SPH particles that moved between 1 m and 100 m. Colour refers to z value.
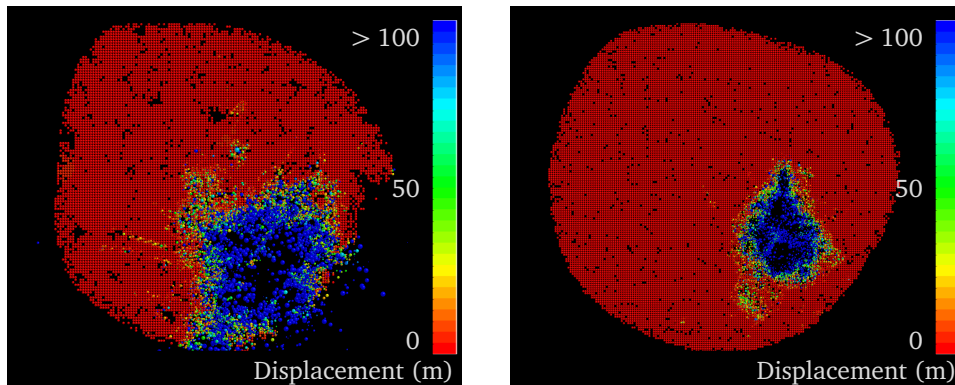
(a) Displacement of SPH pseudo particles in the x–y plane at $z = -1000$ m in model (Sb) (see Figure 4.19).

(b) Displacement of SPH pseudo particles in the x–y plane at $z = -1000$ m in model (Sc) (see Figure 4.23).

Figure 4.28: For comparison, the same plane that revealed the formation of fractures in impacts on model (Sa) shown in Figure 4.25a, here for the asteroid simulants model (Sb) and (Sc) where no fracture formation can be observed.

and break through to the asteroid surface at the end (Fractures 1 and 3) or even at regular intervals (Fracture 2). The width of these fractures ranges from a few SPH pseudo particles, corresponding to a few times the smoothing length, h, of 2 to 3 hundred meters. Assuming a cylindrical shape, the contained volume can roughly be estimated as $V = \pi R^2 l \approx \pi (150\,\text{m})^2 \times (2\,\text{km}) = 1.4 \times 10^8\,\text{m}^3$. If the volume of all craters in Table 4.2 are summed up, approximated as cones with volume $V \approx 1/3 \pi R^2 d$, a volume of $2.8 \times 10^7\,\text{m}^3$ has disappeared into the fracture, so at least within an order of magnitude this process seems to be plausible.

These fractures show many features found on the aligned pit chain as seen on Šteins (Figure 4.8). The pit chain also extends radially from the crater rim, and the regular spacing can be interpreted as an underlying fracture breaching the surface where there are weak links between similar sized rubble pile fragments. The length of the observed pit chain, extending from the crater rim almost to the opposing pole, is not in agreement with the observed fracture described here. This might be due to a slightly higher impact energy of the event forming crater Diamond, or an underlying inhomogeneity in the interior of Šteins that additionally weakened the body at this fracture. Such a pre-existing fracture might also explain the fact that only one catena of pits is seen on Šteins, while there are many, if smaller, fractures present in the simulation.

These fractures do not occur in other simulations with lower void fraction.

As seen in Figures 4.28a and 4.28b, the shock front in both other simulations with the same impactor radius $R_\text{imp} = 50\,\text{m}$ is more even, and no fractures occur. Therefore, if the catena observed on Šteins is indeed connected to a fracture induced by the impact that created crater Diamond, an internal structure similar to model (Sa) with a high void fraction is a better match to observations than interiors with lower void fraction as in model (Sb) and (Sc).

4.6 Asteroid Šteins: Conclusions

Asteroid (2867) Šteins is, by multiple lines of evidence, a fully fractured or rubble pile asteroid, with an estimated macroporosity of $\phi_\text{macro} = 20\,\%$ to $40\,\%$. Therefore, relating surface features as observed by the OSIRIS camera system on board the Rosetta spacecraft to the behaviour of an modeled rubble pile interior during impact events provides a tool to gain insights into the behaviour of rubble pile asteroids in general.

Here, the link of two remarkable surface features on Šteins — a hill-like feature opposite the crater Diamond, and a catena of aligned pit-like structures extending from the crater rim to the north — has been studied. The hill-like feature could not be linked to the impact event, it is likely therefore a remnant of formation and evolution of the asteroid, while the catena of pits can be linked to fractures forming in models containing a high macroporosity.

The underlying fracture forming the catena of pits seems to be modelled best by assuming a high void fraction in between the pebbles or constituent fragment. This is a first answer to the question on how the macroporous void space is distributed inside rubble pile asteroids. Rather than in small cracks and voids homogeneously distributed throughout the body, the catena of craters supports an interior of Šteins with large, consolidated voids. As the macroporosity of Šteins is unlikely to be more than $40\,\%$, the constituent fragments in the interior of Šteins have a low macroporosity themselves and are only lightly fractured during the re-aggregation at the formation of the asteroid.

Chapter 5

Discussion

In this work, a new approach to modelling the interior of rubble pile asteroids in hypervelocity impact events has been developed. A schematic of the approach is shown in Figure 5.1. Rubble pile asteroids reveal a macroporosity of about 40 %. This means, that about 40 % of these bodies are void space, on scales larger than the micrometre sized fractures observed in meteorites. How this void space is distributed, and on what scale, is not yet known, as there have been no in-situ measurements using spacecraft instruments of asteroid interiors yet.

The surface appearance of small asteroids as well as the violent collisional history of small asteroids supports the idea that rubble pile asteroids are aggregates of fragments (Michel et al. 2015) rather than an originally monolithic bodies permeated by fractures. The statistics of observed boulders on asteroid Itokawa can only be interpreted as fragments of a larger parent body (Michikami et al. 2008), and the top-like shape of asteroid Šteins is indicative of YORP reshaping process (Walsh et al. 2008), that also is more efficient if the body is made of multiple fragments as opposed to a large fractured body.

In this work, the consequences of a rubble pile internal structure containing a size distribution of large pebbles are analysed. In the model, these pebbles are represented by spherical structures, and their arrangement inside the asteroid determined using a simplified model of gravitational aggregation. As for the conversion into an impact model, the bulk macroporosity is kept constant, therefore the influence of the void space fraction as the relative volume contained in between the pebbles can be varied.

In this Chapter the applicable range of the rubble pile asteroid model is discussed. The implications of assumptions on the internal structure of rubble
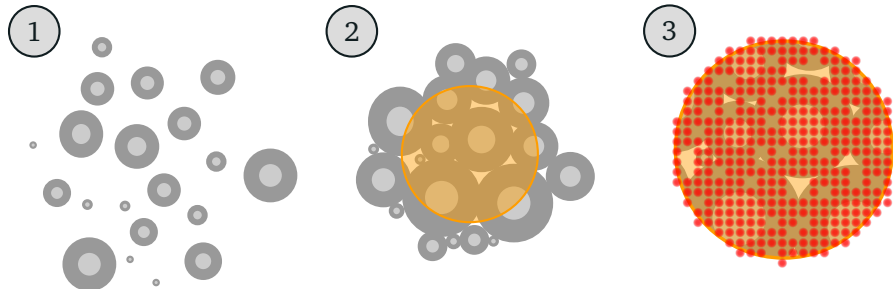
Figure 5.1: Schematic of the rubble pile simulant model. In step (1), the interior is formed by gravitational aggregation of spherical pebbles. In step (2), the model of an asteroid is excised. In step (3), the simulant is created by filling the model with SPH pseudo particles following a radial porosity function.

pile asteroids and their formation scenario are considered in Section 5.2.1. In the model, the large scale interior of rubble pile asteroids is a gravitational aggregate of fragments that are remnants of a disrupted parent body. As these fragments themselves contain fractures, in the model a radial porosity function is considered. The effect of the chosen function is discussed in Section 5.2.2. In the model, all constituting fragments are assumed to be spherical. This is clearly a simplification, and possible implications are discussed in Section 5.2.3.

The focus of this work is to find a link between the large scale rubble pile structure and surface features found on asteroids. This was tested on asteroid Šteins in Chapter 4. One possible link to the interior of Šteins is found in the catena of pit-like features found to extend radially from the rim of crater Diamond. This linkage and the influence of the surface regolith is discussed in Section 5.3.1. Then, conclusions about the large scale interior structure of the rubble pile asteroid Šteins are drawn and analysed, and their implications for the evolution scenario of the asteroid are reviewed.

Šteins is rather small rubble pile asteroid. As the SPH shock physics code used to calculate the impact event is, like all numerical methods, bound in resolution to the available computational resources, the range of other asteroids the model might be applied to is discussed in Section 5.5, and Section 5.6 lists open questions that the application of the model might help to answer.

5.1   A Simulant for the Large Scale Structure of Rubble Pile Asteroids

While the natural limit to size resolution does not allow to analyse small scale effects of regolith and the lower end of the pebble size distribution, the model provides a tool to track restructuring processes in the interior of rubble pile asteroids during impact events.

This study concentrates on small asteroids, the size of a few hundred metres to a few kilometres. Multiple transitions in the characteristics of asteroids as found in the main belt happen on this size, mainly seen in the lack of superfast rotators above that size as discussed in Sections 1.2.2 and 1.2.3 and the transition from the strength to the gravity dominated regime for asteroids as discussed in Section 1.3.6.

The largest fast rotating asteroids that can be interpreted as monolithic bodies are just about 130 m in radius. All bodies larger than the size seem to be limited to a rotation period of 2.2 hours (see Section 1.1.5) , indicating a very weak stability against rotational disruption and therefore only weak cohesive forces. Therefore, most likely all bodies larger than a few hundred metres and smaller than $\sim$ 100 km are rubble piles or a least fractured bodies (Michel et al. 2015).

To simulate impacts in the gravitational disruption regime, the existing code and material model used in this work should be improved first. The simplified material model lacking strain rate effects and size scaling is only a starting point, and should be replaced with a more advanced model and compared again to the results of simulations using other impact code packages. The increase in ejection velocity for simulations that include gravitational forces when compared to simulations neglecting those, lacks a physical explanation and therefore limits the explanatory power of the results in this work when compared to work of others. As in Section 4.4.3 the cause of this behaviour was not found, further investigations are necessary before using the code for further studies in the large-scale gravitational regime of large asteroids.

Rubble pile asteroids with large voids, as the models with a large void fraction in this work show, behave very different in impact events than monolithic ones. Compaction of voids and internal reconfiguration lead to an increased strength of the asteroid against disruption.

To show if this specific model of rubble pile asteroid interiors can be distin-

guished from other internal structures by surface features observed in resolved imaging by spacecraft encounters, the case of asteroid Šteins is analysed. Šteins exhibits a very large crater close to the southern pole, and while the impact is still not considered to be abnormally large, and well below the disruption limit, it still can be expected to have significantly influenced today's appearance of the asteroid.

Assuming that Šteins is an remnant of a catastrophically disrupted parent body, the catena of pit-like features observed extending radially from the crater rim can be well explained. On the other hand, the formation of a hill by coherent movement of one of the pebble constituents in a simulated impact event could not be observed. The observed hill-like feature on Šteins is therefore most likely a remnant of the earlier evolution or even the formation. This gives us additional insight into the size distribution of the original fragments now constituting Šteins and will be discussed in Section 5.3.3.

5.2 The Internal Structure of Rubble Pile Asteroids in Impact Events

In the model described in this work, the interior of a rubble pile asteroid is represented by spherical pebbles following a defined size distribution. The spatial configuration of the pebbles is determined by calculating a simplified gravitational aggregation of particles randomly distributed in space. The starting point of the model is therefore a series of fragments presumably created during a disruptive impact event on a large parent body, subsequently forming rubble pile asteroids. This process has been shown to reproduce the size distribution of asteroid families quite well. Michel et al. (2004a) combined in an attempt to recreate the Koronis family, SPH impact simulations to calculate the disruption, and a gravitational N-body code to follow the evolution and re-aggregation. In their model all of resulting family members were rubble pile aggregates formed during the re-aggregation phase.

5.2.1 Rubble Pile Asteroids as Remnants of Catastrophic Disruption Events

One simplification in the model presented in this work is that initially all pebbles are at rest, while the fragments ejected during a disruption event certainly exhibit
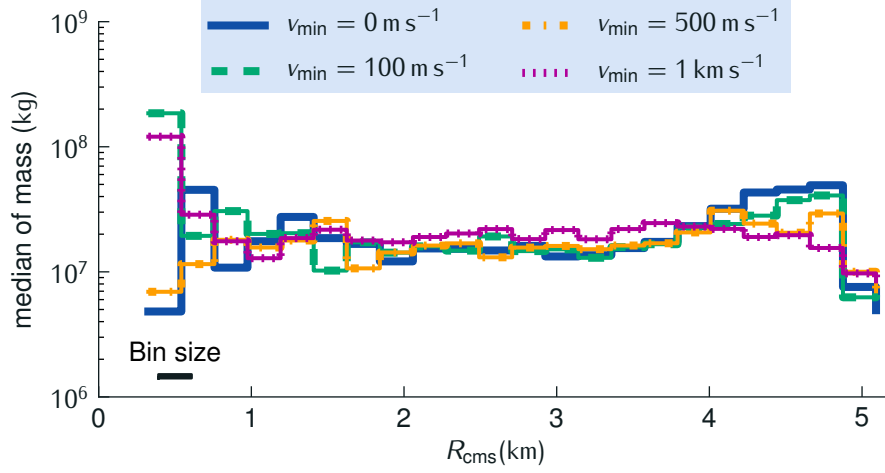
Figure 5.2: Local median of pebble mass as a function of distance to the centre of mass R_{cms} for three different initial velocity conditions in gravitational aggregates. The median is calculated in 25 evenly spaced bins of width w, corresponding to spherical shells from $R_{i,cms}$ to $R_{i,cms} + w$. The initial velocity is distributed according to a power law $v_{initial} = v_{min}M_{max}^{\eta} \times M^{-\eta}$. M_{max} is the mass of the largest pebble allowed with radius R_{max}, η is $1/6$, and the minimal velocity v_{min} is varied. For the pebble size distribution, the parameters $\alpha = 1.95$, $R_{min} = 60\,m$ and $R_{max} = 500\,m$ are identical for all aggregates shown. Please note that the number of pebbles inside of $R_{cms} = 200\,m$ is less than six in all cases.

relative velocities. The angular momentum contained in the initial pebble sample would potentially lead to a different shape of the gravitational aggregate, that was calculated using the N-body code `Rebound`. Generally, smaller particles ejected in an impact event have higher velocities than larger ones. While more recent simulations show that the relation between speed and mass of a fragment is not easily described by an analytic function (Michel et al. 2015), a power law of the form $v \propto M^{-\eta}$ is used in models of collisional evolution (Davis et al. 2002), with a power law slope from $\eta = 0$ to $\eta = 1/6$ while in average approximately $\eta = 1/13$ (Giblin 1998). In Figure 5.2, the pebble distribution inside gravitational aggregates created with different initial velocity conditions using the above power law is shown. Contrary to intuition, there is an enhancement of large pebbles on the surface of the aggregate when no or only weak initial velocity dispersion is assumed. As mean ejecta velocity are at the range of $v_{mean} \approx 200\,m\,s^{-1}$ (Jutzi et al. 2010b) in impacts on a parent body with $R_{tar} = 100\,km$, the cases with a minimal velocity larger than $v_{min} = 100\,m\,s^{-1}$ are unrealistic over-exaggerated

but still shown for illustrative purposes. In the process to create rubble pile simulants the actual shape of the asteroid is excised from the interior of the gravitational aggregate. Because the differences discussed here affect only the surface layer of pebbles, the resulting simulant models will not differ significantly if the dimensions of the aggregate are larger than the dimension of the applied shape model.

Evolution of the Rubble Pile Interior Structure

In the model presented in this work, earlier stages of internal restructuring are not included. During the evolution of the asteroid, multiple processes will change the interior of the asteroid. Seismic shaking by small impact events or by relaxation of stresses during YORP induced spin-up are known to produce a radial size sorting. The so-called Brazil nut effect tends to enhance the number of large particles at the surface. If a granular media is shaken, granular convection leads to particle segregation (Behringer et al. 1999), and therefore to an enrichment of large particles at the surface. Miyamoto et al. (2007) found evidence for this effect on asteroid Itokawa.

Influence of the Evolution on the Modeling

The influence of the exact size distribution and spatial arrangement of the pebbles in the interior of the rubble pile simulant on the general outcome of impact events is most probably small. As seen in Section 3.6, the sensitivity of impact simulations using the rubble pile simulant model to the exact values of the power law parameter controlling the size distribution is small. Therefore the assumption of initially stationary pebbles will not influence the bulk parameters of the outcome of an impact event, such as mass of the largest remnant fragment.

It might, however, be important for the connection of surface features to restructuring processed in the asteroid's interior, as the size distribution of pebbles at the surface directly is likely to influence the result.

5.2.2   The Porosity of the Pebble Building Blocks

In the conversion process from the gravitational aggregate, the shape of the asteroid is excised and the interior is filled with SPH particles. As described in Section 3.3 two assumptions are made during this process: a radial porosity
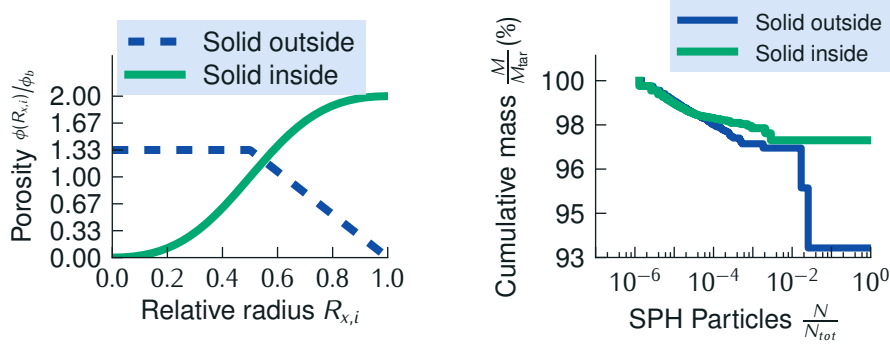
(a) Profiles of the radial porosity function inside the pebbles. *Solid inside* refers to the profile in Equation (3.3), while *solid outside* refers to Equation (5.1). The relative radius $R_{x,i}$ is the distance of $\vec{x}$ to the centre of the nearest pebble i at $\vec{R}_i$ of the gravitational aggregate normalised by the pebble's radius R_i. The porosity $\phi(R_{x,i})$ is divided by the bulk porosity ϕ_b. The integral of both functions in the limits from 0 to 1 is 1

(b) Fragment size distribution for different radial porosity functions $\phi(R_{x,i})$ as in Panel (a). The gravitational aggregates used to create both models are identical ($\alpha = 4$, $R_{min} = 6.9\,\text{m}$, $R_{max} = 32.2\,\text{m}$).

Figure 5.3: Assessing the influence of the assumed radial porosity function inside the pebbles of the gravitational aggregate.

profile $\phi_{in}(R_{x,i})$ is superimposed on each pebble, and a total bulk porosity ϕ_b is ensured.

The porosity profile used in this work (see Equation [3.3]) assumes a process where fragments are fractured by low-speed collisions during the accretion process at or near the surface. On the other hand, for small particles it has been shown by (Beitz et al. 2012; Weidling et al. 2012; Kothe et al. 2013) that during collisional aggregation from micrometre sized particles to millimetre sized spheres, material is compacted at the surface layers. Starting with aggregates of constant porosity, subsequent multiple collisions compacted the outside of the aggregates. To first order, the compaction decreased linearly to the interior of the aggregates, and the outer half of the aggregates was affected. As a simplified model the following radial porosity as a function of the normalised distance $R_{x,i}$

to the centre of pebble i, assuming a total bulk porosity ϕ_b, could be used:

$$\phi_{\text{solid outside}}(R_{x,i}) = \begin{cases} \frac{4}{3} \cdot \phi_b & , 0 < R_{x,i} < 0.5 \\ \frac{4}{3} \cdot \left(-2R_{x,i} + 2\right) \cdot \phi_b & , 0.5 < R_{x,i} < 1 . \end{cases} \tag{5.1}$$

In Figure 5.3a both forms of the radial profile are shown. A test simulation using `Autodyn` for the same internal structure as given by the gravitational aggregate and the same impactor characteristics, differing only in the radial porosity function used, showed some change in the fragment size distribution (Figure 5.3b). While the slope of small fragments looks very similar, the mass of the largest remnant fragment changes: In the case of pebbles solid in the inside, $M_{\text{lr}} = 97.6\%$, and for pebbles solid at the outside $M_{\text{lr}} = 93.3\%$, a change above the threshold for significance of 2% found in Section 3.5.1. This shows that even locally the porosity increases the stability of the objects and inhibits cratering, while for pebbles solid at the outside more material is excavated.

As argued in Section 3.3, pebbles that are solid on the outside can only originate from formerly porous bodies that are compacted at the surface in a series of low velocity collisions, a process happening during the dust grow phase in the PPD in the formation of the Solar System at sizes up to a few centimetre (Johansen et al. 2014). This is not in agreement with the idea of fragments originating in a catastrophic disruption of a parent body, that has been differentiated and therefore should exhibit only a small porosity. Therefore, the porosity model in Equation (5.1) might only be useful in high-resolution simulations of small asteroids, where the smallest pebbles considered as defined by the minimum radius R_{min} of the gravitational aggregate is in the size range of centimetres.

In the simulations presented in this work, all porosity is resolved explicitly. While this is a straightforward way to achieve constant bulk porosity with varying inter-particle void space, it might blur the distinction of small scale porosity inside the pebbles and large scale porosity between pebbles. An interesting experiment would therefore be represent the porosity inside the pebbles using a sub-resolution porosity model as described for example in Jutzi et al. (2010b).

5.2.3   Treatment of Interlocking Pebbles

The form of the fragments resulting from catastrophic disruption will not be spherical. In laboratory-size impact experiments, Capaccioni et al. (1984) found

that fragments, while showing a wide distribution in shapes, have a mean axial ratio of $b/a = 0.72$. A similar value is found for asteroids smaller than $R = 100\,\mathrm{km}$ with $b/a = 0.77 \pm 0.11$ (Capaccioni et al. 1984). While boulders larger than $R = 5\,\mathrm{m}$ on asteroid Itokawa show a slightly different value of $b/a = 0.62 \pm 0.19$, Michikami et al. (2010) argue that this might be due to the sorting by granular motion that has evidently been processing the interior of Itokawa (Miyamoto et al. 2007). The effect of elongated shapes to the rubble pile simulant model is not clear. In a study on the packing of M&M candies Donev et al. (2004) found that ellipsoids can be more closely packed than spherical particles, which could indicate that the void fraction as given by the inter-pebble space is overestimated in the rubble pile simulants compared to real asteroids.

More important than the packing might be the treatment of the contact points between the pebbles. Pebbles most likely will be fractured and damaged at the contact points due to low-velocity collisions and relative movement during formation and evolution. Benavidez et al. (2012) modelled this damage by reducing the density of material at the contact zones by a factor of two (see Figure 1.18). This approach could be extended to pre-damage the material at the contact zone. Completely damaged material in the model used in this work is described using a Mohr-Coulomb dry friction law (see Section 2.1.5). The cumulative damage of each particle is parameterized using the damage parameter D_{dam}, where $D_{\mathrm{dam}} = 0$ for intact material, and $D_{\mathrm{dam}} = 1$ for completely damaged material. Setting the damage parameter D_{dam} to 1 for all SPH particles at the contact zone would result in significantly reducing the yield strength of the material to the value of Y_{d} instead of Y_{i} for the undamaged material.

This would most likely facilitate the formation of cracks. As shown in impact simulations on Šteins (see Section 4.5.5), crack formation is going along the contact zones between the pebbles. A lower material strength in this zone would therefore encourage fracturing. This could possibly result in a lower stability against disruption of the body, as it would be easier to separate whole pebbles from the body.

Furthermore, real fragments with asymmetric shapes will hold together by interlocking. In the case of granular materials — loosely bound aggregates on small scale — the bulk behaviour is determined not by the material properties of the grains themselves, but mostly by surface characteristics and shape (Herle and Gudehus 1999). For millimetre sized grains, the static angle of repose which is the critical angle when avalanching starts on a pile of grains, is almost twice

as high (about 40°) as for spherical particles, even in low-gravity conditions (Kleinhans et al. 2011). It is reasonable to assume that the same effect of interlocking also works on larger scales.

While this indicates a possible deficit in the creation of the gravitational aggregate, the SPH approach inherently includes some interlocking treatment. As discussed in Section 2.1.2, an inherent problem of the SPH formalism is the lack of a clearly defined interface between two distinct solid bodies. As local quantities like density and pressure are defined by evaluating pseudo particles within two smoothing lengths h using a kernel function W, effectively material at the contact zone will be treated as a continuous material if no special treatment of interfaces is implemented as it was the case in the simulations presented in this work. The effect of this welding is eventually similar to a perfect interlocking, where the shear strength needed to fracture the locking is given by the shear strength of the material itself. Scholtès and Donzé (2013) successfully implemented the treatment of interlocking effects into Discrete Element Method (DEM) simulations of brittle rocks by a similar approach, where the DEM elements take into account forces by other elements in an extended neighbourhood, and were able to reproduce the rock behaviour well. Therefore it can be concluded that by using the SPH formalism, some interlocking between the pebbles is implicitly included into the simulations even for spherical pebbles. More problematic is the assumed tensile strength at the interlocking interface, which in our approach is also assumed to be the tensile strength of the intact material. This could be solved by using the material model for totally damaged ($D_{dam} = 1$) material in the effected pseudo particles, highlighting once more the need to implement this feature in further studies.

In Figure 3.9 (Section 3.6), a strong correlation between the mass of the largest remnant fragment and the effectively welded area as the total pebble contact area can be seen. This might indicate a causal relation, as the smaller total contact area results in a decrease of shear strength between the pebbles. However, the data analysed is in the cratering regime with ejected masses of less than 16 % of the target mass. Therefore the contact welding is only a contributing factor, and the decrease in small-scale porosity of the larger pebbles for models with higher void fraction is a more likely explanation for the increase in excavated material.

The effect of the welding on the simulated asteroid collisions can also be estimated by comparison with other studies. In Section 3.5.2, the disruption

threshold for the rubble pile asteroid simulant as well as a non-porous model of same size using the SPH solver in `Autodyn` is compared to results of a study by Jutzi et al. (2010b). It is observed that while for the solid model Jutzi et al. (2010b) find a slightly higher disruption threshold, this is reversed for the rubble pile asteroid simulant, where the disruption threshold is found to be lower than the value found in this work. Because of the simplified material model neglecting size and rate effects, this is contrary to expectations, as the neglected decrease in strength with size should lead to an overestimation of the target strength in the strength regime explored here. It does imply that the welding of pebbles resulting from using the SPH formalism with no extra treatment of interface effects is resulting in a stronger interlocking than expected, as the increase in resistance against disruption for the rubble pile simulant is higher than the increase in strength of the porous models simulated by Jutzi et al. (2010b) compared to the non-porous models. A explaining factor is the tensile strength of the weldings. While interlocking should result only in an effective shear strength between the pebbles, by effectively welding to a continuous, intact material a tensile strength is introduced. This could be avoided by setting the SPH pseudo particles at the contact zones to totally damaged material as described above. Again, it is concluded that this approach has to be implemented in further studies using the rubble pile simulant model described in this work.

In the model presented here, space between pebbles is indeed void space. On real asteroids, it is expected that at least some of these voids are filled by highly porous, regolith like material, as the regolith produced on the surface will be transported into the interior during internal restructuring processes. This regolith is expected to have have negligible tensile strength of well below 1 Pa (Sánchez and Scheeres 2014), and while this may explain the apparent cohesive strength in superfast rotating asteroids as 1950 DA, it might not play a significant role in hyper-velocity impact events where the pressures of several Gigapascal occur.

5.3 Linking Surface Features on Šteins to its Internal Structure

5.3.1 Structures in the Surface Regolith Layer

The Regolith Layer on Šteins

Material at the surface of asteroids is ground down to ever smaller sizes (Housen et al. 1979) by the continuous flux of micro impacts, as well as by thermal fatigue: thermal stresses due to the multiple day-night cycles on asteroids effectively destroy surface rocks (Delbó et al. 2014). All airless bodies are found to be covered by a layer of granular material consisting of small, solid grains. On Itokawa, the smallest asteroid so far visited by spacecraft, shows a regolith of approximately up to centimetre sized pebbles (Miyamoto et al. 2007). The thickness of the regolith layer cannot be inferred from the images. The much larger asteroid Lutetia (dimensions $[121 \pm 1]\,\text{km} \times [101 \pm 1]\,\text{km} \times [75 \pm 13]\,\text{km}$, Sierks et al. 2011) shows a layer of regolith. Even though hard to determine, its thickness is estimated to be approximately 600 m by the depth-to-diameter ratio of a series of buried craters found in the Baetica region. The asteroid (951) Gaspra with dimensions of 18.2 km × 10.5 km × 8.9 km shows a regolith layer of a few tens of metres (Carr et al. 1994). The thickness is a function of the surface gravity of the body, as only material ejected at a speed below the escape velocity will fall back onto the surface. Therefore, both on Itokawa as well as on Šteins, only a thin layer of regolith is expected.

The tensile strength of regolith material is considered to be very low, in the range of below 1 Pa (Sánchez and Scheeres 2014). The shear strength of such a material can be described using a Mohr-Coulomb dry-friction law. For lunar soil, which is much more compressed due to the high surface gravity, shear strength at zero pressure is around a few Kilopascal (Carrier et al. 1991). Therefore the strength of regolith is much lower, and the outcome of impact events will not be effected by neglecting the thin regolith layer on small asteroids like Šteins.

Another effect of the regolith is that it covers surface features. On Šteins, even though the best resolution images have a scale of about $80\,\text{m}\,\text{pixel}^{-1}$, all features appear to be covered by a surface regolith, and the erosion of small craters can best be explained by regolith migration (Besse et al. 2012). In this work only the first stages of crater formation are accounted for. Therefore the settling of the ejecta blanket is not followed.

The Catena of Pit-Like Features as Tracer of Subsurface Fractures

The fractures discussed in Section 4.5.5 will change their appearance by the resettling of ejecta and the flow of surface regolith. If a cavity is opened under a layer of regolith, the regolith will flow down until either the cavity is filled, or the angle of the emerging pit wall becomes smaller than the dynamic angle of repose. Kleinhans et al. (2011) found a dynamic angle of repose of less than 20° at a tenth of the Earth's gravitational surface acceleration g for non-cohesive millimetre sized gravel, and a decrease of dynamic angle of repose with decreasing gravity.

The pit-like features seen on Šteins (see Section 4.2.5 and Figure 4.8) might provide a way to infer characteristics of Šteins regolith. Interpreting them as structures where a cavity opening below the regolith layer was filled by granular flow, the static angle of repose can be estimated from their shape. Because of the low resolution of the shape model, the exact shape of the pit-like features cannot be determined, and the values given in Table 4.2 originate from fitting an idealized semi-hemispherical representation of each feature (Besse et al. 2012). If a conical shape is assumed for the pit-like features, the slope of the walls can be estimated. The steepest slope is in feature Agatea with a slope angle of $\vartheta = 15°$ and the most shallow one in feature Peridota with $\vartheta = 5°$, with a median angle of $\vartheta = (7.5^{+3.8}_{-0.6})°$.

A N-body simulation of the flow of granular regolith into the cavity formed by the shape of the fracture found in Section 4.5.5 might therefore provide a way to both verify the volume of the fracture cavity under the catena and to infer the thickness of the regolith layer on Šteins. Due to the complexity of realistic simulations of granular flow, this is beyond the scope of this work.

5.3.2 Linear Surface Features on Other Minor Bodies

The catena of pits observed on Šteins, extending about all the asteroid but lacking a connecting groove, as well as the absence of other grooves or linear features, appear to be a unique feature in the resolved images of asteroids taken by spacecraft to date. In the following, linear structures on other minor bodies identified in images of other space missions are discussed.

Aligned structures have been identified on other bodies before. In most cases grooves are observed, long but narrow curvilinear features. Ida, shown in Figure 5.4, revealed a number of grooves up to 4 km in length and $\sim$ 100 m width (Sullivan et al. 1996) on a body with dimensions of 29.9 km × 12.7 km × 9.3 km.

Figure 5.4: Mosaic image of asteroid Ida from the Galileo flyby. *NASA/JPL, public domain*
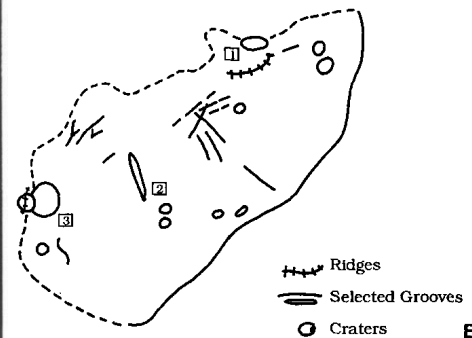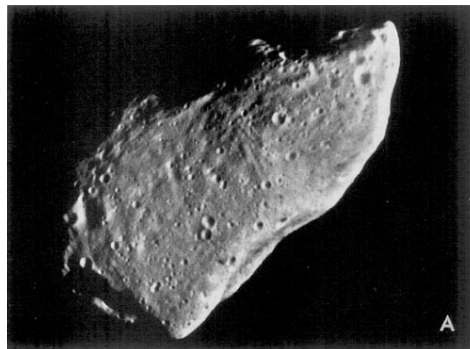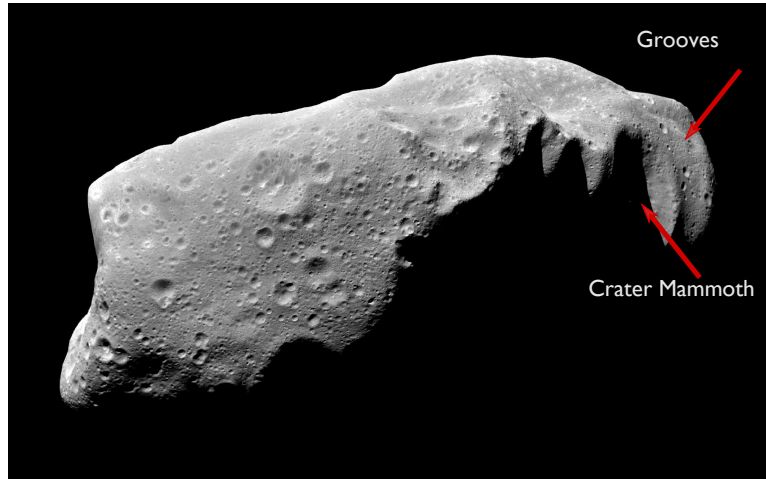
Figure 5.5: Grooves on Gaspra imaged by the Galileo spacecraft, and some large ones marked on a geomorphological map *Reprinted from Veverka et al. 1994*

Figure 5.6: Mosaic image of the Martian moon Phobos showing crater Stickney and grooves extending from the crater. *NASA/JPL, Dr. Edwin V. Bell, II (NSSDC/Raytheon ITSS), public domain*

Similar grooves have been found on the Martian moon Phobos (Thomas et al. 1979). Also, asteroid Gaspra in Figure 5.5 shows a large number of grooves, of length up to 2.5 km and again width of 100 m to 200 m (Veverka et al. 1994). In the case of Gaspra, there is no relation to impact structures found, but again they seem to be connected to the internal structure. On Phobos they extend up to 20 km, while the width is again about a hundred metres. As seen in Figure 5.6, they seem to be connected to the peculiar crater structure Stickney, as the widest and deepest groves occur just at the crater's rim, and groves are absent from the area opposite to the crater. Also, their geological formation time has been determined as shortly after the formation of Stickney (Thomas et al. 1979).

Catena, aligned crater-like structures, have been observed on asteroid Dactyl. The small satellite Dactyl of asteroid Ida, discovered at the flyby of the Galileo spacecraft in 1993, shows a series of four craters extending from the largest crater, Acmon, that seem to be aligned (Veverka et al. 1996). While more suspiciously in the Galileo image Figure 5.7a, the alignment is clearly seen in the morphological map Figure 5.7c. The principal dimensions of Dactyl are 1.6 km × 1.4 km × 1.2 km, and with a equivalent radius of $R_{equiv.} = 0.7$ km the body is about 3.7 times smaller than Šteins. The size of the aligned craters is, starting from Acmon: [280, 120, 90 and <90] km. Therefore the smaller craters have a size ratio to Acmon of 0.42, 0.32 and <0.32. This is significantly larger than the ratio observed on the catena of pits discussed on Šteins: there, the largest crater Agatea has a size ratio of 0.23 to crater Diamond (see Table 4.2).

The catena on Šteins extends at a visible length of approximately 4 km, about twice the diameter of Diamond (see Figure 5.7b). The catena on Dactyl extends approximately 440 m, about $^3/_2$ the diameter of Acmon. Also, the ratio of crater diameter to asteroid size on Dactyl is $^D/_{R_{equiv.}} = 0.4$, about half the value for Šteins ($^D/_{R_{equiv.}} = 0.79$). Acmon is therefore clearly a sub-critical crater, and it is unlikely that the interior of the satellite has been as consequently rearranged as in the impact on Šteins that formed crater Diamond.

The catena of four craters found on Dactyl might therefore be caused by an internal fracture forming or opening during the impact event that formed the main crater Acmon, but as this event has been clearly sub-critical, this conclusion is not compelling. Chapman et al. (1996) explained the catena as a byproduct of the extraordinary formation history assumed for the satellite Dactyl. As they argue, it is highly unlikely that Dactyl is a body that is just by chance bound to Ida. More likely is a common origin as remnants of the larger disrupted body,

the parent body of the Koronis family. The reservoir of slow moving (relative to Ida) fragments that Dactyl is from, is then thought to be the source of closely arranged bodies of similar size, that impacted Dactyl and formed the catena as well as the impact craters close by.

Also, the crater chain could originate from boulders ejected in a cratering event on the much larger Ida. The surface of Ida shows several large craters, and the orbital distance to Dactyl is easily covered by ejected material.

Because only about a quarter of Dactyl's surface has been observed, it is plausible to consider a large crater on the unimaged side, that formed the observed catena of craters in a process similar to the fracturing on Šteins. The maximum topographic variation from the best fit ellipsoid is 0.13 km (Veverka et al. 1996), or 21 % of the shortest dimension. Almost ellipsoidal in shape, Dactyl could be interpreted as rotational relaxed, which would be congruent with an rubble pile interior and advocate the applicability of the model presented here.

5.3.3 Šteins' Constituent Fragment Size Distribution

As discussed in Section 4.5.4, no link of the hill-like feature opposite to the crater Diamond on asteroid Šteins and the restructuring of the large-scale pebble structure in the interior during the crater forming event can be found. Therefore, the hill feature is interpreted as a remnant of the formation and non-impact evolution of the asteroid. If it is assumed that the hill is formed by a single consolidated pebble that is one of the constituent fragments from the formation of the asteroid, it can be used to see which large-scale pebble size distribution is in agreement to the observed appearance of Šteins.

As seen in Section 4.5.4, the estimated volume equivalent radius is $R_{\text{equiv.}} \approx$ 500 m. As there are no larger hill-like features seen on the asteroid, this is likely to be the largest coherent fragment on the surface of the body. The radial distribution of pebble radii in the interior of Šteins depends on the original configuration from the formation of the body and the evolution. The original distribution resulting from the gravitational aggregation of pebbles can be seen in Figure 5.2 and shows that for reasonable initial velocity dispersion, a slight enhancement of large pebbles at the surface occurs.

These Šteins models can be compared with the resulting size distribution of the pebbles in the asteroid simulant as discussed in Figure 3.3 (see Chapter 3 on Page 77). There, large pebbles inside or grazing the surface of the excised
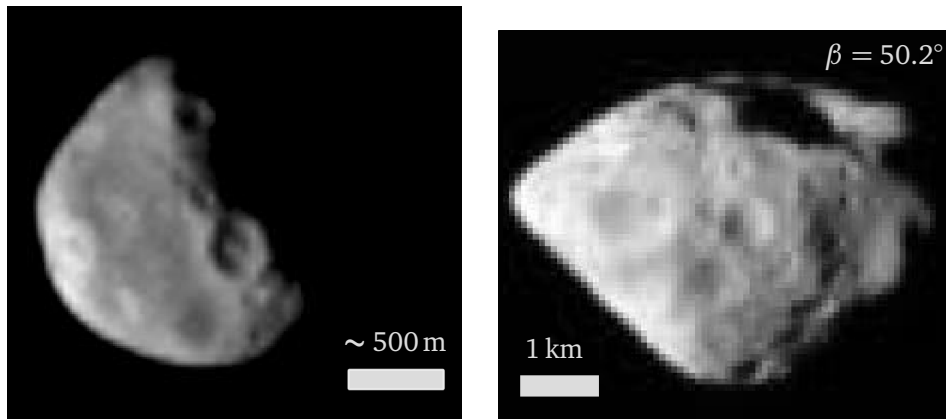
(a) Dactyl, satellite of Ida imaged by the Galileo spacecraft on August 28, 1993. Image resolution is about 39 m pixel^{-1}. *NASA/JPL, public domain*

(b) WAC image of Šteins showing the catena of pits. Image resolution is about ∼ 80 m pixel^{-1}. Same image as Figure 4.3b repeated here for comparison.
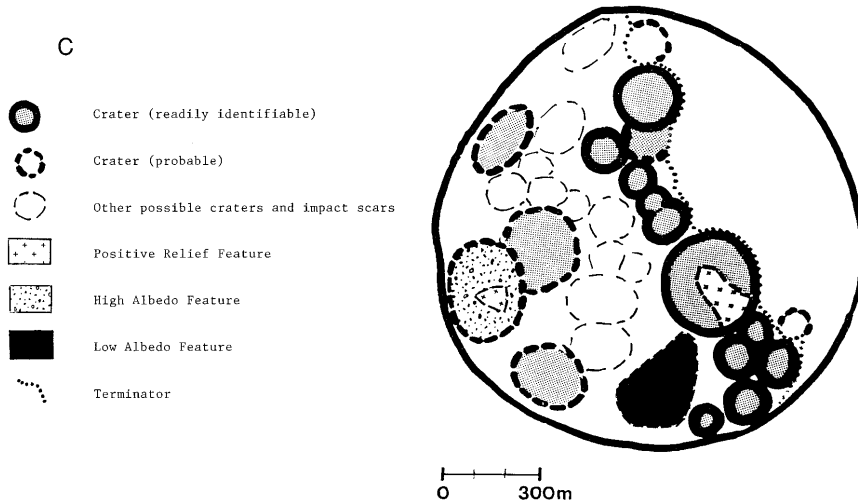
(c) Morphological map of the surface of Dactyl (1.6 km × 1.4 km × 1.2 km), showing the alignment of craters extending from the largest crater Acmon ($D \approx 280$ m). *Reprinted from Veverka et al. 1996*

Figure 5.7: Dactyl, satellite of Ida, showing a series of aligned crater features. Panel (b) shows Šteins for comparison.

asteroid shape are overrepresented, but in the size distribution considering only the excised part this vanishes. This is only possible if a number of the large pebbles are only grazing the surface, and therefore cut away, and in accordance to the radial size distribution discussed here.

Additionally, grain sorting by granular convection (Miyamoto et al. 2007; Behringer et al. 1999) will lift up larger pebbles more easily than smaller ones. It is therefore reasonable to assume that the fragment forming the hill is one of the largest coherent fragments on Šteins, and the upper limit for the power law size distribution of $R_{max} = 500\,m$ was an accurate choice.

The simulations presented here assume a high void fraction of 40 % for asteroid Šteins. As there is no accurate measurement of mass and therefore the bulk density, the only criteria to derive a macroporosity is the ratio of the largest crater diameter to the size of the asteroid (Burchell and Leliwa-Kopystynski 2010).

From the diameter of the largest crater on nine rocky bodies as small as Dactyl ($R \approx 0.7\,km$), six of them in the size range of $R \approx 0.7\,km$ to $26.5\,km$, Leliwa-Kopystynski et al. (2008) found an empirical limit for a sub-critical crater size D_{crit} as a function of the asteroids size, and Burchell and Leliwa-Kopystynski (2010) extended the applicable size range to $R \approx 0.7\,km$ to $120\,km$. Using these scaling laws results in sub-critical crater size limits on Šteins with $R_{equiv.} = 2.63\,km$ of $D_{crit}^{LK} = 3.4\,km$ (Leliwa-Kopystynski et al. 2008, Equation 2) and $D_{crit}^{B} = 2.5\,km$ (Burchell and Leliwa-Kopystynski 2010), significantly larger than crater Diamond. Therefore, crater Diamond is not necessarily at the critical limit, as an asteroid of the size of Šteins could even accommodate a larger crater. A macroporosity of 40 % is considered to be well compatible with the characteristics of Šteins. As long as the mass of Šteins is not determined directly, the question of the exact macroporosity cannot be answered unambiguously.

5.4 Šteins as a YORP Evolved Asteroid

Since the flyby of the Rosetta spacecraft at Šteins, it has been suggested that the asteroid was shaped by spin-up due to YORP torques (Keller et al. 2010). The pronounced bulge at the equator does indeed look similar to other asteroids which are effected by YORP, as for example the primary of the binary asteroid pair 1999 KW4 shown in Figure 1.12, where McMahon and Scheeres (2010) could show that BYORP evolution explained the current state well. Numerical

simulations have shown that such a top-like shape can indeed originate from spin-up of rubble pile agglomerates with only moderate cohesion (Figure 1.11a, Walsh et al. 2008) although Statler (2015) cautions to over-interpret the connection of top-shape and YORP spin-up because the mechanism proposed does not take into account self-limitation of the YORP effect (Cotto-Figueroa et al. 2015).

An evolution scenario for asteroid Šteins has been proposed by Jorda et al. (2012). Starting as a slightly elongated prolate body, the YORP effect increased the spin rate to a period well below 4 hours, where the equatorial bulge formed due to a surface gravity dominated by centrifugal acceleration. For unclear reasons, the spin rate did not increase further to produce an entirely complete circular ridge, and due to changes in shape and obliquity the sign of the C_{YORP} amplitude changed, leading to the large period of ~ 6 hours.

Using the shape model of Šteins obtained during the Rosetta mission (Jorda et al. 2012) with the advanced thermophysical model of Rozitis and Green (2013), the acceleration due to YORP on Šteins current shape was estimated as $d\omega/dt \approx -1.58 \times 10^{-10}$ rad d^{-2} (Rozitis, private communication). This is equivalent to a timescale of 439 Ma needed to spin up starting at a period of 3 hours to todays 6.45 hours. This is in the range of the age of Šteins surface, that Marchi et al. (2010) estimate to be in between 154 Ma to 1600 Ma, but larger than the time from the event that erased small craters 32 to 273 Ma ago (see Section 4.2.2).

The pre-impact shape discussed in Section 4.5.1 shows an accelerations due to YORP of $d\omega/dt = -1.18 \times 10^{10}$ rad d^{-2} (Rozitis, private communication). Even though the pre-impact shape is not well constrained, and only one of multiple plausible solutions, this might allow the conclusion that the formation of crater Diamond lead to an enhanced decelerations of Šteins spin, but most likely was not responsible for the change in sign of the YORP acceleration, turning the spin-up period needed to explain the equatorial ridge to the spin-down episode explaining the observed long period. Taking into account that the shape of Šteins will have changed even when the spin is decelerating due to seismic shaking by small-scale impacts, the scenario proposed by Jorda et al. (2012) is still valid and fits into the observed timescales.

5.5   Applicability of the Rubble Pile Interior Model

The model of rubble pile asteroid interiors used in this work is targeted to follow internal restructuring processes of the large scale pebble structure during impact

events. As shown in Chapter 3, the bulk strength as measured by the disruption threshold Q_D^* is within the range of values comparable to other studies, so it can be said to reproduce the bulk behaviour of rubble pile asteroids during disruptive collisions, implicating applicability for all impact problems involving rubble pile asteroids. For this reason, size limits coincide with the size limits of rubble pile asteroids, and while the existence of superfast rotating bodies with radii $R < 130\,\text{m}$ proves the existence of monolithic bodies below that limit, it does not disprove the occurrence of rubble pile asteroids below that limit. In fact, asteroid Itokawa shows only six boulders larger than 20 m on the surface, the largest one with dimensions of $50\,\text{m} \times 30\,\text{m} \times 20\,\text{m}$ (Michikami et al. 2008). Even of the very small asteroids, most might be rubble piles, and a lower size limit cannot reasonable be drawn.

An upper size limit of rubble pile asteroids limits the models applicable range. Large, differentiated asteroids might have a porous surface layer, but gravel and pebbles start to grind at pressure of $\sim 10\,\text{MPa}$ which is reached a few kilometres below the surface for large asteroids (Britt et al. 2002). The observed bulk density of asteroids is proportional to the radius (Carry 2012), and no bodies with significant macroporosity are observed larger than $R = 155\,\text{km}$. The largest asteroid that could be accounted as a rubble pile is the *X* type asteroid (87) Sylvia with dimensions of $384\,\text{km} \times 264\,\text{km} \times 232\,\text{km}$ and a macroporosity in the range of 25 % to 60 % (Marchis et al. 2005). For this asteroid, the mass has been well constrained due to the two orbiting satellites, but the uncertainty in density because of the lack of a clear link to meteorites results in the not well defined macroporosity. While there is an upper limit for rubble pile asteroids as with larger size the lithostatic pressure will eventually lead to differentiation, it is not valid to conclude from a size below this limit to a rubble pile interior. The high density of asteroid Lutetia has led to the interpretation as a partially differentiated, most likely primordial body (Weiss et al. 2012), and is clearly not a rubble pile. Also many asteroids showing only a few percent macroporosity (Carry 2012) cannot be regarded as rubble pile, and therefore the model presented here is not applicable.

As the implementation using the SPH solver in LS-DYNA takes into account all gravitational interactions, there is in principle no limit to the size of the target. However, how the interior of such a large rubble pile asteroid as Sylvia is structured and how the lithostatic pressure effects the size distribution of the constituent fragment is not yet known and remains to be studied.

5.6   Future Applications of the Model

As rubble pile asteroids are numerous in the inner solar system, the list of interesting features to study is extensive. In the context of this work, there are a few open questions yet to be analysed. In Chapter 3 a spherical asteroid that is equivalent in volume to asteroid Itokawa is used to determine the sensitivity of the modeling process on the parameters of the gravitational aggregate. The dataset is therefore ideally suited for comparison with simulations on the spacecraft derived shape model of Itokawa (Demura et al. 2006; Gaskell et al. 2008). The rubble pile asteroid Itokawa itself poses still some intriguing questions. Lowry et al. (2014) were able to measure YORP induced spin-up of the body, and determined an offset of $\sim 21\,\mathrm{m}$ of the centre of mass along the body's long-axis. This was interpreted as a bi-lobed structure, with a small, but dense head on top of a low-density body. A plausible scenario for this is a primordial Itokawa forming a binary due to YORP spin-up, that re-collided with the body at a later stage. Simulating this collision could bring insights into if such a low-speed, massive collision of two similar sized bodies results in internal restructuring.

A similar process has been proposed as the origin of the conspicuously bi-lobed structure of the comet 67P/Churyumov-Gerasimenko (67P/CG) (Jutzi and Asphaug 2015). 67P/CG, the main target of the Rosetta mission as seen in Figure 5.8 shows indeed a clear bi-lobed structure (Sierks et al. 2015), although if originating from two large scale bodies colliding or a byproduct of cometary activity is not yet resolved. Formation models of comets do also indicate that they might have a rubble pile structure, and the low bulk density on 67P/CG of $[470 \pm 45]\,\mathrm{kg\,m^{-3}}$ (Sierks et al. 2015) does indicate a large porosity as known for most comets. Furthermore, the comet shows a series of pits with enhanced activity. They are attributed to the collapse of sinkholes, large underground cavities (Vincent et al. 2015). How these sinkholes form, is not yet clear. The rubble pile simulant model can help to learn if large void cavity can be original features in the interior of comets, and if they are sustained or formed during low-speed collision events of partners of similar size.

The rubble pile asteroids Šteins is, as discussed in Chapter 4 and Section 5.4 of this Chapter, most likely a body evolved by the YORP effect. While the pronounced YORPoid shape indicates that Šteins must have for some time been fast spinning, with a period of under 3 hours, and therefore been spun up by an accelerating YORP effect, todays long period indicates that the sign of the YORP
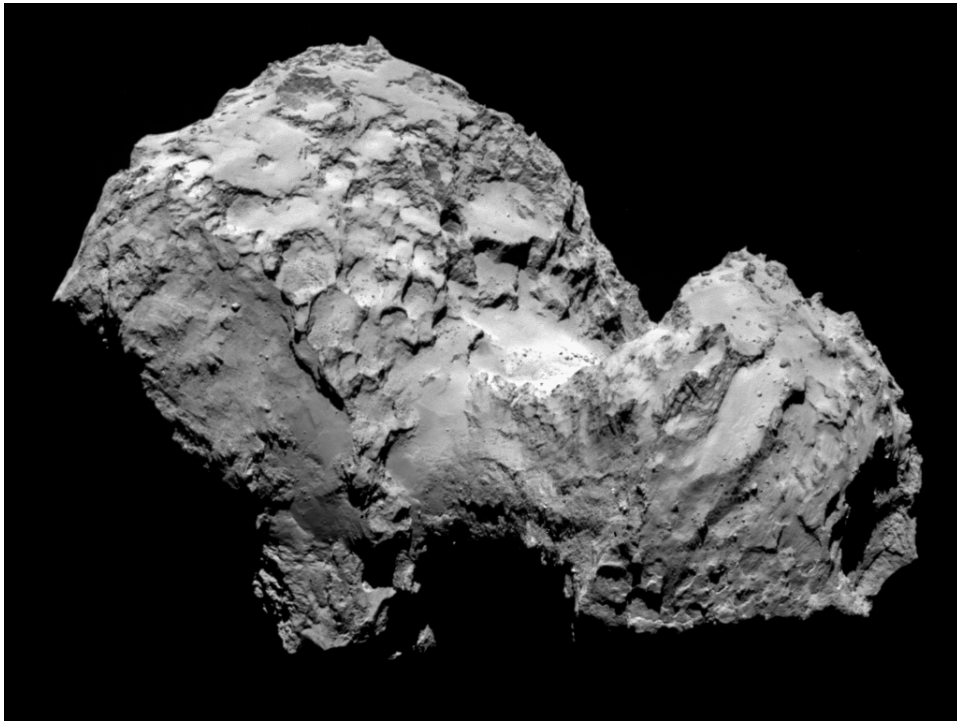
Figure 5.8: Comet 67P/Churyumov-Gerasimenko (67P/CG) imaged by the OSIRIS camera system on board of the Rosetta spacecraft. The image was taken just after arrival at the comet on August 3rd 2014. *Source: ESA/Rosetta/MPS for OSIRIS Team MPS/UPD/LAM/IAA/SSO/INTA/UPM/DASP/IDA*

torque must have changed at some point. While initial calculations have shown a decelerating effect of the shape changes due to the Diamond cratering event, a change in sign could not be observed (again, see Section 5.4). A systematic study to find a plausible pre-impact shape that exhibits the largest change in YORP torque, and reproduces the shape of crater Diamond and the catena of pits, is planned. This would not only help to further explore the evolutionary history of Šteins, but also deepen the understanding of the interplay of YORP and collisional evolution of rubble pile asteroids.

The apparent link of the catena of pits to the cratering event has helped to shed some light on the interior of Šteins, that will not be observed in-situ in the foreseeable future. Although not equipped with in-situ radar or seismic experiments, the OSIRIS-REx mission is promising to provide multiple applications of the model presented here. The target of OSIRIS-REx, Bennu, is a small NEO of $R_{\text{equiv.}} \approx 246\,\text{m}$ that shows the typical YORPoid shape of a YORP evolved rubble pile asteroid. A detailed shape model provided by the OSIRIS-REx Laser Altimeter will be used to search for features that are linked to impact events, as the catena of pits on Šteins to crater Diamond. Modelling of these features again will help to infer the interior of Bennu, and comparison with the gravitational mapping provided by OSIRIS-REx will be the perfect chance to learn from using the rubble pile simulant model presented here as a tool to study the interior of rubble pile asteroids.

Bibliography

Abe, S., T. Mukai, N. Hirata, O. S. Barnouin-Jha, A. F. Cheng, H. Demura, R. W. Gaskell, T. Hashimoto, K. Hiraoka, T. Honda, T. Kubota, M. Matsuoka, T. Mizuno, R. Nakamura, D. J. Scheeres and M. Yoshikawa (2006). 'Mass and Local Topography Measurements of Itokawa by Hayabusa'. *Science* 312.5778, 1344–1347.

Accomazzo, A., K. R. Wirth, S. Lodiot, M. Küppers and G. Schwehm (2010). 'The flyby of Rosetta at asteroid Šteins - mission and science operations'. *Planetary and Space Science* 58.9, 1058–1065.

Ahrens, T. J. J. and J. D. O'Keefe (1977). 'Equations of state and impact-induced shock-wave attenuation on the moon'. *Impact and Explosion Cratering: Planetary and Terrestrial Implications*, 639–656.

Akarca, S. S., X. Song, W. J. Altenhof and A. T. Alpas (2008). 'Deformation behaviour of aluminium during machining: modelling by Eulerian and smoothed-particle hydrodynamics methods'. *Proceedings of the Institution of Mechanical Engineers, Part L: Journal of Materials: Design and Applications* 222.3, 209–221.

Ansys Inc (2012). 'AUTODYN User manual'. 14.5. Canonsburg, Pennsylvania, USA: Ansys Inc.

Armitage, P. J. (2010). 'Astrophysics of Planet Formation'. Cambridge: Cambridge University Press. ISBN: 978-0-521-88745-8.

Asphaug, E. and W. W. Benz (1994). 'Density of Comet Shoemaker-Levy-9 Deduced by Modeling Breakup of the Parent Rubble-Pile'. *Nature* 370.6485, 120–124.

Asphaug, E. (1996). 'Size, Density, and Structure of Comet Shoemaker–Levy 9 Inferred from the Physics of Tidal Breakup'. *Icarus* 121.2, 225–248.

Asphaug, E., E. V. Ryan and M. T. Zuber (2002). 'Asteroid Interiors'. In: *Asteroids III*. Ed. by W. F. Bottke, A. Cellino, P. Paolicchi and R. P. Binzel. University of Arizona Press, pp. 463–484. ISBN: 978-0-8165-2281-1.

August, T. M. and P. A. Wiegert (2013). 'Color Dependence in the Size Distribution of Main Belt Asteroids Revisited'. *The Astronomical Journal* 145.6, 152.

Barnes, J. and P. Hut (1986). 'A hierarchical O(N log N) force-calculation algorithm'. *Nature* 324.6096, 446–449.

Barucci, M. A., M. Fulchignoni, S. Fornasier, E. Dotto, P. Vernazza, M. Birlan, R. P. Binzel, J. Carvano, F. Merlin, C. Barbieri and I. Belskaya (2005). 'Asteroid target selection for the new Rosetta mission baseline. 21 Lutetia and 2867 Steins'. *Astronomy and Astrophysics* 430, 313–317.

Barucci, M. A., S. Fornasier, E. Dotto, P. L. Lamy, L. Jorda, O. Groussin, J. R. Brucato, J. Carvano, A. Alvarez-Candal, D. P. Cruikshank and M. Fulchignoni (2008). 'Asteroids 2867 Steins and 21 Lutetia: surface composition from far infrared observations with the Spitzer space telescope'. *Astronomy and Astrophysics* 477.2, 665–670.

Behringer, R. P., H. Jaeger and S. Nagel (1999). 'Introduction to the focus issue on granular materials'. *Chaos: An Interdisciplinary Journal of Nonlinear Science* 9.3, 509.

Beitz, E., C. Güttler, R. Weidling and J. Blum (2012). 'Free collisions in a microgravity many-particle experiment — II: The collision dynamics of dust-coated chondrules'. *Icarus* 218.1, 701–706.

Benavidez, P. G., D. D. Durda, B. L. Enke, W. F. Bottke, D. Nesvorný, D. C. Richardson, E. Asphaug and W. J. Merline (2012). 'A comparison between rubble-pile and monolithic targets in impact simulations: Application to asteroid satellites and family size distributions'. *Icarus* 219.1, 57–76.

Benz, W. W. and E. Asphaug (1995). 'Simulations of brittle solids using smooth particle hydrodynamics'. *Computer Physics Communications* 87.1, 253–265.

Benz, W. W. and E. Asphaug (1999). 'Catastrophic Disruptions Revisited'. *Icarus* 142, 5–20.

Besse, S., P. L. Lamy, L. Jorda, S. Marchi and C. Barbieri (2012). 'Identification and physical properties of craters on Asteroid (2867) Steins'. *Icarus* 221.2, 1119–1129.

Beuermann, K., S. Dreizler, F. V. Hessman and J. F. Deller (2012). 'The quest for companions to post-common envelope binaries. III. A reexamination of HW Virginis'. *Astronomy and Astrophysics* 543, 138.

Beuther, H., R. S. Klessen, C. P. Dullemond and T. Henning, eds. (2014). 'Protostars and Planets VI'. University of Arizona Press. ISBN: 978-0-8165-3124-0.

Binzel, R. P., P. Farinella, V. Zappalà and A. Cellino (1989). 'Asteroid rotation rates - Distributions and statistics'. In: *Asteroids II; Proceedings of the Conference*. MIT, Cambridge, MA, pp. 416–441.

Birnbaum, N. K., M. Cowler and C. J. Hayhurst (1996). 'Numerical Simulation of Impact Using AUTODYN'. URL: http://hsrlab.gatech.edu/AUTODYN/papers/paper70.pdf.

Bjork, R. L. (1961). 'Analysis of the Formation of Meteor Crater, Arizona: A Preliminary Report'. *Journal of Geophysical Research* 66, 3379–3387.

Bockelée-Morvan, D., J. Crovisier, M. J. Mumma and H. A. Weaver (2004). 'The composition of cometary volatiles'. In: *Comets II*. The University of Arizona Press in collaboration with the Lunar and Planetary Institute, pp. 391–423. ISBN: 0-8165-2450-5.

Boss, A. P. (1998). 'Evolution of the Solar Nebula. IV. Giant Gaseous Protoplanet Formation'. *The Astrophysical Journal* 503.2, 923–937.

Bottke, W. F., A. Cellino, P. Paolicchi and R. P. Binzel, eds. (2002). 'Asteroids III'. University of Arizona Press. ISBN: 978-0-8165-2281-1.

Bottke, W. F., D. D. Durda, D. Nesvorný, R. Jedicke, A. Morbidelli, D. Vokrouhlicky and H. F. Levison (2005a). 'Linking the collisional history of the main asteroid belt to its dynamical excitation and depletion'. *Icarus* 179.1, 63–94.

Bottke, W. F., D. D. Durda, D. Nesvorný, R. Jedicke, A. Morbidelli, D. Vokrouhlicky and H. F. Levison (2005b). 'The fossilized size distribution of the main asteroid belt'. *Icarus* 175.1, 111–140.

Bottke, W. F., D. Vokrouhlicky, D. P. Rubincam and D. Nesvorný (2006). 'The Yarkovsky and YORP effects: Implications for asteroid dynamics'. *Annual Review of Earth and Planetary Sciences* 34, 157–191.

Bowell, E., C. R. Chapman, J. C. Gradie, D. Morrison and B. Zellner (1978). 'Taxonomy of asteroids'. *Icarus* 35, 313–335.

Breiter, S. and D. Vokrouhlicky (2011). 'Yarkovsky-O'Keefe-Radzievskii-Paddack effect with anisotropic radiation'. *Monthly Notices of the Royal Astronomical Society* 410.4, 2807–2816.

Britt, D. T., D. K. Yeomans, K. R. Housen and G. J. Consolmagno (2002). 'Asteroid Density, Porosity, and Structure'. In: *Asteroids III*. Ed. by W. F. Bottke, A. Cellino, P. Paolicchi and R. P. Binzel. University of Arizona Press, pp. 485–500. ISBN: 978-0-8165-2281-1.

Buczkowski, D. L., D. Y. Wyrick, K. A. Iyer, E. G. Kahn, J. E. C. Scully, A. Nathues, R. W. Gaskell, T. Roatsch, F. Preusker, P. M. Schenk, L. Le Corre, V. Reddy, R. A. Yingst, S. Mest, D. A. Williams, W. B. Garry, O. S. Barnouin, R. Jaumann, C. A. Raymond and C. T. Russell (2012). 'Large-scale troughs on Vesta: A signature of planetary tectonics'. *Geophysical Research Letters* 39.18, 1–6.

Burbine, T. H., A. Meibom and R. P. Binzel (1996). 'Mantle material in the main belt: Battered to bits?' *Meteoritics & Planetary Science* 31.5, 607–620.

Burbine, T. H. (2002). 'Small Main-Belt Asteroid Spectroscopic Survey in the Near-Infrared'. *Icarus* 159.2, 468–499.

Burchell, M. J. and J. Leliwa-Kopystynski (2010). 'The large crater on the small Asteroid (2867) Steins'. *Icarus* 210.2, 707–712.

Bus, S. J. (2002a). 'Phase II of the Small Main-Belt Asteroid Spectroscopic Survey A Feature-Based Taxonomy'. *Icarus* 158.1, 146–177.

Bus, S. J. (2002b). 'Phase II of the Small Main-Belt Asteroid Spectroscopic Survey The Observations'. *Icarus* 158.1, 106–145.

Capaccioni, F., P. Cerroni, M. Coradini, P. Farinella, E. Flamini, G. Martelli, P. Paolicchi, P. N. Smith and V. Zappalà (1984). 'Shapes of asteroids compared with fragments from hypervelocity impact experiments'. *Nature* 308, 832–834.

Capuzzo-Dolcetta, R., M. Spera and D. Punzo (2013). 'A fully parallel, high precision, N-body code running on hybrid computing platforms'. *Journal of Computational Physics* 236.C, 580–593.

Carpenter, J. M., E. E. Mamajek, L. A. Hillenbrand and M. R. Meyer (2006). 'Evidence for Mass-dependent Circumstellar Disk Evolution in the 5 Myr Old Upper Scorpius OB Association'. *The Astrophysical Journal* 651.1, L49–L52.

Carr, M. H., R. L. Kirk, A. McEwen, J. Veverka, P. Thomas, J. W. Head and S. Murchie (1994). 'The geology of Gaspra'. *Icarus* 107, 61.

Carrier III, W. D., G. R. Olhoeft and W. Mendell (1991). 'Physical Properties of the Lunar Surface'. In: *Lunar sourcebook - A user's guide to the moon*. Ed. by G. H. Heiken, D. T. Vaniman and B. M. French. Los Alamos National Laboratory, NM, pp. 475–594.

Carroll, M. M. (1972). 'Static and Dynamic Pore-Collapse Relations for Ductile Porous Materials'. *Journal of Applied Physics* 43.4, 1626.

Carroll, B. W. and D. A. Ostlie (2007). 'An introduction to modern astrophysics'. English. 2. ed., international ed. San Franciso, Calif. ; Munich [u.a.]: Pearson, Addison Wesley. ISBN: 0-321-44284-9 ; 978-0-321-44284-0.

Carry, B. (2012). 'Density of asteroids'. *Planetary and Space Science* 73.1, 98–118.

Century Dynamics Ltd (2000). 'Theory Manual, Century Dynamics Ltd'. Dynamics House, Hurst Road, Horsham, West Sussex RH12. 2DT, England: Theory Manual, Century Dynamics Ltd.

Chambers, J. E. (1999). 'A hybrid symplectic integrator that permits close encounters between massive bodies'. *Monthly Notices of the Royal Astronomical Society* 304.4, 793–799.

Chang, C.-K., A. Waszczak, H.-W. Lin, W.-H. Ip, T. A. Prince, S. R. Kulkarni, R. Laher and J. Surace (2014). 'A New Large Super-fast Rotator: (335433) 2005 UW163'. *The Astrophysical Journal* 791.2, L35.

Chapman, C. R., D. Morrison and B. Zellner (1975). 'Surface properties of asteroids - A synthesis of polarimetry, radiometry, and spectrophotometry'. *Icarus* 25, 104–130.

Chapman, C. R., E. V. Ryan, W. J. Merline, G. Neukum, R. Wagner, P. C. Thomas, J. Veverka and R. J. Sullivan (1996). 'Cratering on Ida'. *Icarus* 120.1, 77–86.

Chapman, C. R. (1996). 'S-Type Asteroids, Ordinary Chondrites, and Space Weathering: The Evidence from Galileo's Fly-bys of Gaspra and Ida'. *Meteoritics & Planetary Science* 31, 699–725.

Chesley, S. R., S. J. Ostro, D. Vokrouhlicky, D. Čapek, J. D. Giorgini, M. C. Nolan, J.-L. Margot, A. A. Hine, L. A. M. Benner and A. B. Chamberlin (2003). 'Direct Detection of the Yarkovsky Effect by Radar Ranging to Asteroid 6489 Golevka'. *Science* 302.5, 1739–1742.

Collins, G. S. (2002). 'Hydrocode Simulations of Chicxulub Crater Collapse and Peak-Ring Formation'. *Icarus* 157.1, 24–33.

Collins, G. S., H. J. Melosh and B. A. Ivanov (2004). 'Modeling damage and deformation in impact simulations'. *Meteoritics & Planetary Science* 39, 217–231.

Collins, G. S., H. J. Melosh and K. Wünnemann (2011). 'Improvements to the ϵ-α; porous compaction model for simulating impacts into high-porosity solar system objects'. *International Journal of Impact Engineering* 38.6, 434–439.

Collins, G. S., K. Wünnemann, N. A. Artemieva and E. Pierazzo (2012). 'Numerical modelling of impact processes'. In: *Impact Cratering*. John Wiley & Sons, Ltd, pp. 254–270. ISBN: 9781118447307.

Collins, G. S. and H. J. Melosh (2014). 'Improvements to ANEOS for Multiple Phase Transitions'. *45th Lunar and Planetary Science Conference* 45, 2664.

Collins, G. S. (2014). 'Numerical simulations of impact crater formation with dilatancy'. *Journal of Geophysical Research (Planets)* 119.12, 2600–2619.

Cotto-Figueroa, D., T. S. Statler, D. C. Richardson and P. Tanga (2015). 'Coupled Spin and Shape Evolution of Small Rubble-pile Asteroids: Self-limitation of the YORP Effect'. *Astrophysical Journal* 803.1, 1–18.

Crater Analysis Techniques Working Group, R. E. Arvidson, J. Boyce, C. Chapman, M. Cintala, M. Fulchignoni, H. Moore, G. Neukum, P. Schultz, L. Soderblom, R. Strom, A. Woronow and R. Young (1979). 'Standard techniques for presentation and analysis of crater size-frequency data'. *Icarus* 37, 467–474.

Ćuk, M. and J. A. Burns (2005). 'Effects of thermal radiation on the dynamics of binary NEAs'. *Icarus* 176.2, 418–431.

Davis, D. R., D. D. Durda, F. Marzari, A. Campo Bagatin and R. Gil-Hutton (2002). 'Collisional Evolution of Small-Body Populations'. In: *Asteroids III*. Ed. by W. F. Bottke, A. Cellino, P. Paolicchi and R. P. Binzel. University of Arizona Press, pp. 545–558. ISBN: 978-0-8165-2281-1.

Delbó, M., G. Libourel, J. Wilkerson, N. Murdoch, P. P. Michel, K. T. Ramesh, C. Ganino, C. Verati and S. Marchi (2014). 'Thermal fatigue as the origin of regolith on small asteroids'. *Nature* 508.7495, 233–236.

Deller, J. F. (2012). 'Parameters, Stability, and Dynamics of Circumbinary Planetary Systems'. M. Sc. thesis. Göttingen: Institut für Astrophysik Göttingen.

Deller, J. F., S. C. Lowry, C. Snodgrass, M. C. Price and H. Sierks (2015). 'A new approach to modelling impacts on rubble pile asteroid simulants'. *Monthly Notices of the Royal Astronomical Society* 455.4, 3752–3762.

DeMeo, F. E., R. P. Binzel, S. M. Slivan and S. J. Bus (2009). 'An extension of the Bus asteroid taxonomy into the near-infrared'. *Icarus* 202.1, 160–180.

Demura, H., S. Kobayashi, E. Nemoto, N. Matsumoto, M. Furuya, A. Yukishita, N. Muranaka, H. Morita, K. Shirakawa, M. Maruya, H. Ohyama, M. Uo, T. Kubota, T. Hashimoto, J. J. Kawaguchi, A. Fujiwara, J. Saito, S. Sasaki, H. Miyamoto and N. Hirata (2006). 'Pole and Global Shape of 25143 Itokawa'. *Science* 312.5, 1347–1349.

Dikaiakos, M. D. and J. Stadel (1997). 'A performance study of cosmological simulations on message-passing and shared-memory multiprocessors'. In: *10th ACM International Conference on Supercomputing*. New York, New York, USA: ACM Press, pp. 94–101. ISBN: 0897918037.

Dohnanyi, J. S. S. (1969). 'Collisional Model of Asteroids and Their Debris'. *Journal of Geophysical Research* 74.10, 2531–&.

Dohnanyi, J. S. S. (1971). 'Fragmentation and Distribution of Asteroids'. *Physical Studies of Minor Planets* 267, 263.

Donev, A., I. Cisse, D. Sachs, E. A. Variano, F. H. Stillinger, R. Connelly, S. Torquato and P. M. Chaikin (2004). 'Improving the Density of Jammed Disordered Packings Using Ellipsoids'. *Science* 303.5, 990–993.

Duncan, M. J., H. F. Levison and M. H. Lee (1998). 'A Multiple Time Step Symplectic Algorithm for Integrating Close Encounters'. *The Astronomical Journal* 116.4, 2067–2077.

Durda, D. D., W. F. Bottke, D. Nesvorný, B. L. Enke, W. J. Merline, E. Asphaug and D. C. Richardson (2007). 'Size–frequency distributions of fragments from SPH/N-body simulations of asteroid impacts: Comparison with observed asteroid families'. *Icarus* 186.2, 498–516.

Earth Impact Database (2011). Ed. by PASSC. URL: http://www.passc.net/EarthImpactDatabase/brent.html.
build: 2011; visited on visited on 06/13/2015.

Elbeshausen, D., K. Wünnemann and G. S. Collins (2009). 'Scaling of oblique impacts in frictional targets: Implications for crater size and formation mechanisms'. *Icarus* 204.2, 716–731.

Faraud, M., R. Destefanis, D. Palmieri and M. Marchetti (1999). 'SPH simulations of debris impacts using two different computer codes'. *International Journal of Impact Engineering* 23.1, 249–260.

Farinella, P., P. Paolicchi and V. Zappalà (1982). 'The asteroids as outcomes of catastrophic collisions'. *Icarus* 52, 409–433.

Fornasier, S., I. Belskaya, M. Fulchignoni, M. A. Barucci and C. Barbieri (2006). 'First albedo determination of 2867 Steins, target of the Rosetta mission'. *Astronomy and Astrophysics* 449.2, L9–L12.

Gaffey, M. J., J. F. Bell and D. P. Cruikshank (1989). 'Reflectance spectroscopy and asteroid surface mineralogy'. In: *Asteroids II; Proceedings of the Conference*. Rensselaer Polytechnic Institute, Troy, NY Rensselaer Polytechnic Institute, Troy, NY, pp. 98–127.

Gaffey, M. J., K. L. Reed and M. S. Kelley (1992). 'Relationship of E-type Apollo asteroid 3103 (1982 BB) to the enstatite achondrite meteorites and the Hungaria asteroids'. *Icarus* 100, 95–109.

Garvin, J. B. and R. A. F. Grieve (1982). 'An Analytical Model for Simple Terrestrial Craters: Brent and Meteor'. In: 13th *Lunar and Planetary Science Conference*, pp. 251–252.

Gaskell R., S., M. J. Ishiguro, T. Kubota, T. Hashimoto, N. Hirata, S. Abe, O. Barnouin-Jha and D. Scheeres (2008). 'Gaskell Itokawa Shape Model V1.0'. Visited on 2014.

Gault, D. E., W. L. Quaide and V. R. Oberbeck (1974). 'Impact cratering mechanics and structures'. In: *A Primer in Lunar Geology*. Ed. by R. Greeley and P. H. Schultz, pp. 177–189.

Gault, D. E. and J. A. Wedekind (1978). 'Experimental studies of oblique impact'. In: *9th Lunar and Planetary Science Conference*. California Institute of Technology, Pasadena; Murphys Center of Planetology, Murphys, Calif., pp. 3843–3875.

Geretshauser, R. J., R. Speith and W. Kley (2011). 'Collisions of inhomogeneous pre-planetesimals'. *Astronomy and Astrophysics* 536, A104.

Giblin, I. (1998). 'New data on the velocity-mass relation in catastrophic disruption'. *Planetary and Space Science* 46.8, 921–928.

Gilbert, G. K. (1893). 'The moon's face; a study of the origin of its features.' *Bulletin of the Philosophical Society of Washington* 12, 242–292.

Gingold, R. A. and J. J. Monaghan (1977). 'Smoothed particle hydrodynamics - Theory and application to non-spherical stars'. *Monthly Notices of the Royal Astronomical Society* 181, 375–389.

Gladman, B. J., D. R. Davis, C. Neese, R. Jedicke, G. Williams, J. J. Kavelaars, J.-M. Petit, H. Scholl, M. Holman, B. Warrington, G. Esquerdo and P. Tricarico (2009). 'On the asteroid belt's orbital and size distribution'. *Icarus* 202.1, 104–118.

Gomes, R., H. F. Levison, K. Tsiganis and A. Morbidelli (2005). 'Origin of the cataclysmic Late Heavy Bombardment period of the terrestrial planets'. *Nature* 435.7041, 466–469.

Goyal, V. K., C. A. Huertas and T. J. Vasko (2014). 'Smooth Particle Hydrodynamics for Bird-Strike Analysis Using LS-DYNA'. *American Transactions on Engineering & Applied Sciences* 2.2, 83–107.

Grady, D. E. and M. E. Kipp (1980). 'Continuum modelling of explosive fracture in oil shale'. *International Journal of Rock Mechanics and Mining Sciences & Geomechanics Abstracts* 17.3, 147–157.

Grüneisen, E. (1912). 'Theorie des festen Zustandes einatomiger Elemente'. German. *Annalen der Physik* 344.12, 257–306.

Güttler, C., J. Blum, A. Zsom, C. W. Ormel and C. P. Dullemond (2010). 'The outcome of protoplanetary dust growth: pebbles, boulders, or planetesimals?' *Astronomy and Astrophysics* 513, A56.

Hageman, L. J. and J. M. Walsh (1971). 'HELP, A Multi-Material Eulerian Program for Compressible Fluid and Elastic-Plastic Flows in Two Space Dimensions and Time. Volume 1'. Tech. rep. AD726459. Systems Science and Software La Jolla, CA, USA.

Hainaut, O. R., H. Boehnhardt and S. Protopapa (2012). 'Colours of minor bodies in the outer solar system'. *Astronomy and Astrophysics* 546, A115.

Haisch, K. E. J., E. A. Lada and C. J. Lada (2001). 'Disk Frequencies and Lifetimes in Young Clusters'. *The Astrophysical Journal* 553.2, L153–L156.

Harris, A. W. (1994). 'Tumbling asteroids'. *Icarus* 107, 209.

Harris, A. W. (1996). 'The Rotation Rates of Very Small Asteroids: Evidence for 'Rubble Pile' Structure'. In: *27th Lunar and Planetary Science Conference*. Mail Stop 183-501, Jet Propulsion Laboratory, 4800 Oak Grove Drive, Pasadena, CA 91109, p. 493.

Harris, A. W., E. G. Fahnestock and P. Pravec (2009). 'On the shapes and spins of "rubble pile" asteroids'. *Icarus* 199.2, 310–318.

Hayhurst, C. J. and R. A. Clegg (1997). 'Cylindrically symmetric SPH simulations of hypervelocity impacts on thin plates'. *International Journal of Impact Engineering* 20.1-5, 337–348.

Herle, I. and G. Gudehus (1999). 'Determination of parameters of a hypoplastic constitutive model from properties of grain assemblies'. *Mechanics of Cohesive-Frictional Materials* 4.5, 461–486.

Hernquist, L. (1987). 'Performance characteristics of tree codes'. *Astrophysical Journal Supplement Series (ISSN 0067-0049)* 64, 715–734.

Herrmann, W. (1969). 'Constitutive Equation for the Dynamic Compaction of Ductile Porous Materials'. *Journal of Applied Physics* 40.6, 2490.

Hicks, M. D., J. M. Bauer and A. T. Tokunaga (2004). '(2867) Steins'. *IAU Circulars* 8315, 3.

Hildebrand, A. R., G. T. Penfield, D. A. Kring, M. Pilkington, A. Camargo Z, S. B. Jacobsen and W. V. Boynton (1991). 'Chicxulub Crater: A possible Cretaceous/Tertiary boundary impact crater on the Yucatán Peninsula, Mexico'. *Geology* 19.9, 867.

Hoerner, S. von (1960). 'Die numerische Integration des n-Körper-Problemes für Sternhaufen. I'. German. *Zeitschrift für Astrophysik* 50, 184–214.

Hoerner, S. von (2001). 'How it All Started'. In: *Dynamics of Star Clusters and the Milky Way*. Ed. by S. Deiters, B. Fuchs, A. Just, R. Spurzem and R. Wielen, pp. 1–6.

Hofmann, M. (2014). 'Dynamics of Granular Material on Small Bodies'. PhD thesis. Göttingen. ISBN: 978-3944072081.

Holsapple, K. A. and R. M. Schmidt (1982). 'On the scaling of crater dimensions. II - Impact processes'. *Journal of Geophysical Research: Solid Earth* 87, 1849–1870.

Holsapple, K. A. and R. M. Schmidt (1987). 'Point source solutions and coupling parameters in cratering mechanics'. *Journal of Geophysical Research* 92, 6350–6376.

Holsapple, K. A. (1993). 'The scaling of impact processes in planetary sciences'. *Annual Review of Earth and Planetary Sciences* 21, 333–373.

Holsapple, K. A., I. Giblin, K. R. Housen, A. M. Nakamura and E. V. Ryan (2002). 'Asteroid Impacts: Laboratory Experiments and Scaling Laws'. In: *Asteroids III*. Ed. by W. F. Bottke, A. Cellino, P. Paolicchi and R. P. Binzel. University of Arizona Press, pp. 443–462. ISBN: 978-0-8165-2281-1.

Holsapple, K. A. and K. R. Housen (2007). 'A crater and its ejecta: An interpretation of Deep Impact'. *Icarus* 187.1, 345–356.

Holsapple, K. A. (2007). 'Spin limits of Solar System bodies: From the small fast-rotators to 2003 EL61'. *Icarus* 187.2, 500–509.

Holsapple, K. A. (2009). 'On the "strength" of the small bodies of the solar system: A review of strength theories and their implementation for analyses of impact disruptions'. *Planetary and Space Science* 57.2, 127–141.

Housen, K. R., L. L. Wilkening, C. R. Chapman and R. Greenberg (1979). 'Asteroidal regoliths'. *Icarus* 39, 317–351.

Housen, K. R. and K. A. Holsapple (1990). 'On the fragmentation of asteroids and planetary satellites'. *Icarus* 84, 226–253.

Housen, K. R. and K. A. Holsapple (1999). 'Scale Effects in Strength-Dominated Collisions of Rocky Asteroids'. *Icarus* 142.1, 21–33.

Houten, C. J. van, I. van Houten-Groeneveld, P. Herget and T. Gehrels (1970). 'The Palomar-Leiden survey of faint minor planets'. *Astronomy & Astrophysics Supplement Series* 2, 339–448.

Hsieh, H. H., D. C. Jewitt and Y. R. Fernandez (2004). 'The strange case of 133P/Elst-Pizarro: A comet among the asteroids'. *The Astronomical Journal*.

Hsieh, H. H., D. C. Jewitt, P. Lacerda, S. C. Lowry and C. Snodgrass (2010). 'The return of activity in main-belt comet 133P/Elst-Pizarro'. *Monthly Notices of the Royal Astronomical Society* 403.1, 363–377.

Huss, G. R., G. J. MacPherson, G. J. Wasserburg, S. S. Russell and G. Srinivasan (2001). '26Al in CAIs and chondrules from unequilibrated ordinary chondrites'. *Meteoritics & Planetary Science* 36, 975–997.

Ivanov, B. A., D. Deniem and G. Neukum (1997). 'Implementation of dynamic strength models into 2D hydrocodes: Applications for atmospheric breakup and impact cratering'. *International Journal of Impact Engineering* 20.1, 411–430.

Ivanov, B. A. (2003). 'Modification of ANEOS for Rocks in Compression'. *Impact Cratering: Bridging the Gap Between Modeling and Observations*, 40.

Ivanov, B. A. (2005). 'Numerical Modeling of the Largest Terrestrial Meteorite Craters'. *Solar System Research* 39.5, 381–409.

Jewitt, D. C., H. A. Weaver, J. Agarwal, M. Mutchler and M. Drahus (2010). 'A recent disruption of the main-belt asteroid P/2010 A2'. *Nature* 467.7317, 817–819.

Johansen, A., A. N. Youdin and Y. Lithwick (2012). 'Adding particle collisions to the formation of asteroids and Kuiper belt objects via streaming instabilities'. *Astronomy and Astrophysics* 537, A125.

Johansen, A., J. Blum, H. Tanaka, C. Ormel, M. Bizzarro and H. Rickman (2014). 'The Multifaceted Planetesimal Formation Process'. *Protostars and Planets VI*, 547–570.

Jorda, L., P. L. Lamy, R. W. Gaskell, M. Kaasalainen, O. Groussin, S. Besse and G. Faury (2012). 'Asteroid (2867) Steins: Shape, topography and global physical properties from OSIRIS observations'. *Icarus* 221.2, 1089–1100.

Jutzi, M., P. P. Michel and W. W. Benz (2010a). 'A large crater as a probe of the internal structure of the E-type asteroid Steins'. *Astronomy and Astrophysics* 509, L2.

Jutzi, M., P. P. Michel, W. W. Benz and D. C. Richardson (2010b). 'Fragment properties at the catastrophic disruption threshold: The effect of the parent body's internal structure'. *Icarus* 207.1, 54–65.

Jutzi, M. and E. Asphaug (2015). 'The shape and structure of cometary nuclei as a result of low-velocity accretion'. *Science* 348.6241, 1355–1358.

Kaasalainen, M. (2001a). 'Optimization Methods for Asteroid Lightcurve Inversion I. Shape Determination'. *Icarus* 153.1, 24–36.

Kaasalainen, M. (2001b). 'Optimization Methods for Asteroid Lightcurve Inversion II. The Complete Inverse Problem'. *Icarus* 153.1, 37–51.

Kaasalainen, M. (2011). 'Multimodal inverse problems: Maximum compatibility estimate and shape reconstruction'. *Inverse Problems and Imaging* 5.1, 37–57.

Keller, H. U., C. Barbieri, P. L. Lamy, H. Rickman, R. Rodrigo, K. P. Wenzel, H. Sierks, M. F. A'Hearn, F. Angrilli, M. Angulo, M. E. Bailey, P. Barthol, M. A. Barucci, J.-L. Bertaux, G. Bianchini, J. L. Boit, V. Brown, J. A. Burns, I. Büttner, J. M. Castro, G. Cremonese, W. Curdt, V. Da Deppo, S. Debei, M. De Cecco, K. Dohlen, S. Fornasier, M. Fulle, D. Germerott, F. Gliem, G. P. Guizzo, S. F. Hviid, W.-H. Ip, L. Jorda, D. Koschny, J. R. Kramm, E. Kuhrt, M. Küppers, L. M. Lara, A. Llebaria, A. López, A. López-Jimenez, J. J. Lopez-Moreno, R. Meller, H. Michalik, M. D. Michelena, R. Müller, G. Naletto, A. Origné, G. Parzianello et al. (2007). 'OSIRIS The Scientific Camera System Onboard Rosetta'. *Space Science Reviews* 128.1, 433–506.

Keller, H. U., C. Barbieri, D. Koschny, P. L. Lamy, H. Rickman, R. Rodrigo, H. Sierks, M. F. A'Hearn, F. Angrilli, M. A. Barucci, J.-L. Bertaux, G. Cremonese, V. Da Deppo, B. J. R. Davidsson, M. De Cecco, S. Debei, S. Fornasier, M. Fulle, O. Groussin, P. J. Gutierrez, S. F. Hviid, W.-H. Ip, L. Jorda, J. Knollenberg, J. R. Kramm, E. Kuhrt, M. Küppers, L. M. Lara, M. Lazzarin, J. L. Moreno, F. Marzari, H. Michalik, G. Naletto, L. Sabau, N. Thomas, K. P. Wenzel, I. Bertini, S. Besse, F. Ferri, M. Kaasalainen, S. C. Lowry, S. Marchi, S. Mottola, W. Sabolo, S. E. Schröder, S. Spjuth and P. Vernazza (2010). 'E-Type Asteroid (2867) Steins as Imaged by OSIRIS on Board Rosetta'. *Science* 327.5962, 190–193.

Kenkmann, T., G. S. Collins and K. Wünnemann (2012). 'The Modification Stage of Crater Formation'. In: *Impact Cratering*. Ed. by G. R. Osinski and E. Pierazzo. John Wiley & Sons, Ltd, pp. 60–75. ISBN: 9781118447307.

Kleinhans, M. G., H. Markies, S. J. de Vet, A. C. in 't Veld and F. N. Postema (2011). 'Static and dynamic angles of repose in loose granular materials under reduced gravity'. *Journal of Geophysical Research* 116.E11, E11004.

Kothe, S., J. Blum, R. Weidling and C. Güttler (2013). 'Free collisions in a microgravity many-particle experiment. III. The collision behavior of sub-millimeter-sized dust aggregates'. *Icarus* 225.1, 75–85.

Kresak, L. (1976). 'Mass content and mass distribution of the asteroid system'. *Astronomical Institutes of Czechoslovakia* 28.2, 65–82.

Kryszczyńska, A. (2013). 'Do Slivan states exist in the Flora family?' *Astronomy and Astrophysics* 551, A102.

Küppers, M., R. Moissl, J.-B. Vincent, S. Besse, S. F. Hviid, B. Carry, B. Grieger, H. Sierks, H. U. Keller, S. Marchi and the OSIRIS team (2012). 'Boulders on Lutetia'. *Planetary and Space Science* 66.1, 71–78.

Kwiatkowski, T. (2010). 'Photometric survey of the very small near-Earth asteroids with the SALT telescope'. *Astronomy and Astrophysics* 509, A95.

Lacerda, P., S. Fornasier, E. Lellouch, C. Kiss, E. Vilenius, P. Santos-Sanz, M. Rengel, T. G. Müller, J. Stansberry, R. Duffard, A. Delsanti and A. Guilbert-Lepoutre (2014). 'The Albedo-Color Diversity of Transneptunian Objects'. *The Astrophysical Journal Letters* 793.1, L2.

Lacome, J. L. (2000). 'Smooth Particle Hydrodynamics (SPH): A New Feature in LS-DYNA'. In: *6th International LS-DYNA Users Conference*, pp. 7–30–7–36.

Lamy, P. L., M. Kaasalainen, S. C. Lowry, P. R. Weissman, M. A. Barucci, J. Carvano, Y.-J. Choi, F. Colas, G. Faury, S. Fornasier, O. Groussin, M. D. Hicks, L. Jorda, A. Kryszczyńska, S. Larson, I. Toth and B. D. Warner (2008). 'Asteroid 2867 Steins. II. Multi-telescope visible observations, shape reconstruction, and rotational state'. *Astronomy and Astrophysics* 487.3, 1179–1185.

Leinhardt, Z. M. and S. T. Stewart (2011). 'Collisions Between Gravity-dominated Bodies. I. Outcome Regimes and Scaling Laws '. *The Astrophysical Journal* 745.1, 79.

Leliwa-Kopystynski, J., M. J. Burchell and D. Lowen (2008). 'Impact cratering and break up of the small bodies of the Solar System'. *Icarus* 195.2, 817–826.

Leyrat, C., S. Fornasier, M. A. Barucci, S. Magrin, M. Lazzarin, M. Fulchignoni, L. Jorda, I. Belskaya, S. Marchi, C. Barbieri, H. U. Keller, H. Sierks and S. F. Hviid (2010). 'Search for Steins' surface inhomogeneities from OSIRIS Rosetta images'. *Planetary and Space Science* 58.9, 1097–1106.

Libersky, L. D. and A. G. Petschek (1991). 'Smooth particle hydrodynamics with strength of materials'. In: ed. by H. E. Trease, M. F. Fritts and W. P. Crowley. Advances in the Free-Lagrange Method Including Contributions on Adaptive Gridding and the Smooth Particle Hydrodynamics Method, pp. 248–257.

Livermore Software Technology Corporation (2006). 'LS-DYNA Theory Manual - March 2006'. 971st ed. Livermore, California: Livermore Software Technology Corporation. ISBN: 0-9778540-0-0.

Love, S. G., F. Hörz and D. E. Brownlee (1993). 'Target Porosity Effects in Impact Cratering and Collisional Disruption'. *Icarus* 105.1, 216–224.

Love, S. G. and T. J. J. Ahrens (1996). 'Catastrophic Impacts on Gravity Dominated Asteroids'. *Icarus* 124.1, 141–155.

Lowry, S. C., A. Fitzsimmons, P. Pravec, D. Vokrouhlicky, H. Boehnhardt, P. A. Taylor, J.-L. Margot, A. Galád, M. Irwin, J. Irwin and P. Kusnirák (2007). 'Direct detection of the asteroidal YORP effect.' *Science* 316.5822, 272–274.

Lowry, S. C., P. R. Weissman, S. R. Duddy, B. Rozitis, A. Fitzsimmons, S. F. Green, M. D. Hicks, C. Snodgrass, S. D. Wolters, S. R. Chesley, J. Pittichova and P. van Oers (2014). 'The internal structure of asteroid (25143) Itokawa as revealed by detection of YORP spin-up'. *Astronomy and Astrophysics* 562, A48.

Lowry, S. C. (2015). 'The Search for Observational Detections of the YORP Effect'. In: *Thermal Models for Planetary Sciences II*. Puerto de la Cruz, Conference Abstract.

Lucy, L. B. (1977). 'A numerical approach to the testing of the fission hypothesis'. *Astronomical Journal* 82, 1013–1024.

Macke, R. J., D. T. Britt and G. J. Consolmagno (2011). 'Density, porosity, and magnetic susceptibility of achondritic meteorites'. *Meteoritics & Planetary Science* 46.2, 311–326.

Malvern, L. E. (1969). 'Introduction to the mechanics of a continuous medium'. English. Englewood Cliffs, N J: Prentice-Hall, Inc. ISBN: 134876032.

Marchi, S., C. Barbieri, M. Küppers, F. Marzari, B. J. R. Davidsson, H. U. Keller, S. Besse, P. L. Lamy, S. Mottola, M. Massironi and G. Cremonese (2010). 'The cratering history of asteroid (2867) Steins'. *Planetary and Space Science* 58.9, 1116–1123.

Marchis, F., P. Descamps, D. Hestroffer and J. Berthier (2005). 'Discovery of the triple asteroidal system 87 Sylvia'. *Nature* 436.7052, 822–824.

Marsh, S. P. (1980). 'Lasl Shock Hugoniot Data'. English. Univ of California Press. ISBN: 9780520040083.

McCoy, T. J., T. L. Dickinson and G. E. Lofgren (1999). 'Partial melting of the Indarch (EH4) Meteorite: A textural, chemical and phase relations view of melting and melt migration'. *Meteoritics & Planetary Science* 34, 735–746.

McCoy, T. J., D. W. Mittlefehldt and L. Wilson (2006). 'Asteroid Differentiation'. In: ed. by D. S. Lauretta and H. Y. McSween Jr. Meteorites and the Early Solar System II, pp. 733–745.

McGlaun, J. M., S. L. Thompson and M. G. Elrick (1990). 'CTH: A three-dimensional shock wave physics code'. *International Journal of Impact Engineering* 10.1–4, 351–360.

McMahon, J. and D. J. Scheeres (2010). 'Detailed prediction for the BYORP effect on binary near-Earth Asteroid (66391) 1999 KW4 and implications for the binary population'. *Icarus* 209.2, 494–509.

McQueen, R. G., S. P. Marsh and J. N. Fritz (1967). 'Hugoniot Equation of State of Twelve Rocks'. *Journal of Geophysical Research* 72, 4999.

Melosh, H. J. (1989). 'Impact cratering: ' A geologic process. New York: Oxford Monographs on Geology and Geophysics. ISBN: 0-19-510463-3.

Melosh, H. J., E. V. Ryan and E. Asphaug (1992). 'Dynamic fragmentation in impacts - Hydrocode simulation of laboratory impacts'. *Journal of Geophysical Research (ISSN 0148-0227)* 97, 14735.

Melosh, H. J. and E. V. Ryan (1997). 'NOTE: Asteroids: Shattered but Not Dispersed'. *Icarus* 129.2, 562–564.

Melosh, H. J. and B. A. Ivanov (1999). 'Impact Crater Collapse'. *Annual Review of Earth and Planetary Sciences* 27, 385–415.

Melosh, H. J. (2007). 'A hydrocode equation of state for SiO2'. *Meteoritics & Planetary Science* 42.1, 2079–2098.

Merz, H., U.-L. Pen and H. Trac (2005). 'Towards optimal parallel PM N-body codes: PMFAST'. *New Astronomy* 10.5, 393–407.

Michel, P. P., W. W. Benz, P. Tanga and D. C. Richardson (2001). 'Collisions and Gravitational Reaccumulation: Forming Asteroid Families and Satellites'. *Science* 294.5547, 1696–1700.

Michel, P. P., W. W. Benz, P. Tanga and D. C. Richardson (2002). 'Formation of Asteroid Families by Catastrophic Disruption: Simulations with Fragmentation and Gravitational Reaccumulation'. *Icarus* 160.1, 10–23.

Michel, P. P., W. W. Benz and D. C. Richardson (2003). 'Disruption of fragmented parent bodies as the origin of asteroid families.' *Nature* 421.6923, 608–611.

Michel, P. P., W. W. Benz and D. C. Richardson (2004a). 'Catastrophic disruption of asteroids and family formation: a review of numerical simulations including both fragmentation and gravitational reaccumulations'. *Planetary and Space Science* 52.12, 1109–1117.

Michel, P. P., W. W. Benz and D. C. Richardson (2004b). 'Catastrophic disruption of pre-shattered parent bodies'. *Icarus* 168.2, 420–432.

Michel, P. P. and D. C. Richardson (2013). 'Collision and gravitational reaccumulation: Possible formation mechanism of the asteroid Itokawa'. *Astronomy and Astrophysics* 554, L1.

Michel, P. P., D. C. Richardson, D. D. Durda, M. Jutzi and E. Asphaug (2015). 'Collisional Formation and Modeling of Asteroid Families'. *arXiv.org*. arXiv: `1502.03929v1 [astro-ph.EP]`.

Michikami, T., A. M. Nakamura, N. Hirata, R. W. Gaskell, R. Nakamura, T. Honda, C. Honda, K. Hiraoka, J. Saito, H. Demura, M. Ishiguro and H. Miyamoto (2008). 'Size-frequency statistics of boulders on global surface of asteroid 25143 Itokawa'. In: *Earth Planets and Space*. Fukushima Natl Coll Technol, Iwaki, Fukushima 9708034, Japan, pp. 13–20.

Michikami, T., A. M. Nakamura and N. Hirata (2010). 'The shape distribution of boulders on Asteroid 25143 Itokawa: Comparison with fragments from impact experiments'. *Icarus* 207.1, 277–284.

Mie, G. (1903). 'Zur kinetischen Theorie der einatomigen Körper'. German. *Annalen der Physik* 316.8, 657–697.

Mitchell, J. K., W. N. Houston, W. D. Carrier III and N. C. Costes (1974). 'Apollo soil mechanics experiment S-200'. Tech. rep. 15.

Miyamoto, H., H. Yano, D. J. Scheeres, S. Abe, O. S. Barnouin-Jha, A. F. Cheng, H. Demura, R. W. Gaskell, N. Hirata, M. Ishiguro, T. Michikami, A. M. Nakamura, R. Nakamura, J. Saito and S. Sasaki (2007). 'Regolith Migration and Sorting on Asteroid Itokawa'. *Science* 316.5, 1011–.

Monaghan, J. J. (1988). 'An introduction to SPH'. *Computer Physics Communications* 48.1, 89–96.

Morbidelli, A., H. F. Levison, K. Tsiganis and R. Gomes (2005). 'Chaotic capture of Jupiter's Trojan asteroids in the early Solar System'. *Nature* 435.7041, 462–465.

Morbidelli, A., W. F. Bottke, D. Nesvorný and H. F. Levison (2009). 'Asteroids were born big'. *Icarus* 204.2, 558–573.

Morbidelli, A., J. I. Lunine, D. P. O'Brien, S. N. Raymond and K. J. Walsh (2012). 'Building Terrestrial Planets'. *Annual Review of Earth and Planetary Sciences* 40, 251–275.

Morris, A. J. W., M. C. Price and M. J. Burchell (2013a). 'Is the Large Crater on the Asteroid (2867) Steins Really an Impact Crater?' *The Astrophysical Journal* 774.1, L11.

Morris, A. J. W., M. J. Burchell, M. C. Price and M. J. Cole (2013b). 'Rotationally Dependant Catastrophic Disruption: Light Gas Gun and SPH Hydrocode Experiments'. In: *8th Workshop on Catastrophic Disruption in the Solar System*. Hawaii, pp. 1–2.

Movshovitz, N., E. Asphaug and D. G. Korycansky (2012). 'The physics of granular flow and the tidal disruption of comet Shoemaker-Levy 9'. *arXiv.org*, 3386. arXiv: `1207.3386 [astro-ph.EP]`.

Nakazawa, S., S. Watanabe, M. Kato, Y. Iijima, T. Kobayashi and T. Sekine (1997). 'Hugoniot equation of state of basalt'. *Planetary and Space Science* 45, 1489–1492.

Nesvorný, D., A. Morbidelli, D. Vokrouhlicky, W. F. Bottke and M. Broz (2002). 'The Flora Family: A Case of the Dynamically Dispersed Collisional Swarm?' *Icarus* 157.1, 155–172.

Nolan, M. C., E. Asphaug, H. J. Melosh and R. Greenberg (1996). 'Impact Craters on Asteroids: Does Gravity or Strength Control Their Size?' *Icarus* 124.2, 359–371.

Norris, T. L., A. J. Gancarz, D. J. Rokop and K. W. Thomas (1983). 'Half-life of Al-26'. In: *Lunar and Planetary Science Conference Proceedings*. Los Alamos National Laboratory, Los Alamos, NM, B331–B333.

O'Brien, D. P. and R. Greenberg (2003). 'Steady-state size distributions for collisional populations:' *Icarus* 164.2, 334–345.

Opik, E. J. (1951). 'Collision probability with the planets and the distribution of planetary matter'. *Proc. R. Irish Acad. Sect. A* 54, 165–199.

Orphal, D. L. (1977a). 'Calculations of explosion cratering. I - The shallow-buried nuclear detonation JOHNIE BOY.' *Impact and Explosion Cratering: Planetary and Terrestrial Implications* -1, 897–906.

Orphal, D. L. (1977b). 'Calculations of explosion cratering. II - Cratering mechanics and phenomenology'. *Impact and Explosion Cratering: Planetary and Terrestrial Implications* -1, 907–917.

Osinski, G. R., P. Lee, J. Parnell, J. G. Spray and M. Baron (2005). 'A case study of impact-induced hydrothermal activity: The Haughton impact structure, Devon Island, Canadian High Arctic'. *Meteoritics* 40.1, 1859–1877.

Osinski, G. R. and E. Pierazzo, eds. (2012). 'Impact Cratering'. Processes and Products. John Wiley & Sons, Ltd. ISBN: 9781118447307.

Ostro, S. J., J. L. Margot, L. A. M. Benner, J. D. Giorgini, D. J. Scheeres, E. G. Fahnestock, S. B. Broschart, J. Bellerose, M. C. Nolan, C. Magri, P. Pravec,

P. Scheirich, R. Rose, R. F. Jurgens, E. M. De Jong and S. Suzuki (2006). 'Radar Imaging of Binary Near-Earth Asteroid (66391) 1999 KW4'. *Science* 314.5803, 1276–1280.

Pierazzo, E. and H. J. Melosh (2000a). 'Hydrocode modeling of oblique impacts: The fate of the projectile'. *Meteoritics & Planetary Science* 35, 117–130.

Pierazzo, E. and H. J. Melosh (2000b). 'Understanding Oblique Impacts from Experiments, Observations, and Modeling'. *Annual Review of Earth and Planetary Sciences* 28, 141–167.

Pierazzo, E., N. A. Artemieva, E. Asphaug, E. C. Baldwin, J. Cazamias, R. Coker, G. S. Collins, D. A. Crawford, T. M. Davison, D. Elbeshausen, K. A. Holsapple, K. R. Housen, D. G. Korycansky and K. Wünnemann (2008). 'Validation of numerical codes for impact and explosion cratering: Impacts on strengthless and metal targets'. *Meteoritics & Planetary Science* 43.1, 1917–1938.

Pope, K. O., K. H. Baines, A. C. Ocampo and B. A. Ivanov (1994). 'Impact winter and the Cretaceous/Tertiary extinctions: Results of a Chicxulub asteroid impact model'. *Earth and Planetary Science Letters* 128.3, 719–725.

Pravec, P. and A. W. Harris (2000). 'Fast and Slow Rotation of Asteroids'. *Icarus* 148, 12–20.

Pravec, P., A. W. Harris and T. Michalowski (2002a). 'Asteroid Rotations'. In: *Asteroids III*. Ed. by W. F. Bottke, A. Cellino, P. Paolicchi and R. P. Binzel. University of Arizona Press, pp. 113–122. ISBN: 978-0-8165-2281-1.

Pravec, P., P. Kusnirák, L. Šarounová, A. W. Harris, R. P. Binzel and A. S. Rivkin (2002b). 'Large coherent asteroid 2001 OE84'. In: *Proceedings of Asteroids, Comets, Meteors (ACM 2002)*, pp. 743–745.

Pravec, P., A. W. Harris, P. Scheirich, P. Kusnirák, L. Šarounová, C. W. Hergenrother, S. Mottola, M. D. Hicks, G. Masi, Y. N. Krugly, V. G. Shevchenko, M. C. Nolan, E. S. Howell, M. Kaasalainen, A. Galád, P. Brown, D. R. DeGraff, J. V. Lambert, W. R. Cooney Jr. and S. Foglia (2005). 'Tumbling asteroids'. *Icarus* 173.1, 108–131.

Pravec, P., D. Vokrouhlicky, D. Polishook, D. J. Scheeres, A. W. Harris, A. Galád, O. Vaduvescu, F. Pozo, A. Barr, P. Longa, F. Vachier, F. Colas, D. P. Pray, J. Pollock, D. Reichart, K. Ivarsen, J. Haislip, A. LaCluyze, P. Kusnirák, T. Henych, F. Marchis, B. Macomber, S. A. Jacobson, Y. N. Krugly, A. V. Sergeev and A. Leroy (2010). 'Formation of asteroid pairs by rotational fission'. *arXiv.org* 7310, 1085–1088. arXiv: `1009.2770v1 [astro-ph.EP]`.

Price, M. C., A. T. Kearsley, M. J. Burchell, L. E. Howard, J. K. Hillier, N. A. Starkey, P. J. Wozniakiewicz and M. J. Cole (2012). 'Stardust interstellar dust calibration: Hydrocode modeling of impacts on Al-1100 foil at velocities up to $300 \, \mathrm{km \, s^{-1}}$ and validation with experimental data'. *Meteoritics & Planetary Science* 47.4, 684–695.

Price, M. C., C. Solscheid, M. J. Burchell, L. Josse, N. Adamek and M. J. Cole (2013). 'Survival of yeast spores in hypervelocity impact events up to velocities of $7.4 \, \mathrm{km \, s^{-1}}$'. *Icarus* 222.1, 263–272.

Rein, H. and S. F. Liu (2012). 'REBOUND: an open-source multi-purpose N-body code for collisional dynamics'. *Astronomy and Astrophysics* 537, A128.

Richardson, D. C., Z. M. Leinhardt, H. J. Melosh, W. F. Bottke and E. Asphaug (2002). 'Gravitational Aggregates: Evidence and Evolution'. In: *Asteroids III*. Ed. by W. F. Bottke, A. Cellino, P. Paolicchi and R. P. Binzel. University of Arizona Press, pp. 501–515. ISBN: 978-0-8165-2281-1.

Rozitis, B. and S. F. Green (2011). 'Directional characteristics of thermal-infrared beaming from atmosphereless planetary surfaces - a new thermophysical model'. *Monthly Notices of the Royal Astronomical Society* 415.3, 2042–2062.

Rozitis, B. and S. F. Green (2012). 'The influence of rough surface thermal-infrared beaming on the Yarkovsky and YORP effects'. *Monthly Notices of the Royal Astronomical Society* 423.1, 367–388.

Rozitis, B. and S. F. Green (2013). 'The influence of global self-heating on the Yarkovsky and YORP effects'. *Monthly Notices of the Royal Astronomical Society* 433.1, 603–621.

Rozitis, B., E. MacLennan and J. P. Emery (2014). 'Cohesive forces prevent the rotational breakup of rubble-pile asteroid (29075) 1950 DA'. *Nature* 512.7513, 174–176.

Rubincam, D. P. (2000). 'Radiative Spin-up and Spin-down of Small Asteroids'. *Icarus* 148, 2–11.

Ryan, E. V. and H. J. Melosh (1998). 'Impact Fragmentation: From the Laboratory to Asteroids'. *Icarus* 133.1, 1–24.

Saito, J., H. Miyamoto, R. Nakamura, M. Ishiguro, T. Michikami, A. M. Nakamura, H. Demura, S. Sasaki, N. Hirata, C. Honda, A. Yamamoto, Y. Yokota, T. Fuse, F. Yoshida, D. J. Tholen, R. W. Gaskell, T. Hashimoto, T. Kubota, Y. Higuchi, T. Nakamura, P. Smith, K. Hiraoka, T. Honda, S. Kobayashi, M. Furuya, N. Matsumoto, E. Nemoto, A. Yukishita, K. Kitazato, B. Dermawan, A. Sogame,

J. Terazono, C. Shinohara and H. Akiyama (2006). 'Detailed Images of Asteroid 25143 Itokawa from Hayabusa'. *Science* 312.5778, 1341–1344.

Saito, T., K. Kaiho, A. Abe, M. Katayama and K. Takayama (2008). 'Hypervelocity impact of asteroid/comet on the oceanic crust of the earth'. *International Journal of Impact Engineering* 35.12, 1770–1777.

Salo, H. (1987). 'Numerical simulations of collisions between rotating particles'. *Icarus* 70, 37–51.

Sánchez, P. and D. J. Scheeres (2012). 'DEM simulation of rotation-induced reshaping and disruption of rubble-pile asteroids'. *Icarus* 218.2, 876–894.

Sánchez, P. and D. J. Scheeres (2014). 'The strength of regolith and rubble pile asteroids'. *Meteoritics & Planetary Science* 49.5, 788–811.

Scheeres, D. J., E. G. Fahnestock, S. J. Ostro, J. L. Margot, L. A. M. Benner, S. B. Broschart, J. Bellerose, J. D. Giorgini, M. C. Nolan, C. Magri, P. Pravec, P. Scheirich, R. Rose, R. F. Jurgens, E. M. De Jong and S. Suzuki (2006). 'Dynamical Configuration of Binary Near-Earth Asteroid (66391) 1999 KW4'. *Science* 314.5803, 1280–1283.

Schenk, P. M., E. Asphaug, W. B. McKinnon, H. J. Melosh and P. R. Weissman (1996). 'Cometary Nuclei and Tidal Disruption: The Geologic Record of Crater Chains on Callisto and Ganymede'. *Icarus* 121.2, 249–274.

Scholtès, L. and F.-V. Donzé (2013). 'A DEM model for soft and hard rocks Role of grain interlocking on strength'. *Journal of the Mechanics and Physics of Solids* 61.2, 352–369.

Schröder, S. E., H. U. Keller, P. J. Gutierrez, S. F. Hviid, R. Kramm, W. Sabolo and H. Sierks (2010). 'Evidence for surface variegation in Rosetta OSIRIS images of asteroid 2867 Šteins'. *Planetary and Space Science* 58.9, 1107–1115.

Schulte, P., L. Alegret, I. Arenillas, J. A. Arz, P. J. Barton, P. R. Bown, T. J. Bralower, G. L. Christeson, P. Claeys, C. S. Cockell, G. S. Collins, A. Deutsch, T. J. Goldin, K. Goto, J. M. Grajales-Nishimura, R. A. F. Grieve, S. P. S. Gulick, K. R. Johnson, W. Kiessling, C. Koeberl, D. A. Kring, K. G. MacLeod, T. Matsui, H. J. Melosh, A. Montanari, J. V. Morgan, C. R. Neal, D. J. Nichols, R. D. Norris, E. Pierazzo, G. Ravizza, M. Rebolledo-Vieyra, W. U. Reimold, E. Robin, T. Salge, R. P. Speijer, A. R. Sweet, J. Urrutia-Fucugauchi, V. Vajda, M. T. Whalen and P. S. Willumsen (2010). 'The Chicxulub Asteroid Impact and Mass Extinction at the Cretaceous-Paleogene Boundary'. *Science* 327.5, 1214.

Schulz, R., C. Alexander, H. Boehnhardt and K.-H. Glassmeier, eds. (2009). 'Rosetta : ESA's mission to the origin of the solar system'. New York: Springer.

Schwer, L. E. (2004). 'Preliminary Assessment of Non-Lagrangian Methods for Penetration Simulation'. In: *8ᵗʰ International LS-DYNA Users Conference*. Dearborn, Michigan, pp. 8–1–8–12.

Sierks, H., P. L. Lamy, C. Barbieri, D. Koschny and H. Rickman (2011). 'Images of asteroid 21 Lutetia: a remnant planetesimal from the early solar system'. *Science* 334, 487–490.

Sierks, H., C. Barbieri, P. L. Lamy, R. Rodrigo, D. Koschny, H. Rickman, H. U. Keller, J. Agarwal, M. F. A'Hearn, F. Angrilli, A.-T. Auger, M. A. Barucci, J.-L. Bertaux, I. Bertini, S. Besse, D. Bodewits, C. Capanna, G. Cremonese, V. Da Deppo, B. J. R. Davidsson, S. Debei, M. De Cecco, F. Ferri, S. Fornasier, M. Fulle, R. W. Gaskell, L. Giacomini, O. Groussin, P. Gutierrez-Marques, P. J. Gutierrez, C. Güttler, N. Hoekzema, S. F. Hviid, W.-H. Ip, L. Jorda, J. Knollenberg, G. Kovacs, J. R. Kramm, E. Kuhrt, M. Küppers, F. La Forgia, L. M. Lara, M. Lazzarin, C. Leyrat, J. J. Lopez-Moreno, S. Magrin, S. Marchi, F. Marzari, M. Massironi, H. Michalik et al. (2015). 'On the nucleus structure and activity of comet 67P/Churyumov-Gerasimenko'. *Science* 347.6220, aaa1044–1–5.

Slivan, S. M. (2002). 'Spin vector alignment of Koronis family asteroids'. *Nature* 419.6, 49–51.

Slivan, S. M., R. P. Binzel, L. D. Crespo da Silva, M. Kaasalainen, M. M. Lyndaker and M. Krčo (2003). 'Spin vectors in the Koronis family: comprehensive results from two independent analyses of 213 rotation lightcurves'. *Icarus* 162.2, 285–307.

Statler, T. S. (2009). 'Extreme Sensitivity of the YORP Effect to Small-Scale Topography'. *arXiv.org*. arXiv: `0903.1119v1 [astro-ph.EP]`.

Statler, T. S. (2015). 'Obliquities of "top-shaped" asteroids may not imply reshaping by YORP spin-up'. *Icarus* 248.C, 313–317.

Stellingwerf, R. F. and C. A. Wingate (1994). 'Impact Modelling with SPH'. *Memorie della Società Astronomia Italiana* 65, 1117.

Sullivan, R. J., R. Greeley, R. Pappalardo, E. Asphaug, J. M. Moore, D. Morrison, M. J. S. Belton, M. H. Carr, C. R. Chapman, P. E. Geissler, R. Greenberg, J. Granahan, J. W. I. Head, R. Kirk, A. McEwen, P. Lee, P. C. Thomas and J. Veverka (1996). 'Geology of 243 Ida'. *Icarus* 120.1, 119–139.

Swegle, J. W., S. W. Attaway, M. W. Heinstein, F. J. S. N. L. Mello and D. L. M. T. U. Hicks (1994). 'An analysis of smoothed particle hydrodynamics'. Tech. rep.

Tancredi, G., A. Maciel, L. Heredia, P. Richeri and S. Nesmachnow (2012). 'Granular physics in low-gravity environments using discrete element method'. *Monthly Notices of the Royal Astronomical Society* 420.4, 3368–3380.

Tanga, P., A. Cellino, P. P. Michel, V. Zappalà, P. Paolicchi and A. dell'Oro (1999). 'On the Size Distribution of Asteroid Families: The Role of Geometry'. *Icarus* 141, 65–78.

Tanga, P., C. Comito, P. Paolicchi, D. Hestroffer, A. Cellino, A. dell'Oro, D. C. Richardson, K. J. Walsh and M. Delbó (2009). 'Rubble-Pile Reshaping Reproduces Overall Asteroid Shapes '. *The Astrophysical Journal* 706.1, L197–L202.

Taylor, G. (1950). 'The Formation of a Blast Wave by a Very Intense Explosion. II. The Atomic Explosion of 1945'. In: *Proceedings of the Royal Society of London. Series A*, pp. 175–186.

Taylor, P. A., J. L. Margot, D. Vokrouhlicky, D. J. Scheeres, P. Pravec, S. C. Lowry, A. Fitzsimmons, M. C. Nolan, S. J. Ostro, L. A. M. Benner, J. D. Giorgini and C. Magri (2007). 'Spin Rate of Asteroid (54509) 2000 PH5 Increasing Due to the YORP Effect'. *Science* 316.5822, 274–277.

Terebey, S., F. H. Shu and P. Cassen (1984). 'The collapse of the cores of slowly rotating isothermal clouds'. *Astrophysical Journal* 286, 529–551.

Tholen, D. J. (1989). 'Asteroid taxonomic classifications'. In: *Asteroids II; Proceedings of the Conference*. Ed. by R. P. Binzel, T. Gehrels and M. S. Matthews, pp. 1139–1150.

Thomas, P., J. Veverka, A. Bloom and T. Duxbury (1979). 'Grooves on PHOBOS - Their distribution, morphology and possible origin'. *Journal of Geophysical Research* 84, 8457–8477.

Thomas, P. C., J. W. Parker, L. A. McFadden, C. T. Russell, S. A. Stern, M. V. Sykes and E. F. Young (2005). 'Differentiation of the asteroid Ceres as revealed by its shape'. *Nature* 437.7056, 224–226.

Thompson, S. L. (1990). 'ANEOS analytic equations of state for shock physics codes input manual'. *Sandia Report SAND89-2951*.

Tillotson, J. H. (1962). 'Metallic equations of state for hypervelocity impact '. Tech. rep. AD486711.

Tsiganis, K., R. Gomes, A. Morbidelli and H. F. Levison (2005). 'Origin of the orbital architecture of the giant planets of the Solar System'. *Nature* 435.7041, 459–461.

Turtle, E. P., E. Pierazzo, G. S. Collins, G. R. Osinski, H. J. Melosh, J. V. Morgan and W. U. Reimold (2004). 'Impact structures: What does crater diameter mean'. In: *Large Meteorite Impacts III*. Geological Society of America, pp. 1–24. ISBN: 9780813723846.

Udry, S. and N. C. Santos (2007). 'Statistical Properties of Exoplanets'. *Annual Review of Astronomy and Astrophysics* 45.1, 397–439.

Veverka, J., P. Thomas, D. Simonelli, M. J. S. Belton, M. H. Carr, C. R. Chapman, M. E. Davies, R. Greeley, R. Greenberg and J. Head (1994). 'Discovery of grooves on Gaspra'. *Icarus* 107, 1–12.

Veverka, J., P. C. Thomas, P. Helfenstein, P. Lee, A. Harch, S. Calvo, C. R. Chapman, M. J. S. Belton, K. Klaasen, T. V. Johnson and M. E. Davies (1996). 'Dactyl: Galileo Observations of Ida's Satellite'. *Icarus* 120.1, 200–211.

Vincent, J.-B., D. Bodewits, S. Besse, H. Sierks, C. Barbieri, P. L. Lamy, R. Rodrigo, D. Koschny, H. Rickman, H. U. Keller, J. Agarwal, M. F. A'Hearn, A.-T. Auger, M. A. Barucci, J.-L. Bertaux, I. Bertini, C. Capanna, G. Cremonese, V. Da Deppo, B. J. R. Davidsson, S. Debei, M. De Cecco, M. R. El-Maarry, F. Ferri, S. Fornasier, M. Fulle, R. W. Gaskell, L. Giacomini, O. Groussin, A. Guilbert-Lepoutre, P. Gutierrez-Marques, P. J. Gutierrez, C. Güttler, N. Hoekzema, S. Höfner, S. F. Hviid, W.-H. Ip, L. Jorda, J. Knollenberg, G. Kovacs, R. Kramm, E. Kuhrt, M. Küppers, F. La Forgia, L. M. Lara, M. Lazzarin, V. Lee, C. Leyrat, Z.-Y. Lin, J. J. Lopez-Moreno et al. (2015). 'Large heterogeneities in comet 67P as revealed by active pits from sinkhole collapse'. *Nature* 523.7558, 63–66.

Vokrouhlicky, D., D. Nesvorný and W. F. Bottke (2003). 'The vector alignments of asteroid spins by thermal torques'. *Nature* 425.6954, 147–151.

Vokrouhlicky, D., W. F. Bottke, S. R. Chesley, D. J. Scheeres and T. S. Statler (2015). 'The Yarkovsky and YORP Effects'. *arXiv.org*. arXiv: `1502.01249v1 [astro-ph.EP]`.

Wahlberg Jansson, K. and A. Johansen (2014). 'Formation of pebble-pile planetesimals'. *Astronomy and Astrophysics* 570, A47.

Walsh, K. J., D. C. Richardson and P. P. Michel (2008). 'Rotational breakup as the origin of small binary asteroids'. *Nature* 454.7201, 188–191.

Walsh, K. J., A. Morbidelli, S. N. Raymond, D. P. O'Brien and A. M. Mandell (2012). 'Populating the asteroid belt from two parent source regions due to the migration of giant planets—"The Grand Tack"'. *Meteoritics & Planetary Science* 47.1, 1941–1947.

Warner, B. D., A. W. Harris and P. Pravec (2009). 'The asteroid lightcurve database'. *Icarus* 202.1, 134–146.

Warner, B. D., A. W. Harris and P. Pravec (2014). 'Asteroid Lightcurve Database (LCDB)'. URL: http://www.MinorPlanet.info/lightcurvedatabase.html visited on 15/12/2014.

Weibull, W. (1939). 'A Statistical Theory of Strength of Materials'. *Generalstabens Litografiska Anstalts Förl.* 45.

Weidenschilling, S. J. (2011). 'Initial sizes of planetesimals and accretion of the asteroids'. *Icarus* 214.2, 671–684.

Weidling, R., C. Güttler and J. Blum (2012). 'Free collisions in a microgravity many-particle experiment. I. Dust aggregate sticking at low velocities'. *Icarus* 218.1, 688–700.

Weiss, B. P., L. T. Elkins-Tanton, M. A. Barucci, H. Sierks, C. Snodgrass, J.-B. Vincent, S. Marchi, P. R. Weissman, M. Pätzold, I. Richter, M. Fulchignoni, R. P. Binzel and R. Schulz (2012). 'Possible evidence for partial differentiation of asteroid Lutetia from Rosetta'. *Planetary and Space Science* 66.1, 137–146.

Weissman, P. R., S. C. Lowry and Y.-J. Choi (2005). 'CCD Photometry of Asteroid 2867 Steins: Flyby Target of the Rosetta Mission'. *American Astronomical Society* 37, 644.

Weissman, P. R., S. C. Lowry and Y.-J. Choi (2007). 'Photometric observations of Rosetta target asteroid 2867 Steins'. *Astronomy and Astrophysics* 466.2, 737–742.

Weissman, P. R., M. D. Hicks, P. A. Abell, Y.-J. Choi and S. C. Lowry (2008). 'Rosetta target asteroid 2867 Steins: An unusual E-type asteroid'. *Meteoritics & Planetary Science* 43.5, 905–914.

Windmark, F., T. Birnstiel, C. W. Ormel and C. P. Dullemond (2012a). 'Breaking through: The effects of a velocity distribution on barriers to dust growth'. *Astronomy and Astrophysics* 544, L16.

Windmark, F., T. Birnstiel, C. Güttler, J. Blum, C. P. Dullemond and T. Henning (2012b). 'Planetesimal formation by sweep-up: how the bouncing barrier can be beneficial to growth'. *Astronomy and Astrophysics* 540, A73.

Wood, C. A. and L. Anderson (1978). 'New morphometric data for fresh lunar craters'. In: *9th Lunar and Planetary Science Conference*. Brown University, Providence, R.I., pp. 3669–3689.

Wozniakiewicz, P. J., M. C. Price, S. P. Armes, M. J. Burchell, M. J. Cole, L. A. Fielding, J. K. Hillier and J. R. Lovett (2014). 'Micron-scale hypervelocity

impact craters: Dependence of crater ellipticity and rim morphology on impact trajectory, projectile size, velocity, and shape'. *Meteoritics & Planetary Science* 49.10, 1929–1947.

Wünnemann, K., G. S. Collins and H. J. Melosh (2006). 'A strain-based porosity model for use in hydrocode simulations of impacts and implications for transient crater growth in porous targets'. *Icarus* 180.2, 514–527.

Wyatt, M. C. (2008). 'Evolution of Debris Disks'. *Annual Review of Astronomy and Astrophysics* 46.1, 339–383.

Yoshida, F. and T. Nakamura (2007). 'Subaru Main Belt Asteroid Survey (SMBAS) — Size and color distributions of small main-belt asteroids'. *Planetary and Space Science* 55.9, 1113–1125.

Youdin, A. N. and J. Goodman (2005). 'Streaming Instabilities in Protoplanetary Disks'. *The Astrophysical Journal* 620.1, 459–469.

Zellner, B., D. J. Tholen and E. F. Tedesco (1985). 'The eight-color asteroid survey - Results for 589 minor planets'. *Icarus* 61, 355–416.

Zsom, A., C. W. Ormel, C. Güttler, J. Blum and C. P. Dullemond (2010). 'The outcome of protoplanetary dust growth: pebbles, boulders, or planetesimals?' *Astronomy and Astrophysics* 513, A57.

Appendix A

Tables

Table A.1: Parameters controling the implementation of the k-D tree gravity solver used.

Symbol	Name	Description	Default value
θ	Opening angle	Opening angle, parameter in calculating the opening radius R_θ of each cell	0.600
R_{save}	Safety radius	Safety factor for maximum movement of particles in cell before the tree has to be rebuild	0.400
C_{max}	Maximum Ratio	Maximum ratio of longest to smallest dimension of a cell	10
N_{emax}	Max particles per cell	Maximum number of elements in a single leaf of the tree	8
N_{steps}	Skip timesteps	Maximum number of timesteps before rebuilding the tree	20
ζ	Softening paramter	Softeing parameter for regularization of the gravitational force	1×10^{-9}
t_{ramp}	Ramptime	Ramptime to scale gravitational forces at initation of simulation	1×10^{-3}

Appendix B

Code listings

Input: An array particleList containing indices to particles
Result: A balanced *k*-D tree tree structure
Data: All data for the particles, like mass and positions, can be
         accessed by the indices in particleList

1 particleList ← Index of particles to be distributed
2 theCell ← Root cell
3 **RecursiveFunction** `CreateCell(`theCell*: type Cell,*particleList*:*
  *index,*Level*: int*`)`:
4   **if** *number of* particleList $> N_{emax}$ **then**
5   `// End of the tree not reached, distribute particles`
6         $d \leftarrow$ Level mod 3   `// bisect along dimension d`
7   sort particleList.x along dimension d
8   `// create daughter cells:`
9   `CreateCell(`LeftCell,*left part of* particleList,Level $+ 1$`)`
10   `CreateCell(`RightCell,*right part of* particleList,Level $+ 1$`)`
11   theCell.M_{tot} ← sum of the masses of the daughter cells
12   theCell.x_{cms} ← based on x_{cms} of the daughter cells
13   theCell.quadrupoleTensor ← quadrupole Tensor based on
         daughter cells
14   `// if one of the daughter cells contains only one`
         `particle, its opening Radius is ill defined, so`
         `replace it here`
15   **foreach** subCell ← *(*LeftCell,RightCell*)* **do**
16   **if** subCell.particleList *has only* 1 *entry* **then**
17   subCell.x_{cms} ← theCell.x_{cms} subCell.R_{θ} ← theCell.R_{θ}
18   **else**
19   `// End of tree reached`
20   `// save indeces of particles belonging to this leaf`
         `cell:`
21   theCell.particleList ← particleList
22   theCell.M_{tot} ← sum of the masses
23   theCell.x_{cms} ← center of mass
24   theCell.quadrupoleTensor ← quadrupole Tensor
25   `// Calculate opening radius, see Equation (2.26)`
26   theCell.$R_{\theta} = \frac{2}{\sqrt{3}} \max(|x_i - x_{\text{cms}}|) + \max(|x_i - x_{\text{cell}}|)$
27   **return**

Algorithm 1: Creating the *k*-D tree tree by recursivley distributing the particles into daughter cells until each cell contains no more than N_{emax} particles.

Input: A cell theCell for which we are building the lists
Result: The list PPlist will contain all particles to which forces have to be evaluated directly, the list PClist will contain all cell of which forces will be approximated using the gravitational moment
Data: A tree containing all particles, treeNode refers to the current node

1   theCell ← Current cell to search interaction lists for
2   treeNode ← Root tree cell
3   **RecursiveFunction** `InteractionListWalk(`theCell*: type Cell,*treeNode*: type Cell*`)`**:**
4   **if** *(*treeNode **is** *a leaf of the tree)* **then**
5   `// Reached end of the tree`
6   **add** (all particles **in** treeNode) **to** theCell.PPlist
7   **return**   `// Done with this tree branch, end recursion`
8
9   **foreach** subCell ← *(the two daughter cells of* treeNode*)* **do**
10   D ← cell center distance from subCell to theCell
11   **if** *(*subCell.cellRatio $> C_{max}$*)* **or** *($D <$ (*subCell.$R_\theta +$ theCell. $\max(|x_i - x_{cell}|)$*))* **then**
12   `// Check if we have to open the subCell`
13   `// Decent to daughter cell:`
14   `InteractionListWalk(theCell,subCell)`
15   **else**
16   `// We can use the approximation for this daughter cell`
17   **add** subCell **to** theCell.PClist
18   **return**

Algorithm 2: Creating the interaction lists. R_θ is the opening radius of a cell as by Equation (2.26), $\max(|x_i - x_{\text{cell}}|)$ the maximum distance of any element to the cell center.

Input: A leaf of the k-D tree, theCell
Result: Accelerations due to gravity for all particles in theCell
Data: All data for the particles, like mass and positions, can be accessed by the indices

1 theCell ← Leaf of tree
2 **RecursiveFunction** CalculateGravity(theCell: type Cell):
3   // Initialize acceleration array to zero
4   theCell.$\ddot{x}$ ← 0
5   // Check if theParticle has moved to far:
6   d_{save} ← max(theCell.R_θ) × R_{save}, theCell.$maxCdist$)
7   **foreach** theParticle **in** theCell.particleList **do**
8   **if** |theCell.x − theCell.x_{cms}| > d_{save} **then**
9   RemakeTree ← *True*
10   // Calculate direct forces in the cell:
11   **foreach** theParticle **in** theCell.particleList **do**
12   **foreach** otherParticle **in** *(* theCell.particleList ≠theParticle*)* **do**
13   **add to** theParticle.$\ddot{x}$ accelerations between theParticle and otherParticle
14   // Calculate direct forces to nearby particles:
15   **foreach** theParticle **in** particleList **do**
16   **foreach** otherParticle **in** theCell.PPlist **do**
17   **add to** theParticle.$\ddot{x}$ accelerations between theParticle and otherParticle
18   // Calculate forces from far away cells
19   **foreach** theParticle **in** theCell.particleList **do**
20   **foreach** otherCell **in** theCell.PClist **do**
21   **add to** theParticle.$\ddot{x}$ accelerations between theParticle and otherCell by evaluating the gravitational moment
22   **return**

Algorithm 3: Calculate accelerations due to gravity to all particles in a single cell belonging to a k-D tree.

Appendix C

Glosssary

Parameters of the Gravitational Model

$C_{\mathbf{max}}$ Maximum ratio of longest to smallest dimension of a cell.

$N_{\mathbf{emax}}$ Maximum number of elements in a single leaf of the tree.

$N_{\mathbf{steps}}$ Maximum number of timesteps before rebuilding the tree.

$R_{\mathbf{save}}$ Safety factor for maximum movement of particles in cell before the tree has to be rebuild.

R_θ Opening radius, threshold value from which distance the gravitational force will be calculated using a pseudoparticle approximation a group of mass elements.

θ Opening angle, parameter in calculating the opening radius R_θ of each cell.

$t_{\mathbf{ramp}}$ Ramptime to scale gravitational forces at initation of simulation.

ζ Softeing parameter for regularization of the gravitational force.

Minor Bodies Mentioned in this Work

Apollo (1862) Apollo, 1932 HA.

Bennu Bennu, a NEO of small, YORPoid shape, is the target of the OSIRIS-REx mission. (p. 160)

Ceres (1) Ceres, the largest object in the asteroid belt. (pp. 3, 27)

67P/CG Comet 67P/Churyumov-Gerasimenko, main target of the Rosetta mission. (pp. 97, 99, 158)

1950 DA (29075) 1950 DA. (pp. 11, 31, 148)

Dactyl Dactyl ((243) Ida I Dactyl), small satellite of Ida. (pp. 152, 153, 155, 195)

Deimos Deimos, moon of Mars. (pp. 101, 109)

Eros Asteroid (433) Eros, primary tyarget of the NEAR Shoemaker spacecraft. (pp. 101, 109)

Gaspra Asteroid (951) Gaspra. (pp. 148, 150)

Golevka (6489) Golevka. (p. 21)

Hygiea Asteroid (10) Hygiea. Fourth largest MBA. (p. 3)

Ida Asteroid (243) Ida MBA in the Koronis family, flyby target of the Galileo spacecraft. (pp. 101, 109, 150, 152, 153)

Itokawa (25143) Itokawa. Main target of the Hayabusa mission. Other names: 1998 SF36. (pp. 11, 19, 23, 25, 39, 42, 47, 49, 75, 79, 106, 114, 138, 143, 145, 148, 156, 157, 195)

1999 KW4 (66391) 1999 KW4. (pp. 23, 102, 155)

Lutetia Asteroid (21) Lutetia. (pp. 18, 27, 99, 114, 148, 157)

Mathilde Asteroid (253) Mathilde. (p. 101)

OE84 (2001) OE84, superfast rotating asteroid with a diameter $D \approx 700\,\text{m}$, rotating above the spin barrier (Pravec et al. 2002b). (pp. 11, 29)

Pallas (2) Pallas. (p. 3)

Phobos Phobos, moon of Mars. (pp. 101, 109, 150)

Šteins Asteroid (2867) Šteins, flyby target of the Rosetta mission. Other designations: 1969 VC. See Table 4.1 for orbital paramters. (pp. i, ii, xiii, 11, 27, 39, 42, 46–49, 72, 73, 75, 97, 99–106, 109, 111–115, 117–119, 122, 124, 128, 133, 136–141, 146, 148–150, 152, 153, 155, 156, 158, 160, 194)

Sylvia Asteroid (87) Sylvia is probably the largest rubble pile asteroid (Marchis et al. 2005), exhibits two small satellites. (p. 157)

Vesta Asteroid (4) Vesta, second largest object in the asteroid belt. (pp. 3, 27)

(54509) YORP (54509) YORP, formerly 2000 PH5. (p. 23)

Software Mentioned in this Work

ANEOS Analytic Equations of State for Shock Physics Codes (Thompson 1990). (pp. 51, 53)

Autodyn Hydocode package by Ansys Autodyn, (Century Dynamics Ltd 2000). Includes a variety of solvers, the SPH solver is described in Birnbaum et al. (1996). (pp. 52–54, 56, 57, 72, 73, 79, 82, 114, 145, 147)

CADFEM CADFEM GmbH, Munich, Germany. German distributer of Ansys and support provider. www.cadfem.de. (p. 64)

CTH CTH 2D/3D, Eulerian shock physics code developed at Sandia National Laboratories (McGlaun et al. 1990). www.sandia.gov/CTH. (p. 53)

iSALE iSALE 2D/3D, Wünnemann et al. (2006) and Collins et al. (2004). (pp. 52, 53, 72)

LS-DYNA Hydocode package by Ansys Autodyn, (Century Dynamics Ltd 2000). Includes a variety of solvers, the SPH solver is described in Birnbaum et al. (1996). (pp. 57, 58, 64, 65, 72, 114, 115, 117, 118, 157)

MPI API for distributed-memory parallel programing. www.mcs.anl.gov/research/projects/mpi/. (p. 65)

MPP Massively Parallel Processing is a synonym for using computation clusters of multiple, independet machines. (p. 65)

OpenMP API for shared-memory parallel execution of program loops using threads. `openmp.org/wp.` (pp. 58, 65)

PKDGRAV SPH3D Benz and Asphaug (1995). (p. 63)

Rebound A modular gravity N-body code. Published under open source license, described in Rein and Liu (2012). Available at `https://github.com/hannorein/rebound.` (pp. 76, 141)

SALE SALE 2D shock physics code, a predecessor of `iSALE`, Melosh et al. (1992). (pp. 45, 53)

Glossary

Acmon Crater Acmon is the largest crater on Dactyl with a size of $D \approx 280 \, \text{m}$ (Veverka et al. 1996). (p. 152)

Atlanta The Atlanta meteorite was found 1938 in Louisiana. The 5.5 kg meteorite has been classified as an brecciated, low-iron Enstatite Chondrite. See `http://www.mindat.org/loc-256625.html` and `http://www.lpi.usra.edu/meteor/metbull.php?code=4886.` (p. 97)

aubrite `http://www.lpi.usra.edu/meteor/metbullclass.php?sea=Aubrite.` (p. 104)

Chixculub The Chixculub impact event created a crater at the north of Yucátan, Mexico. Because it was quickly burried by sedimentary rocks, it is one of the best preserved giant crater structures. It is believed to coincide with the CretaceousPaleogene transition and the extinction of dinosaurs 64 million years ago (Schulte et al. 2010). (pp. 33, 45)

Dawn The Dawn spacecraft was launched in September 2007. From July 16 2011, Dawn was in orbit of asteroid Vesta, and transfered later to orbit Ceres, where it arrived March 6 2015. `dawn.jpl.nasa.gov/.` (p. 27)

Diamond Crater Diamond is the largest crater on (2867) Šteins, located near the southern pole. Equivalent to the crater called 'Ruby' in Jorda et al. (2012). (pp. i, 46, 100–102, 105, 106, 109, 111–113, 119, 122, 124, 128, 136, 137, 139, 152, 153, 155, 156, 158, 160)

Drucker-Prager criterion The Drucker-Prager yield criterion defines the failure or plastic yielding limit of a material. (pp. 29, 30)

EL EL chondrites are ordinary chondrites, low of total iron and with ferroan alabandite. (p. 97)

Galileo The primary mission is the exploration of the Galileo project was the exploration of the Jupiter system in 1995-97. On the way to Jupiter it imaged asteroid Gaspra and Ida with its moon Dactyl. (pp. 150, 152, 153)

Haughton impact crater The Haughton impact structure, located on Devon Island, Canada, was formed 39 Ma ago. The rim diameter is about 23 km, and is very well preserved (Osinski et al. 2005). (p. 32)

Hayabusa The Hayabusa mission by JAXA started in 2003 to the NEO Itokawa, and returned a sample of dust to earth in 2010. `http://hayabusa.jaxa.jp`. (pp. 23, 47, 49, 79, 192)

Hugoniot The Rankine-Hugoniot conditions connect the state of two materials connected through a discontinous shock front. Together with an additional relation, usually the equation of state (EOS), they allow to derive the state of the shocked material from the know state of the initial material without having to know the state inside the shock front.. (p. 37)

k-D tree k-D tree is a balanced sorting tree for, where elements in the k-dimensional space are hierarchically divided in two buckets in alternating directions. (pp. xiii, 63, 65, 67, 76, 116, 186, 187)

LCDB The Asteroid Lightcurve Database is a continous effort to improve the dataset available on asteorid lightcurve parameters and other information, e.g., estimated/measured diameters, absolute magnitudes (H), phase slope parameters (G), albedos, and more. It is hosted on `http://www.minorplanet.info/lightcurvedatabase.html` and described in Warner et al. (2009). (pp. 11, 201)

oct-tree An oct-tree is a sorting tree, where elements in the three-dimensional space are hierarchically sorted into the corresponding octant until each cell contains just a single element. (p. 63)

OSIRIS The OSIRIS camera system (Optical, Spectroscopic, and Infrared Remote Imaging System) is the scientific imagin system on the Rosetta spacecraft. Led by the Max-Planck-Institute for Solar System Research, a consortium of 9 institutes developed and build this instrument, consisting of two cameras, a high resolution Narrow Angle Camera (NAC) and a Wide Angle Camera (WAC) (Keller et al. 2007). (pp. x, 47, 97, 99, 100, 104, 109, 114, 137, 158, 197, 198)

OSIRIS-REx OSIRIS-REx is a sample return mission by NASA to the NEO Bennu. Start is scheduled for the year 2016. `http://www.asteroidmission.org`. (p. 160)

Rosetta Rosetta launched in 2004 and arrived at Comet 67P/Churyumov-Gerasimenko on 6 August 2014. It is the first mission in history to rendez-vous with a comet, escort it as it orbits the Sun, and deploy a lander to its surface. Rosetta is an ESA mission with contributions from its member states and NASA. Rosetta's Philae lander is provided by a consortium led by DLR, MPS, CNES and ASI. *ESA, `http://rosetta.esa.int/`* . (pp. i, x, 47, 49, 97, 99, 137, 155, 156, 158, 192, 196, 197)

R-Plot Standardized plot to examine the cratering saturation (Crater Analysis Techniques Working Group et al. 1979). (p. 105)

Stickney Stickney is the largest crater on Phobos. (p. 150)

Acronyms

ALE Arbitrarily Lagrangian Euler. (p. 53)

BYORP Binary YORP. (pp. 25, 155)

CAI Calcium-Aluminium Rich Inclusions. (pp. 13, 26)

CDO Classical Disk Object. (p. 17)

DDO Detached Disk Object. (p. 17)

DEM Discrete Element Method. (p. 147)

ECAS Eight-Color Asteroid Survey, `http://sbn.psi.edu/pds/resource/ecas.html`, first release by Zellner et al. 1985. (p. 7)

EOS equation of state. (pp. 37, 45, 51, 53, 56, 60, 195)

HSL Crater production scaling law by Holsapple and Housen (2007). (p. 106)

IAU International Astronomical Union. (p. 101)

IRS Infrared Spectrograph of the Spitzer space telescope (SST). (p. 99)

LCDB Asteroid Lightcurve Database. (pp. viii, 11, 195, 201)

MBA Main Belt Asteroid. (pp. 3, 97, 192)

MBC Main Belt Comet. (pp. 3, 15)

MPC Minor Planet Center. (pp. 2, 97)

NAC Narrow Angle Camera of OSIRIS. (pp. 99, 100, 104, 106, 109, 111)

NEO Near-Earth Object. (pp. 19, 21, 160, 195)

NSL Crater production scaling law by Nolan et al. (1996). (p. 106)

PC Particle–Cell. (pp. 67, 68)

PLS Palomar-Leiden survey. (pp. 5, 75)

PP Particle–Particle. (pp. 67, 68)

PPD Proto-Planetary Disk. (pp. 13, 15, 16, 26, 145)

RSI Radio Science Investigation of the Rosetta spacecraft. (p. 103)

SDSS Sloan Digital Sky Survey, `http://www.sdss.org`. (p. 5)

SFD Size Frequency Distribution. (pp. 5, 16, 18)

SKADS Sub-Kilometer Asteroid Diameter Survey. (pp. 5, 75)

SL9 D/Shoemaker-Levy 9. (pp. 28, 112)

SMASSII Small Main-Belt Asteroid Spectroscopic Survey, Phase II (Bus 2002b). (pp. 7, 8)

SMASSIR Small Main-Belt Asteroid Spectroscopic Survey in the near-infrared (Burbine 2002). (p. 7)

SMBAS Subaru Main Belt Asteroid Survey (Yoshida and Nakamura 2007). (p. 5)

SPH Smoothed Particle Hydrodynamics. (pp. i, 47, 48, 52–58, 72, 73, 75, 76, 78, 79, 81, 82, 94, 96, 113–117, 119, 124, 133, 138, 139, 141, 143, 146, 147, 157, 199)

SST Spitzer space telescope. (p. 197)

TNO Trans-Neptunian Object. (pp. 2, 8, 17)

WAC Wide Angle Camera of OSIRIS. (pp. 100, 102, 104, 106, 109, 153)

YORP Yarkovsky-O'Keefe-Radzievskii-Paddack. (pp. ii, 19, 21–23, 49, 102, 128, 138, 143, 155–158, 160)

YORPoid A asteroid with the typical top-like shape most likely originating from YORP induced spin-up. (pp. ii, 23, 100, 102, 106, 119, 158, 160)

Mathematical Symbols, Latin

A Geometric albedo.

a Long axis of ellipsis or spheroid, semimajor axis.

B Linear coefficient of the Ivanov failure model.

b Short axis of ellipsis or spheroid.

C Coupling parameter; see Holsapple and Schmidt (1987).

c heat capacity.

C_1 Constant term relating shock velocity and particle velocity in many materials.

C A constant.

C_{YORP} YORP amplitude factor.

D Diameter.

d Depth.

D Dimension.

d_{crater} Depth of the final crater.

D_{crit} Critical diameter of cratering on a small body before disruption.

d_{tc} Depth of the transient crater cavity.

D_{dam} Damage parameter.

e Internal energy.

E_{bd} Gravitational binding energy.

E_{kin} Kinetic energy..

E_{pot} Potential energy..

F Force.

G Newtons gravitational constant.

G Phase function slope parameter.

g Surface acceleration due to gravity.

H Absolute magnitude.

h Smoothing length in Smoothed Particle Hydrodynamics (SPH) simulations. The kernel function is usually defined to be zero for distances further away than $2h$ from the particle.

i Integer index number.

I Moment of inertia.

i Inklination.

$\mathbf{J}$ Shear stress invariant.

j Integer index number.

K Thermal conductivity.

k Limiting shear strength.

$k_{\mathbf{W}}$ Weibull parameter, linear coefficient.

l Length or typical lengthscale.

M_a Mean anomaly.

M Mass.

$M_{\mathbf{imp}}$ Mass of the impactor.

$M_{\mathbf{tar}}$ Mass of the target body.

$M_{\mathbf{tot}}$ Total Mass.

$M_{\mathbf{lr}}$ Mass of the largest remnant fragment.

$m_{\mathbf{W}}$ Weibull parameter, exponent of power law.

N Integer number.

P Period.

p Pressure.

p Deviatoric part of the stress tensor.

p_c Linear coefficient of the Ivanov failure model.

Q Specific energy of impact.

q Perihelion distance.

Q^* Specific disruption energy threshold. Q^* denotes the kinetic energy of the impactor in units of target mass where the largest remaining fragment left after the impact has 50 % of the target mass.

Q_D^* Specific energy threshold leading to disruption.

$Q_{RD\,\mathbf{1:1}}^*$ Equivalent equal mass specific impact energy at disruption.

Q_S^* Specific energy threshold leading to shattering.

R Radius.

$R_{\mathbf{C1}}$ Effective radius of mass-equivalent sphere at reference density $\rho_0 = 1000\,\mathrm{kg\,m^{-3}}$.

$R_{\mathbf{equiv.}}$ Radius of volume-equivalent sphere.

$R_{\mathbf{imp}}$ Impactor radius.

$R_{\mathbf{max}}$ Maximum Radius.

$R_{\mathbf{min}}$ Minimal Radius.

$R_{\mathbf{tar}}$ Target radius.

s Friction coefficient, the slope of the failure envelope in the Drucker-Prager failure criterion.

S_1 Linear term relating shock velocity and particle velocity in many materials.

s Deviatoric part of the stress tensor.

t Time.

$T_{\mathbf{J}}$ Tisserand parameter.

$\mathbf{U}$ Quality parameter of the LCDB database.

v Velocity vector.

$v_{\mathbf{esc}}$ Escape velocity.

$v_{\mathbf{imp}}$ Velocity vector of the impactor.

V Volume.

$v_{\mathbf{s}}$ Shock front velocity.

W Kernel function in the SPH formalism.

X Probability.

x Position.

$x_{\mathbf{cell}}$ Centre of cell.

$x_{\mathbf{cms}}$ Centre of mass.

Y Yield strength.

$Y_{\mathbf{d}}$ Yield strength of damaged material.

$Y_{\mathbf{d}0}$ Damaged strength at zero pressure.

$Y_{\mathbf{i}}$ Yield strength of undamaged material.

$Y_{\mathbf{i}0}$ Intact strength at zero pressure.

$Y_{\mathbf{i\,lim}}$ Limiting strength of material.

$Y_{\mathbf{i\,dam}}$ Limiting strength of damaged material.

$Y_{\mathbf{M}}$ von Mises plastic limit.

Mathematical Symbols, Greek

α Power law index.

α Distension, the ratio of specific volumns of a porous material and the matrix material.

β Phase angle, angle between sun – surface – observer.

δ Kronecker delta.

ϵ Excentricity.

ε Strain.

$\dot{\varepsilon}$ Strain rate.

$\varepsilon_{\mathbf{ero}}$ Geometric strain limit for erosion.

$\varepsilon_{\mathbf{f}}$ Plastic strain at failure.

$\varepsilon_{\mathbf{fc}}$ Minimum failure strain.

$\varepsilon_{\mathbf{p}}$ Accumulated plastic strain.

η Power law exponent for the mass dependence of the fragment velocity.

Γ Gruneisen coefficient.

γ Thermal inertia.

μ Coupling parameter velocity exponent.

$\mu_{\mathbf{i}}$ Coefficient of internal friction.

ν Coupling parameter density exponent.

Ω Argument of ascending node.

ω Angular frequency.

ω Argument of perihelion.

Φ Angle of friction.

π Circle constant.

ϕ Porosity.

ϕ_b Bulk Porosity.

$\phi_{\mathbf{macro}}$ Macroporosity.

$\phi_{\mathbf{micro}}$ Microporosity.

ρ Density.

$\rho_{\mathbf{bulk}}$ Bulk density.

$\rho_{\mathbf{grain}}$ Grain Density, $\rho_{\mathrm{grain}} = {1 - \rho_{\mathrm{bulk}}}/{\phi_{\mathrm{micro}}}$.

ρ_0 Reference density.

σ Shear stress or stress tensor.

σ Strength of material.

$\tau_{\mathbf{cc}}$ Contact and compression time scale parameter.

$\tau_{\mathbf{exc}}$ Time scale for the excavation phase in cratering events on planets.

$\tau_{\mathbf{rel}}$ Time scale for relaxation of exited rotational states of asteroids.

Θ Obliquity, angle between impactor velocity vector and the targets surface.

ϑ Surface slope angle.

Declaration

This thesis has not been submitted as an exercise for a degree at any other university.

Except where stated, the work described therein was carried out by me alone.

I give permission for the Library to lend or copy this thesis upon request.

SIGNED: